SHOCK COMPRESSION OF SOLIDS

Lee DAVISON and R.A. GRAHAM

Sandia Laboratories, Albuquerque, New Mexico 87185, U.S.A.

NORTH-HOLLAND PUBLISHING COMPANY – AMSTERDAM

PHYSICS REPORTS (Review Section of Physics Letters) 55, No. 4 (1979) 255–379. North-Holland Publishing Company

SHOCK COMPRESSION OF SOLIDS

Lee DAVISON and R.A. GRAHAM

Sandia Laboratories, Albuquerque, New Mexico 87185, U.S.A.

Received April 1979

Contents:

Abstract:

This review contains a brief, comprehensive, critical assessment of the status of investigations concerning the response of solids to shock compression. Mechanical, metallurgical, electrical, optical and other phenomena occurring in substances subjected to shock pressures covering the range from about 0.1 to 6000 GPa are considered. Emphasis is placed on physical interpretation of observations peculiar to the shock environment and on the relationships among observations in the various areas of investigation.

1. Introduction

The introduction of a plane shock wave into a solid body provides a means for subjecting it to large, carefully controlled compression. Study of the effects of this compression, and the ensuing decompression, has formed the primary objective of the research to be reviewed here. Plane shock compression is accompanied by shear, so the shear strength of the material and its inelastic response are additional important considerations. Finally, shock compression is accompanied by heating attributable to both compression and dissipation and effects of this heating must be taken into account.

In typical experiments, loading is accomplished by impact or explosion. In some cases shock loading has been used to produce compressions as small as a fraction of one per cent while, in others, the density of the solid has been increased more than fourfold. The shock heating causes increases in temperature ranging from negligible amounts for weak shocks to values as high as several electron volts (several tens of thousands of kelvins) for the strongest shocks examined experimentally.

On a macroscopic scale, a shock-compression experiment comprises a precise, orderly, and comprehensible sequence of events. However, this sequence evolves rapidly. The shock itself may rise to full amplitude in a time not exceeding a few nanoseconds and a typical experiment runs its entire course in only about a microsecond. It is during this period, while the substance is in a thermodynamic state that is difficult or impossible to produce by other means, that interesting physical phenomena present themselves for examination. Unfortunately, one cannot terminate a completed experiment in the same orderly fashion in which it was conducted. The aftermath imprinted in our human experience is often a violent explosion accompanied by much rending of metal, splintering of wood, and emission of light and sound. With this experience in mind, it is difficult for many to appreciate the underlying orderly process. Indeed, Duvall [63D2]* has found it necessary to point out that the rapidity and violence of an explosion do not vitiate Newton's laws, nor those of thermodynamics, chemistry, or quantum mechanics. They do, however, force matter into states quite different from those with which we customarily deal. These states provide a stringent testing ground for some of our favorite assumptions about the bulk properties of matter.

Research on plane shock compression of solids began during World War II. In the early investigations, materials were compressed by plane detonation of a contacting block of high explosive. The compressions achieved in metals by this means were generally in the range of 10 to 30 per cent and correspond to compressive stresses of from 10 to 50 GPa.**

These stresses so exceeded the yield strength of the metals that shear stresses were neglected entirely and the state of the solid characterized just as if the material were fluid. Values of pressure, specific volume, and internal energy density in states of compression achieved by shocks of various strengths were measured and additional information such as temperature was inferred theoretically.

The first review of the field, that prepared by Rice, McQueen and Walsh [58R1] some twenty years ago, was devoted entirely to their work on measurement of the compressibility of metals in the pressure range that can be achieved by contact detonation. This review was instrumental in

* References are arranged at the end of the review by year of publication, within which they are alphabetized by the first author's surname and assigned a serial number within that letter grouping.

** 1 GPa $\equiv 10^9$ N/m^2 = 10 kbar = 145038 lb/in^2.

demonstrating the scientific potential of studies of solids under shock compression and it remains the most widely cited work in the field.

In the years that have passed since this early work, the limits to the pressure range investigated experimentally have been extended some one-hundredfold both upward and downward. The low-pressure portion of this range now overlaps that accessible to investigation by a variety of static techniques, but the higher pressures are the unique province of shock-compression research. The range of phenomena considered has grown to include at least some aspect of most subjects treated in textbooks on solid-state physics, physical metallurgy, and continuum mechanics.

Military applications originally motivating research in this field continue to provide an important stimulus, but the subject has developed into one of scientific interest in its own right and has found application in other areas of physics, geophysics, and metallurgy. Shock and static-high-pressure studies are mutually supportive. Nonmilitary technological application of the methods or results of shock-compression research have been slow to materialize, although there have been several notable successes. Metal parts are now routinely shaped, joined, and welded with explosive loading methods and these applications of shock waves have been found economically advantageous in many instances [71E1]. Diamonds suitable for use as industrial abrasives have been synthesized from graphite. Some of the first sandwich coins minted in the United States were made from explosively-laminated metal and miniaturized explosive bonding is used to repair electronic microcircuits.

The field under review remains in its infancy. Only a few laboratories are involved in this work, but their number has steadily increased and interest in the subject is worldwide. Workers tend to think of themselves as specialists in "shock-wave physics" rather than as investigators of particular physical phenomena. This, too, is changing, but interpretation of the effects of the unique conditions of a shock-compression experiment still imposes a certain requirement of specialized knowledge. Early work required rather special facilities where large amounts of high explosive could be detonated. The advent of technology for controlled projectile impact has made it possible to conduct shock-wave experiments in more conventional laboratory settings, however, and with finer control over appropriate variables. Improvements in instrumentation, primarily the result of advances in electronics and optics, are making it possible to conduct experiments on a smaller scale than was previously possible. These two developments would seem to open the way for more widespread application of the method than has heretofore been possible.

The basis of research on shock compression of solids is firmly experimental and is so presented in this review. One cannot doubt the influence of theoretical developments, and quantitative interpretation and generalization of observations is the goal of most work. The relative importance of theoretical research is increasing as experimental investigations have been successful in delineating the physical nature of shock processes.

We have attempted to provide a concise, critical review of the status of investigations of the properties of shock-compressed solids and have provided adequate reference to original and review sources. We emphasize studies directed toward underlying physical phenomena and the relationship among results from diverse areas of investigation. Repetition of work summarized in recent reviews has been avoided and original material has been added in a few instances.

1.1. Guide to the review literature

The literature on shock compression of solids has grown dramatically over the past twenty years and the lack of a single comprehensive reference source to this field presents a formidable barrier to entry. Even the review literature is difficult to follow since both the range of subjects covered and the degree of detail presented in the numerous reviews are highly variable. Because the field has changed in technical content, depth, and emphasis, most material in reviews more than ten years old is dated.

Our background study of prior reviews resulted in a summary and evaluation that may prove useful to the reader. This work is presented in three tables. Table 1.1 covers broad, general reviews,

Table 1.1
General review articles

Reference	No. of pages	No. of refs.	Topics covered: Technique	Eq. of state	Viscous	Transition	Strength	Fracture	Electrical	Residual	Remarks
Rice et al. [58R1]	63	41	×	×		×	×				Classic first, most widely cited, dated
Duvall [61D2]	37	78		×		×	×				General, dated
Duvall and Fowles [63D3]	82	145	×	×	×	×	×	×		×	Comprehensive
McQueen [64M1]	86	64	×	×	×	×	×	×		×	Author's own work
Al'tshuler [65A2]	39	169	×	×		×	×	×			Soviet literature
Doran and Linde [66D3]	61	237				×			×	×	Broad, uncritical
McQueen et al. [70M1]	124	52	×	×	×	×	×	×			Authors' work, thorough
Jones [72J3]	23	32			×		×	×		×	Elementary
Murri et al. [74M3]	163	527	×	×	×	×	×	×	×	×	Contemporary, comprehensive

while table 1.2 summarizes detailed reviews of specific topical areas. Table 1.3 summarizes articles in which various investigators have reviewed the status of their own work and lists proceedings of conferences devoted to shock compression of solids. There is no single textbook covering any appreciable fraction of the subject matter of the field. Chapters of interest in published volumes include Chapter XI of Zel'dovich and Raizer [66Z1] and Chapter VIII of Cristescu [67C4]. Other tutorial treatments are: [68D5, 73D6, 73T3, 73F1, 73J1, 73O2, 76H2, 77S2]. Popularized accounts of the subject have been published by Duvall [63D2] and Linde and Crewdson [69L1].

A very complete, recently updated, tabulation of high-pressure shock-compression data is given by van Thiel et al. [77V1] and data from the Los Alamos Scientific Laboratory have been tabulated by McQueen and coworkers [69G2, 70M1]. Keeler [72K3] has derived and tabulated isothermal compression curves using shock-compression data. Hugoniot elastic limit data have been tabulated by Jones and Graham [71J4], and data on shock-induced phase transitions are included in a review of the subject by Duvall and Graham [77D6].

Table 1.2
In-depth reviews of specific topical areas*

Geophysics
Ahrens et al. [69A1] (74, 67)
Ahrens [72A1] (30, 124)
Stöffler [72S4] (63, 256)
Grady [77G2] (50, 91)

Phase transitions
Dremin and Breusov [68D4] (11, 92)
Jones and Graham [71J4] (12, 102)
Hayes [77H3] (49, 28)
Duvall and Graham [77D6] (57, 405)
Al'tshuler [78A6] (10, 46)**

Equations of state
Knopoff [63K2, 63K3] (18, 30; 16, 35)
Al'tshuler and Bakanova [69A2] (12, 45)
Royce [71R1] (16, 44)
Royce [71R2] (11, 11)
Duvall [73D5] (32, 21)

Viscoplastic behavior
Hopkins [61H1] (14, 136)
Wilkins [64W1] (53, 17)
Herrmann [69H1] (54, 101)
Herrmann and Nunziato [73H2] (158, 81)
Herrmann [76H3] (26, 54)

Composites
Bedford et al. [76B4] (54, 83)

Viscoelastic behaviour
Nunziato et al. [74N4] (108, 217)

Metallurgical effects and metalworking
Dieter [62D2] (16, 100)
Appleton [65A3] (6, 59)
Zukas [66Z2] (19, 61)
Otto and Mikesell [67O1] (44, 65)
Crossland and Williams [70C2] (21, 95)
Leslie [73L1] (76, 100)

Technique
Deal [62D1] (26, 27)
Doran [63D1] (27, 57)
Keeler [71K1] (30, 45)
Fowles [73F2] (75, 60)
Grady [77G2] (50, 91)
Graham and Asay [78G5] (36, 218)

Numerical methods
Wilkins [64W1] (53, 17)
Herrmann and Hicks [73H1] (34, 32)

Spall fracture
Davison and Stevens [71D1] (88, 68)

Optical properties
Kormer [68K5] (25, 178)

Magnetic properties
Royce [71R3] (13, 40)

Electrical conductivity
Kormer [68K5] (25, 178)
Styris and Duvall [70S3] (22, 75)
Keeler [71K2] (20, 44)
Yakushev [78Y1] (16, 65) (Technique)

Shock-induced electrical polarizations
Mineev and Ivanov [76M4] (19, 148)

Chemical physics
Adadurov et al. [73A1] (12, 55)

* Numbers in parentheses indicate number of pages and number of references cited, respectively.
** *Added in proof.* We have been unable to cite this recent review elsewhere in the text.

Table 1.3
Reviews of current status*

Duvall [62D3] (5, 30)	General
Skidmore [65S1] (36, 50)	General
Graham [67G1] (7, 43)	Technique, electronic properties
Gilman [68G2] (16, 80)	Viscoplasticity; see also [69G1]
Karnes [68K1] (23, 19)	Technique
Jones et al. [70J4] (67, 119)	Very high pressure
Jones [71J3] (11, 41)	Plastic deformation
Keeler [71K3] (13, 22)	X-ray diffraction, Brillouin scattering
Barker [72B2] (6, 27)	Interferometric technique
Carter [73C1] (13, 16)	Phase transitions
Carter [73C2] (11, 17)	Phase transitions
Duvall [73D4] (36, 42)	Applications
Clifton [74C1] (65, 96)	Viscoplasticity
Duvall [76D4] (17, 38)	Phase transitions
Curran et al. [77C2] (9, 15)	Spall

Conference proceedings

Editors	Reference	Emphasis
Shewmon and Zackay	[61S1]	Metallurgical effects
Ribaud	[62R2]	General
Williams	[63W1]	General
Jacobs	[65J1]	Principally detonation
Berger	[68B3]	General
French and Short	[68F1]	Geophysical
Jacobs and Roberts	[70J1]	Principally detonation
Kinslow	[70K2]	General
Burke and Weiss	[71B1]	General
Lloyd	[71L1]	Static and shock
Chou and Hopkins	[73C7]	Mechanical phenomena, low stress
Rohde et al.	[73R3]	Metallurgical
Osugi	[75OS1]	Static and shock, very broad
Edwards	[76E1]	Principally detonation
Varley	[76V1]	General
Manghnani and Akimoto	[77M7]	Geophysical, static and shock
Dubovitskii	[78D2]	Principally detonation, in Russian
Timmerhaus and Barber	[79T1, 79T2]	Static and shock, very broad

* Numbers in parentheses give number of pages and number of references, respectively.

2. Background

Research on shock compression of solids involves consideration of both microscopic and macroscopic phenomena; but the direct experimental observations, with very few exceptions, are made at the macroscopic level. The substance of this section is a brief summary of certain background material necessary to understand these observations. Additional background information related to electrical phenomena is given in sections 4.1 and 4.2.

2.1. Kinematical and dynamical relations

In this subsection, we discuss the motion of continuous bodies and the equations representing the principles of balance of mass, momentum, and energy as applied to such bodies. Kinematical and dynamical aspects of continuum theories of matter are discussed in great detail by Truesdell and Toupin [60T1], while simplified treatments adequate for most discussions of plane waves have been given by Cristescu [67C4], Zel'dovich and Raizer [66Z1], Chou and Hopkins [73C7], Jones [72J3, 73J1], Murri et al. [74M3], and in other general references cited in section 1.

Kinematics. In this review we consider material bodies that reside in an inertial space in which the places are denoted by Cartesian coordinates x_i, $i = 1, 2, 3$. The material points (usually called "particles", a term to be understood in the continuum sense rather than in terms of microscopic concepts) comprising the body are designated by the components X_i, $i = 1, 2, 3$, of the place they occupy when the body is in some reference configuration. The reference configuration may be, and usually is, the initial state of the material as it is about to undergo some deformation of interest. This is not necessarily the case, however, and we allow for reference to some configuration existing at absolute-zero temperature, before a prior wave interaction, etc. A motion of the body is described by a relation of the form $x_i = X_i + d_i(X_1, X_2, X_3, t)$, where the vector $\boldsymbol{d}$ represents the *displacement* of a material point from its reference position to its current position.

The components of the *particle velocity* $\boldsymbol{u}(\boldsymbol{X}, t)$ and the *particle acceleration* $\dot{\boldsymbol{u}}(\boldsymbol{X}, t)$ of the material point $\boldsymbol{X} \equiv (X_1, X_2, X_3)$ are given by the equations

$$u_i = \partial d_i/\partial t, \qquad \dot{u}_i = \partial u_i/\partial t. \tag{2.1}$$

The relative motion of neighboring material points of the body is important in studies of material behavior so the *deformation gradient* $\boldsymbol{F}$ having components $F_{ij} = \delta_{ij} + \partial d_i/\partial X_j$ and the *material strain tensor* $\boldsymbol{\eta}$ or, for small strains, the *linearized tensor* $\boldsymbol{S}$ having the components

$$\eta_{ij} = \frac{1}{2}\left(\frac{\partial d_i}{\partial X_j} + \frac{\partial d_j}{\partial X_i} + \frac{\partial d_k}{\partial X_i}\frac{\partial d_k}{\partial X_j}\right) \quad \text{and} \quad S_{ij} = \frac{1}{2}\left(\frac{\partial d_i}{\partial X_j} + \frac{\partial d_j}{\partial X_i}\right), \tag{2.2}$$

respectively, assume important roles.

The use of the spatial (also called "Eulerian" or "laboratory") coordinate frame, x, is quite common, seems very natural, and is most appropriate for problems (usually fluid dynamics) where instrumentation is fixed in space and monitors the passing flow. The material (or "Lagrangian") frame X is more appropriate for problems of solid dynamics in which instruments are fixed to the moving sample. Material coordinates are also required for the analysis of problems in which the separate material points have, or acquire, distinguishing properties.

Uniaxial strain. Most shock-compression experiments involve application of normal forces uniformly over the face of a material slab. Since the experiment is conducted in the central part of the slab, and is completed before the arrival of any wave originating at its edge, the analysis can be carried out as though the slab were of infinite lateral extent. In materials having suitable symmetry of response (for example, those that are isotropic) the coordinates can be chosen so that all material points move in the 1 direction. In this case the motion takes the form $x_1 = X_1 + d_1(X_1, t)$, $x_2 = X_2$, $x_3 = X_3$. The only non-zero components of the strain tensors corresponding to this motion are

$$\eta_{11} = \partial d_1/\partial X_1 + \tfrac{1}{2}(\partial d_1/\partial X_1)^2 \quad \text{and} \quad S_{11} = \partial d_1/\partial X_1. \tag{2.3}$$

As these equations show, the component S_{11} of the linearized strain tensor can be used in exact finite-strain analyses in the special case of uniaxial strain. The components η_{11} and S_{11} are related by the exact direct and approximate inverse relations

$$\eta_{11} = S_{11} + S_{11}^2, \quad S_{11} = \eta_{11} - \eta_{11}^2 + 2\eta_{11}^3 + \dots . \tag{2.4}$$

The specific volume and density changes are related to the strain by the equations

$$S_{11} = v/v_R - 1 = \rho_R/\rho - 1, \tag{2.5}$$

where $\rho = 1/v$ is the mass density of the material at a given point and the subscript R designates evaluation in the reference state. When a body is subjected to uniaxial strain, its shape as well as its volume is changed and this change in shape is described by an angle γ (called the tensor component of the *shear strain*) that is related to the strain by the equation:

$$\gamma = (\tan^{-1}(S_{11} + 1)) - \tfrac{1}{4}\pi = \tfrac{1}{2}S_{11} + \dots . \tag{2.6}$$

Uniaxial strain is one of the simplest cases one can encounter and considerable effort is expended to ensure that it is the deformation produced in most shock-compression experiments.

Stress. The boundary loads and internal forces in continuous bodies can be represented by the symmetric tensor $\boldsymbol{t}$ called the *Cauchy stress tensor.* The component t_{ij} of this tensor is the component in the x_j direction of the force per unit area (in the deformed configuration) acting across a surface having its normal in the x_i direction. Because of its symmetry, $\boldsymbol{t}$ can be expressed in diagonal form. That is, the coordinates x can be chosen so that $t_{ij} = 0$ for all $i \neq j$. In this case the diagonal components are called *principal stresses.* Our sign convention has been chosen so that a positive value of one of the principal stresses corresponds to tension in the associated direction in the body.

When a slab of isotropic material, or a suitably oriented slab of lower symmetry, is loaded uniformly over one or both faces, a coordinate normal to the faces is an axis of principal stress. Suitably chosen directions in the plane of the slab are also directions of principal stress. When the response of the material is isotropic, the two lateral principal stresses are equal, so that

$$t_{11} \neq 0, \quad t_{22} = t_{33} \neq 0, \quad t_{ij} = 0, \quad i \neq j. \tag{2.7}$$

When these relations hold (with $t_{11} \neq t_{22}$), every plane in the body except those exactly parallel or perpendicular to the 1 axis is subjected to a shear stress. The magnitude of this stress is maximized on planes lying at 45° to the 1 axis, and its value on these planes is

$$\tau = \tfrac{1}{2}(t_{11} - t_{22}). \tag{2.8}$$

The pressure in the body is defined in terms of the average of the principal stresses:

$$p = -\tfrac{1}{3}(t_{11} + t_{22} + t_{33}) = -\tfrac{1}{3}(t_{11} + 2t_{22}). \tag{2.9}$$

From these formulae we see that the longitudinal stress component can be expressed in the form

$$t_{11} = -p + \tfrac{4}{3}\tau, \tag{2.10}$$

which shows how the applied load is borne in part by the pressure in the material and in part by its resistance to shear. The lateral stress components can be written $t_{22} = t_{33} = -p - \frac{2}{3}\tau$. In an experiment, the stress component t_{11} is subject to control by the imposed boundary conditions. The lateral stresses $t_{22} = t_{33}$ are not normally controlled and take whatever values are consistent

with the state of uniaxial strain until they are altered by the arrival of waves from the lateral boundaries of the sample. It is this situation that leads to the statement that the sample is inertially confined.

Equations of balance. The forces in material bodies, and the motions they undergo, are constrained by the requirement that the equations representing the principles of conservation of mass and of balance of momentum and energy be satisfied. When the fields of interest are smooth enough, these relations can be expressed in terms of partial differential equations that take the forms

$$\frac{\partial \rho}{\partial t} + \frac{\partial}{\partial x}(\rho u) = 0, \qquad \frac{\partial t_{11}}{\partial x} = \rho \dot{u}, \qquad \rho\left(\frac{\partial \varepsilon}{\partial t} + \frac{\partial \varepsilon}{\partial x} u\right) = t_{11} \frac{\partial u}{\partial x} \tag{2.11}$$

when restricted to motions of uniaxial strain in which body forces, thermal conduction and radiation are neglected. The quantity ε appearing in eq. $(2.11)_3$ is the *internal energy density*. Here, and subsequently, we have omitted the subscript 1 from vector components in the x_1 direction and from the coordinate itself.

The smoothness conditions required for the validity of equations (2.11) are satisfied for most values of x and t of interest in specific problems, but they may be violated on certain surfaces propagating through the material. One such surface, the *shock wave* (or simply *shock*), forms the principal subject of this review. A shock is a propagating surface across which the particle velocity and stress are discontinuous. At such a surface the differential equations of balance are replaced by the algebraic equations

$$[\rho(u - u_n)] = 0, \qquad [\rho u(u - u_n) - t_{11}] = 0, \qquad [\rho(\varepsilon + \tfrac{1}{2}u^2)(u - u_n) - t_{11}u] = 0.$$

In these relations u_n is the velocity of normal displacement of the shock relative to the x_1 coordinate, and the brackets designate the jump in the enclosed quantity at the wave: $[\varphi] = \varphi^- - \varphi^+$, where φ^+ and φ^- are limits of some function φ as the wave is approached from the front (the material into which it is advancing) and from the rear, respectively.

A less severe discontinuity than a shock is the acceleration wave, so called because the particle acceleration experiences a jump across the wave even though the particle velocity is continuous. Acceleration waves have been the subject of considerable theoretical [73C4, 76C1] and some experimental [74N4, 79G2] interest in recent years. Investigation of these waves is closely related to the present subject and offers considerable scientific promise.

The foregoing differential equations of motion and jump conditions have been expressed in terms of the independent variables x and t, the spatial or laboratory coordinates and time. In many cases it is convenient to deal with equivalent relations expressed in terms of the material coordinates. When this transformation is made, the field equations become

$$\partial t_{11}/\partial X = \rho_R \dot{u}, \qquad \rho_R \dot{\varepsilon} = t_{11} \partial u/\partial X, \tag{2.12}$$

with the density and displacement gradient standing in the relation (2.5). Similarly, the jump conditions for a shock wave take the form

$$[u + (\rho_R/\rho)U] = 0, \qquad [t_{11} + \rho_R u U] = 0, \qquad [\rho_R(\varepsilon + \tfrac{1}{2}u^2)U + t_{11}u] = 0, \tag{2.13}$$

where U is the "Lagrangian" velocity of the wave, i.e., that relative to the X ($\equiv X_1$) coordinate. These latter relationships are often rewritten in the form

$$[\rho_R/\rho] = -[u]/U, \qquad [-t_{11}] = \rho_R U[u], \qquad [\varepsilon] = \frac{1}{2\rho_R}(t_{11}^- + t_{11}^+)[\rho_R/\rho], \tag{2.14}$$

where t_{11}^+ and t_{11}^- are values of the stress on the two sides of the shock. In this form, the first two equations express the thermodynamic variables ρ and t_{11} in terms of the kinematical quantities u and U. These equations can alternatively be written to express these latter quantities in terms of the former:

$$U^2 = \frac{1}{\rho_R}\frac{[\![t_{11}]\!]}{[\![\rho_R/\rho]\!]}, \qquad [\![u]\!]^2 = \frac{1}{\rho_R}[\![t_{11}]\!][\![\rho_R/\rho]\!]. \tag{2.15}$$

Equation $(2.14)_3$, often called the *Rankine–Hugoniot equation*, has the important property that it involves only the thermodynamic variables.

The jump conditions $(2.13)_{1,2}$ can be arranged in the form $[\![-t_{11}]\!] = \rho_R U[\![u]\!]$, $[\![-t_{11}]\!] = -(\rho_R U^2[\![v]\!]$ to show that the jump in stress is proportional to the jump in particle velocity through the coefficient $\rho_R U$ and to the jump in specific volume through the coefficient $-(\rho_R U)^2$. Lines in the $([\![-t_{11}]\!], [\![u]\!])$ and $([\![-t_{11}]\!], [\![v]\!])$ planes that connect states preceding and following a shock transition are called *Rayleigh lines* and have slopes corresponding to these coefficients. The quantity $\rho_R U$ itself is called the *shock impedance* of the material and is a measure of the difficulty with which it is compressed.

The shock jump equations are normally interpreted as constraints on the allowable discontinuous fields. They have an alternate interpretation, however, in terms of steady waves. Indeed, it is easy to show that the jump relations hold between any two points of a smooth waveform that is propagating steadily at a velocity U (see, for example, [73S7, 74H2]).

If the form of a smooth steady wave can be recorded experimentally, application of the jump relations to a succession of points on this waveform is sufficient to determine the entire deformation path in the (t_{11}, ρ) and (ε, ρ) planes traversed by a material point during passage of the wave. This procedure has been applied by Johnson and Barker [69J1] and Prieto and Renero [73P2] to a study of the viscoplastic behavior of an aluminum alloy and by Schuler [70S1] to the study of a viscoelastic polymer, poly(methylmethacrylate). In many cases recorded waveforms are not steady, and some similarly rigorous, deductive means for interpreting these observations would be most useful. Such a method, based on equations (2.12), has been proposed by Fowles and Williams [70F1] and further developed by Cowperthwaite and Williams [71C7] and Seaman [74S2]. This method is extremely attractive from the theoretical point of view but has so far proven difficult to implement experimentally.

2.2. The Hugoniot curve

Propagation of plane shocks. If the reference density, ρ_R, and the state $\mathscr{S}^+ = \{\varepsilon^+, t_{11}^+, u^+, \rho^+\}$ of the material into which the shock is advancing are specified, there remain five unknown variables, U and $\mathscr{S}^- = \{\varepsilon^-, t_{11}^-, u^-, \rho^-\}$ describing the shock. Specification of the boundary loading producing the shock establishes one of these variables. The jump conditions, say in the form (2.14), comprise three relations among the remaining four variables. One additional relationship is needed to complete the determination of all five variables. This additional relationship is called a *Hugoniot curve* and reflects the differing behaviors of specific materials. Measurement of Hugoniot curves forms one of the major tasks of shock-compression research.

The most commonly measured of the variables are the shock velocity U and the particle velocity u^-. The locus of associated values of U and u^- determined from a set of experiments involving

shocks of varying strength defines a Hugoniot curve. This curve depends on the state $\mathscr{S}^+$ of the material into which the shock is propagating and is said to be *centered* on this state. The Hugoniot curve centered on the state of rest at normal laboratory ambient conditions is called the *principal* Hugoniot curve of the material in question.

Experimental measurements are normally made relative to coordinates chosen so that $u^+ = 0$ and $U > 0$. When this choice is made we write $u^- \equiv u$. It has been found experimentally that some hundreds of materials are described to good approximation over the entire range of the available data by the linear relation between U and u:

$$U = a + bu \tag{2.16}$$

where a and b are positive constants characteristic of the material and of the initial state $\mathscr{S}^+$, in which the material is at rest under conditions of atmospheric pressure and temperature. By combining a measured Hugoniot curve with the jump conditions, a number of other Hugoniot relationships (ten in all) can be obtained between pairs of variables in the set $\{U, \mathscr{S}\}$. In the case where eq. (2.16) holds, these relationships include

$$[-t_{11}] = \rho_R(a + bu)u, \qquad [t_{11}] = (\rho_R a)^2[v](1 + b\rho_R[v])^{-2}, \tag{2.17}$$

and seven other less frequently used relationships. Because shocks can propagate in either the $+X$ or $-X$ direction, Hugoniot curves involving shock or particle velocity have two branches. Specifically, a Hugoniot curve relating stress and particle velocity jump can be reflected and translated in u so that a given jump in stress can be obtained for a wave having either positive or negative velocity and/or propagating into material in uniform motion. Information about the Hugoniot curve is the normal outcome of a series of shock-compression experiments. Hugoniot curves for three representative metals are shown in fig. 2.1.

It is significant that the foregoing discussion has been concerned entirely with mechanical variables and has not involved temperature or entropy. These quantities increase upon shock compression of a body but are not normally measured experimentally and cannot be calculated without invoking additional assumptions. Restricting attention to fluids, we see that when the Rankine–Hugoniot equation $(2.14)_3$ is combined with the first law of thermodynamics the differential equations

$$\frac{ds_H}{dv} = \frac{1}{2\theta_H}\left[(v^+ - v)\frac{dp_H}{dv} + p_H - p^+\right], \qquad \frac{d\theta_H}{dv} = -\frac{\gamma}{v}\theta_H + \frac{1}{2C_v}\left[(v^+ - v)\frac{dp_H}{dv} + p_H - p^+\right] \tag{2.18}$$

for calculating the entropy and temperature of Hugoniot states can be obtained. In these relations $p_H(v)$, $s_H(v)$ and $\theta_H(v)$ are the pressure, entropy density, and temperature along the Hugoniot curve centered on $\mathscr{S}^+$, $\gamma \equiv v(\partial p/\partial \varepsilon)_v$ is Grüneisen's parameter, and C_v is the specific heat at constant volume. Evaluation of θ_H and s_H requires that γ and C_v be known at all states on the Hugoniot curve. Expansion of $s_H(v)$ about the point $v = v^+$ gives, in consideration of eq. $(2.18)_1$, the result

$$[s] = -\frac{1}{12\theta_H}\left(\frac{d^2 p_H}{dv^2}\right)_{v^+}[v]^3 + \ldots . \tag{2.19}$$

From this relation we see that the increase in entropy of an element of material upon passage of a shock is of third order in the compression, i.e., small for small compressions. The Hugoniot curve

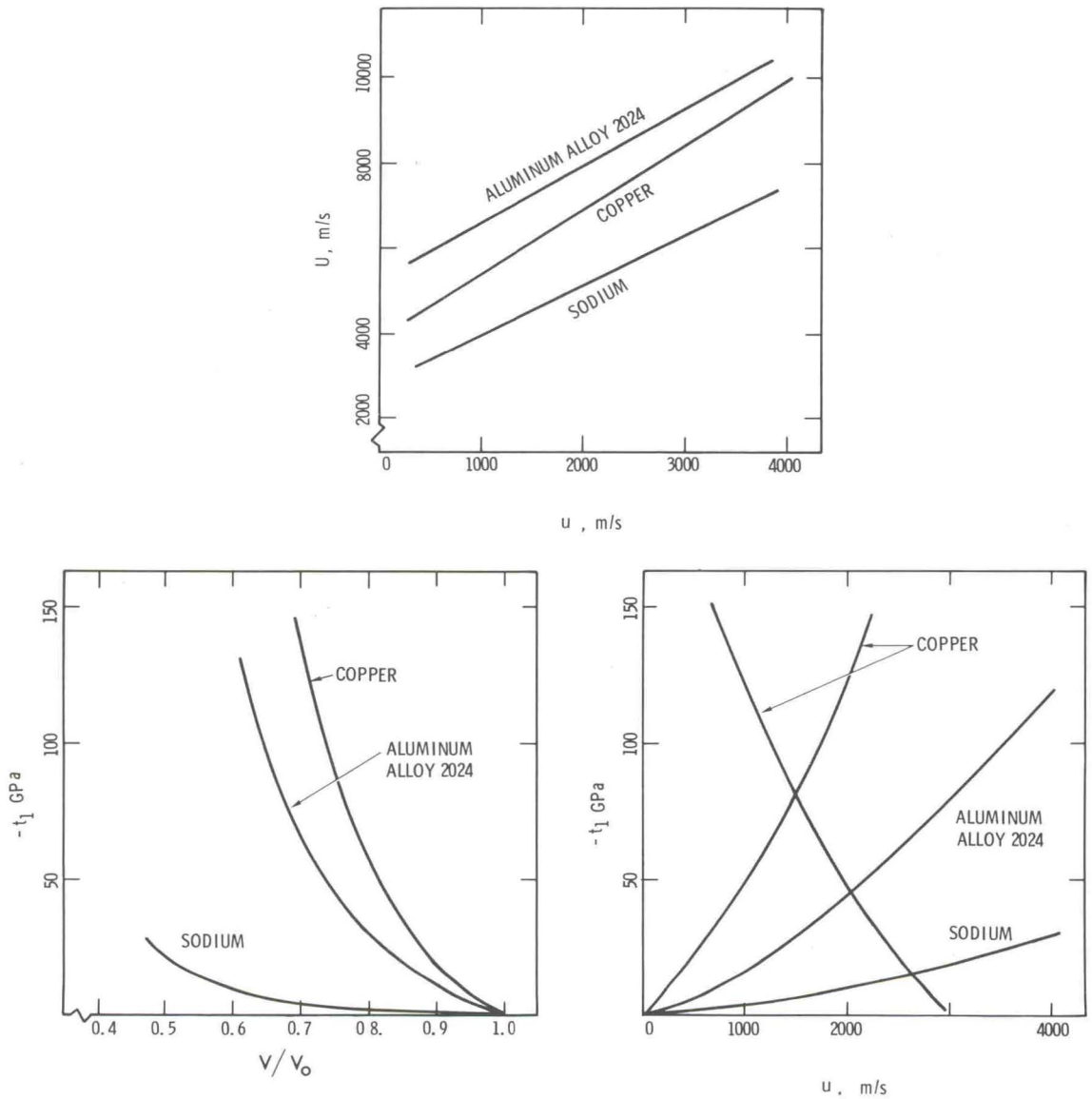

Fig. 2.1. Hugoniot curves in the (U, u), $(-t_1, v/v_0)$ and $(-t_1, u)$ planes are shown for three metals. Sodium is one of the most compressible of the solids normally studied, the aluminum alloy is an intermediate case, and the copper is less compressible, but comparable to nickel, chromium and stainless steels. Materials such as platinum, tungsten and gold are among the least compressible solids. The two $(-t_1, u)$ curves shown for copper illustrate the fact that reflection and translation in u is permissible.

centered on the point (p^+, v^+) has the same slope and curvature as the isentrope through this point.

Stability of shocks. One important problem that must be mentioned is that of stability of shocks. It will suffice for our purpose to present heuristic arguments and to point out two important cases where a stable shock transition between given states is not possible. Consider first the Hugoniot curve (A) in fig. 2.2a. A shock transition from the state $\mathscr{S}^+$ to the state $\mathscr{S}^-$ will propagate at a

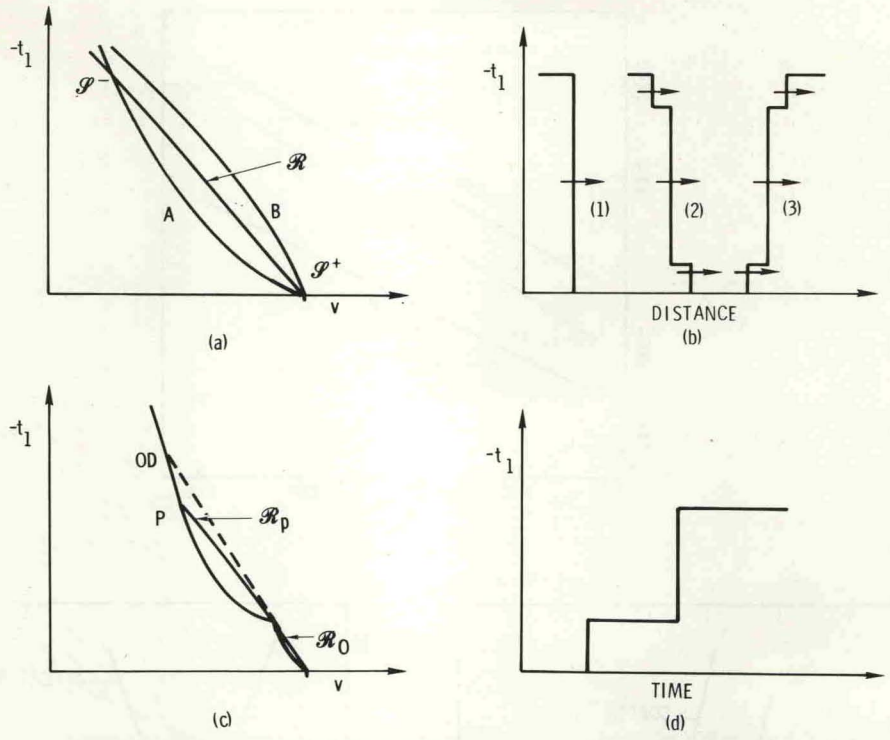

Fig. 2.2. Elementary considerations of the stability of shocks involve resolving the question of whether a small perturbation (see part (b) of the figure) advancing ahead of the shock, or falling behind, will propagate at a velocity that allows it to merge with the shock or at one that causes it to disperse further. In the former case the shock is stable, while in the latter it is unstable. As discussed in the text, this analysis shows that compression shocks are stable in material having a Hugoniot curve of the form of curve A in part (a) of the figure, and are unstable for Hugioniot curves of the form B. The reverse situation obtains for decompression waves. Parts (c) and (d) of the figure illustrate the Hugoniot curve and the corresponding stress history of a propagated compressive disturbance for a case where an elastic-plastic transition or collapse to a dense phase produces a discontinuity in the slope of a Hugoniot.

velocity proportional to the negative square root of the slope of the Rayleigh line $\mathscr{R}$. It can be expected to be a step in stress that advances in time as suggested by waveform (1) of fig. 2.2b. Suppose the shock were to exhibit a tendency to increase in thickness by virtue of small high-pressure wavelets falling behind and/or small low-pressure wavelets advancing ahead of the shock as illustrated by waveform (2) of the figure. These weak shocks will propagate at velocities essentially proportional to the slope of the Hugoniot curve at the maximum shock pressure and at its foot, respectively. By examination of the relative slopes of the Rayleigh line and these two tangents, we see that a waveform perturbed to look like (2) will tend to restore itself to form (1). We conclude that the shock is stable. The opposite conclusion would follow if we consider a decompression wave for this material or a compression wave for a material governed by the curve B in fig. 2.2a; the shock is not a stable solution to these problems (this issue can also be discussed in terms of an entropy production requirement and eq. (2.19)). The nature of the instability suggests that a smooth, spreading wave will form. Such a disturbance would have to satisfy the differential equations of motion (2.12), not the shock jump conditions, and such solutions do exist and have been studied extensively (see, for example, the classical treatment of Courant and Friedrichs [48C1]).

A second common source of instability is a cusp in the Hugoniot curve such as is illustrated in fig. 2.2c. This often occurs at the point defining the onset of plastic flow or structural phase transformation of the material. Waves of amplitudes falling below the cusp are analyzed as in the previous case. Supposing the low-pressure region to be one of stable shocks, waves of intermediate amplitude corresponding to point P separate into two shocks as indicated in fig. 2.2d. One shock takes the material from the initial state to that corresponding to the cusp. Its speed is that given by the slope of the Rayleigh line $\mathscr{R}_0$. The second shock takes the material from the state at the cusp to that at point P, and propagates at the lower speed corresponding to $\mathscr{R}_P$. Stronger shocks, those of amplitude greater than that corresponding to the overdrive point (OD) where the extension of $\mathscr{R}_0$ meets the Hugoniot curve, are stable. Hugoniot curves can exhibit a variety of slopes, curvatures, discontinuities, etc., that permit various combinations of the behavior discussed above.

The shock stability problem has many facets and has been the subject of a number of investigations (see, e.g., Nunziato and Herrmann [72N2], Swan and Fowles [75S4, 75F2], and Pleshanov [76P1]).

2.3. Experimental methods

The properties of shock-compressed solids became amenable to serious scientific investigation when methods were devised for producing plane shocks of controlled amplitude and for measuring the motions they induced in material samples. Workers in this field are greatly concerned with experimental methods and interpretation of even the most routine measurement involves consideration of the limitations imposed by the method used. Misinterpretations, errors in interpretation, and differences in interpretation often rest on different assessments of the influence of experimental method.

In spite of the major role played by experimental method, no comprehensive critical review is available and one must resort to separate reviews of specific aspects of the subject. The reviews of Graham and Asay [78G5], Grady [77G2], and Murri et al. [74M3] provide critical assessments of modern methods of observing stress or particle-velocity histories. McQueen et al. [70M1] describe the methods they employ in their hydrodynamic measurements. The reviews by Fowles [73F2] and Keeler [71K1] give overall treatments of both loading methods and methods of measuring wave profiles.

Loading methods influence the control that can be achieved over the increments of pressure that can be applied, the simultaneity of the loading over the sample face, and the decompression process. The methods most frequently used include detonation of contacting explosives, impact by explosively-driven flying plates, and impact by gun-driven projectiles. Intense pulses of radiation from electron beam accelerators, lasers, and X-ray and neutron sources have also been used.

Detection methods have evolved from measurement of displacement as either a discrete or continuous function of time to direct measurement of particle velocity or stress histories. With this change, a one-hundredfold improvement in the time resolution with which these histories can be measured has been achieved. Resolutions of particle velocity histories to within a few nanoseconds are not uncommonly reported and subnanosecond resolution has been achieved under restrictive conditions [78G5]. Recent improvements in electrical shorting pins provide the capability for subnanosecond time-of-arrival measurements [79M1].

Measurement of the (U, u) *Hugoniot curve.* The most basic aspect of the study of shock compression of materials is the measurement of a Hugoniot curve. In the high-pressure regime, this involves

measurement of the shock velocity U and the particle velocity jump $[u]$ at the shock transition.

There are three methods by means of which most data have been obtained: (1) the plate-impact or deceleration method, (2) the (stress-) free-surface velocity method, and (3) the impedance-mismatch or reflection method. An indication of the principles of each of these methods is given in fig. 2.3. The symmetric plate-impact method, that in which the impacting plate and the sample are of the same material, is the most basic and direct method, but the impedance-mismatch experiment is the most easily conducted and, therefore, the basis for most of the available data. The free-surface velocity method is restricted to compressions at which only moderate shock heating is encountered, but has been used extensively in this regime. These methods have been listed approximately in increasing order of the amount of material-property information that is needed either prior to interpreting a given experiment or that must be determined by iterative calculation during the interpretation process.

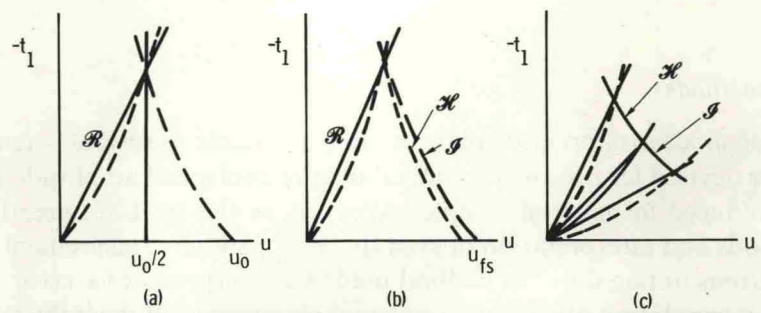

Fig. 2.3. Experimental methods of measuring Hugoniot curves are usually based on interpreting the wave interactions illustrated. In each case the solid lines represent known material properties or Rayleigh lines inferred from a measurement of the shock velocity U. The Hugoniot curve of the substance under investigation is shown dashed. The diagram (a) represents a symmetric impact in which the measured impact velocity u_0 is exactly twice the induced particle velocity. Measurement of u_0 and U suffices to determine the Hugoniot state. When the impactor is of a different material from the sample, but one having a known Hugoniot curve, measurement of u_0 and U also suffices to determine a Hugoniot state. Experiment (b) is interpreted on the basis of the approximation that the decompression isentrope ($\mathscr{I}$) differs little from the reflected Hugoniot curve ($\mathscr{H}$) so that measurement of U and the velocity, u_{fs}, of the free surface after shock reflection suffices to determine a Hugoniot state. Two cases of the impedance-mismatch experiment are shown in part (c) of the figure. The Rayleigh line and Hugoniot curve in the middle of the figure represent the known behavior of the standard base plate and the measurement of U in this base plate. When the advancing shock encounters the interface with the sample material, a shock is transmitted to the sample and either a second shock or an isentropic decompression wave is reflected back into the base plate. The Rayleigh line for the shock in the sample, as determined by measuring the velocity of this shock, can be plotted to establish the type of the reflected wave. With this information, the second-shock Hugoniot curve ($\mathscr{H}$) or the decompression isentrope ($\mathscr{I}$) plotted using the known behavior of the base plate material completes the determination of a point on the Hugoniot curve for the sample.

The Hugoniot curves and decompression isentropes of a number of materials ("*standards*") have been determined with the highest possible precision so they can be used as base plates in the determination of Hugoniot curves for other materials by the reflection method. The wave interactions encountered in these experiments have been discussed by Duvall [71D2] and others.

The actual conduct of experiments of the sort discussed above is time consuming and expensive and must be done with exacting attention to both design and execution if useful data are to be obtained. The methods by means of which these measurements are made in various laboratories will not be discussed in this review, as they have been reported elsewhere [65A2, 66J1, 70M1, 71K1, 75G2]. Measurement of electrical, magnetic, optical, and other properties involves special considerations discussed in subsequent sections of this review.

3. Mechanical and structural behavior

Work relative to viscoelastic solids [74N4], composite solids [74M3, 76B4], and materials undergoing phase transformation [77D6] has been reviewed in the references indicated, which we believe represent the current state of work in these fields. Past work on shock compaction of porous solids is the subject of current reviews [71H1, 74M3], but attention must also be called to certain fundamentally new work on this subject [78N3, 79N1].

3.1. Elastic solids

The continuum theory of deformation of elastic solids is old and well developed [65T1, 74T1]. In its linear version it is widely applied, but routine application of the nonlinear theory is of much more recent origin. Most of this application has been to the behavior of highly deformable materials such as rubber or to the explanation of subtle effects observed by precise ultrasonic measurements at small strain. Shock-compression experiments present an intermediate case in that materials such as vitreous silica and crystalline quartz or sapphire remain elastic to compressive strains as large as 5 to 10 per cent, exhibiting distinctly nonlinear responses over this range. In fact, nonlinear elastic effects are readily apparent in the response of a wide variety of materials to shock compression.

The stress relation obtained from an expansion of the internal energy function to fourth order in the finite strain $\boldsymbol{\eta}$ takes the form

$$t_{ij} = \frac{\rho}{\rho_R} F_{ik} F_{jl} (C_{kl} + C_{klmn}\eta_{mn} + \tfrac{1}{2} C_{klmnpq}\eta_{mn}\eta_{pq} + \tfrac{1}{6} C_{klmnpqrs}\eta_{mn}\eta_{pq}\eta_{rs} + \ldots). \tag{3.1}$$

The coefficients in this equation are functions of entropy, and are subject to a variety of thermodynamic constraints and to conditions imposed by the point symmetry of materials of interest. Various means, mostly involving very precise ultrasonic measurements at small strain, have been developed for measuring the coefficients of this equation. Some of these coefficients have been measured in shock-compression experiments and it is to this work that we now direct our attention. Relative to the ultrasonic work, shock experiments usually involve a less precise measurement at a much larger strain. Since the strains encountered in shock-compression experiments cover the entire range of elastic response, no extrapolation is involved in applications and the elastic range itself is determined.

Uniaxial strain. Plane waves of uniaxial strain can propagate in any direction into an undeformed isotropic body and in certain specific directions in anisotropic bodies [65B4]. If the 1-axes are chosen to lie in one of these allowable directions, the associated longitudinal stress is obtained from eq. (3.1) in the form

$$t_1 = \frac{\rho_R}{\rho} (C_1 + C_{11}\eta_1 + \tfrac{1}{2} C_{111}\eta_1^2 + \tfrac{1}{6} C_{1111}\eta_1^3 + \ldots), \tag{3.2}$$

where we have adopted the Voigt condensation of subscripts for symmetric tensors: $11 \to 1$, $22 \to 2$, $33 \to 3$, 23 and $32 \to 4$, 31 and $13 \to 5$, and 12 and $21 \to 6$. In dealing with the stress components and coefficients, one simply replaces the subscripts in adjacent pairs according to the above prescription, but the strains are treated according to the prescription $\eta_1 = \eta_{11}$, $\eta_2 = \eta_{22}$,

$\eta_3 = \eta_{33}$, $\eta_4 = 2\eta_{23}$, $\eta_5 = 2\eta_{13}$, $\eta_6 = 2\eta_{12}$ (similar relations hold for the linearized strain tensor S_{ij}). If, as we assume here, the material is unstressed in the reference state, the coefficient C_1 vanishes at the reference entropy. The change in entropy occasioned by passage of a shock is of the order η_1^3 (see eq. (2.19)), which means that the entropy dependence of the coefficients is negligible to the order of the expansion given except that the coefficient C_1 contributes to the highest-order term. This contribution is presumed to be small relative to errors in the determination of this coefficient in all work to date and is neglected in subsequent discussion. Using eq. $(2.4)_1$, the longitudinal stress component t_1 can be expressed in the form

$$t_1 = C_{11}S_1 + \tfrac{1}{2}(C_{111} + 3C_{11})S_1^2 + \tfrac{1}{6}(C_{1111} + 6C_{111} + 3C_{11})S_1^3 + \ldots . \tag{3.3}$$

It is noteworthy that, as pointed out by Thurston [69T1], the nonlinear material responds to finite uniaxial strain (to fourth order) as though it were linear if $C_{111} = -3C_{11}$ and $C_{1111} = 15C_{11}$. As discussed in section 2.2, a compression wave will propagate as a shock only if $C_{111} + 3C_{11} \leq 0$ (assuming the fourth-order term is negligible). This is the case with most materials and, when it prevails, the elastic coefficients can be obtained by fitting eq. (3.3) to stress-strain states obtained from shock-compression experiments conducted over the range of elastic response or from a single experiment in which the continuum of states realized in a centered decompression waveform is recorded. Graham [72G2], using data obtained by Barker and Hollenbach [70B2], has characterized Z-cut sapphire to fourth order by this method.

If $C_{111} + 3C_{11} > 0$, a centered simple wave will be produced by impact loading, and a record of this waveform suffices to determine the entire uniaxial stress-strain relation over the range of strains encountered. Vitreous silica is a material responding in this manner and its coefficients have been determined by Barker and Hollenbach [70B2] (see also [72G2]) on the basis of a simple wave analysis.

The simple wave produced by impacting vitreous silica has approximately the form of a linear ramp of velocity. When this ramp wave is used to load another elastic solid placed in contact with the vitreous silica, a measurement of the resulting smooth waveform introduced into the second material can be interpreted to yield its stress-strain response [79G2]. Because of the peculiar high-pressure properties of vitreous silica, it is capable of producing its characteristic low-pressure ramp wave even when loaded by contact with detonating high explosive (see Wackerle [62W1]). This fortuitous circumstance makes certain low-pressure measurements possible in laboratories otherwise equipped only for conducting the high-pressure hydrodynamic investigations discussed in the next section.

Shock-compression experiments carried out at stresses beyond the elastic range frequently produce a single stress-strain datum at the limit of this range (called the Hugoniot elastic limit). Knowledge of this limiting point is insufficient to fully determine the higher-order elastic properties of the material, and the measured value cannot be certified to be devoid of effects of a small amount of inelastic flow. Nevertheless, it is of interest to examine such data for evidence of contributions due to fourth-order elastic effects in cases where the third-order constants have been determined ultrasonically. To do this, we evaluate C_{111} from eq. (3.3). Neglecting the highest-order term, we find that $C_{111} = 2[(t_1 - C_{11}S_1)/S_1^2] - 3C_{11}$. Substituting tabulated values of C_{11} and the measured stress and strain at the Hugoniot elastic limit into this equation, we arrive at a result which we call C_{111}^{HEL}. A comparison of this result to other available data is shown in table 3.1. It is notable that in almost every case the absolute value of the third-order constant inferred from the Hugoniot elastic limit measurement is greater than the absolute value of the corresponding

Table 3.1
Comparison of third-order elastic constants determined from Hugoniot elastic limit measurements to other measurements*

Material	S_{xx} %	C_{xxx}^{HEL} TPa	C_{xxx}** TPa	C_{xxx}^{HEL}/C_{xxx}
[111] NaCl	1.8	−0.2 [70M2]	−0.175 [69B1]	1.14
[100] MgO	2.5	−6.0 [66A2]	−4.9 [69B1]	1.22
[100] MgO	0.64–0.83	−6.2 [77G2]	−4.9 [69B1]	1.27
[100] InSb***	2.9	−0.58 [65K2]	−0.31 [69B1]	1.87
[110] InSb***	2.4	−0.53 [65K2]	−0.59 [69B1]	0.90
[100] Silicon	4.6–5.7	−1.0 [71G6]	−0.83 [69B1]	1.20
[110] Silicon	2.1–2.9	−1.8 [71G6]	−1.50 [69B1]	1.20
[111] Silicon	2.5	−1.6 [71G6]	−1.33 [69B1]	1.20
X-cut quartz	5.6–6.8	−0.56 [67F1]	−0.30 [72G3]	1.87
X-cut quartz	5.3–8.1	−0.54 [62W1]	−0.30 [72G3]	1.80
Z-cut quartz	6.7–9.7	−1.4 [67F1]	−0.82 [69B1]	1.71
Z-cut quartz	4.5	−1.2 [62W1]	−0.82 [69B1]	1.46
[111] Ge	1.35, 2.2	−1.6 [66G1]	−1.12 [69B1]	1.43
[111] Ge	2.6	−1.3 [72G5]	−1.12 [69B1]	1.2
[110] Ge	3.2	−1.6 [72G5]	−1.31 [69B1]	1.22
[110] Ge	4.5	−0.81 [72G5]	0.73 [69B1]	1.11
a axis CdS***	3.6	−0.30 [66K1]	—	—
c axis CdS***	4.3	−0.40 [66K1]	—	—
[100] TiO_2	2.3	−4.0 [68A2]	—	—
[001] TiO_2	2.1	−2.0 [68A2]	—	—
X-cut $CaCO_3$	1.5	−1.0 [68A2]	0.579 ± 0.017 [69B1]	1.75
Z-cut $CaCO_3$	2.2	−0.4 [68A2]	0.498 ± 0.13 [69B1]	0.8

* The x direction is taken to be the wave propagation direction.
** These values are as determined from the various ultrasonic investigations.
*** These shock data relate to the limiting elastic compression just prior to a polymorphic phase transformation.

ultrasonically-determined constant. This indicates that the fourth-order terms contribute significantly to the stress-strain response of these materials, even at strains of only a few per cent.

Relatively few measurements of higher-order elastic response have been made by the method of shock compression. Those that are available are summarized and compared to ultrasonic measurements in table 3.2. The agreement of third-order constants determined by the two methods is, in general, quite good. The third-order constants determined for vitreous silica by shock compression are probably the most accurate available for that material, with those obtained at high temperature illustrating a unique capability of the method. The shock experiments are the only source of fourth-order constants for most of the materials.

The work reviewed in this section shows that shock-compression experiments provide an effective method for determination of nonlinear elastic properties and that, by the same token, the effects of nonlinear elastic response should generally be taken into account in investigations of shock compression (see, e.g., Asay et al. [72A2]). Fourth-order contributions are readily apparent, but few coefficients have been measured. Tabulations of third-order constants are given in the Landölt–Börnstein tables [69B1] and by Zarembo and Krasil'nikov [71Z1].

Linear elasticity theory. It is convenient at this point to note, for future reference, that the linear approximation to eq. (3.1) takes the form $t_{ij} = C_{ijkl}S_{kl}$. When the material exhibits isotropic

Table 3.2
Longitudinal elastic constants determined ultrasonically and under shock compression*

Material/Method	C_{xx}, GPa	C_{xxx}, GPa	C_{xxxx}, GPa
Vitreous silica-GE151			
shock [72G2]	77.4	+550	+11000
sonic	77.7 [74F1]	+603 [73Y2]**	—
Vitreous silica-Dynasil 1000			
shock [77A3]	77.5	+550	+12000
shock (473K) [77A3]	81.2 ± 0.4	+660	+14000
X-cut quartz			
sonic	86.8 [69B1]	−210 [66T2]	—
shock [72G3]	86.8 ± 1	−300 ± 30	+7500 ± 2500
X-cut Al_2O_3			
sonic	49.4 [69B1]	−3900 [70H1, 68G1]	—
shock [72G2]	—	−3300 ± 300	50000 ± 15000
Z-cut Al_2O_3			
sonic	49.6 [69B1]	3300 [70H1]	—
		3100 [68G1]	—
shock [72G2]	—	3250 ± 100	—
shock [72G2]	—	3300 ± 300	50000 ± 15000

* Measurements are made at room temperature, ~ 300 K, except for the single high-temperature measurement on vitreous silica. The wave propagation direction is taken to be the x direction.

** Cantrell and Breazeale [78C1] have recently reported third-order elastic constants of other vitreous silica materials which range from 670 to 730 GPa.

symmetry, as is usually assumed to be the case for polycrystalline substances, this relation yields the results

$$t_1 = (K + \tfrac{4}{3}\mu)S_1, \qquad t_2 = t_3 = (K - \tfrac{2}{3}\mu)S_1, \qquad t_{ij} = 0 \text{ for } i \neq j \tag{3.4}$$

(in Voigt notation) for states of uniaxial strain. In these relations the constants K and μ are called the bulk and shear moduli, respectively. Application of equations (2.8) and (2.9) shows that the pressure and maximum shear stress are $p = -KS_1$ and $\tau = \mu S_1$, respectively, so that the part $-KS_1$ of the applied stress is borne by the resistance of the material to compression (or expansion) while the part $\frac{4}{3}\mu S_1$ is borne by its resistance to shear.

Transverse waves. Experiments involving plane waves of uniaxial strain produce proportional strain in compression and shear. If applied to a linearly elastic and isotropic solid, they permit determination only of the combination $K + \frac{4}{3}\mu$ of the bulk and shear moduli. An additional measurement is required to separate the effects of resistance to compression and shear, and thus complete the characterization of even this simplest solid. The situation is more complicated when the material is nonlinear and/or anisotropic, but the basic problem is the same: the uniaxial strain experiment does not allow independent variation of compression and shear strain. Theoretical analyses of combined longitudinal and shear motions have been available for some time (see, e.g., Davison [66D1, 68D1]), but, until recently, shock-loading apparatus and instrumentation have been limited to production and measurement of longitudinal motion. Recent development of methods for producing and measuring transverse components of velocity and displacement histories promise significant enhancement of existing capabilities for studying shear stress in shock-loaded solids.

The first apparatus to produce and measure transverse displacement histories was developed by Abou-Sayed et al. [76A1, 76A2]. Direct measurements of transverse velocity histories were later reported by Gupta [76G5] and by Koller and Fowles [79K2]. Abou-Sayed et al. impacted an inclined-face projectile on a similarly inclined sample, with both impact velocity and angle of inclination varied to produce a range of combined longitudinal and transverse motions. A similar approach has been used by Gupta [78G6] to induce pressure and shear waves in an epoxy sample.

Combined motions are also encountered in crystals subjected to normal impact when the direction of wave propagation is not a "specific" direction [65B4]. Johnson [71J1] and Luzin [75L1] have given a linearized analysis of this problem and Kim et al. [77K2] and Chhabildas et al. [79C1] have recently made such measurements on Y-cut quartz. It has been shown in this latter work that the strong transverse waves generated in the quartz can be introduced into other materials to study their response to shear. A recent symposium on transverse waves is summarized in Bull. Am. Phys. Soc. 24 (1979) 715.

3.2. Hydrodynamic approximation to the behavior of solids

When the strength of a shock greatly exceeds the maximum shear stress that a material can sustain, the differences among the principal stress components (the shear stresses) in the compressed material are small relative to their average value, which is the pressure, p. The neglect of this relatively small shear stress reduces consideration of the response of a solid to that of an inviscid fluid and is called the *hydrodynamic approximation*. The validity of this approximation involves the two rather separate issues of (1) whether the thermodynamic properties of the material are adequately approximated by relations derived from an energy density function depending on specific volume and temperature or entropy density (see section 3.2.4), and (2) whether the influence of the shear stress, rate effects, etc., that are being neglected have a negligible effect on the mechanical behavior of the material in a given circumstance. Certain phenomena, such as attenuation of stress pulses, are profoundly affected by shear stresses having negligible thermodynamic consequences.

Investigations of the behavior of solids in the hydrodynamic regime form the oldest and most fully-developed branch of the subject of shock compression of solids. Various aspects of this work have been reviewed by Rice et al. [58R1], Al'tshuler [65A2], Zel'dovich and Raizer [66Z1], Zharkov and Kalinin [71Z2], McQueen et al. [70M1], Royce [71R1], Duvall [73D5], and in several of the other works mentioned in section 1.1.

The hydrodynamic model is used to interpret data obtained in most shock-compression experiments conducted at applied stresses that are an order of magnitude or so greater than the static yield strength of the material. For a typical metal this threshold may be 10 to 20 GPa. In this section, material behavior at pressures ranging from this rather ill-defined lower limit to the upper limit of the experimental measurements, presently about 6000 GPa, is considered.

Stresses in the lower part of the hydrodynamic regime, say from 10 to 50 GPa, were first produced by detonation of explosives in contact with the material under investigation. This limit was raised to about 250 GPa when investigators began to impact samples with thin plates accelerated to high velocity ($\sim$ 5 km/s) using explosives. A further increase to over 500 GPa occurred when convergent geometries were employed [62S2, 68A4]. Soviet investigators have reported measurements in the range 300–1000 GPa; they have not described the methods by which these pressures were produced but it appears that convergent detonation waves were used. With the development of gun techno-

logy, stresses covering the range from about 0.1 to over 600 GPa became accessible to well-controlled plane-wave experiments [68I1, 74M2, 75M1, 79M1]. The highest pressure experiments conducted in the United States [77R1] have used underground nuclear explosions and the same is undoubtedly true in the Soviet Union [68A3]. Preliminary investigations have been conducted of the feasibility of applying large pulsed lasers [78V1, 79T3] and electron beam accelerators intended for fusion energy research to the production of strong shocks. The use of small projectiles accelerated to very high velocity by electrically vaporized metal foils is also being considered [78S5].

3.2.1. Hugoniot data

High-pressure Hugoniot data have been obtained for some hundreds of materials. This work has been done over a span of thirty years and in laboratories scattered throughout the world. Most of the lower-pressure data, say from 10–200 GPa, have been obtained by J.M. Walsh, M.H. Rice, R.G. McQueen, J.N. Fritz, J.W. Taylor, S.P. Marsh, W.J. Carter, and others at the Los Alamos Scientific Laboratory [69G2, 70M1]. Most data for shocks stronger than this have been reported by L.V. Al'tshuler, A.A. Bakanova, S.B. Kormer, R.F. Trunin, and others in the Soviet Union [65A2, 77A1]. The experimental methods of the Los Alamos group have been described in considerable detail [70M1] but the Soviet workers have not provided a similarly detailed description of their techniques.

The "Compendium of Shock Wave Data", compiled by van Thiel et al. [77V1] is a reasonable place to start in any search for high-pressure Hugoniot data. The data contained in these volumes have not been critically reviewed, however, and this necessary step must be taken by the user. Some references to recently published data are given in table 3.3. This list is not comprehensive, but gives a selection of summary data, recent works where other references can be found, data on materials of special interest, etc.

Any discussion of experimental measurement must include some consideration of errors. Formulae for the relative error in inferring pressure and density of the shock-compressed material from measurements of U and u are easily derived [58A1, 68A3]. When measurements involve the use of equations of state for other materials, rational analysis of errors is possible, but becomes complicated and remains somewhat subjective. Each case requires careful, individual consideration if a convincing estimate is to be made. Most investigators estimate the precision of their recent particle and/or shock velocity measurements to be about 1 per cent. This corresponds to an error of about 0.5 per cent in compression and 2 per cent in pressure. In addition to these errors of measurement, Hugoniot data are subject to a variety of errors of interpretation, as discussed in section 3.2.4.

For most purposes it is convenient to smooth, summarize, and interpolate Hugoniot data by fitting a smooth function, the *Hugoniot curve*, through them. When the coordinate is chosen so that $U > 0$ and $u^+ = 0$, this curve can usually be the straight line: $U = a + bu$ of eq. (2.16). This linear relation does not describe liquids or porous metals satisfactorily, and the addition of a small quadratic term improves the representation of some other data. When materials undergo shock-induced transformations from one crystalline phase to another, the Hugoniot curve exhibits a discontinuity or change of slope, but data in the separate intervals above and below the transition are often accurately represented by linear relations. Numerous investigators have remarked on the widespread validity of the linear representation of the (U, u) Hugoniot, and the matter of its generality and significance has been discussed [67R4, 71S3]. No fundamental explanation has been given for the linearity, however, and both experimental data and theoretical considerations

Table 3.3
Selected hydrodynamic data

Reference	Remarks
McQueen et al. [67M2]	12 rocks, 10 to 100 GPa
Isbell et al. [68I1]	Gun data to 500 GPa for 11 materials
Group GMX-6 [69G2]	Published data reanalyzed using [70M1]
Dick [70D1]	C_6H_6, CS_2, CCl_4, N_2, 19 to 63 GPa
Dick et al. [70D2]	Solid argon, 1.8–6.45 GPa
McQueen et al. [70M1]	60 technical materials, 5 standards
Zharkov and Kalinin [71Z2]	Elements, alkali halides and rocks
Carter et al. [71C2]	Al 2024, Cu, Ag, Na, Mo, Pd, Mg, MgO
Fritz et al. [71F2]	NaCl crystals, 3 to 26 GPa
Ahrens et al. [71A1]	Forsterite (Mg_2SiO_4), 11 to 37 GPa
Ahrens and Gaffney [71A2]	Enstatite ($Mg_{0.86}Fe_{0.14}$)SiO_3, 6–48 GPa
Lysne [72L3]	Organic liquids at low pressure
Kalashnikov et al. [73K1]	Six calcite minerals, 10 to 100 GPa
Gust et al. [73G6]	TiB_2, SiC, Be_4B to $\sim$100 GPa
Lysne and Hardesty [73L4]	Nitromethane
Carter [73C3]	LiF, NaF, LiCl, LiBr, 7 to 100 GPa
Dobratz [74D3]	25 unreacted explosives
van Thiel et al. [74V1]	Liquid deuterium, 20 and 90 GPa
Simakov et al. [74S4]	12 minerals, 10 to 300 GPa
Syono et al. [74S7]	Fe_2O_3 and Fe_3O_4 to 50 GPa
Syono et al. [74S8]	TiO
Mitchell et al. [74M1]	Brass at 50 and 100 GPa, various temp.
Morgan [74M2]	Platinum, 290 to 680 GPa
Barker [75B1]	α-phase iron
Morgan [75M1]	Stainless steel alloy 347, 183–384 GPa
Bakanova et al. [76B1]	Water, 3–50 GPa
Goto et al. [76G2]	GaAs to 40 GPa
Ragan et al. [77R1]	Molybdenum at 2000 GPa
Al'tshuler et al. [77A1]	Latest Soviet work at extreme pressure
McMahan et al. [77M6]	Metallic iodine, 74–180 GPa
Al'tshuler and Pavlovskii [71A4]	Clay and clay shale, 3 to 77 GPa
Kalashnikov et al. [72K1]	Polytetrafluoroethylene 1.4 to 175 GPa
Podurets et al. [72P1]	Water to 1400 GPa. See also [76B1]
Grady et al. [76G3]	Dolomite, 18 to 42 GPa
Mitchell and Nellis [79M1]	Water, 30 to 220 GPa
Ahrens [79A1]	Pyrrhotite ($Fe_{0.9}S$), 3 to 158 GPa

suggest that some downward curvature can be expected to become apparent when the range of u is great enough. In the latest work of Al'tshuler et al. [77A1], in which data at extreme pressures are considered, the slope of the (U, u) Hugoniot is found to decrease significantly with increasing compression. In spite of these considerations, the linearity of the (U, u) Hugoniot curve is so common an outcome of a program of shock-compression experiments that instances in which pronounced deviations are observed deserve examination for evidence of elastic-plastic response, collapse of porosity unintentionally present in the material, a phase transformation, systematic error in measurement, or other identifiable cause.

Example: the high-pressure Hugoniot curve of copper. It is not possible to discuss all of the available (U, u) Hugoniot data in a review of this length, but it seems worthwhile to give a flavor of the work that has been done by considering, as an example, the data that describe the Hugoniot

Table 3.4
Measurements of the high-pressure Hugoniot curve of copper

reference	Pressures (GPa)	No. of data	Loading method[a)]	Detector method[b)]	Interpretation method[c)]	Hugoniot U, m/s	Remarks
an [55W1]	18–46	12	CD	F	FSV		
2]	22–51	5	CD	F	FSV and R	$3944+1.514u$	aluminum st
8A2]	45–380	3	U	P	R	$3900+1.46u$	iron standar
0A1]	108–418	3	FP (U)	P	D	$4200+1.41u$	
rsh [60M1]	88 and 144	3 and 3	FP	F	R	$3958+1.497u$	brass standa
2A1]	907	1	U	P	D		iron striker a
on (1964), [77V1]	72–127	9	U	F	D	$4640+0.98u$	
ignon (1964), [77V1]	74–164	45	U	P, F	U	$4120+1.81u$	
é [68A4]	20–441	16	CD, FP, I	F	FSV	$3940+1.55u-1.5\times10^{-5}(u)^2$	ten highest v convergent w
	99–450	12	G	P	D	$3964+1.463u$	
2]	1569	1	N	P	R		lead standar polated). p corrected t in [77A1]
0M1]	8–217	127	CD, FP	F	FSV, R	$3940+1.489u$	Al, Fe and U standards
3]	3800	1	N	P	R		lead standar polated). p corrected t in [77A1]

etonation, FP = explosively driven impactor, G = gun-driven impactor, I = impactor driven by convergent detonation, N = nuclear expl
ed, U = unspecified. We believe pressures in the range ~200–1000 GPa to have been achieved by method I (except [68I1]).
act pins, F = optical flasher.
ct or deceleration method, R = impedance mismatch or reflection method, FSV = velocity of the stress-free surface measured.

curve for copper. This material is easily studied because it has a low elastic limit, does not exhibit any transitions between crystalline phases, and is not subject to significant structural or compositional variation. The various reported investigations are summarized in table 3.4 and fig. 3.1. Related literature on shock compression of porous copper, elastic-plastic behavior of both mono- and polycrystalline samples, acoustic behavior, spall fracture, metallurgical effects, theoretical interpretation, and other matters is extensive.

The general agreement among the data plotted in fig. 3.1 is quite striking. In practice, most investigations cover only a small fraction of the range shown and, as indicated in the table, coefficients of straight-line fits through data on these short intervals can differ considerably even though the points themselves look well placed on the large graph. This suggests that caution be exercised in extrapolating data, even if it be granted that a linear relation is adequate.

A variety of experimental methods have been used in the reported investigations. The low-pressure range has been covered by contact detonation. At somewhat higher pressures, explosively-driven flying plates have been used. The range to 450 GPa has also been covered using gun-driven

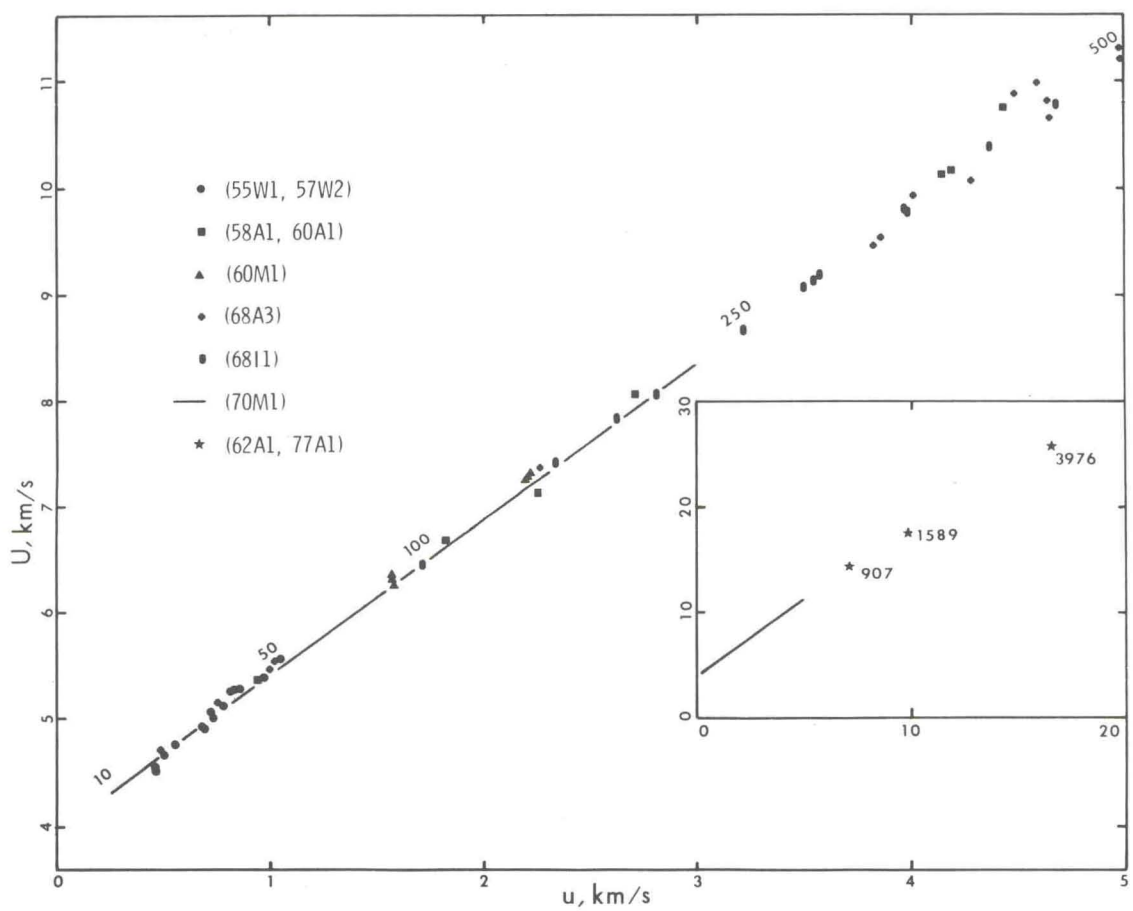

Fig. 3.1. High-pressure (U, u) Hugoniot data for copper obtained by several investigators. The numerals along the curve indicate pressures in GPa. The line on the small inset figure represents the entire range of the larger figure, while the three points represent the results of Soviet ultrahigh pressure experiments (see table 3.4).

impactors. The high-pressure experiments of Argous and Aveillé have employed flying plates driven by a spherical implosion. Al'tshuler et al., have failed to report any details of the loading method used to obtain their 907 GPa point, except that an iron impactor driven at 14.68 km/s was used. These data, if augmented by various elastic-plastic data discussed elsewhere in this review, cover the entire range of compression to 2.854 times normal, i.e., to a density of 25490 kg/m^3.

The most recent Hugoniot curves from the United States [68I1, 70M1], the Soviet Union [77A1], and France [68A4] agree to 1 per cent at 50 GPa; the United States and Soviet Hugoniot curves agree to 0.1 per cent. It should be noted, however, that two of the Hugoniot curves given in table 3.2 are in serious disagreement with the others. These latter curves also disagree with extrapolations of static and ultrasonic data. (Ultrasonic measurements of Barsch and Chang [67B2] suggest the Hugoniot curve $U = 3916 + 1.62u$.) A systematic error seems to have occurred in the collection or processing of these data and they serve to exemplify the need for careful evaluation and cross-checking of any data before they are used.

3.2.2. Shock compression of porous solids

The principal Hugoniot curve of a substance is a single locus on its equation-of-state surface. To locate the entire surface, other state points must be determined. This has been done by shock compression of porous samples and by multiple-shock compression.

As indicated in fig. 3.2a, shock compression of loosely-compacted powder or other distended material to a given pressure gives rise to larger thermal effects than compression of the same material from its normal solid form to the same pressure. By varying the initial distention, it is possible to produce a family of widely separated Hugoniot curves, as illustrated in fig. 3.2b. The temperatures achieved can easily exceed several thousand kelvins and the associated thermal pressures are sometimes so great that the density of the shock-compressed material is less than the normal density of the cold solid.

Zel'dovich [57Z1] was the first to call attention to the behavior of porous materials under shock compression, and to point out that the knowledge of a family of Hugoniot curves corresponding to various initial distentions would suffice for decomposition of the pressure at a given specific volume into its cold and thermal components. This method was adopted by Al'tshuler [58A1] and, in a more comprehensive investigation, by Krupnikov et al. [62K2, see also 65A2]. Some work has been done since this time [70M1, 71N1, 76B1] but the technique has not been widely used.

All states achieved by shock compression of distended solids lie at higher internal energy than states on the principal Hugoniot curve, i.e., they have higher pressure for a given specific volume. When interest lies with temperature effects such as anharmonicity or excitation of the electron gas in metals, study of the behavior of distended solids is indicated. When interest lies with measuring such effects of compression as the volume dependence of Grüneisen's parameter, these experiments have the disadvantage that they not only fail to provide access to states of the highest possible density, but also produce thermal effects that serve to complicate interpretation of the volume dependencies.

Experimental investigation of distended materials presents special difficulties and requires unusual care in design of the test assemblies. Precision is very important in this work because interest usually lies not only with the position of the Hugoniot curves, but with differences in position of adjacent curves. Early concern that a steady shock would be slow to evolve in coarse-grained material has been alleviated [62K1, 70B4] but thermal equilibration may still not have been achieved and many practical experimental problems remain.

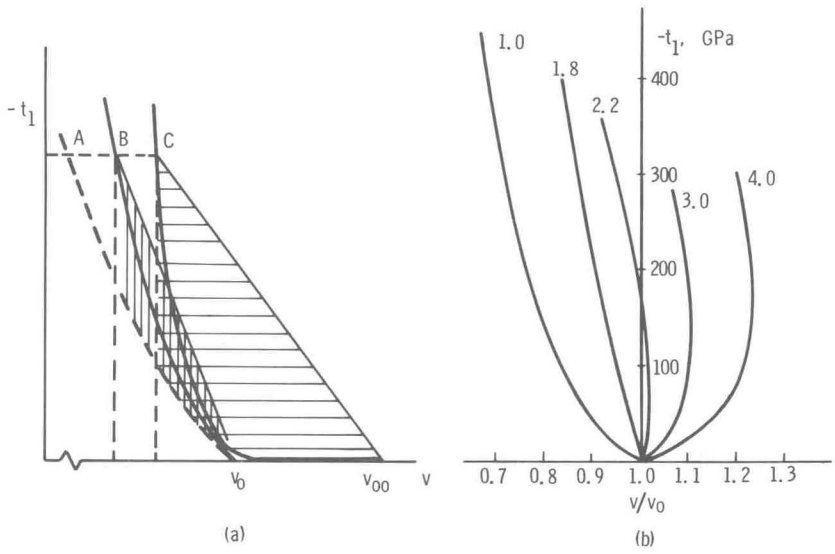

Fig. 3.2. The internal energy imparted to material by shock compression corresponds to the area under the Rayleigh line. The thermal energy is represented by the shaded portion of this area between the Rayleigh line and the cold-compression curve (A), in part (a) of the figure. For shock compression to a given stress, this thermal energy is much greater for material that was initially distended to a specific volume v_{00} (Hugoniot curve C) than for material compressed from its normal specific volume v_0 state (Hugoniot curve B). The additional energy is almost entirely thermal, and gives rise to thermal pressures sufficient to produce the widely separated Hugoniot curves shown for various distention ratios v_{00}/v_0 in part (b) of the figure (plotted from data of Krupnikov [62K 2]).

3.2.3. Multiple-shock compression

A second method of obtaining the additional (p, v, ε) data required for thermodynamic studies involves subjecting the sample to successive shocks. This leaves it in a state that can be determined experimentally and which is different from one on the principal Hugoniot curve. This method has been used by Walsh and Rice [57W1, 57R1] to determine the equation of state of water, and by Al'tshuler and Petrunin [61A2], van Thiel et al. [66V1, 74V1], Al'tshuler and Pavlovskii [71A5], Neal [77N1, 79N2], Nellis et al. [78N1] and others to study several other materials. Some experiments involving Mach reflections have been conducted by Al'tshuler et al. [62A2], Leygonie and Bergon [68L1], and Neal [75N1, 76N1]. It is only in the most recent of this latter work that practical results are being obtained, but the method shows promise.

When a substance is compressed to a given density by multiple shocks rather than a single shock of greater strength, the compression is achieved with a smaller increase in entropy and temperature so this experiment provides access to states of higher density than the principal Hugoniot state at the same pressure.

Studies of the propagation of weak disturbances into shock-compressed material provide additional information about the material in its compressed state and are necessary to assess the errors implicit in the hydrodynamic approximation. Consideration of this matter must await the next section on elastic-plastic response, however, because the response of the material to these weak disturbances is often that of a solid, not a fluid.

3.2.4. Compressible fluid approximation to the high-pressure equation of state of solids

A basic application of Hugoniot data is to the thermodynamic characterization of materials at high pressure and temperature. The development of an equation of state based on shock-compres-

sion data rests on the assumption that these data represent an equilibrium thermodynamic state in which the pressure and internal energy are functions of the variables v (or ρ) and s (or θ).

In the absence of any specific evidence to the contrary, it is assumed that experimental data refer to states of equilibrium. In some cases a transformation to a dense phase may proceed so slowly that the measurements refer to "metastable" properties of the low-density phase. The treatment of melting is uncertain since its effect on Hugoniot data, particularly when it occurs at high pressure, is usually so small as to escape detection [66U1, 71M2, 75A3].

The question of whether or not the state achieved by shock compression is adequately described by the usual thermodynamic variables is more troublesome. It is necessary, of course, that effects of shear strain be negligible, or that the measured stress component t_1 and internal energy density ε be corrected to yield the associated pressure p and compression energy. It is also necessary that the defect structure in the lattice be in equilibrium, that it not vary with compression, or that the changes that do occur have negligible effect. Shock compression is known to produce profound changes in the defect structure of solids, but the effect of these changes on thermodynamic properties of the compressed solid has not been investigated in detail. Zharkov and Kalinin [71Z2] have estimated the increase in pressure attributable to the presence of lattice vacancies and found it to be negligible for equilibrium concentrations. Concentrations orders of magnitude greater than thermal-equilibrium values have been found by metallurgical examination of material recovered after shock compression, however (see section 3.6), and a proportionate increase in their effect would produce a large pressure correction. Electrical resistivity data (see section 4.10) provide evidence for vacancy concentrations sufficient to contribute several per cent to the total pressure. The effect of these and other shock-induced defects on equations of state deduced from shock-compression measurements is a basic issue requiring further study.

In some cases yielding has been shown to proceed heterogeneously (see section 3.4), and there is reason to believe that this situation becomes increasingly common as the shock strength is increased. The formation of deformation bands is an extreme example of defect production and presents a case where thermal inhomogeneities are obviously present and where the measured properties must be those of a mixture of the material in various states. That it seems not to be noticeable in comparison of shock-compression and other pressure-volume data may be due to the insensitivity of the measurement or may indicate that the deformation bands are of sufficiently fine structure that they reach thermal equilibrium in times negligible relative to the duration of a typical experiment.

All of the effects discussed result from shear stresses. This and other evidence confirms their existence at the highest pressure where they have been sought, certainly to 100 GPa in several metals. These stresses produce significant mechanical effects of both qualitative and quantitative nature at pressures where they have been studied. The thermodynamic contribution of the distortional energy is small [73D5] and the same seems to be true for other effects, although their contribution has not been carefully assessed.

One must not infer from the foregoing remarks that shock compression produces a state of complete disorder in a crystal. The most direct evidence for retention of crystalline order comes from flash X-ray diffraction patterns obtained from material in the shock-compressed state. The technique for obtaining these patterns is still under development, and the interpretation is a subject of some discussion, but useful results have been obtained by Johnson et al. [72J4], Egorov et al. [72E1], Müller and Schulte [78M11], Kondo et al. [79K3], and Jamet and Bauer [78J1]. These investigators find that crystalline order is retained in a variety of solids. The considerable line broadening observed is taken as a measure of defect or mosaic structures formed.

3.2.5. Empirical equation of state

Because shock-compression experiments provide information on ε and v, we are led to consider preparing a complete description of a substance in terms of the entropy density function $s = \hat{s}(v, \varepsilon)$. The pressure and temperature are given in terms of the function $\hat{s}$ by the relations $p/\theta = \partial\hat{s}/\partial v$ and $1/\theta = \partial\hat{s}/\partial\varepsilon$. Elimination of θ from these equations give the equation

$$\partial\hat{s}/\partial v - p\partial\hat{s}/\partial\varepsilon = 0, \tag{3.5}$$

where $p = \hat{p}(v, \varepsilon)$. The function $\hat{p}(v, \varepsilon)$ would be determined over a certain domain of the (v, ε) plane if Hugoniot curves centered on several initial states were measured. With this function in hand, eq. (3.5) can be solved for the entropy density function $\hat{s}$.

From the form of eq. (3.5) we see that the total derivative of $\hat{s}$ vanishes along curves (called *characteristic curves*) in the (v, ε) plane having the slope $\mathrm{d}\varepsilon/\mathrm{d}v = -p(v, \varepsilon)$. Since $\mathrm{d}s = 0$ along these curves, they are isentropes. The *shape* and *position* of the isentropes are thus obtained from a knowledge of Hugoniot curves centered on several initial states. To complete the determination of $\hat{s}$, it is necessary to specify the value of the entropy on each isentrope. This can be done if s is known along some data curve, say the atmospheric pressure isobar, that intersects the isentropes. When these data are specified, a unique solution $\hat{s}(v, \varepsilon)$ is obtained in the region of the (v, ε) plane where $\hat{p}$ is defined and which lies between the isentropes through the end points of the data curve. The great strength of this method is that it proceeds on the basis of the data, invoking no assumptions about the form of the equation of state. This feature is also its greatest liability in that no means of extrapolating the equation of state beyond the range of experimental data is suggested, nor is any connection to theoretical models provided.

Cowperthwaite and Blackburn [71C6] attempted to determine the equation of state of a silicone oil by this method, but were unsuccessful because the differences between Hugoniot curves centered on different initial temperatures were too small in comparison to the uncertainty in their measurement. Lysne and Hardesty [73L4] did carry out a successful determination of the equation of state of nitromethane, but found it necessary to extrapolate the results to pressures above the highest-lying isentrope through the initial data. The difficulties that these investigators experienced are general ones that have so far precluded further application of the method.

3.2.6. Theoretical equations of state

Equations of state based in varying degrees on fundamental considerations of atomic interaction are widely used to describe shock-compressed material. The majority of the work has been directed toward metals but alkali halides, rare gas solids, liquefied gases, and other substances have also been considered. The theories share the common assumption that the energy density (either the internal energy or the Helmholtz free energy) can be expressed as the sum of terms representing the effect of several independently functioning mechanisms. The most basic of these terms, called the potential energy density, represents the static interaction of the atoms or ions and, in the case of metals, the energy of the cold electron gas. A contribution representing the energy of zero-point oscillations is added to the potential energy density to obtain the cold-compression energy density function $\varepsilon_c(v)$ characterizing the behavior of the solid at absolute-zero temperature. At temperatures above absolute zero the thermal energy $\varepsilon_\theta(v, \theta)$ of lattice oscillations is added and at very high temperatures the electronic energy density $\varepsilon_e(v, \theta)$ representing effects of thermal excitation of conduction electrons becomes important. Each of these energy contributions gives rise to an associated pressure contribution according to the formula $p = -\partial\varepsilon/\partial v$. The various contributions

are discussed separately in the following sections. We do not take explicit account of the melting transition that may be expected to occur as a result of compression by sufficiently strong shocks, nor do we review models of the behavior of matter in the liquid state. These problems have been investigated at some length by direct computer simulation of atomic interactions. The results of some such calculations have been summarized by Grover [77G8] in terms of a scaling model.

Cold compression. Calculation of the cold-compression behavior of a substance can be begun by a priori assumption of the form of the interatomic potential, by first-principles determination of this potential, or by deducing it from Hugoniot data on the basis of assumptions about the other contributions to the total pressure. This latter approach is the most common by far, but a significant effort is being expended on more basic work, particularly with regard to metals.

When the cold-compression behavior is interpreted specifically in terms of atomic interactions, these interactions are represented by an effective pair potential. Early Soviet work often employed the Born–Mayer (exponential) repulsion potential combined with inverse power attractive potentials to model the interaction in metals and ionic crystals. Other investigators [65A2, 64P2, 70D2, 71Z2, 73R4, 74P1, 74R1] studying these materials, rare-gas solids, liquid hydrogen and an organic crystal, have followed this path or have used Morse, Lennard-Jones, or other potentials in a similar way. Ross [73R4] has shown a favorable comparison of an exponential-six potential fit to shock-compression data on solid argon with a potential inferred from molecular beam experiments. Following a somewhat different approach, Barnes [67B1, 78B2] has used a cold-compression curve based on a Morse attractive term fit to bulk modulus data and a repulsive term fit to results of a calculation based on the Thomas–Fermi model.

Zhdanov and Polyakov [75Z1, 76Z1, 76Z2] have approximated the compression behavior of several alkali halide crystals by a calculation in which the energy of the lattice is determined using Hartree–Fock wave functions for the free ions. These results, which are obtained without appeal to any shock-compression data, are used to calculate Hugoniot curves that are, in several cases, in quite reasonable agreement with observation for both low and high pressure phases of the materials. Hardy and coworkers [77H1, 77H2, 78B3] have developed an alternative model, but have not applied it in the regime of pressure and temperature achieved by shock compression.

Considerable effort has gone into prediction of the cold-compression behavior of metals. Pastine [67P1] and Pastine and Carroll [71P1] have discussed a calculation of the behavior of sodium and aluminum in which the cold energy function is constructed as the sum of terms representing the interaction potential of the atom cores (regarded as incompressible), and the ground state, Fermi, exchange, and correlation energies of the valence electrons. Approximate expressions for each of these terms are taken from the literature and their sum is a closed-form expression for the potential. The simplicity of this analysis lies in the fact that the core structure of the atom is held fixed, that the Fermi surface is taken to be spherical, and that the band structure of these materials had previously been determined as a function of lattice parameter. Detailed band-structure calculations of compression behavior have now been made in several cases [70R2, 74R1, 76R3, 77M1, 78M3, 79M2]. The potential of these solutions for providing insight into the behavior of matter and their unique capability for providing information about states not accessible to experimental observation (e.g., metallic hydrogen [77R2]) ensures that their importance will continue to increase in spite of the difficulty and expense of obtaining them. The importance and potential value of detailed theoretical studies of compressibility were pointed out by Royce [67R3, 71R2] and Al'tshuler and Bakanova [69A2] who showed how the atomic volume of a number of metallic solids bore a systematic relationship to their electronic configuration and how

prediction of changes in this electronic configuration with pressure was correlated to observations of compressibility.

It is generally agreed that the behavior of matter at very large compressions (more than about fivefold) is satisfactorily described by corrected variants of the Thomas–Fermi theory [72K2, 76K2]. Unfortunately, there is a large gap between the twofold or threefold compressions that are experimentally accessible and those for which this theory is likely to be useful. Soviet workers [77A1], particularly, have assumed that this gap can be bridged by relatively straightforward interpolations. Other workers, noting that effects of the shell structure of atoms are often apparent at the limit of the experimental range, argue that a succession of electronic transitions must precede the collapse of the atomic structure to the state modeled by the Thomas–Fermi theory. If this is the case, the interpolation will have to be guided by detailed electronic calculations (see, for example, [77G1, 79M2]).

Thermal energy and pressure. The internal energy of a solid is mostly that of cold compression but thermal energy, in this case associated with oscillatory motion of the atoms, cannot be neglected. As an example, we note that when copper is subjected to a 100 GPa shock, 13 per cent of this pressure is of thermal origin. At 1500 GPa the thermal pressure is about one-half the total. The thermal energy is a much larger fraction of the total in each case. As more compressible substances are considered, thermal effects increase in importance and can dominate the response of highly compressible substances at the limit of the experimentally accessible range of pressures.

Analysis of thermal effects proceeds by direct numerical simulation of the motion of large arrays of atoms (see, e.g., [67R2, 70H3, 74R1, 78W2]), by detailed lattice-dynamic analyses (see, e.g., [70H3, 74D1]), by application of cell models (see, e.g., [70D2, 70H3, 73R4]) or, most often, by rather pragmatic application of the Mie–Grüneisen theory. The Mie–Grüneisen equation, $p_\theta = (\gamma/v)\varepsilon_\theta$, is a relation between the thermal energy ε_θ and the thermal pressure of a solid. The coefficient γ, called Grüneisen's parameter, is defined thermodynamically by the relation $\gamma = v(\partial p/\partial \varepsilon)|_v$ or, as in Grüneisen's theory, in terms of the way in which the frequencies of quasi-harmonic lattice oscillations vary with compression. This latter interpretation leads to the conclusion that γ is a function of v alone, and it is this result that forms the substance of the theory. Various aspects of the Mie–Grüneisen theory as its relates to the present subject are discussed by Knopoff and Shapiro [69K6], Zharkov and Kalinin [71Z2], Royce [71R1], and Romain and coworkers [76R2, 77M5].

A thermodynamic measure of Grüneisen's parameter is readily obtained at atmospheric pressure by substituting compressibility, specific heat, and thermal expansion data into an appropriate form of the thermodynamic definition. Measurements at smaller specific volumes can, in principle, be made by means of shock compression of porous samples or by multiple shock experiments, as discussed previously. Accurate determination of γ has proven difficult, however, because the thermal pressure to which γ is related is too small in comparison to the cold pressure to be measured accurately at small compressions, while interpretation of observations at large compression are complicated by effects of anharmonicity and electronic excitation not included in the Mie–Grüneisen model. The errors of determination of Grüneisen's parameter by shock-compression experiments are not less than ± 10 per cent. Under the circumstances, a rough fit to the data is adequate and the relation $\gamma(v)/v = \text{constant}$, where the constant is evaluated from atmospheric-pressure data, has proven quite satisfactory [68M2, 76N1]. Since the thermal pressure is small at low compressions, a crude estimate of γ is adequate for such purposes as extraction of an isotherm from Hugoniot data.

The importance of Grüneisen's parameter, and the difficulty of determining it experimentally, have led to widespread use of theoretical models. Since $\gamma(v)$ is related to oscillations of atoms in the same force field giving rise to the cold pressure, it is to be expected that it will be related to the function $p_c(v)$. Three models, called the Slater–Landau, Dugdale–MacDonald, and Vahchenko–Zubarev or free-volume models relating $\gamma(v)$ to the cold-compression moduli have been proposed (see, e.g., [71R1]). These models are in serious disagreement at small compressions but converge on one another as the compression is increased. None of the models (nor the formula γ/v = constant) has been demonstrated to be accurate at large compressions. If a relation between $\gamma(v)$ and $p_c(v)$ is adopted, both functions can be evaluated from Hugoniot data. Such calculations have been made by McQueen and Marsh [60M1], Al'tshuler et al. [60A1], and Keeler [72K3], and various methods of obtaining these functions have been discussed by Takeuchi and Kanamori [66T1], Shapiro and Knopoff [69S3], Zharkov and Kalinin [71Z2], and O'Keeffe [70O1, 73O1].

When the thermal pressure and cold pressure are added to give the total pressure $p = p_c(v) + [\gamma(v)/v]\varepsilon_\theta$, an incomplete equation of state relating p, v, and ε $(= \varepsilon_c + \varepsilon_\theta)$ is obtained. This relation has been found to be valid near the Hugoniot curve and is sufficient for the calculation of the recompression Hugoniot curves and expansion isentropes needed for interpretation of experimental observations [70M1].

A complete equation of state is obtained by combining the Mie–Grüneisen pressure–energy relation with the Debye relation between thermal energy and temperature. Usually the classical-limit value is adequate and we have $\varepsilon_\theta = C_v\theta$, where the specific heat C_v takes the value $3R$ with R being the gas constant. When this relation is used, the thermal pressure is given by $p_\theta = (3R/v)\gamma\theta$ and the necessity of having an accurate value of γ if temperatures are to be estimated from pressure measurements is apparent.

Effects of anharmonicity and electronic excitation. At elevated temperatures the Grüneisen model must be modified to take account of anharmonicity of the lattice vibrations and thermal excitation of conduction electrons. When a substance is heated to a significant fraction of its melting temperature, the amplitude of the crystal lattice oscillations becomes large enough to destroy the accuracy of the quasi-harmonic approximation. In most cases where the heating is by shock compression, the temperature at which this effect becomes pronounced is increased over its usual value because of the increase in the melting temperature caused by the compression (the increase in the repulsive potential restricts the motion of the atoms). The cases in which anharmonic effects are especially important are those where the shock heating is anomalously large relative to the specific volume, as in the case of shock-compressed porous substances.

In the quasi-harmonic approximation the thermal pressure is given by $(\gamma/v)C_v\theta$. The fourth-order anharmonic theory (see, e.g., [71Z2]) yields a correction term proportional to θ^2. This term can simply be added to the quasi-harmonic thermal pressure, or can be incorporated into γ, yielding a "temperature-dependent Grüneisen parameter". In early Soviet work [62A1, 62K1, 63A1] high-temperature effects were taken into account by using an empirical interpolation between values $\gamma = \gamma_0$ and $C_v = 3R$ appropriate for a solid under normal conditions and the values $\gamma = \frac{2}{3}$ and $C_v = \frac{3}{2}R$ appropriate for an ideal gas. This reduction of γ and C_v is equivalent to assuming that the vibrational frequencies of the lattice increase with increasing temperature [65A2]. Pastine [67P1, 68P1], in a slightly different formulation, has also made use of the idea that anharmonic effects can be taken into account by allowing the mode frequencies to increase with increasing temperature.

When the temperature of shock-compressed material reaches several thousand kelvins, the

effect of thermal excitation of conduction electrons becomes important. In simple metals this effect has conventionally been taken into account by adding the "electronic terms" $\varepsilon_e = \frac{1}{2}\beta\theta^2$, $p_e = \frac{1}{2}(\gamma_e/v)\beta\theta^2$ to the energy and pressure sums, respectively, appearing in the Mie–Grüneisen equation [71Z2, 66Z1]. These contributions follow from the fact that internal energy and pressure increase as θ^2 for a degenerate electron gas and in approximately this manner to temperatures of 30 000 to 50 000 K following other models. Assuming the θ^2 dependence to be exact, the coefficients β and γ_e, called the *electronic specific heat* and *electronic Grüneisen parameter*, respectively, are functions only of specific volume. The values of γ_e suggested (usually $\frac{1}{2}$ or $\frac{2}{3}$) are not too different from the lattice γ at large compression, so neglect of this term may not greatly influence the estimation of $p_c(v)$ from Hugoniot data. Proper inclusion of the electronic excitation is necessary, however, if temperatures exceeding a few thousand kelvins are to be estimated accurately.

It has been known for some years that this simple treatment is inadequate for ionic crystals and transition metals [65A2] and, indeed, for many other substances. Since γ_e actually depends on the details of the electronic band structure of the material, it can vary significantly.

The particular case of rubidium has been considered by Grover [71G4] and Ross [72R2]. Interest arose in this case because of a disagreement between static and shock measurements of compressibility. The possibility that anomalous electronic behavior was involved was suggested by the occurrence of an electronic transition in cesium at 4.5 GPa. Ross was able to show that the shock compression of rubidium produced a sufficiently great change in the band structure of this material that the high temperatures also present were sufficient to excite electrons into an upper band and thus significantly lower the thermal pressure.

3.2.7. Extended equations of state

The development of digital computers and the associated software necessary for solving complex flow problems has given rise to the need for equations of state covering extended ranges of the state variables. Such equations of state are developed on the basis of a broad range of theoretical and experimental information. Usually they cover the entire range of solid behavior, and extend to molten and vaporized states. Shock-compression experiments cover only a small portion of the range of interest, but are unique in providing the only data at both high temperature and high density. Since shock-compressed solids may melt or vaporize on decompression, access is also provided to states of high temperature and low density.

It is usual to represent the most extreme states of high temperature and both high and low density by the relatively simple theoretical models valid in these regions, while the states that are both more accessible to experimental observation and more difficult to describe theoretically are represented by semi-empirical models fit to experimental data. Because of the range of states covered by these models, they are presented in the form of distinct functional or tabular relations covering various regions. Emphasis is laid on thermodynamic consistency and validity under various limiting conditions of temperature and density. Two widely used families of equations of state of this sort are implemented in the CHART D [72T2] and GRAY [71R4] computer codes.

Shock-compression and other data are also used to develop more detailed equations of state for various materials on a case-by-case basis. Andrews [73A2] has marshaled a variety of theoretical and experimental information to construct a detailed equation of state for the α and ε phases of iron. Johnson et al. [74J2] have developed a simple but very satisfactory description of the solid I, solid II and liquid phases of bismuth using the Mie–Grüneisen model with γ/v and C_v held constant. Equations of state describing the behavior of a number of solids are included in the SESAME

[78B2] library. Skidmore and Morris [62S2] and Barnes [75B2] have described applications of shock-compression data to the development of equations of state of uranium and sodium, respectively, in low pressure, high temperature regions of interest in nuclear reactor analyses.

3.2.8. Comparison of shock-compression and other data

Matter can be compressed by static means as well as shock loading, and comparison of the data obtained by these two methods permits testing the basic assumptions made in each case. Agreement, as a whole, is sufficiently good and wide-spread that significant disagreement in a particular instance is possible evidence for occurrence of unrecognized or unquantified physical phenomena. The comparability of shock- and static-compression data takes on a particular significance when the former are involved in determination of pressure standards for static measurements. This standardization takes two forms: (1) use of phase-transformation pressures measured in shock-compression experiments for fixed-point calibration and (2) use of isotherms calculated from Hugoniot data to calibrate marker materials for use as continuous-reading internal standards when static measurements are made by X-ray diffraction (for recent reviews of this work, see Decker et al. [72D2] and Bassett and Takahashi [74B1]).

Static- and shock-compression data are commonly compared on the basis of the pressure along room-temperature isotherms although a more sensitive, and perhaps more revealing, comparison can be made in terms of the bulk modulus and its various pressure derivatives. Comparison of pressure is most appropriate in the case of calibration standards and for certain geophysical investigations, whereas comparison of moduli is necessary in more basic equation-of-state studies.

The use of phase transformation pressures determined by shock compression for fixed-point calibration of static measurements is an important application that is presently a subject of some debate. Duvall and Graham [77D6] carefully compared determinations of the onset of phase transformations by the two methods and found good agreement in most cases. Nevertheless, there is abundant evidence that shock-induced transformations are subject to influences other than pressure and temperature so that particular cases must be critically examined before the shock data are used to establish fixed-point calibrations.

Isotherms derived from shock data have been compared with Bridgman's isotherms since the earliest days of this research, but the improved static and ultrasonic methods developed in recent years have now provided much more dependable sources of data for comparison. Some recent comparisons to Bridgman's pressures occur in works of Carter et al. [71C2], Fritz et al. [71F2], and Carter [73C3]. Similar comparisons to more recent data are those of Drickamer et al. [66D4]. Their static data were taken by X-ray diffraction methods and were compared to a few very early shock experiments [57C1] on alkali halides. The compressions reach about 40 per cent in the more compliant materials and the disagreement in compression at a given pressure is a few per cent. The data of Drickamer et al. on NaCl and LiF have since been found to be in excellent agreement with more recent shock data of Fritz et al. [71F2] and Carter [73C3], respectively, but their data on NaF fail to agree with most other data on this substance and are also in poor agreement with Carter's [73C3] shock isotherm. Carter's (p, v) data on NaF are in good agreement with those of Olinger and Jamieson [70O2] and Spieglan and Jamieson [74S6], although a systematic divergence at high pressure is apparent, so the agreement of the pressure derivative of the modulus is much less satisfactory.

The extensive group of static-compression experiments of Vaidya and Kennedy [70V1, 71V2] and Vaidya et al. [71V1] have been compared to shock-compression data and this comparison

has been critically examined by Grover [70G2, 71G4, 73G7]. These static data were obtained by use of a piston-cylinder apparatus and are limited to pressures below 4.5 GPa. This limit is below the range of most shock-compression measurements so that comparison is to an extrapolated shock isotherm. The comparisons are in terms of tabular values of the ratio of compressed to original sample volume (v/v_0) and disagreements amount to only a few tenths of 1 per cent in most cases. This comparison is somewhat deceiving, however, because the total compressions are very small. A more easily interpreted comparison would be of the compressions, $1 - (v/v_0)$, in which case the difference between the shock and static values is typically 5 per cent.

The use of isotherms extracted from Hugoniot data for standardization of marker materials seems reasonable subject to the reservations expressed previously about obtaining equation-of-state information from Hugoniot data. The uncertainties are reduced when ductile metals are used in pressure ranges where the thermal pressure is small. Carter et al. [71C2] and Fritz et al. [71F2] have discussed the suitability of a number of materials for this purpose and Mao et al. [78M2] have continued this work, with specific attention to the use of copper, molybdenum, palladium, and silver in the pressure range from 6 to 100 GPa. Some further attention to the behavior of these materials and interpretation of available data would seem indicated, but there is reason to believe that they do permit establishing pressure to an accuracy of a few per cent. The internal consistency of the results for the four metals is most encouraging.

The linear (U, u) Hugoniot relation of eq. (2.16) is equivalent to a Hugoniot relationship between pressure and specific volume. Making certain reasonable assumptions, Ruoff [67R4] has shown that the coefficients of eq. (2.17) are given by

$$a = (K^s/\rho^+)^{1/2}, \qquad b = \tfrac{1}{4}[1 + \mathrm{d}K^s/\mathrm{d}p] \tag{3.6}$$

where K^s and $\mathrm{d}K^s/\mathrm{d}p$ are the isentropic bulk modulus and its pressure derivative, respectively, at the initial state. The value of a given by eq. $(3.6)_1$, can be identified with the isentropic bulk sound speed.

Ruoff and Chhabildas [77R3] have compared piston-cylinder, ultrasonic, and shock determinations of the isothermal bulk moduli and their first pressure derivatives for the alkali halides. Comparison of these parameters is a very sensitive test of agreement, which is found to be reasonable in most cases. The comparisons do show that, almost without exception, the shock-compression experiment yields a larger value for the modulus and a smaller value for its derivative than the ultrasonic measurement. Comparison with piston-cylinder data shows more variation but a similar trend is apparent. This trend has been noted previously by Pastine and Piacesi [66P1] and it seems reasonable to interpret it as evidence for nonlinearity in the (U, u) Hugoniot curve as they have done.

Syassen and Holzapfel [78S6] have recently found that X-ray data to 12 GPa for aluminum disagree with shock and ultrasonic data by less than 1 per cent for the bulk modulus and 3 per cent for its derivative. The corresponding values for silver are more scattered, but the shock data agree with their estimate of the true value to 1 per cent for the modulus and 15 per cent for its derivative. Agreement with piston-cylinder data is somewhat poorer in each case. A similar recent comparison by Ming and Manghnani [78M4] of shock, ultrasonic, and X-ray data for six transition metals shows agreement within about 1 per cent for modulus and 10 per cent for its pressure derivative. Sodium chloride is a material that has received considerable attention and the results of this work have been subjected to critical review by Birch [78B4].

3.3. Plastic and viscoplastic solids

3.3.1. Introduction

In this subsection we review observations of the response of solids to rapidly applied stresses in the range between the Hugoniot elastic limit and the value at which the elastic precursor wave is overtaken by the plastic wave. In this regime a shock evolves into a structured wave similar to the ideal elastic-plastic profile of fig. 2.2d, but differing from it in ways that reveal information about the mechanisms of rapid inelastic deformation, as indicated in fig. 3.3. Waveform measurements carried through to the decompression phase and those arising from the introduction of a sequence of shocks into a sample provide data on the shear strength of solids and permit some assessment of the limits of validity of the hydrodynamic approximation. Much of the technological interest in shock compression of solids centers on elastic-plastic phenomena.

The unique features of shock-loading experiments are that measurements of plastic flow can be made in precisely-controlled states of uniaxial strain and at strain rates that are higher than those achieved by most other means. The discussion of this section relates primarily to observations involving sufficiently low compressions that effects of shock heating and nonlinear elastic response are small. Investigations to determine material response have concentrated on four different features of the problem: (1) the elastic precursor to the plastic wave, (2) the profile of the plastic wave, (3) the profile of the decompression wave, and (4) the response of shock-compressed matter to the introduction of additional compression waves.

The first report of measurement of wavespeeds in a shock-loaded solid was that of Pack et al. [48P1], while the earliest experimental measurements permitting resolution of an elastic-plastic wave profile were made by Minshall [55M2]. Detailed continuum-theoretical analysis was begun by Wood [52W1] and continued by Morland [59M1] and Fowles [61F2], who also obtained the first experimental results confirming, in a general way, the predictions of the ideal elastic-plastic model. With improved instrumentation, wave profiles in metals were examined by Butcher and Canon [64B5], Barker et al. [64B1], Butcher and Munson [65B5], Novikov et al. [66N1], Butcher and Karnes [66B4], and others. This work demonstrated the existence of strain-hardening and viscoplastic effects and represented an attempt to incorporate them into a mechanical theory. During this same period, Jones and coworkers [62J2, 64J1] measured Hugoniot elastic limits of a number of metals and found many in substantial disagreement with predictions based on a rate-

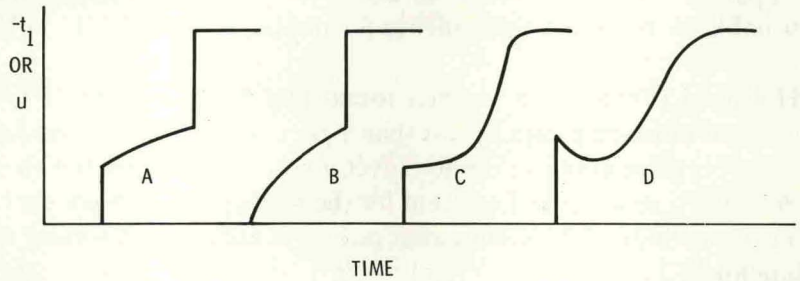

Fig. 3.3. Deviations from ideal elastic-plastic response often lead to variants of the waveforms shown. In example (A) an increase in shear strength during the early stages of the inelastic deformation is indicated, an effect usually described as "strain hardening". The waveform of example (B) is interpretable as involving either large strain hardening following a very weak wavefront or, more plausibly, as some form of gradual yielding. The dispersed plastic ave of example (C) is usually taken as evidence of viscoplastic flow, while example (D) represents the viscoplastic response observed in high-quality monocrystals.

independent interpretation of static observations. Minshall [61M1], Taylor and Rice [63T2], and Ivanov et al. [63I1] observed precursor-wave amplitudes that decreased with increasing distance of propagation. Duvall [64D2], Taylor [65T2], and Ahrens and Duvall [66A2] demonstrated that such behavior could be accounted for by stress relaxation. Decompression-wave profiles are strongly influenced by elastic-plastic response and early measurements on metals by Curran [63C1], Erkman and Christensen [67E1], Fuller and Price [65F1, 69F1], Barker [68B2], Kusubov and van Thiel [69K5], and others demonstrated that the hydrodynamic approximation did not adequately describe this wave in the range of compressive stresses to a few tens of GPa. These early phenomenological investigations, which are briefly summarized by Herrmann [69H1, 74H1, 76H3] and Murri et al. [74M3] are sufficient to demonstrate that neither the hydrodynamic approximation nor the ideal elastic-plastic model adequately describes the material response. Most recent work centers on interpretation of observations in terms of microscopically-based viscoplastic response models and on studies of shear strength of the compressed material, although several especially comprehensive continuum-mechanical investigations of metals have been conducted by Christman and coworkers [70C1, 71C3, 71C4, 72C2, 72C3, 72I1].

Much of the early work reflects the confrontation of inadequate theoretical models and experimental techniques with a complicated physical phenomenon. Viewed in retrospect, the most useful outcome of this work, besides realization and acceptance of the complexity of the problem, was the development of improved experimental techniques and computational methods that permit numerical simulation of experiments in terms of realistic material models.

3.3.2. Theory

When an elastic body is compressed in uniaxial strain, the pressure and magnitude of the shear stress increase by approximately proportional amounts. This proportional increase ceases when the shear stress reaches some critical level called the elastic limit or yield stress. In the simplest case the shear stress remains constant at this limiting value during further compression, while the pressure continues to increase as before. This behavior, shown in fig. 3.4a, is called ideal elastic-plastic response. The steep low-stress part of the heavily-drawn curve represents the elastic response of the material as described by eq. $(3.4)_1$. The limit of the elastic range is marked HEL. The portion of the curve beyond this limit represents the combined effects of isotropic elastic compression, some elastic response to shear, and the inelastic shear response. If an elastic-perfectly plastic body compressed to the state A is allowed to expand, the expansion process comprises an elastic expansion AB followed by plastic flow to C. These processes are discussed in detail by various authors, including Wood [52W1], Morland [59M1], Fowles [61F2], Zel'dovich and Raizer [66Z1], and Cristescu [67C4].

Because plastic deformations involve hysteretic effects, it is customary to express the theory in terms of equations relating incremental changes in stress and strain, or the rates of these quantities, rather than their current values. In uniaxial strain, $\boldsymbol{S}$ takes the diagonal form discussed in section 2.1, but is decomposed into two parts so that $\boldsymbol{S} = \boldsymbol{S}^{\mathrm{e}} + \boldsymbol{S}^{\mathrm{p}}$, where $\boldsymbol{S}^{\mathrm{e}}$ represents an elastic and $\boldsymbol{S}^{\mathrm{p}}$ an inelastic contribution to the strain. The associated strain rate tensor is defined to be $\dot{\boldsymbol{S}} = \dot{\boldsymbol{S}}^{\mathrm{e}} + \dot{\boldsymbol{S}}^{\mathrm{p}}$. The symmetry of the problem (for isotropic materials) suggests that each of these parts of the strain rate be symmetric about the X_1 axis but the separate parts need not be, and in fact are not, uniaxial. The plastic strain corresponds essentially to a displacement of the lattice from one to another equivalent arrangement of the atoms, so it does not involve any volume change. This interpretation of plastic strain also means that the stress rate is to be calculated from the elastic part of the strain

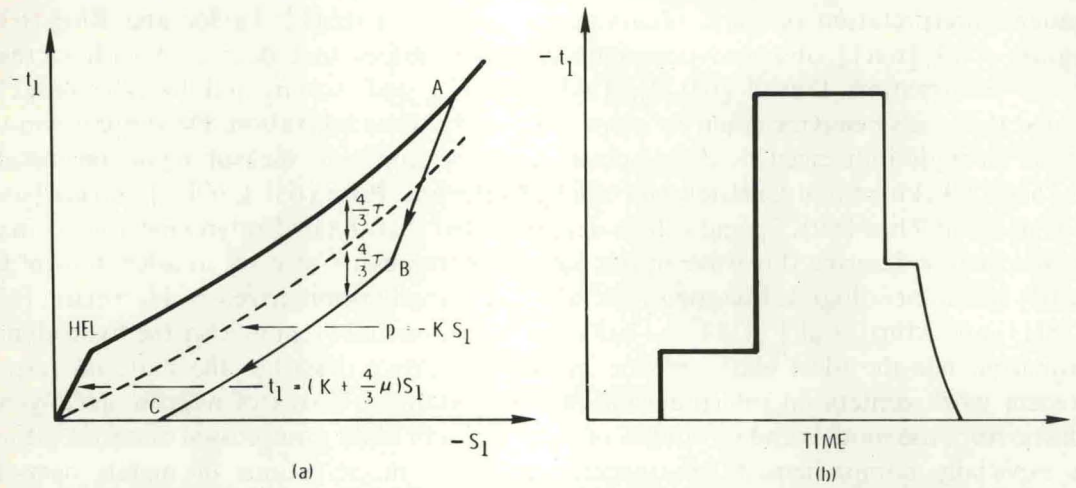

Fig. 3.4. Ideal elastic-plastic response. Part (a) of the figure shows the Hugoniot curve (as a heavy line), with the part of the stress attributable to the pressure response shown as the dashed line. The decompression process originating at a state (A) follows the lightly drawn path (ABC). The stress history that results at a point within a slab from short-duration application of stress at its boundary is shown in part (b) of the figure.

rate, and the result can be written in the form

$$\dot{t}_1 = (K + \tfrac{4}{3}\mu)\dot{S}_1 - \tfrac{8}{3}\mu\dot{\gamma}^p, \qquad \dot{t}_2 = (K - \tfrac{2}{3}\mu)\dot{S}_1 + \tfrac{4}{3}\mu\dot{\gamma}^p, \tag{3.7}$$

where $\dot{\gamma}^p$ is the rate of plastic shear strain, given by $\dot{\gamma}^p = (\dot{S}_1^p - \dot{S}_2^p) = \frac{3}{4}\dot{S}_1^p$. The ideal elastic-plastic response can be recovered from equations (3.7), but our interest here lies with the more complicated responses.

The variety and complexity of elastic-plastic phenomena make the development of a mechanical model of observed behavior a very difficult task even though, in essence, all that has to be done is represent the dependence of the plastic shear strain rate $\dot{\gamma}^p$ in eq. $(3.7)_1$ in terms of other variables of the problem.

The first breakthrough in this area came with the application of elementary concepts of dislocation mechanics. According to this model the plastic shear rate $\dot{\gamma}^p$ on a given slip system is related to the dislocation motion by the Orowan relation

$$2\dot{\gamma}^p = bNV_d, \tag{3.8}$$

where b is the length of Burgers' vector (a constant of the order of the lattice constant), N is the total length of mobile dislocation line in a unit volume of material, and V_d is the average velocity of the mobile dislocations. The dislocation density N depends in a complicated way (usually through a differential equation) on the entire history of the deformation in a neighborhood of the point in question, and V_d is a function of the resolved shear stress, τ, i.e., the component of $\boldsymbol{t}$ on the slip plane in the direction of the slip. The regime of elastic response is introduced into the theory by setting $V_d(\tau)$ to zero when $|\tau| < \tau_0$ for some limiting shear stress τ_0. Strain hardening is taken into account by allowing τ_0 to increase as plastic strain is accumulated. The dependence of V_d on τ is sufficiently strong that it is not unreasonable to assume that all slip occurs on planes lying at 45° to the X_1 axis. When this is done, the shear rate given by eq. (3.8) can be substituted directly

into the plastic flow eq. $(3.7)_1$ to yield the result

$$\dot{t}_1 - (K + \tfrac{4}{3}\mu)\dot{S}_1 = \hat{F}(\tau), \tag{3.9}$$

where $\tau = \frac{1}{2}(t_1 - t_2)$ and $\hat{F}(\tau) = -\frac{8}{3}\mu b N V_d(\tau)$. The function $\hat{F}(\tau)$ is called the relaxation function. Equation (3.9) was derived in its present form by Duvall [64D2] and Taylor [65T2], and its thermodynamic basis has recently been discussed by Nunziato and Drumheller [78N2].

The theory of dynamic plasticity outlined accommodates nonlinear elastic response in that K and μ are allowed to depend on S_1, although several aspects of this treatment are inconsistent with modern theories of finite plastic deformation.

3.3.3. Dynamic yielding – the elastic precursor wave

The amplitude of the elastic precursor to a plastic wave provides direct evidence for the onset of plastic flow under the particular conditions of the experiment. The early work by Jones et al. [62J2], Taylor and Rice [63T2], and Ivanov et al. [63I1] has stimulated continuing investigations. These studies have been concerned with microscopic explanations of the form of elastic precursor waves and the observed decreases in their amplitude with increasing propagation distance. Both single crystal and polycrystalline materials have been studied and metallurgical condition, temperature, and impurity and initial defect concentrations have been varied.

The first detailed application of dislocation-mechanical concepts to elastic-plastic wave propagation phenomena was Taylor's [65T2] analysis of the decay of the elastic precursor wave in iron. The attenuation of this wave can be calculated without solving the equations for the entire waveform since it is identified with the variation of the stress jump along the leading characteristic for an elastic shock, a quantity that can be determined independently of the remainder of the flow field. When this shock is propagating into unstressed material, a linearized analysis gives the wavefront equation

$$\frac{\mathrm{d}}{\mathrm{d}X}(t_1^-) = \tfrac{1}{2}\hat{F}C_\ell, \text{ where } C_\ell = [(K + \tfrac{4}{3}\mu)/\rho^+]^{1/2}. \tag{3.10}$$

The corresponding nonlinear result, taking account of hydrodynamic attenuation as well as stress relaxation, has been obtained by Ahrens and Duvall [66A2]. Experimental measurement of t_1^- at various propagation distances permits determination of valves of $\hat{F}$ through application of eq. (3.10). Since the relaxation function $\hat{F}$ depends on the number of dislocations participating in the yield process, the average speed with which they move, and the way in which these quantities depend on other variables, its determination provides information about the microscopic aspects of the yield process. The sensitivity of calculations to changes in the form of the velocity function is not great, but the way in which the number of mobile dislocations evolves during the passage of a wave is important and has been investigated in some detail.

Formulae relating dislocation velocity to stress that have been suggested in the literature include one derived from a reaction rate model, one based on linear damping, and one proposed by Gilman on the basis of experimental observations (see, e.g., [69R1]). Taylor adopted the Gilman form in his work, although the other relations could have been used as well since the differences among them become apparent only at very short propagation distances [67K1], or when temperature dependence or phenomena other than precursor decay rates are considered. Rohde [69R1] found that none of the dislocation-velocity formulae satisfactorily explained both the amplitude decay data of Taylor and Rice and his own observation of the temperature independence of this amplitude.

This led him to suggest twinning as a significant contributor to the deformation and subsequent work [71J2] has confirmed this hypothesis for the iron he studied.

Several investigators [71C5, 73S6, 73R1] have suggested more detailed models for calculation of dislocation velocity but the validity of such models cannot be verified without a critically-oriented experimental program. In recent work by Tyunyaev and Mineev on boron-doped single crystal silicon [76T1], it was observed that such doping did not change elastic wave attenuation. From this observation they concluded that the velocity of dislocations was controlled by non-thermally-activated mechanisms.

Holland [67H1] conducted the first dynamic yielding investigation in which the metallurgical condition of the samples was systematically varied. Observation of the effect of thermal aging of prestrained samples on the waveform propagated in Ferrovac-E iron led him to conclude that shock loading was extraordinarily effective in mobilizing pinned dislocations and/or effective in creating new ones. Subsequent work supports this conclusion but it now seems clear from work of Johnson and Rohde [71J2] and Rohde et al. [72R1] that Holland's original interpretation of his observations was in error due to neglect of twinning as an important deformation mechanism.

As pointed out by Jones and Holland [68J2], Taylor's analysis of the data of Taylor and Rice suggests that a great many dislocations participate in the yielding process, but that their average velocity is low. To investigate this point further, they measured the amplitude of elastic waves emerging from 19-mm thick samples of mild steel with grain sizes ranging from 9 to 70 μm. By comparing their data to static yielding observations and by using Taylor's dislocation parameters, they concluded that the average velocity of dislocations was low, that supersonic motion need not occur, and that yielding could be explained as a result of the conventional behavior of a large number of dislocations.

Dynamic studies in single crystals offer the advantages that slip on various systems can be activated selectively and that effects of grain boundaries and random crystallographic orientation are avoided. Investigation of single crystals of copper, NaCl, beryllium, zinc [73S6], tungsten [70J3], and LiF have been reported and the calculations required for analysis of the data prepared by Johnson et al. [70J3]. The first work in this area was undertaken by Jones and Mote [69J2], who studied copper crystals of 99.99+ % purity oriented so that shocks could be propagated in the [100], [110] and [111] directions. Unfortunately, little variation of precursor amplitude can be expected as the resolved shear stress on the primary slip system for this crystal does not vary greatly with its orientation. The ordering of the small variations that were observed was as predicted, however, and tended to confirm the hypothesis that yielding occurred when the shear stress resolved on the slip system reached a critical value. The initial dislocation density in the crystals studied was estimated to be 10^{10} m^{-2}, but a dislocation density of the order of 10^{12} to 10^{13} m^{-2} was required to explain the observed attenuation. The requirement that the density of mobile dislocations be very large if this model is to explain observed precursor attenuation rates has been found to hold in all cases considered since this early work. Its reconciliation with known initial values and credible mechanisms for increase in dislocation density has been an important objective of most subsequent research.

A rather detailed examination of the yielding of monocrystalline NaCl, a much more (plastically) anisotropic material was reported by Murri and Anderson [70M2]. They observed precursor waves of amplitude 0.027, 0.077, and 0.74 GPa emerging from 7-mm thick samples when the wave propagated in the [100], [110], and [111] direction, respectively. These data are in the order one would expect on the basis of the resolved shear stress on the primary $\{110\}\langle 110\rangle$ slip system;

the very large precursor amplitude observed for the [111] crystal is a result of the fact that the primary slip system is unstressed and yielding must occur on a secondary system. Gupta [77G7] has recently reported analogous results for another alkali halide crystal, lithium fluoride. This effect of orientation is taken as strong evidence of the relevance of dislocation glide to dynamic yielding.

Members of the Shock Dynamics group at Washington State University, including G.E. Duvall, G.R. Fowles, J.R. Asay, and Y. Gupta, have investigated dynamic yielding in lithium fluoride crystals [72A2, 72A3, 72A4, 73G5, 75G7, 75G8, 75A4, 75F1, 76D2, 77G7, 78R1]. These studies are much more extensive than any other similar investigations and are distinguished by unusually thorough material characterization and attention to other details, both theoretical and experimental. This work has confirmed the assumption that (for this material) the explanation of dynamic yielding is to be found in the motion of dislocations on established glide systems, and has resolved a number of other basic questions. Specifically, the results are consistent with the hypothesis that the instantaneous response to impact is elastic, that there is a stress threshold below which wave attenuation does not occur, and that precursor attenuation is attributable to both stress relaxation and hydrodynamic attenuation (primarily the former). The accumulation of plastic strain permitting stress relaxation is attributable to both grown-in dislocations and dislocations nucleated heterogeneously at point defects (interstitial Mg^{++} ions and radiation-induced Frenkel defects). The concentration of these defects and their state of aggregation have been shown to have a profound influence on precursor attenuation, with the attenuation rate being increased by increasing defect concentration or decreasing clustering of the existing defects. This and other evidence supports the conclusion that the large dislocation density necessary to produce the observed attenuation rate is a consequence of heterogeneous nucleation of dislocations at the point defects. The investigations have shown that regenerative multiplication processes cannot account for the observed decay. Neither variations in surface damage produced during sample preparation nor variations in the density of subgrain boundaries influences observations significantly.

Taylor [68T1], Pope and Stevens [73P1], and Pope and Johnson [75P1] have studied dynamic yielding in beryllium single crystals (hcp). This crystal is especially interesting because dislocations can move on distinct primary $\langle 11\bar{2}0\rangle \{0001\}$ (basal), secondary $\langle 11\bar{2}0\rangle \{10\bar{1}0\}$ (first-order prism), and tertiary $\langle 11\bar{2}3\rangle \{11\bar{2}2\}$ (second-order pyramidal) glide systems for which the resolved shear stress for static yield are in the approximate ratios 1:7:100. These differences are sufficient to permit the conduct of shock-compression experiments in which each glide system is activated separately. In experiments in which the shock propagated in the *a* direction (producing secondary slip) or the *c* direction (producing tertiary slip) precursor waves rise to sharp peaks in a few nanoseconds and relax within ~ 20 ns to minimum values which then increase with the arrival of the plastic wave (see fig. 3.3d). A difference in yield strength of the secondary and tertiary glide systems is quite apparent from the observations, but the complexity of the waveforms makes quantitative comparison of static and dynamic yield strengths uncertain. Investigation of basal slip presents an additional complexity in that the crystal must be impacted at an angle to the *c* axis if a shear stress is to be imposed on the basal plane. Such an impact does not produce a precursor in which the motion is strictly longitudinal but calculation shows that transverse motion effects are negligible in the elastic wave and the critical resolved shear stress for basal yield can be measured as though the material were elastically isotropic. Experiments conducted on crystals about 4-mm thick and cut at angles ranging from 23° to 61° to the *c* axis indicated that dynamic yield occurred at critical resolved shear stresses ranging from 0.06 to 0.19 GPa. This variation was attributed to a depen-

dence on the normal stress applied to the glide plane (consistent with observations of ⟨111⟩ LiF by Rosenberg [78R1]), but we believe experiments conducted at other propagation distances would be required to confirm this interpretation.

In the foregoing discussion, the precursor wave has been assumed to rise instantaneously. In many cases this approximation is satisfactory, but a number of polycrystalline metals exhibit precursor risetimes so great as to suggest distinctly anomalous response. In the case of beryllium the observations have been explained by Stevens and Pope [73S5] in terms of differences in yield point among the grains arising from residual thermal microstresses. In the case of tantalum, Gillis et al. [71G2] have offered an explanation based on a similar gradual development of plastic flow associated with dislocation multiplication in the wavefront. In contrast to these materials in which observed risetimes exceed 50 ns, the precursor risetime in aluminum is of the order of 10 ns, a value comparable to the uncertainty in its measurement. Nevertheless, Arvidsson et al. [75A2] noted a systematic increase in risetime with propagation distance, and have shown that the observation is consistent with the effect of adding a small viscosity term to the elastic constitutive equation. Meyers [77M3] has recently reviewed a range of published waveforms and has shown that the explanation of certain of the observations lies with the effect of various scattering phenomena that occur as the wave propagates through the polycrystalline material.

3.3.4. Plastic wave profile

Analysis of an entire elastic-plastic waveform can provide information about deformation mechanisms beyond that obtainable from examination of precursor decay alone. The difficulty of this analysis is that many variables are changing simultaneously. It is only in the case of a steady wave that quantitative information can be obtained by direct analysis of the observed waveform. Johnson and Barker [69J1] (see also [73P2]) applied this analysis to the profile of the main plastic compression wave in aluminum alloy 6061-T6 on the assumption that it had fallen far behind the precursor wavefront and was propagating with unchanging form. With this approach both the stress dependence of dislocation velocity $V_d(\tau)$ and the way in which the number of mobile dislocations increased with accumulation of plastic strain were determined. The function $V_d(\tau)$ was found to depend more strongly on τ than had been indicated by quasi-static investigations, but dislocation multiplication was in good agreement with such results. The steady-wave technique offers the advantage of simplicity, but is subject to error if applied to evolving waveforms and is not applicable to analysis of the most interesting part of many waveforms, that of rapid relaxation immediately behind the front of a precursor wave. Usually it is necessary to study evolving waveforms. In this case the experiment must be simulated numerically using a computer code incorporating the theory of section 3.3.2. Various models of dislocation velocity, nucleation and/or multiplication, immobilization, etc., can be considered. Calculations are performed with varying models and/or parameter values until, by trial and error, acceptable agreement between calculation and observation is achieved. Calculation of the entire profile of waves governed by the viscoplasticity theory outlined was first undertaken by Johnson and Band [67J1], Wilkins [68W3], and Gilman [68G2]. These calculations successfully reproduced qualitative features of the waveforms but the results were compromised by the artificial viscosity method used. The waveform dispersion introduced into calculations by this method can be avoided by use of the method of characteristics, or of hybrid methods. Such calculations have been made by Herrmann et al. [71H2], Clifton [71C5], and, most recently, by Asay et al. [75A4]. This latter work bore on the analysis of waveforms in high purity [100] crystals of lithium fluoride, and showed the power of a

complete analysis. Good quantitative agreement between calculated and observed waveforms was achieved. The dislocation density was calculated on the basis of a model in which they were nucleated in numbers increasing linearly with the maximum stress in the precursor and expanded as circular loops with velocity given by Gilman's relation. Calculations based on regenerative multiplication of dislocations could not be brought into agreement with observation using credible values for the initial density of mobile dislocations, thus adding additional support to the earlier inferences that heterogeneous nucleation was occurring.

In a series of experiments mentioned previously, Pope and Stevens [73P1] and Pope and Johnson [75P1] impacted beryllium monocrystals on planes cut at varying angles to the c axis to produce coupled longitudinal and transverse plastic waves. The theory of such waves has been developed by Johnson [72J1, 74J1] and Luzin [75L1]. Application of Johnson's theory to the problem of plane wave propagation in rotated c-cut beryllium crystals indicates that a plastic disturbance comprising two waves can be expected. As with the purely elastic case, the faster of these waves is primarily longitudinal while the slower is primarily transverse. Some of the general features of the theoretical predictions are present in the observations but the differences are pronounced enough to suggest that some deformation mechanism besides dislocation motion was operative. They have suggested that this mechanism may have been twinning, but have not examined this issue directly.

Kim and Clifton [79K1] have recently conducted an investigation of aluminum alloy 6061-T6 in which combined longitudinal and transverse waves were produced by inclined impact and measured by interferometric means. These preliminary results are most encouraging in that they demonstrate both the feasibility of the experiment and the sensitivity with which it can probe shear phenomena.

Twinning. In the case of iron, Johnson and Rohde [71J2] were led to consider the influence of twinning on observed compression waveforms. The motivation for this was provided, in part, by the fact that twins were known to form in this material when it was subjected to shock compression and, in part, by difficulty in explaining measured wave profiles on the basis of dislocation mechanics alone. A theory of twinning deformation analogous to that used for slip was constructed and specific formulae for the growth rate of the twins were postulated. With a suitable choice of parameters, calculated waveforms were in good agreement with observations. Experimental evidence indicated that twins were formed at a critical resolved shear stress of 0.075 GPa and grew at a rate depending on the excess of the applied stress over this threshold. The shear stress was limited in magnitude to 0.3 GPa by the onset of dislocation motion.

Christman et al. [72C3] have observed twinning in α-titanium (hcp) samples recovered after shock compression to 4.0 and 12.5 GPa, but no attempt was made to explain the observed wave profiles on the basis of a theory incorporating microscopic deformation models.

It is unfortunate that, in spite of the success of the early work of Johnson and Rohde, there seems to have been no further attempt to incorporate twinning into theories of wave profiles arising from shock compression. There is reason to believe that twinning is an important dynamic deformation mechanism that must be included in any realistic model of materials in which it occurs. Resolution of questions concerning yield mechanisms would be facilitated by examination of samples carefully recovered from shock experiments (see section 3.6).

The research on plastic wave propagation that has been reviewed seems to support the hypothesis that, for many materials, yielding and plastic flow arise as consequences of the motion of dislocations. The considerations leading to the representation (3.9) of the material behavior have

been quite elementary, involving only the most loosely defined average microscopic behavior of the dislocations. Observations of collective motion of dislocations producing heterogeneous deformation fields are common (see sections 3.4 and 3.6). Such deformations are associated with correspondingly nonuniform temperature fields and the coupling between this heating and the deformation process itself opens the way for the occurrence of deformation processes quite different from those that have been discussed.

From the continuum-mechanical viewpoint, the equations derived on the basis of the microscopic models must be regarded as extremely successful. Continuum theories of plasticity have been a subject of active research for many years. Results of practical utility have been obtained, but no truly satisfying theory has emerged. In recent years research into the microscopic aspects of deformation has spawned a number of dynamic theories of plasticity which, while still evolving, show the way to progress in this area. Specific applications of this work to the problem at hand have been discussed by Clifton [74C1] and Davison et al. [77D1].

3.3.5. Strength and rigidity of shock-compressed solids

The introduction of waves of either compression or decompression into material already in a shock-compressed state permits evaluation of the properties of this compressed material. Al'tshuler et al. [60A2] and, more recently, Holt and Grover [71H4], and others have shown how knowledge of the elastic moduli of a compressed substance can be exploited in determining its equation of state. Studies of variations in the shear strength of a solid, as conducted, for example, by Dremin and Kanel' [76D3] and Lipkin and Asay [77L2, 78A5] are also of interest and knowledge of these values is necessary for assessing the validity of the hydrodynamic approximation, for solving the practical problem of attenuation of stress pulses and for interpretation of spall studies and recovery observations.

The earliest experimental investigation of elastic-plastic decompression from high pressures was conducted by Al'tshuler et al. [60A2] and continuations of this work have been reported by Novikov and Sinitsyna [70N1] and Al'tshuler et al. [71A3]. In this latest work it is reported that iron is able to sustain a shear stress of about 0.5 GPa at a pressure of 111 GPa, and this value increases to about 1.4 GPa at a pressure of 185 GPa (iron is in the ε phase at these pressures). The corresponding value for copper is about 0.8 GPa at a pressure of 122 GPa. Interpretation of the observations for iron is complicated by the occurrence of the $\alpha \rightarrow \varepsilon$ phase transformation and Simonov and Chekin [75S1] have recently reevaluated the data in light of this complication and have arrived at even larger values for the yield strength. The data for copper are not subject to this uncertainty and also exhibit a large (over fivefold) increase in shear strength over its low-pressure value. Al'tshuler et al. have also evaluated the increase in the elastic moduli of copper as it is compressed.

Both the elastic moduli and shear strength observed in material that has been compressed by a strong shock reflect the effects of an increase due to the compression and a decrease due to the associated heating. When the material is shock compressed into the melt region its properties will, of course, be those of a fluid and both the shear strength and the shear modulus will vanish. These effects are discussed by Al'tshuler et al. [71A3] and are quite apparent in the work of McMillan et al. [71M1] and Asay and Hayes [75A3]. As pointed out by the latter investigators, observation of a loss of rigidity may be the only way of accurately determining the point at which shock-induced melting occurs.

Other investigations include early work by Curran [63C1] who observed a very strong elastic

decompression wave in aluminum alloy 2024 subjected to 10 and 17 GPa shocks. Curran later concluded [65C4] that the apparent high strength was an effect of the high rate of inelastic deformation rather than the compression, but Erkman and Christensen [67E1] were able to explain wave profiles obtained in similar circumstances on the basis of a rate-independent model. This issue has been investigated on a number of subsequent occasions, but remains to be resolved [74H1, 77L2].

When an observation of an elastic-plastic wave profile is carried through to the decompression phase, the observed pulse shapes deviate markedly from the ideal elastic-plastic stress pulse of fig. 3.4b. In particular, the distinction between the elastic and plastic decompression waves is so blurred as to suggest that the elastic range itself is poorly defined. Examination of a broad range of published compression waveforms reveals that they approach the ideal elastic-plastic form more closely as the peak compression increases. The approach of the decompression waveform to the ideal is correspondingly improved. When decompression from pressures of a few GPa is studied in copper and aluminum alloy 6061-T6, it is found that the elastic decompression wave overtakes the plastic compression wave prematurely because of the disperse structure of this latter wave. At pressures of about 10 GPa this plastic wave approximates a shock much more closely, and overtaking occurs at the time predicted by the elastic-plastic model [71C3, 71C4]. The decompression profile observed under these conditions still fails to exhibit a well-defined elastic-plastic form, although some structure is certainly evident.

For many years it has been assumed that a properly implemented model based either on dislocation-mechanical concepts or on their continuum-mechanical equivalents would describe both compression and decompression waveform observations. This objective has been accomplished in several instances [73R1, 74H1], but the models are quite complex and recent time-resolved wave profile measurements show considerable detail not yet explained. In recent years evidence has been accumulating to suggest that inhomogeneous mechanisms must be taken into account in explaining at least some of the observed deformation phenomena. This need is most apparent for the case of nonmetallic materials, as is discussed in section 3.4, but investigations of incremental compression or decompression of shock-compressed metals suggest that the effect may be influential for these materials as well [77L2, 78A5].

Strong solids. An important but generally unrecognized property of brittle solids is their possession of unusually large Hugoniot elastic limits. In a shock-compression experiment, strain is imposed very rapidly and gives rise to high pressure as well as a large shear stress. Under these conditions crack propagation may be inhibited or may not occur with sufficient rapidity to prevent shear stresses from exceeding the inherent strength of the material. Data summarized in [71G3] show that some solids exhibit strength ranging from 1 to almost 10 per cent of their shear modulus. More recent data on the response of several strong polycrystalline solids to shock loading are reported by Gust et al. [73G6], while Pope and Johnson [75P1] have reported high strengths for *c*-cut beryllium monocrystals which they attributed to tertiary slip. The strains to failure for a number of strong solids have been summarized in table 3.1. It appears that such data could profitably be used to study the inherent shear strength of solids.

3.4. Heterogeneous yielding and reduction of shear strength

Evidence that heterogeneous yielding is a dominant feature in the shock compression of certain solids is largely indirect and the process is not yet subject to quantitative analysis. Nevertheless, substantial anomalies in strengths observed upon loading just above the Hugoniot elastic limits

for quartz, sapphire, magnesium oxide and lithium niobate based on conventional models of yield and plastic flow require that unique deformation modes be invoked. A yield process in which the local dissipation of the elastic shear strain energy leads to high local temperatures appears to have the correct semi-quantitative features to explain the strength anomalies. Such heterogeneous yielding has been ascribed to brittle solids but exceptions observed for brittle solids such as monocrystalline germanium and polycrystalline Al_2O_3 blur that distinction. Based on the present review of experimental observations and theory, it appears that those solids which can be expected to undergo heterogeneous yielding are perhaps best described as *strong solids with low thermal diffusivity*.

The present phenomenon of heterogeneous yielding is thought to be an adiabatic shear process similar to the shear banding phenomenon observed in metal deformation under large rapid shear loading (see, e.g., [78W1]). Heterogeneous yielding is distinguished from the more general phenomenon by the unique feature that it occurs within the first few nanoseconds or tens of nanoseconds after shock loading and is controlled by inherent strength and thermophysical material properties.

Table 3.5 summarizes the principal developments in studies of reductions in shear strength. The first observations of the effect resulted from both electrical and mechanical measurements on α-quartz by Neilson et al. [62N2], Wackerle [62W1], and Fowles [61F2, 67F1]. In 1971 there were

Table 3.5
Studies of reduction of shear strength

Material	Date	Measurement	Strength reduction?	Remarks	Reference
α quartz	1961	piezoelectric	yes	loss of strength	Neilson et al. [62N2]
α quartz	1961	luminescence	—	linear features	Neilson et al. [62N2]
α quartz	1962	$U - u$	yes	loss of strength	Wackerle [62W1]
α quartz	1962	$U - u$	yes	loss of strength	Fowles [61F3, 67F1]
MgO	1966	$U - u$	yes?	possible loss	Ahrens [66A1]
Al_2O_3 ceramics	1968	$U - u$	no	strength retained	Ahrens et al. [68A1]
B_4C ceramics	1971	$U - u$	yes	loss of strength	Gust and Royce [71G5]
BeO ceramic	1971	$U - u$	yes?	5.6% porosity	Gust and Royce [71G5]
Al_2O_3 ceramics	1971	$U - u$	no	1 to 6.6% porosity	Gust and Royce [71G5]
α Al_2O_3	1971	$U - u$	yes	some strength retained*	Graham and Brooks [71G3]
α Al_2O_3	1973	optical absorption	yes	loss of strength	Gaffney and Ahrens [73G1]
α quartz	1974	recovery	—	observed slip bands*	Ananin et al. [74A2]
α quartz	1974	piezoelectric	yes	some strength retained*	Graham [74G2]
quartzite	1975	decompression	yes	first thermal model*	Grady et al. [75G3]
α Al_2O_3	1976	decompression	yes	partial strength recovery	Bless and Ahrens [76B6]
Tungsten	1976	t_1 vs. u	yes	small effect	Dandekar [76D1]
MgO, (100)	1977	$U - u$, decompression	yes	loss of strength*	Grady [77G2]
MgO, polyxtal	1977	lateral release	no	slow strength reduction	Meier and Ahrens [77M2]
Theory	1977	theory	yes	explicit thermal model*	Grady [77G2]
Glass	1978	longitudinal and normal stress	yes	stress anisotropy	Kanel' et al. [78K1]
$LiNbO_3$	1979	$U - u$	yes	strength reduction*	Stanton and Graham [79S2]
$LiTaO_3$	1979	$U - u$	yes	strength reduction*	Stanton and Graham [79S2]
α Al_2O_3	1979	optical absorption	yes	loss of strength	Goto et al. [79G1]

(See also review of geophysical phenomena resulting from meteorite impacts Chao [67C2] and Stöffler [72S4].)

* These papers review status of knowledge and propose mechanisms.

a sufficient number of observations to begin to speculate on general mechanisms [71G3] and in 1974 and 1975 the present view of heterogeneous yielding came into focus with the papers of Ananin et al. [74A2], Graham [74G2], and Grady [75G3]. Grady [75G3] first explicitly treated localized temperature distributions and later [77G2] extended these analyses to effects on phase transitions. These time-dependent temperature models also explain discrepancies between strengths determined in shock-compression and decompression measurements. Recent attempts at direct stress anisotropy measurements apparently indicate a loss of strength in glass [78K1].

The only direct evidence for the presence of localized melting upon yielding has been presented in a thorough investigation by Ananin et al. [74A2]. They recovered samples of X-cut quartz shock loaded above the Hugoniot elastic limit and below the phase transition at 14.5 GPa and observed that the recovered sample was composed of blocks of α-quartz surrounded by layers of quartz glass. Although similar observations have been made in naturally- and artificially-shocked quartz, prior work was complicated by stresses above the phase transitions and the explicit association with yielding had not been made. (See the review of petrographic features in quartz minerals by Stöffler [72S4], and a typical controlled shock loading by Müller and Defourneaux [68M4].) Recent shock measurements on lithium niobate in which hot or melted regions have a significantly different bulk modulus show major anomalies in the pressure derivative of bulk modulus which can partially be explained by heterogeneous yielding [79S2].

Grady [77G2] showed that the normal temperature distribution due to a local dissipation of shear strain energy could be conveniently expressed as

$$\theta = \theta_s + [Q/\sqrt{4\pi\chi t}] \exp(-h^2/4\chi) \tag{3.14}$$

where θ is the temperature, θ_s is the temperature resulting from isentropic homogeneous compression, $Q = \varepsilon/\rho C$ where ε is the thermal energy per unit area deposited at the position $h = 0$, ρ is the mass density, C the specific heat, and χ is the thermal diffusivity.

Solutions for typical temperature distributions at various times indicate the dominant role of thermal diffusivity in reducing local temperatures. If diffusivity is high, the temperatures may be reduced to background levels before melting or softening can occur. If diffusivity is low, high temperatures may persist for times appropriate for shock-compression experiments. Thermal time constants for low diffusivity materials are approximately 1 μs for distances of a few microns which are typical spacings between slipped regions in quartz.

The thermal energy deposited will depend directly on the elastic shear energy which may be roughly approximated by the area on the stress volume curve between the elastic compression and isotropic compression curve at constant stress. The density of slip bands must then be known to estimate the thermal energy per unit area. This latter quantity is unknown but can be estimated to affect 1 to 10 per cent of the sample volume based on observations of recovered samples by Ananin et al. [74A2]. The spacing between slipped regions is expected to vary from material to material and with magnitude of the loading and is likely to vary throughout a given sample.

In order to delineate the conditions under which heterogeneous yielding will occur, the results of various investigations of yielding and reduction of shear strength are summarized in fig. 3.5, which shows combinations of elastic shear strain energy (not thermal energy) and thermal diffusivity for which reduction of strength upon yielding is or is not observed. As expected from eq. (3.14), the figure shows that strong solids with low thermal diffusivity show reductions in strength in almost every case. Although there are insufficient data to delineate the boundary between

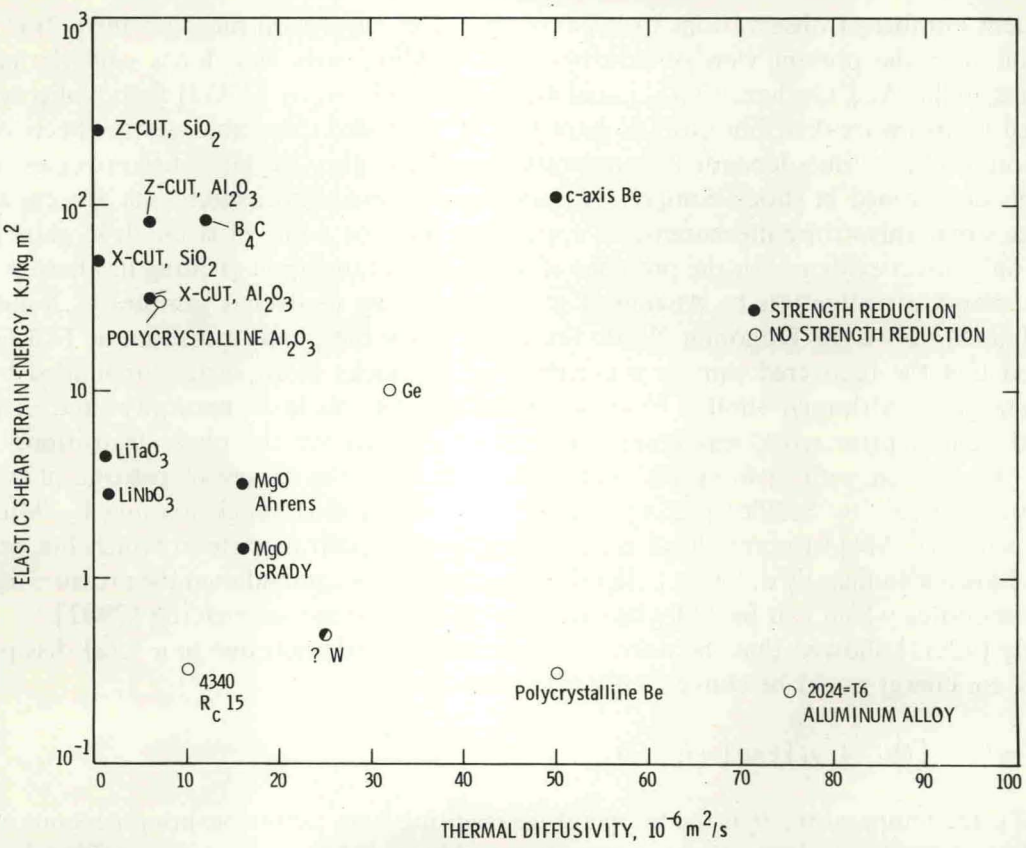

Fig. 3.5. The conditions of elastic shear strain energy and thermal diffusivity for which there is strong evidence for either strength reduction or strength retention are shown for a wide range of materials. Experiments in which complications such as porosity cloud the strength question are not shown. Metals are generally acknowledged to retain a relatively constant shear strength. Data are from sources in table 3.5 except *c*-axis Be [75P1], Ge [66G1], 4340 steel alloy [65B5] and aluminum alloy [61F2]. The point for tungsten is indicated ambivalently since recent work by Asay and Dandekar [78A4] has shown that strength reduction is relatively gradual. Except for the metal alloys, tungsten and polycrystalline Al_2O_3, the data are for monocrystalline materials.

materials which show strength reduction and those which retain their strength, the figure shows some indication that germanium, beryllium and MgO are close to critical boundaries.

The collected data shown in fig. 3.5 provide qualitative support for explanation of strength reductions in terms of local hot regions resulting from dissipation of elastic shear strain energy. The notable exception is polycrystalline Al_2O_3. Since the yield process is localized on the scale of a few microns, the exception may possibly be the result of impurities at grain boundaries where local thermal diffusivity may be much higher than for the bulk material. Alternately, the polycrystalline behavior might possibly result from much finer spacing between slip regions. Decompression measurements from states above the Hugoniot elastic limit of polycrystalline MgO [77M2] indicate significant strength. This behavior is consistent with the local heating model since decompression occurs at times for which significant reductions in temperature may be expected.

The consequences of such heterogeneous response to shock loading are profound. Usual assumptions of homogeneous, equilibrium thermodynamic behavior are clearly violated. Local

conditions are significantly time dependent. Such gross deviation from equilibrium behavior as a result of yielding leads to a situation in which critical thermodynamic variables are controlled by the yield process rather than by the nominal conditions of uniform temperature and pressure. The effect of such a situation is well demonstrated in quartz in which recovery experiments indicate higher concentrations of dense phases, stishovite and coesite, along regions that have experienced localized melting (see section 3.7). Furthermore, the anomalous metastable mixed phase region observed in quartz may be a consequence of such heterogeneous processes. This view is strengthened by the recent observation of a similar extended mixed phase region above the phase transition initiated in $LiNbO_3$ at 15 GPa [79S2]. It is also apparent that in strong solids of low thermal conductivity, the sample is no longer in its virgin state and changes induced by such yielding must be explicitly considered in interpretation of experimental results. Grady [78G2] has recently developed more explicit models for the thermodynamic consequences of shock-induced phase transitions on heterogeneous yielding.

3.5. *Spall fracture*

A *spall* is a material fracture produced by the action of tensile stress developed in the interior of a solid body when two decompression waves collide. Spalls result from impact, detonation of contacting explosive, contact with an electrically-exploded wire or foil, deposition of intense pulses of radiation produced by electron beam accelerators or lasers, and other causes. Knowledge of spall phenomena is important in military applications, for the design of explosive metal-working processes, and to ensure that it does not occur inadvertently during other shock experiments. Fracture processes can be construed as deformation mechanisms and, as such, must be included in comprehensive theories of the mechanical behavior of solids. Finally, spall experiments have begun to take their place among other means of scientific investigation of fracture processes. A natural extension of investigations of spallation is to the study of dynamic fragmentation processes, a topic now being pursued for its application to mining operations [73S2, 74S3].

Early investigators, using explosive systems to introduce stress waves into their samples, attempted to determine conditions of stress, duration of stress application, etc., under which a spall would occur and to investigate various metallurgical aspects of the spall process. Much of this early work has been reviewed by Butcher et al. [64B4]. The experimental method offering the greatest control over the variables of importance to spallation involves impacting a target plate made of the sample material by a thinner impactor plate of the same material that has been accelerated to the desired velocity using a gun. The magnitude and duration of the tensile stress pulse produced in this experiment is controlled by varying the impact velocity and the thickness of the impactor plate, respectively.

The material response to brief application of tensile stress is frequently the development of a diffuse distribution of small cracks or voids in the material. For stress pulses of sufficient amplitude and duration, this damage may accumulate to the point where the sample fractures completely. The tensile stress required to produce some given level of damage (however this may be defined) is called the *spall strength*. Since an increase in either the tensile stress or the duration of its application increases the amount of damage produced, the spall strength of a material varies with both the degree of damage taken to constitute a spall and the duration of the tensile stress pulse.

A number of investigations in which plate-impact experiments were conducted to provide quantitative information at low-to-moderate damage levels are summarized in table 3.6. Most

of these investigations have had as their objective the determination of conditions under which damage is produced in structural materials.

Spall damage develops in stages dominated by (1) the nucleation of cracks or voids or the activation of growth at existing damage sites, (2) growth of individual fracture nuclei, and (3) coalescence of neighboring cracks or voids. The process may be arrested at any point of its course.

Nucleation of spall damage. Spall damage can develop at material defects such as grain boundaries, inclusions, microcracks, etc., or at sites at which no defect is apparent upon metallographic examination [73S3]. The nature of fracture nuclei when no obvious defect is present has been a subject of speculation for many years. Attempts have been made to identify them with various atomic-scale defects such as dislocation pile-ups or to assume they arise as a normal consequence of thermal motion of the lattice. Neither these nor other microscopic models have been subjected to critical test in spall experiments because they deal with phenomena occurring below the level at which observations have been made. Occasional observations such as one by Seaman et al. [71S1] on annealed, high-purity polycrystalline aluminum suggest a nucleation mechanism related to the dislocation substructure within individual grains. Galbraith and Murr [75G1] and Murr [76M5] have suggested that nucleation at grain boundaries in beryllium and molybdenum may be controlled by dislocations and ledge structures present there. Even if fundamental damage-nucleation mechanisms are operative, however, they may be dominated by effects of gross pre-existing flaws. Most research on spallation has been related to technical materials and, in the overwhelming majority of cases, damage has been observed to form at sites of gross defects. It is clear that even material samples of rather high perfection contain defects in sufficient quantity to account for the observed concentrations of damage sites, and the defect concentration can be expected to increase significantly in the compression phase of the stress history that precedes development of a spall. Stevens and Tuler [71S2] found that this precompression history had no effect in mild steel or aluminum alloy 6061-T6, but an effect might be expected in more nearly perfect materials. Spall experiments designed to explore nucleation phenomena in materials of high perfection seem useful in arriving at a basic understanding of fracture phenomena generally, but few suitable experiments have been conducted and none have been interpreted in terms of basic nucleation models.

If we accept the premise that damage develops at flaws inherent in the material, then the issue becomes one of activation rather than nucleation. Explaining the activation of ductile growth of voids seems not to present a problem as the stress thresholds above which voids have been observed to develop exceed the elastic limit of the material in question. The case of plane cracks is more interesting, and one having a long history. The issue as it relates to spallation has recently been investigated by Kalthoff and Shockey [77K1]. They found that the onset of growth of cracks (in this case rather large ones) in a polycarbonate plastic is interpretable in terms of a generalization of concepts of static fracture mechanics. This generalization includes the use of a dynamic value for the critical stress-intensity factor and a requirement that the stress intensity be maintained for a minimum time. If this or some similar model can be shown to apply in sufficient generality, and if damage develops primarily at pre-existing cracks, then the nucleation phase of the spall process would be replaced by an activation phase. Some, as yet unstudied, intermediate conditions can be expected to prevail when damage is initiated at the grain boundaries, inclusions, etc., present in technical metals.

Growth of spall damage. In homogeneous material, damage takes the rather distinct forms of voids produced by plastic flow or cracks produced by cleavage. An example of ductile void growth

Table 3.6
Incipient spall strengths

Material	Spall strength GPa*	Impactor thickness mm	Character of damage	Method**	Remarks	Reference
Aluminum and alloys						
Aluminum	1.0	1.58	ductile voids	M	Annealed	[71S1]
1145	0.5–1.1	1.14–5.84	ductile voids	M	NAG parameters given	[70B1, 71S1, 72B1]
2024-T4	1.25	3.8	blunt cracks	M	30% weaker at 541 K	[70B5]
2024-T81	0.6	3.36	blunt cracks	M	NAG parameters given	[71S1]
2024-T86	2.0–1.8	0.3–1.0		V, PB	e-beam data on 4 metals	[78S1]
6061-T6	1.5–0.8	0.25–1.75	blunt cracks	M		[64B4]
6061-T6	1.0	3.17	blunt cracks	M	No effect of precompression	[71S2]
6061-T6	2.0–1.3	0.25–4.0	blunt cracks	M, PB	Broad investigation	[71C4]
6061-T6	2.3–0.8	0.25–6.35	blunt cracks	M		[63B1]
2014–T6	1.76–1.47	0.61–1.57	blunt cracks	M		[71B2]
AMg-6	2.14–1.36	3.0–5.0	blunt cracks	M, V		[73T2]
Beryllium						
a-cut crystal	1.0	1.27 (quartz)	prism cleavage	M		[73P1]
c-cut crystal	1.15	0.76 (quartz)	basal cleavage	M		[73P1]
HP-10	0.92	1.02 (quartz)	cleavage	M, PB		[73S5]
HP wrought ingot	0.54–0.36	1.27–5.08	cleavage	M	35% stronger at 533 K	[70C1]
S-200	1.3–0.78	0.64–2.54			Stronger hot	[68W2]
N50A	0.9–0.5	0.25–5.08	irregular crack	M		[68W1]
Brass, 60/40	1.4	6.35		M		[70S2]
Copper						
OFHC	0.95–0.75	1.5–3.2	blunt cracks	M	Cold rolled	[63S1]
OFHC	2.5–1.8	0.5–3.0	voids and cracks	M	Half hard	[71C3]
OFHC	2.3–0.62	0.4–1.6	voids and cracks	M	Believed annealed (NAG)	[71S1, 72B1]
Graphite, ATJ-S	0.062–0.047	0.79–3.18	irregular crack	M	Independent of temperature	[68W2]
Plastics						
Lucite	0.1	0.25–6.35	fine cracks	V		[63B1, 63K1]
Lexan	0.16		plane cracks	V	Polycarbonate plastic (NAG)	[73C8]
Epon 828 Epoxy	0.076	5.08	plane crack	V	Single crack	[68G6]
Plexiglas	0.15–0.14	1.0–2.8	plane cracks	M, V		[73T2]
PMMA		1.0–2.0	plane cracks	M, V	80 to 333 K	[73T1]
ABS	0.1–0.06	0.55–4.5	fine crazing	V		[72T1]
Iron and steel						
Fe (99.99%)	1.9	1.16	brittle cracks		Light damage	[71S1]
Armco iron	3.5–1.7	0.51–2.36	brittle cracks	M	NAG	[70B1, 71S1, 72B1]
1020	1.6	3.17	brittle cracks	M	No effect of precompression	[71S1]
4340 Rc 15	2.5	6.35			Annealed	[67B4]
Rc 54	4.1	6.35			Quench to max. hardness	[67B4]
Rc 52	5.3	6.35			Quenched and tempered	[67B4]
Armco 21-6-9	3.7	3.2–12.8		PB		[69G3]
AM 363	4.5–2.1			PB		[71D1]
Titanium	3.9–2.1	0.22–4.09	blunt cracks	PB	25% stronger at 533 K	[72C3]
	3.7–2.2	0.4–6.0	voids, cracks	M	Cracks at grain boundaries	[78S3]
Uranium	2.4	0.77–3.01		PB	Also Cu, Ta, two steels	[77C1]
Rock***						
Oil shale	0.017–0.023			PB	Strength increases with kerogen content	[76S1]
Quartzite	0.04		plane cracks	V, M	Arkansas novaculite	[73S2, 74S3]

* All values inferred from plate-impact experiments done with thickness ratios approximately 2 to 4. Values are measured at room temperature ($\sim$ 20°C).

** V - visual inspection, M - microscopic examination, PB - inferred from free-surface velocity history.

*** See also the recent measurements on 21 rocks by Grady and Hollenbach [79G3].

is found in an investigation of Stevens et al. [72S2, 73S4] in which spall damage in high-purity aluminum monocrystals took the form of octahedral voids with {111} planes of the fcc crystal as faces. This observation was explained as a consequence of volume being transported into the void by edge dislocations moving into it in response to the surrounding stress concentration. A model developed on this basis indicates that, at constant stress, the volume of a void increases at a rate proportional to its current value, i.e., exponentially in time. This result is consistent with the law previously discovered empirically by Barbee et al. [72B1] and since shown to hold rather generally for the early phase of the growth process.

Formation of well-defined plane cracks has been noted in iron, beryllium, poly(methyl methacrylate), and polycarbonate. The work on iron [71C8, 72B1, 73S1], which is quite detailed as to the statistical properties of the crack distribution, indicates a 50 per cent higher strength for Armco iron over that of a similar but more nearly pure material, and notes a transition to ductile behavior at high temperatures. At temperatures where brittle fracture is observed, the cracks are randomly oriented, probably lying on {100} planes of the various grains comprising the polycrystalline sample [61E1, 68B1]. Experiments [73P1] on beryllium monocrystals showed that impact along the a axis produced cleavage along type-II prism planes, while impact along the c axis produced cracks along basal planes. In each case the spall plane was that subjected to the greatest tension. Impact of a crystal cut at 45° to the c axis produced a spall fracture surface comprising elements of basal and pyramidal planes, and perhaps other planes, of micrometre diameter. Spall damage nucleated at grain boundaries in polycrystalline samples of beryllium is observed to propagate in both inter- and intragranular modes. The work on poly(methyl methacrylate) [73T1] and polycarbonate [73C8] plastics shows that damage results from stress activation of pre-existing flaws. The cracks, which are circular and lie perpendicular to the direction of maximum principal stress, grow in a complicated way that involves dynamic phenomena associated with the individual cracks and also seems to include coalescence of large cracks with small cracks forming in the path of their advance.

In technical materials, where damage is most frequently nucleated at gross defects, the distinction between ductile and brittle response is often blurred with "blunted cracks" being observed in most materials. There is a large, but not very definitive, literature describing such observations and the matter is discussed in most of the work listed in table 3.6.

The effect on spallation of variations in metallurgical characteristics of aluminum alloys and beryllium can be inferred from existing work, and Jones and Dawson [73J2] have surveyed the effects of varying dislocation density, stacking-fault energy, and state of second-phase precipitation in several materials. Unfortunately, metallurgical changes that influence fracture phenomena influence propagated waveforms as well, and this effect must be taken into account if data are to be interpreted with assurance.

Most research on spallation has been directed toward finding a criterion for its occurrence [72D1]. Several criteria have been proposed, all sharing a number of serious shortcomings among which is that the concept of spall damage itself is not given a quantitative interpretation. In modern work, spall damage is quantified by the number density and size distribution of the cracks or voids in the material. At low damage levels these might typically be $10^4/\text{mm}^3$ and 1 to 100 μm radius, respectively. Experimental investigations have concentrated on measuring these quantities in samples subjected to various histories of load application. Theoretical interpretation of the results has been in terms of equations relating the rate of nucleation and growth of cracks or voids to the stress.

In an extensive series of investigations conducted by T.W. Barbee Jr., D.R. Curran, L. Seaman, D.A. Shockey and others at the Stanford Research Institute [72B1, 73S1, 73C8, 76S2, 77C2] it has been shown that cracks or voids are nucleated at a rate that increases exponentially with the excess of the tensile stress over a threshold value. The radius of each crack or void has been found to increase at a rate proportional to the product of its current value and the excess of the tension over a threshold value for growth. The parameters entering these rate equations are called nucleation and growth (NAG) parameters and work in which they have been measured is noted in table 3.6. The nucleation and growth laws have been inferred, on the basis of a number of assumptions, from the results of counting and measuring individual cracks or voids appearing on cross-sections of recovered samples [78S2]. The void growth results are in reasonable accord with continuum-mechanical models [71S1] and a microscopic model [72S2, 73S4]. The empirical conclusion that the same viscous growth law applies to the radius of penny-shaped cracks is rather surprising, as conventional continuum-mechanical analysis predicts that the crack boundary should move at constant velocity after a brief period of acceleration. DeRosset [73D2] has pointed out that one must expect some coalescence of cracks when they are present at the observed densities, and has shown that coalescence of cracks expanding at constant velocity leads to apparent exponential growth.

Because spall damage accumulates gradually and affects the stress field through its effect on the gross mechanical properties of the material, detailed analysis of spall phenomena requires combining rather complicated mechanical theories with detailed time-resolved wave profile

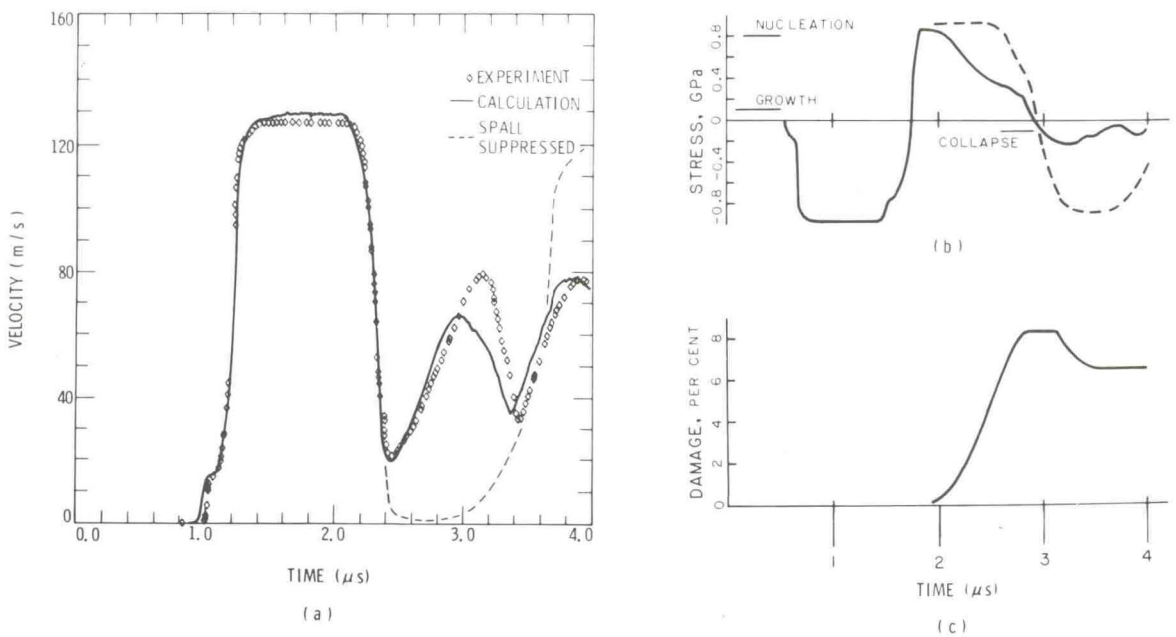

Fig. 3.6. The measured velocity history of the stress-free surface of a 6.4 mm thick aluminum plate impacted by a fused silica plate having a thickness 3.2 mm and moving at a velocity of 142 m/s is shown in part (a) of the figure. This result is compared with elastic-viscoplastic calculations in which spallation is suppressed and in which it is allowed to develop and interact with the stress field. The corresponding calculated stress histories at the midplane of the aluminum plate are shown in part (b) of the figure, along with threshold stresses for nucleation, growth, and collapse of voids. The history of damage accumulation at this plane (defined as volume fraction of voids) is shown in part (c), (after Davison et al. [77D1]).

measurements and a quantitative description of the damage observed in recovered samples. Several such theories have been developed [73D1, 76S2, 77D1, 77C1, 79D1] and some results of an example calculation that illustrates both the sort of prediction obtainable from a typical theory and some features of the spall process itself are given in fig. 3.6. It is noteworthy that, in the ductile case, at least, the theoretical predictions are in general conformity with a broad range of observations [79D1]. The complexities introduced by the varying orientation of the cracks that develop in some polycrystalline metals have so far prevented analyzing their behavior on the basis of a completely sound, internally consistent theory.

The state of knowledge of spall phenomena can be summarized by saying that much practical information is available and pragmatic understanding is well advanced, but almost nothing fundamental is known about either the nucleation or late growth stages of the process and much remains to be learned about the early growth phase. The influence of viscous heating and inertial resistance to growth are cases in point. Some calculations suggest that the heating attributable to plastic flow can raise the temperature of void surfaces to nearly the melting point, but this effect has not been included in the growth models. Inertial effects are known to slow the exponential growth observed for small voids [71S1] but this effect is not included in interpretations of data. The influence of void coalescence on observed growth rates also remains to be investigated, and this influence could be very great if nucleation at adjacent sites is correlated. Finally, the effect of variations in microstructural parameters is almost completely unknown.

3.6. Residual metallurgical effects of shock loading

The limited mechanical, electrical, and optical measurements that can be made during shock compression, or while the material is held in the compressed state, can usefully be augmented by examination of samples recovered after the load is removed. These examinations not only disclose features of the shock process, but also provide a means for extending many conventional metallurgical investigations to conditions of strain rate and compression not achievable by other means.

The value of careful examination of recovered samples was demonstrated in an early investigation of Smith [58S1] in which twinning was disclosed as a high-strain-rate deformation mechanism in copper and a number of unusual effects were found to result from the $\alpha \rightarrow \varepsilon$ phase transformation in iron. The field has remained active since this early work, and has been reviewed periodically as indicated in section 1.1. Two recent reviews are of particular interest; that by Otto and Mikesell [67O1] because it contains tabular and graphical information on residual mechanical properties, and that by Leslie [73L1], who provides an authoritative summary of work in the area of physical metallurgy through 1972. Some subsequent work is summarized in table 3.7.

Typical peak compressions achieved in investigations of residual metallurgical effects have been 5 to 20 per cent (pressures to $\sim$ 50 GPa), with most of this compression occurring during the few nanoseconds required for the plastic wave to pass a given material point. The uniaxial compression process is, of course, accompanied by a substantial and rapid inelastic shear. Following passage of the compression waves, the material is held in the compressed state for a time depending on the experimental configuration but not exceeding a few microseconds, after which a decompression wave allows the material to expand adiabatically to atmospheric pressure. Significant shock heating also occurs; for example, compression to 30 GPa causes the temperature of aluminum to increase by about 400 K and that of copper to increase by almost 200 K. Even after decompression, temperatures are increased by 170 and 70 K, respectively. Few experiments have been

Table 3.7
Recent investigations of residual metallurgical effects of shock loading

Material, Reference	Peak pressure, p GPa	Stress pulse duration, Δt μs	Remarks
Copper			
Hooker et al. [71H5]	100	0.7	Elongated dislocation cells, 0–5° misorientation, no twins
Higgins [71H3]	43.3	1.0	Cube-oriented samples develop well-defined subgrains, recrystallize on annealing
Chojnowski and Cahn [73C6]	15.5, 41.0	2.0	Annealing studies correlated to hardness and microstructure
Dietrich and Greenhut [73D3]	5.0–10.0	—	Annealing studies correlated to microstructure
Kingman [73K2]	3.0–14.0	—	Introduces X-ray topography as a probe of shock-induced microstructure
Chang et al. [75C1]	0.2–8.5	—	Shock-induced decreases of 1–7 % in Young's modulus
Teslenko [77T1]	10.0–31.0	—	X-ray line broadening and hardness
Murr [78M8]	5.5–34.5	2.0	Dislocation structure correlated to mechanical properties
Copper - 1.9 % beryllium			
Nordstrom et al. [75N3]	10.0–50.0	0.66	Microstructure and thermomechanical properties
Copper - 8.6 % germanium			
Mikkola and coworkers [73B1, 76M1, 78L1, 78W4]	1.6–47.5	0.004–3.5	Broad investigation, recently emphasizing hardening mechanisms
Aluminum alloy 2024			
Lee and Ma [78L2]	0.15–1.1	—	Shock-induced decreases in Young's modulus
Aluminum - 3.85 % copper			
Stein [75S3]	1.4	0.85	Precipitation phenomena considered
Nickel			
Murr and coworkers [75M2, 78M8, 78M9]	8.0–46.0	0.5–6.0	Microstructure, stored energy, hardness, and strength quantitatively related to p, Δt
Meyers [77M4]	20.0	1.2–10.1	Work softening in static tension after shock loading
Teslenko [77T1]	10.0–36.0	—	X-ray line broadening and hardness
Chromel A and Inconel 600			
Murr and Huang [75M2]	25.0	0.5–6.0	Dislocation and twin densities, and hardness correlated to t_1, Δt
Inconel 718			
Meyers and Orava [76M2]	51.0	—	Effect of shock on thermomechanical behavior
Stainless steel 304			
Murr and coworkers [75M3, 78M10]	15.0–45.0	0.5–6.0	Formation of twin faults, bct and hcp phases correlated to t_1, Δt
Kestenbach and Meyers [76K1]	10.0	2.8	Microstructural changes correlated to grain size
Hadfield steels			
Dorph [77D4]	—	—	Shock hardening mechanisms investigated
Iron, mild steel			
Bouchard and Claisse [73B2]	—	—	Effect or ordering by Al alloying and heat treatment on twinning
Huo and Ma [75H2, 75H3]	10.0, 30.0	—	X-ray line broadening
Ganin et al. [78G1]	—	—	Hardness related to twin spacing and dislocation density
β-Titanium alloy			
Rack [76R1, 78R2]	2.0–26.0	1.8	Strength correlated to microstructure
Molybdenum			
Murr and coworkers [76M6, 78W3, 78M10]	14.0–35.0	0.5–8.0	Direct observation of vacancies, vacancy clusters. Twinning investigated
Beryllium			
Galbraith and Murr [75G1]	0.9	—	Shock-induced microstructures observed

conducted in apparatus subject to careful analysis (for an example of such an analysis, see [72S3]), but experience shows that the use of a well-designed and carefully fabricated experimental assembly incorporating suitable momentum-trapping plates permits satisfactory recovery for most purposes [64M1, 67R1, 77K4].

In early investigations, recovered samples were subjected to mechanical testing and examination by optical microscopy. These probes have subsequently been augmented by observations of X-ray line broadening, energy release and resistivity changes during annealing, magnetic effects, etc. Examination is now predominantly by transmission electron microscopy.

Except for effects of certain phase transformations, the metallurgical changes produced by shock loading involve the same general features as those produced by other means, but they appear at much lower levels of deformation. Some effects arising as a result of the high rates of shear present in shocks can be produced by quasi-static deformation only at very low temperatures.

Recovery observations of bcc metals are dominated by those of iron [65A3, 66Z2, 73L1], which develops dense distributions of dislocations and twins easily and profusely, although it has recently been shown that twinning is suppressed when the imposed shear can be accommodated by motion of a sufficient number of dislocations [72R1]. Murr and coworkers have recently investigated another bcc metal, molybdenum, in some detail [76M5, 76M6, 78W3, 78M10].

Most recent investigations of the residual effects of shock compression have dealt with fcc metals and alloys. Deformation structures produced in these materials are strongly correlated to their stacking fault energy, with dense planar arrays of stacking faults and dislocations predominating in materials in which this parameter has a low value and dislocation cell structures developing when the stacking fault energy is large. The dislocation cell structure that develops in these materials becomes increasingly dense and of finer scale with increases in the applied stress. Twins are produced by stress pulses exceeding some threshold of amplitude and duration and continue to grow for the duration of stress application. They eventually become a prominent feature in the structure of even such a high stacking-fault-energy material as nickel. Some observations suggest that twins form when the dislocation cell size is reduced to some minimum value of the order of 0.15 μm. Various observers have reported misalignments of the cells, indicating grain rotation during the course of deformation.

Copper has been subjected to detailed examination on several occasions since the early work of Smith, with several rather comprehensive studies having been reported [66D3, 67B3, 73L1]. Murr [78M8] has recently summarized observations of the relationship between dislocation arrangements and work hardening. Nickel has also been the subject of considerable investigation and quantitative relationships among dislocation parameters, mechanical properties, and history of applied stress have recently been proposed and interpreted by Murr and Kuhlmann-Wilsdorf [78M9] and Murr [78M8].

Studies of electrical resistivity (see section 4.10), and electron spin resonance [64G1] have been interpreted to mean that point defects develop in high concentrations in shock-loaded samples. Observations by transmission electron microscopy have disclosed high concentrations of dislocation loops resulting from aggregation of vacancies and interstitials, but it is only recently that direct observations have been made of both these dislocation loops and individual vacancies [76M6]. This investigation, conducted on molybdenum, shows an increase in total density from $5 \times 10^{13}/m^3$ loops of 57 Å average diameter in the initial annealed material to 4×10^{18} and $7 \times 10^{18}/m^3$ loops of average diameter 104 and 157 Å, respectively, in material loaded to 15 and 25 GPa for 2 μs. At the lower stress 75 per cent of the observed loops were collapsed vacancy

aggregates, with this fraction rising to 80 per cent at the higher stress. Examination by field-ion microscopy showed that only a very small proportion of the vacancies had coalesced to form these loops, with the remainder being present as monovacancies or small aggregates. The total vacancy concentration increased from an apparent background of 1.2 per cent (including artifacts) to 6 per cent after 25 GPa shock.

Early investigations disclosed shock compression as a particularly effective means of hardening metals, with roughly linear increases in indentation hardness with shock stress being observed in a variety of metals [63D3]. Shock hardening has since been observed to vary with stress pulse duration for pulses shorter than about 1 μs, but to be insensitive to variations in duration of the longer pulses that have been used for most work [78M7]. Hardening mechanisms vary from one material to another, and with changes in the strain history to which a given material is subjected. All of the defect structures observed have been implicated in hardening on at least some occasions. The stress-pulse dependence observed suggests that the mechanisms primarily responsible for the hardening operate rapidly and an investigation involving pulse durations as short as 4 ns has been undertaken by Mikkola and coworkers [78L1, 78W4] on Cu-8.6 per cent Ge. They find that, in the regime of short pulse durations, the hardening does not increase monotonically with duration as might be expected, but the observations remain to be explained.

Summary comments on recovery observations relate to the validity and interpretation of the experiments themselves and to the relation of this work to other aspects of the more general subject under review. Beginning with the first point, we note that much of the work has been done using inadequate recovery fixtures and poorly characterized loading histories. Much careful and sophisticated metallurgical work has been compromised by these deficiencies.

In early investigations, data were interpreted in terms of the peak compressive stress to which the samples were subjected, but both recent experimental work and theoretical considerations show that the duration of the stress pulse is equally important. Not all relevant parameters are subject to independent control since compression normally occurs more quickly in high-stress experiments than in those involving lower peak stresses and, of course, these experiments involve higher temperatures as well. The time required for the decompression process increases with both the peak stress achieved and the duration of its application, and observations or suggestions that various residual microstructures (e.g., twins) develop during this phase makes this correlation significant. The issue of conditions under which various defect structures form, and the rate of their development, deserves serious attention.

Much of the disagreement among observations cited by Leslie [73L1] now seems to stem from variations in loading history and such features of initial sample microstructure as grain size. No investigation can be interpreted with confidence in the absence of detailed knowledge of these matters. The complexity of observed behaviors and terminal microstructure also necessitates a rather comprehensive characterization of residual properties.

The recent trend toward more quantitative reporting of microstructural observations is encouraging and must continue if this work is to be related to other aspects of the study of shock-compression phenomena.

Dislocations and twins have been discussed in a rather idealized way in connection with the considerations of plastic deformation in section 3.3. The present discussion is not unrelated, but no precise connection has been made between the continuum version of the concepts and the more realistic versions encountered in recovery observations. These observations do confirm dislocation motion and twinning as important deformation mechanisms, but the complexity of

deformation phenomena is also disclosed with observation of deformation band structures, formation of dislocation cells, grain rotation, effects of phase instability in alloys, etc., all being involved in various contexts. It seems clear that the influence of these phenomena on observed wave profiles must be assessed and, as necessary, incorporated into mechanical constitutive equations. The fact that a variety of residual effects appears to depend on the duration of the period for which the sample is under compression indicates that the assumption that the compressed material is in a state of equilibrium at a point on its yield surface stands in need of some reevaluation.

The discussion of this section has been limited to metals, but shock-induced defects are found in other substances as well (see, e.g., the observations of MgO by Klein and coworkers [64G1, 65K3, 66K2, 66K3]), and may be expected to have equally significant effects on their mechanical, electrical, and optical behavior.

Shock-induced defects must be given special consideration in interpretation of other observations because they are usually present in much larger concentration than in samples subject to similar deformation by static means, and occasionally take forms not normally found in statically deformed material. The shock loading environment presents unique problems of interpretation of defect-sensitive phenomena.

3.7. Material synthesis

Polymorphic phase transitions are readily induced by shock compression (see, e.g., [77D6]), and it is of considerable interest to obtain samples of dense phases for scientific studies and for technological applications. Unfortunately, few materials remain in their high-pressure phases after decompression, and it is unusual to recover them in other than trace amounts. Nevertheless, there are some notable exceptions: dense boron nitride is recovered with good yield from graphitic boron nitride, diamond is recovered with good yield from shock-loaded graphite and yields as large as 90 per cent are reported for a dense orthorhombic form of TiO_2 obtained from shock-loaded rutile. There are also a few isolated cases of dense phase recovery in AlN [69V2], Ti [70G1], Zr [70G], Se [77D2], yellow and red phosphorus [58G1], bcc Fe-Ni alloys [68R2, 65L1], plagioclase [63M1], Fe-Ni-Cr alloys [60D1], and cobalt [57L1].

Unfortunately, there are no systematic attempts to explore *failure to recover* dense phases, but such failures are reported for iron [64M1], most iron alloys [61F1], Ge [65K1], Si [65K1], CdS [65K1], InSb [65K1], CdSe [65K1], NaCl [69B2], and $LiNbO_3$ [79S2]. Some of these reported failures may be due to insufficient effort since identification of trace amounts requires skill and persistence; for example, DeCarli's identification of diamond and stishovite in shock-loaded samples required considerable persistence along with special chemical processing and concentration.

The considerable geophysical work on changes in defects and structure produced by natural and laboratory shock loading of rocks and minerals has recently been thoroughly reviewed [72S4] and need not be discussed here. Diamond synthesis is routine with static-high-pressure techniques [77B2] and static high pressures are routinely used to aid the synthesis of other single crystals [77W1].

Much of the early material synthesis work was performed on samples close to solid density, whose full composition was the material to be transformed. This approach limits both the temperature and pressure achieved and gives no control over the local temperature history of the materials.

It has become apparent that in some cases dense phases can be recovered in larger yields and with better control on crystallite size by mixing the transforming materials in a metallic host such as copper or iron [68C3, 74S5]. Porous samples have also been used to achieve higher temperatures. There is some indication that particle size of both the transforming and host materials may influence yields by changing quenching rates [77D3].

In addition to the extensive work on boron nitride, diamond and dense quartz which is discussed here in more detail, Leiserowitz et al. [66L1] have been successful in recovering dense phases of CdS, β lead oxide and calcite by adding about 10 per cent water to the samples as a quenching agent.

Boron nitride has been extensively studied because its behavior is somewhat analogous to carbon, because of the ease with which large yields of dense phases are obtained and because this hard, dense phase is of practical utility. The summary of shock-wave synthesis of dense BN given in table 3.8 shows the various investigations and their principal results. There has been almost continuous activity since 1965 and very considerable activity in the past few years.

BN was first synthesized in static-high-pressure studies of Bundy and Wentorf [63B3] who found a wurtzite form of BN, denoted wBN, and at lower temperatures a zinc blende form of BN, denoted zBN. The principal questions in shock synthesis revolve around the circumstances under which the wurtzite or zinc blende forms are obtained and the conditions which determine the yields. Resolution of such important detail has been hampered by use of tubular loading methods and the possibility of contamination. Some investigators have suggested that the identified zBN may be copper contamination while others feel that zBN is obtained when higher temperatures are achieved. In any event, it is clear that wBN is more frequently obtained and that yield depends more on the extent of crystallinity of the starting material than on the pressure. Phase stability data on samples under planar loading, analogous to those for static conditions [75C2, 75T1], are needed to clarify shock synthesis conditions.

Kurdyumov and coworkers (see table 3.8) have carried out detailed examination of fine structures in X-ray patterns on shock-synthesized BN to study transformation mechanisms. Their studies have demonstrated the crucial role that stacking faults produced by plastic deformation play in the transformation process. These stacking faults have been observed in samples recovered below the transition pressure. Kurdyumov and Frantsevich believe that the two-dimensional stacking faults are regions in which wBN cannot be transformed but may be the source of nucleation for zBN.

The synthesis of diamond has fascinated scientists for over a century. Certainly the most spectacular achievement in material synthesis by shock compression is the formation of diamond from graphite. Following the static-high-pressure synthesis of diamond with catalysts by Bundy et al. [55B1], attempts to obtain direct conversion of graphite to diamond were unsuccessful. The first direct conversion was achieved in shock-compression experiments by DeCarli and Jamieson [61D1]. Bundy reported the first direct conversion of graphite to diamond in a static pressure apparatus [63B2] in 1963. Work on this problem is summarized in table 3.8.

DeCarli and Jamieson [61D1] first proposed that transformation to diamond took place in rhombohedral graphite but not in hexagonal graphite. More recent evidence derived from fine structure in X-ray diffraction studies of recovered samples by Kurdyumov [75K4, 72K5] indicates that formation of stacking faults by plastic deformation provides a crucial intermediate step for diamond formation. DeCarli [79D2] has proposed a nucleation and growth model for diamond formation. The importance of such a model has been demonstrated by Pujols and Boisard [70P1]

Table 3.8
Material synthesis with shock loading

Authors	Reference	Observations
Boron nitride		
Batsanov et al.	[65B2]	"E" phase recovered
Adadurov et al.	[67A1]	wBN recovered, no zBN or "E" phase
DeCarli	[67D2]	both wBN and zBN recovered
Coleburn and Forbes	[68C2]	zBN recovered, trace wBN
Dulin et al.	[69D1]	recovered predominantly wBN, some zBN
Johnson and Mitchell	[72J2]	real-time flash X-ray, wBN lines
Riter	[73R2]	wBN deformation mechanism
Kurdyumov et al.	[73K3]	fine structure of wBN examined
Soma et al.	[74S5]	Cu/BN mixture; wBN recovered
Sawaoka and Soma	[74S1]	Cu/BN mixture; wBN recovered; Cu contamination to explain zBN?
Kurdyumov and Frantsevich	[75K4]	wBN recovered, copper contamination to explain zBN?
Bavina et al.	[75B3]	zBN from porous sample, X-ray interpretation?
Soma et al.	[75S2]	Cu/BN mixture; wBN recovered
Kurdyumov et al.	[75K5]	multiple shock loads; investigates untransformed products
Kurdyumov	[75K3]	crystallographic mechanisms for transformations
Kurdyumov	[76K3]	stacking faults below transition pressure
Kurdyumov	[76K4]	athermal wBN mechanism
Akashi et al.	[76A3]	multiple shock loads; wBN then zBN recovered
Nesterenko	[77N2]	Cu/BN mixture; effects of particle size
Dubovitskii	[77D5]	synthesis of borozon, polycrystalline zBN
Saito et al.	[78S1]	sintered polycrystalline zBN, wBN compact produced
Densification of vitreous silica		
Wackerle	[62W1]	densification at 25 GPa, not at 50 GPa
Deribas et al.	[66D2]	axisymmetric loading
Gibbons and Ahrens	[71G1]	index of refraction, 8 to 46 GPa
Arndt et al.	[71A6]	index of refraction, 6 to 46 GPa
Ananin et al.	[74A1]	4 to 24 GPa
Graphite to diamond		
Parsons	[20P1]	possible recovery of diamond
Riabinin	[56R1]	failed to recover diamond
DeCarli and Jamieson	[61D1]	diamonds recovered from artificial graphite
Lipschutz	[64L1]	diamonds from meteorites and artificially shocked graphite
Trueb	[68T2]	Fe/graphite mixture; yield vs. particle size, hexagonal and cubic diamond
Trueb	[70T1]	graphite "ghosts" of diamond nuclei
Pujols and Boisard	[70P1]	hard graphite from diamond microseeds, stacking faults
Trueb	[71T2]	Cu/graphite mixtures; 20–40% yield; all cubic diamonds
Fournier and Oberlin	[71F1]	recovered diamond; graphite with stacking faults
Kurdyumov	[72K5]	graphite below transition; large increase in packing defects
Vdovykin et al.	[73V1]	shock meteoritic material; diamonds recovered
Kurdyumov	[75K3]	transition mechanisms
Glass and Sharma	[76G1]	unique gaseous implosion, 5% yield of diamonds
Deribas and Staver	[77D3]	Cu/graphite, Fe/graphite mixtures
Trefilov et al.	[78T2]	control initial temperature
DeCarli	[79D2]	nucleation and growth model
Amorphous and dense quartz from α-quartz		
DeCarli and Jamieson	[59D1]	amorphous quartz recovered
Chao et al.	[60C1]	coesite, meteor crater
Chao et al.	[62C1]	stishovite, meteor crater
Wackerle	[62W1]	amorphous quartz recovered
DeCarli and Milton	[65D1]	stishovite (trace) recovered

Table 3.8 (con't.)

Authors	Reference	Observations
Deribas et al. [66D2]	[66D2]	coesite (trace), amorphous quartz recovered
Dremin and Breusov	[68D4]	review of laboratory observations
Deribas et al.	[68D2]	coesite, stishovite (trace) discovered
Stöffler	[72S4]	review of geophysical observations
German	[73G2]	amorphous, orthorhombic quartz recovered
Ananin et al.	[74A2]	amorphous quartz recovered

who found hard graphite, presumably the reversion products of diamond microseeds, in graphite loaded with short duration pulses.

Although the ratio of hexagonal diamond to cubic diamond appears to be a function of pressure, temperature and quench rate from the surrounding matrix, details have not been published. Deribas and Staver [77D3] have reported progress in control of temperature and pressure with the use of copper and iron matrix materials and have begun exploration of a stability diagram for shock synthesis of diamond. Deribas and Staver [74D2] also performed studies to better understand the tubular loading systems widely used for recovery in the Soviet Union. Trefilov et al. [78T2] have reported shock synthesis of more perfect diamonds by preheating graphite such that the final shock temperature is > 4300 K.

Shock-synthesized diamonds have different abrasive properties from those of their natural or synthetic static-high-pressure counterparts. Because they are particularly effective for lapping and polishing of hard materials, they have been produced commercially by Allied Chemical Company and DuPont and in the Soviet Union.

Dense forms of quartz are of less technological interest than diamond and zBN but widespread geophysical interest and other technical uses for crystalline quartz and vitreous silica have led to significant effort in shock-wave synthesis of dense forms. Coesite, with a density of 3.01 Mg/m^3 and hexagonal symmetry, was first synthesized by Coes [53C1] at a static pressure of 3.5 GPa in 1953. Subsequently, Stishov and Popova [61S2] synthesized a rutile-structure quartz with a density of 4.35 Mg/m^3 at static pressures greater than 16 GPa, which is called stishovite in the United States and stipovorite in the Soviet Union. Although yields are not large, both coesite and stishovite have been synthesized in crystalline quartz by shock compression. Permanent densification has been observed in shock-loaded vitreous silica [62W1], but dense crystalline phases have not been recovered from shock-loaded solid samples. Deribas et al. [68D2] have successfully recovered dense crystalline quartz from powdered vitreous silica samples and Ananin et al. [74A1] have reported recovery of an unspecified partially crystallized form of quartz from vitreous silica. Work on synthesis of dense and amorphous quartz from α-quartz is summarized in table 3.8.

Large yields of amorphous quartz are achieved from crystalline quartz shock loaded between 25 and 50 GPa [62W1]. This threshold pressure is apparently dependent upon the recovery fixture [74A1]. Whereas yields of stishovite of a few per cent are found in quartz rocks subjected to meteoritic impact [72S4], stishovite is only obtained in trace amounts in laboratory experiments. The longer pressure pulse durations associated with meteoritic impacts are apparently effective in growth of both stishovite and coesite. It is also of interest that meteor crater samples show larger yields of coesite than stishovite whereas the opposite is true for laboratory experiments.

Coesite and stishovite in meteor crater samples are selectively associated with regions of diaplectic glass (layered glass with alternate layers of isotropic and anisotropic glass). Recalling the previous discussion of heterogeneous yielding in section 3.4, it is likely that local hot regions caused by heterogeneous yielding provided the conditions necessary for nucleation of these dense phases.

Deribas et al. [66D2, 68D2] have been the only group successful in recovering coesite in the laboratory. It is notable that they utilized powder samples of low density to achieve significantly higher shock temperatures than would be obtained with samples of normal density.

Bridgman and Simon [53B1] first observed that vitreous silica undergoes a permanent increase in density under static high pressure. In a detailed investigation, Wackerle [62W1] found permanent densification in samples recovered after shock loading to 25 GPa. The results of these and other observations are summarized in table 3.8. The data from various investigators are somewhat scattered but data from a given investigator show consistent behavior. Such differences are probably due to different stress and temperature histories achieved in different recovery fixtures and the use of different starting materials. In spite of the scatter, general features are clear: (1) permanent densification to densities between 2.4 and 2.5 Mg/m^3 is observed; (2) at sufficiently high pressure (or temperature) densification is not observed or is greatly reduced; and (3) there is a stress threshold between 4 and 8 GPa for the onset of densification. Ananin et al. [74A1] have annealed the recovered dense samples and formed crystobolite.

There has been considerable interest in the possibility of recovering metallic hydrogen from high-pressure experiments. Because of the large increase in temperature in shock-compression experiments, metallic hydrogen would not be expected to be observed (see Ross and Shiskivich [77R2]). Isentropic compression experiments with pulsed magnetic implosion minimize the increase in temperature but have also not proven successful in producing metallic hydrogen. A short summary of the work is given by Duvall and Graham [77D6].

There are considerable data on unique chemical reactions and introduction of unique defects in samples achieved under shock compression. Most of this work is carried out in the Soviet Union and has been reviewed by Adadurov et al. [73A1]. The reder can find other summaries by Dremin and Breusov [68D4] and Duvall and Graham [77D6].

Material synthesis with shock loading appears to be an endeavor of considerable promise and past work has shown notable results. In all cases examined in detail the role of shock-induced defects in nucleating dense phases has been shown to be crucial. The use of quenching materials appears to be of critical importance. The determination of phase stability data for interesting materials is of immediate importance and shock-compression experiments appear to be ideally suited for determination of higher-pressure phase diagrams. Phase diagrams [74W2] based on a supposed metallic carbon transition under shock loading [61A1] should certainly be revised now that those measurements are thought to be in error (see, e.g., [77D6]).

4. Electrical and magnetic properties

4.1. General considerations

When physical properties are studied under shock loading, basic difficulties are encountered in both experimental design and physical interpretation that are not experienced in either the

studies of mechanical response, described in sections 2 and 3, or in static-high-pressure studies of physical properties as described, for example, by Paul and Warschauer [63P2] or Drickamer [65D2]. In spite of significant complications in interpreting physical property measurements under shock loading, work to date has resulted in considerable progress toward understanding physical effects in solids under large deformation and in identifying electrical phenomena unique to shock deformation. These unique phenomena have provided insight into fundamental features of shock deformation. Measurements within the elastic range are subject to detailed interpretation and can be carried out with the highest precision. On the other hand, interpretation of measurements in solids with complex mechanical properties is among the most complex problems encountered in the field of shock compression of solids. Basic complications and characteristics of the shock-loading experiment as applied to physical property measurements are considered below before description of the various specific material responses.

The amplitude of the disturbance impinging upon a sample is subject to reasonable control, but the actual loading is carried out as an inertial reaction to the disturbance. Accordingly, the stress and deformation histories at various points throughout the sample depend explicitly on both its Hugoniot curve and strength properties. Such properties are not usually under the control of the experimenter and situations may be encountered for which the essential independent variables of strength, stress and volume are poorly characterized.

When the shear strength of a solid is exceeded, the material flows in inelastic deformation which is a macroscopic manifestation of microscopic processes involving dislocation motion, their complex interactions, possible twinning, formation of vacancies, higher-order vacancy complexes and possible relaxation in the defect states. As a result, a physical property measurement under shock loading is made on a sample whose defect state is essentially unknown but radically different from that of the virgin sample. It is well known that many physical properties are sensitive to, if not dominated by, defects. Thus, formation of shock-induced defects seriously complicates interpretation of physical property measurements. Any interpretation of defect-sensitive properties that ignores such shock-induced defects is of limited value and fails to take advantage of the unique opportunity afforded to probe defect states through physical property measurements.

The presence of shock-induced defects can easily lead to a situation in which deformation and temperature are highly localized (see section 3.4) and resulting physical effects may also be localized and not characteristic of bulk behavior. Accordingly, the validity of interpretation of observations in terms of bulk physical processes must be explicitly verified.

Restrictions on sample configurations play a major limiting role in our ability to carry out physical-property measurements. Two characteristically different configurations involving either a *thin sample* or a *thick sample* are used to achieve conditions subject to ready interpretation. Whereas measurements by the thick-sample method are made synchronously during the passage of the stress waves, measurements by the thin-sample method are made after a uniform stress is achieved due to impedance matching with buffers or after wave reverberations within the sample. The thin-sample method is, from a conceptual framework, the simpler of the two since, unlike the thick-sample method, it is possible to describe final stress-volume states achieved in the sample without detailed consideration of wave propagation. The thin-sample method is employed, for example, in resistance measurements on thin metallic samples placed directly in electrically insulating buffer disks or in conducting buffers insulated with polymeric films.

The conceptual simplicity of the thin-sample method results from limited consideration of the details of the transient loading within the sample. Furthermore, the measured electrical wave-

forms contain virtually no information on that loading process. Verification of representative conditions within the thin sample requires measurements using samples of varying design.

The thick-sample method is more difficult in both concept and practice, as potentially complex wave propagation within the sample must be explicitly analyzed. The measured electrical waveforms help to alleviate this difficulty since they contain a wealth of real-time information on both mechanical and electrical processes occurring in the space being probed. The direct effect of wave propagation forces explicit consideration of the transient loading. The configuration allows separation of elastic and plastic contributions and allows electrical boundary conditions to be varied. As more representative models of mechanical response are developed and incorporated in computer codes, the utility of the thick-sample method will be greatly increased. This method is typically employed in physical property measurements on dielectrics and the most critical mechanical detail is control of the simultaneity of the loading over the sample face, i.e., the "tilt".

4.2. Piezoelectrics

Favorable electrical properties and large Hugoniot elastic limits, combined with ready availability, has led to the widespread use of quartz and lithium niobate crystals for time-resolved stress gauges in shock-compression experiments. The importance of this application has motivated sufficiently quantitative studies that their piezoelectric, dielectric, and elastic properties have been determined in detail throughout the elastic range. The principal unique results from these investigations are determinations of second-order piezoelectric, higer-order piezoelectric, dielectric, and elastic constants, and investigation of unusual shock-induced dielectric breakdown phenomena.

Studies of piezoelectrics under shock compression stem from an extraordinarily perceptive investigation carried by Neilson and Benedick and first reported in 1961 [62N2]. They explained the electrical waveforms produced from explosively-loaded X-cut quartz in terms of a "three-zone model" incorporating the following principal assumptions: (1) above the Hugoniot elastic limit an elastic and inelastic wave structure separates the sample into three distinct zones, (2) the elastic precursor wave has an amplitude of about 4 GPa, (3) the shear stress vanishes in the region behind the inelastic wave, and (4) shock-induced conduction occurs in either the elastic or inelastic zone depending upon the piezoelectric polarity. This model is not only complex, but incorporates features at variance with then-current ideas of material strength and inelastic behavior. The assumptions concerning mechanical behavior were soon confirmed by Wackerle [62W1] and Fowles [61F2, 67F1], and investigations of large Hugoniot-elastic-limit values and loss of shear strength continue to the present time (see section 3.4). The dielectric breakdown phenomena observed electrically by Neilson and Benedick [62N1] and optically by Brooks [65B3] are still not understood and work continues on this problem as well (see section 4.6). A summary of investigations of piezoelectric crystals under shock loading is shown in table 4.1.

Studies of the response of piezoelectric solids to elastic shock compression are part of a larger question of nonlinear piezoelectric response. Although this problem is of considerable interest in connection with microwave acoustic phenomena (see, e.g., [67C1, 68M1, 71T1, 72K4, 72L1]), there are few quantitative data on nonlinear piezoelectric constants. Order-of-magnitude estimates based on ultrasonic investigations have been given for lithium niobate [75K2], while quantitative values are reported for quartz by Hruska [78H3], who was the first to detect a nonlinear piezoelectric effect [61H2]. Pressure derivatives of hydrostatic piezoelectric constants have been

Table 4.1
Piezoelectrics under shock compression

Authors	Date	Reference	Stress, GPa	Results
Tourmaline				
Minshall	(1955)	[55M2]	7 to 10	shock arrival only
Goranson et al.	(1955)	[55G1]	1.6 to 32	thin sample technique
Bancroft et al.	(1956)	[56B1]	1.6 to 20	thin sample technique
Hearst et al.	(1964)	[64H1]	0.7 GPa	thin sample technique
Hearst et al.	(1965)	[65H2]	2.1 GPa	thin sample technique
Quartz				
Neilson et al.	(1961)	[62N2]	0.8 to 30	electrical and optical response
Graham	(1961)	[61G1]	0.8 to 4.5	linear to 2.5 GPa
Graham	(1961)	[61G2]	0.5 to 7	gun technique
Fowles	(1961)	[61F3]	4 to 23	HEL, strength loss
Graham	(1962)	[62G1]	0.5 to 5	minus-x anomaly
Neilson and Benedick	(1962)	[62N1]	2.5 to 30	three-zone model
Wackerle	(1962)	[62W1]	4 to 70	HEL, strength loss
Graham et al.	(1965)	[65G1]	0.2 to 4.9	guard ring, material constants
Brooks	(1965)	[65B3]	3 to 27	luminescence
Jones	(1967)	[67J2]	0.6 to 2.1	79 K, material constants
Rohde and Jones	(1968)	[68R3]	0.6 to 2.1	573 K, material constants
Graham and Halpin	(1968)	[68G4]	0.6 to 2.1	dielectric breakdown, recovery
Jones and Halpin	(1968)	[68J1]	0.5 to 3	shorted guard ring
Lysne	(1972)	[72L2]		multiple reverberations
Graham and Ingram	(1972)	[72G4]	1 to 2.5	short pulse anomaly
Graham	(1972)	[72G3]	0.2 to 4	precise material constants
Chen and McCarthy	(1973)	[73C5]	theory	singular surface, nonlinear
Thurston	(1974)	[74T1]	theory	nonlinear theory, weak coupling
Graham	(1974)	[74G2]	4.5 to 13	yielding and multiple wave response
Graham	(1974)	[74G1]	0.2 to 4	nonlinear piezoelectrics
Graham	(1975)	[75G4]	1 to 3	shorted guard ring, conduction
Graham and Yang	(1975)	[75G6]	1 to 5	time delay dielectric breakdown
Graham and Chen	(1975)	[75G5]	theory	rate coupling effect
Chen et al.	(1976)	[76C2]	theory	coupled theory
Lawrence and Davison	(1977)	[77L1]	analysis	computer solutions, fully coupled
Duvall	(1977)	[77D7]	theory	piezoelectric as Maxwellian solid
Lithium niobate				
Graham	(1973)	[73G4]	0.2 to 1.4	material constants
Graham	(1974)	[74G1]	0.2 to 1.4	nonlinear piezoelectrics
Graham	(1977)	[77G6]	0.18 to 1.7	material constants
Stanton and Graham	(1977)	[77S1]	2 to 90	above HEL
Stanton and Graham	(1979)	[79S2]	2 to 44	HEL, strength loss, phase transition

accurately measured to 2.6 GPa for lithium niobate and lithium tantalate [76G4]. Gagnepaign and Besson [75G9] have studied nonlinear piezoelectric constants under uniaxial stress.

4.2.1. Elastic dielectric theory

When a stress pulse is propagated into a piezoelectric solid, the resulting strain produces a local polarization through the direct piezoelectric effect. This polarization causes an electric field to develop in the space between the electrodes and an associated current to flow an external circuit connecting the electrodes. The fields cause secondary stresses to develop in the sample through the indirect piezoelectric effect. The magnitude and distribution of the electric fields depend on

the form of the stress pulse and the character of the external circuit, while details of the secondary stress depend on the electromechanical coupling coefficients and the mechanical boundary conditions. This coupling between electrical and mechanical effects, which is a fundamental characteristic of piezoelectric materials, considerably complicates analysis of their response to mechanical loads. In the present case nonlinear effects cause further complication. In fact, no fully-coupled closed form solution for nonlinear dynamic piezoelectric response has been developed, although solutions have been obtained numerically [76C2, 77L1]. Fortunately, electromechanical coupling is often weak and advantage can be taken of this fact to obtain approximate solutions that are accurate to within a few per cent.

Constitutive relations. Piezoelectric solids are characterized by constitutive relations among the stress, $\boldsymbol{t}$, strain, $\boldsymbol{\eta}$, entropy, s, electric field, $\boldsymbol{E}$, and electric displacement, $\boldsymbol{D}$. When uncoupled solutions are sought, it is convenient to express $\boldsymbol{t}$ and $\boldsymbol{D}$ as functions of $\boldsymbol{\eta}$, $\boldsymbol{E}$, and s, while fully-coupled solutions are more easily obtained from expressions for $\boldsymbol{t}$ and $\boldsymbol{E}$ as functions of $\boldsymbol{\eta}$, $\boldsymbol{D}$, and s. The formulation of nonlinear piezoelectric constitutive relations has been considered by numerous authors (see the list cited in [77G6]) but there is no generally-accepted form or notation. With some modification in notation, we adopt the definitions of thermodynamic potentials developed by Thurston [74T1]. This leads to the constitutive relations

$$\begin{aligned} t_{rs} &= \frac{\rho}{\rho_R} F_{ri}F_{sj}(C^{\boldsymbol{E}}_{ijkl}\eta_{kl} - e_{kij}E_k + \tfrac{1}{2}C^{\boldsymbol{E}}_{ijklmn}\eta_{kl}\eta_{mn} + \tfrac{1}{6}C^{\boldsymbol{E}}_{ijklmnpq}\eta_{kl}\eta_{mn}\eta_{pq} - \tfrac{1}{2}f_{klij}E_kE_l \\ &\quad - \tfrac{1}{2}e_{ijklm}E_m\eta_{kl}) \\ D_i &= e_{ijk}\eta_{jk} + \varepsilon^{\boldsymbol{\eta}}_{ij}E_j + \tfrac{1}{2}e_{ijklm}\eta_{jk}\eta_{lm} + \tfrac{1}{2}f_{ijkl}E_j\eta_{kl} + \tfrac{1}{2}\varepsilon^{\boldsymbol{\eta}}_{ijk}E_jE_k \end{aligned} \tag{4.1}$$

in the independent variables $\boldsymbol{\eta}$, $\boldsymbol{E}$, and s (the coefficient tensors are functions of s). In these equations, the tensor components $C^{\boldsymbol{E}}_{ijk}$, $C^{\boldsymbol{E}}_{ijklmn}$, and $C^{\boldsymbol{E}}_{ijklmnpq}$ are second-, third-, and fourth-order elastic stiffness coefficients at constant field, e_{kij} and e_{kijlm} are second- and third-order piezoelectric stress constants, $\varepsilon^{\boldsymbol{\eta}}_{ij}$ and $\varepsilon^{\boldsymbol{\eta}}_{ijk}$ are second- and third-order dielectric permittivities at constant strain, and f_{ijkl} is the electrostrictive coefficient. In applying these relations, the principal stress and strain components are positive in tension. Small pyroelectric contributions to electric displacement due to isentropic heating of certain crystals are treated in reference [77G6]. The contribution $\frac{1}{2}\varepsilon^{\boldsymbol{\eta}}_{ijk}E_jE_k$ to the electric displacement of X-cut quartz is extremely small and is neglected in analysis of both quartz and lithium niobate.

For many problems it is convenient to separate the piezoelectric (i.e., strain-induced) polarization $\boldsymbol{P}^{\boldsymbol{\eta}}$ from electric-field-induced polarizations by defining $\boldsymbol{D} = \boldsymbol{P}^{\boldsymbol{\eta}} + \boldsymbol{\varepsilon}\boldsymbol{E}$, where $\boldsymbol{\varepsilon}$ is the permittivity tensor. When the material is constituted according to equation $(4.1)_2$ with the E^2 term omitted, we have

$$P^{\boldsymbol{\eta}}_i = (e_{ijk} + \tfrac{1}{2}e_{ijklm}\eta_{lm})\eta_{jk}, \qquad \varepsilon_{ij} = \varepsilon^{\boldsymbol{\eta}}_{ij} + \tfrac{1}{2}f_{ijkl}\eta_{kl}. \tag{4.2}$$

Mechanical wave-propagation problems are analyzed on the basis of quasi-static electromagnetic conditions. This is an excellent approximation since the electromagnetic wavespeed greatly exceeds the mechanical wavespeed and the particle velocity is typically only about one-tenth of the mechanical wavespeed (see the discussion by Thurston [74T1]).

Configurations of interest are those using disk-shaped samples cut from crystals in orientations that permit plane waves of uniaxial strain to propagate through their thickness when a uniform

load is applied to their face. When the diameter of the disk is sufficiently great in comparison to its thickness, and a suitable guard-ring electrode configuration is used, the fields throughout the inner region of the sample will be normal to the faces of the disk [65G1].

In the absence of free charge in the disk, the electric displacement will be independent of position, although it will vary with time: $\boldsymbol{D} = (D(t), 0, 0)$. The current induced in the external circuit is attributable to changes in electric displacement within the disk and is given by

$$i(t) = A\, \mathrm{d}D(t)/\mathrm{d}t, \tag{4.3}$$

where A is the area of the charge-collecting electrode on the face of the disk. The voltage across the disk is the integral of the electric field in the space between the electrodes,

$$V(t) = \int_{\hat{x}(0,t)}^{\hat{x}(L,t)} E(x, t)\, \mathrm{d}x. \tag{4.4}$$

When the electrodes are connected by a short circuit, the voltage is zero but only the average field need vanish and local values are often quite large.

Piezoelectric response to shock compression: uncoupled short-circuit solution. The "uncoupled" response of a piezoelectric sample to elastic shock compression is determined on the assumption that the mechanical response of the material is independent of any electric fields that may be present. In this approximation, a steady shock introduced into material at rest in its reference configuration will advance at some constant velocity U and divide the thickness of the sample into two parts. The part ahead of the shock will remain undeformed and at rest while the part behind the shock will be uniformly compressed to a strain $S_1 = -u/U$, where u is the particle velocity of the compressed material. The compression will produce a piezoelectric polarization $\boldsymbol{P}^{\mathrm{I}} = (P^{\mathrm{I}}, 0, 0)$ in the compressed material and will cause a change in the permittivity component in the x direction from some value ε_{11} to a new value $\bar{\varepsilon}_{11}$ that depends on the strain according to eq. (4.2). From equations (4.2)–(4.4), it can be shown that, when the electrodes are connected by a short circuit ($V(t) = 0$) [72G3],

$$\frac{i(t)L}{P^{\mathrm{I}}AU} = \frac{\alpha(1 - u/U)}{[(1 - u/U)(t/t_0) + \alpha(1 - t/t_0)]^2}, \quad 0 < t < t_0 \tag{4.5}$$

where L is the original thickness of the sample, $t = 0$ at the instant of introduction of the shock into the sample, $t_0 = L/U$ is the transit time of the shock through the sample, and $\alpha = \bar{\varepsilon}_{11}/\varepsilon_{11}$. From eq. (4.2), we see that the magnitude of the piezoelectric polarization is directly dependent on the magnitude of the strain but eq. (4.5) shows that this dependency does not affect the current history for the case considered. For both quartz and lithium niobate, $u/U < 0.04$ and $1 \leq \alpha < 1.01$ in the elastic range. With these restrictions, eq. (4.5) indicates that the current history is a step function to close approximation. Deviations from this ideal form occur as a geometrical result of large compressions or when the permittivity changes significantly upon compression.

The current immediately after impact, $i(0+)$, is calculated from the limiting case

$$\frac{i(0+)L}{AU} = \frac{1 - (u/U)}{\alpha} P^{\mathrm{I}} \tag{4.6}$$

of eq. (4.5). This relation holds universally for shock-induced polarization effects and is useful for evaluation of various shock-induced polarization phenomena.

In the low-signal limit in which nonlinearities in material behavior are negligible and $u/U \ll 1$ the analysis given above can easily be extended to stress pulses of arbitrary form, with the result [65G1]

$$\frac{i(t)L}{AU} = \frac{e_{111}}{C^{E}_{1111}} t_{11}(0, t), \qquad 0 < t < t_0, \tag{4.7}$$

which indicates that the current history is proportional to the history of stress at the input electrode, $t_{11}(0, t)$. This relation, which is also followed to a close approximation at larger strains if e_{111}/C^{E}_{1111} is replaced by an experimentally-determined strain-dependent coefficient, forms the basis for the widely used current-mode piezoelectric gauges [65G1, 75G4].

Electric fields. Shock compression of piezoelectric solids, even under short-circuit conditions, causes large electric fields of varying amplitude and polarity within the material. In the uncoupled approximation to the solution of the short-circuit problem, the field is easily determined from the condition on uniformity of electric displacement, from eq. (4.4), and the expression $\boldsymbol{D} = \boldsymbol{P}^{\eta} + \varepsilon \boldsymbol{E}$ [74G2]

$$E = \frac{P^{\eta}/\varepsilon_{11}}{(1 - u/U)(t/t_0) + \alpha(1 - t/t_0)} \begin{cases} (1 - u/U)(t/t_0), & \text{for } x > Ut \\ 1 - t/t_0, & \text{for } x < Ut \end{cases} \tag{4.8}$$

for $0 < t < t_0$. The magnitude of the field in each region varies between zero and a maximum value of $P^{\eta}/\varepsilon_{11}$ during passage of the shock through the sample. Since u/U is small and α near unity for most cases of interest, the field at a given point varies approximately linearly with time except for a discontinuity when the shock passes. When a 2 GPa shock passes through X-cut quartz, the maximum field strength is about 10^8 V/m, while a maximum field of 3×10^7 V/m is realized in Z-cut lithium niobate subjected to a stress slightly in excess of 1 GPa. Fields of these magnitudes are of concern in that they are about one-tenth of the breakdown strength values at atmospheric pressure. From this analysis we see that shock-compressed piezoelectric materials are subjected to the simultaneous effects of high stress and high electric field. As discussed in section 4.6, such fields are crucial in activating shock-induced conduction.

The electric fields for stress pulses of arbitrary profile can be evaluated by noting that eq. (4.7) gives an expression relating a measured current history to the piezoelectric polarization $\boldsymbol{P}^{\eta}(0, t)$ at the input electrode. Combined with eq. (4.3) and the relation, $\boldsymbol{D} = \boldsymbol{P}^{\eta} + \varepsilon \boldsymbol{E}$, the measured current and its integral can then be used to calculate the fields in a point-by-point approximate solution. *Piezoelectric pulse diagrams* in which expressions for polarization and displacement versus time are superimposed and the field determined as their differences, provide graphical solutions for the time dependence of the fields. Consideration of the simple case of a square pulse whose duration is less than t_0 shows that the field can be varied independently of the stress (see section 4.6).

Weakly- and fully-coupled solutions. Uncoupled solutions for current and electric field give simple and explicit descriptions of the response of piezoelectric solids to shock compression, but the neglect of the influence of the electric field on mechanical behavior (i.e., the electromechanical coupling effects) is a troublesome inconsistency. A first step toward an improved solution is a weak-coupling approximation in which it is recognized that the effects of coupling may be relatively small in certain materials and it is assumed that electromechanical effects can be treated as a perturbation on the uncoupled solution.

The contribution to the stress from electromechanical coupling is readily estimated from the constitutive relation, eq. (4.1). Under conditions of uniaxial strain and field, and for an open circuit, we find that the elastic stiffness is increased by the multiplying factor $(1 + K^2)$ where $K^2 = e_{111}^2/(\varepsilon_{11}^{\eta} C_{1111}^{E})$, the square of the *electromechanical coupling factor* for uniaxial strain, is a measure of the stiffening effect of the electric field. Values of K^2 for various materials are: X-cut quartz, 0.008; Z-cut lithium niobate, 0.055; Y-cut lithium niobate, 0.074; barium titanate ceramic, 0.5; PZT-5H ceramic, 0.75. These examples show that electromechanical coupling effects can be expected to vary from barely detectable to quite substantial.

Stuetzer [67S2, 67S3] and Thurston [74T1] have determined the coupled response of *linear* piezoelectrics to step loading, while both Lysne [72L2] and Thurston [74T1] have obtained solutions for the corresponding problem for weakly-coupled nonlinear piezoelectrics. In each case the short-circuit current exhibits the same initial jump as for the uncoupled solution, with the current at later times being greater in the coupled than the uncoupled case by an amount that depends on the electromechanical coupling factor for the material and the mechanical boundary conditions to which the sample disk is subjected.

Chen et al. [76C2] and Lawrence and Davison [77L1] have recently placed the fully-coupled nonlinear theory of uniaxial piezoelectric response in a form that is convenient for numerical solution of problems and have simulated a number of experiments in terms of this theory. An example of the results obtained is given below.

From a constitutive relation of the form, $\boldsymbol{t} = \boldsymbol{t}(\boldsymbol{D}, \boldsymbol{\eta})$, it can be readily shown that, since there is no change in electric displacement in an open-circuit, thick-sample configuration, there are no secondary stresses due to electromechanical coupling. Nevertheless, the wavespeed is that of a piezoelectrically stiffened wave.

4.2.2. Experimental

The piezoelectric behavior of both quartz and lithium niobate has been studied in a series of careful, systematic investigations. The experimental arrangement is as shown in fig. 4.1. (For more detail see [65G1, 70I1, 72G3, 75G4].) The impactor, preferably the same material as the piezoelectric sample (or perhaps another standard material), is accelerated to a preselected velocity and impacted, in vacuum, upon the sample. Measured quantities include the impactor velocity immediately prior to impact and the short-circuited current pulse produced during the passage of the shock through the sample. Based on eq. (4.6), each experiment yields a value for piezoelectric polarization at a given strain; a collection of such data over a wide range of strain permits the linear and nonlinear piezoelectric constants to be determined. The current-pulse amplitude can be measured to an accuracy of $\pm 1\%$ and, since the impact velocities from which strains are computed are known to $\pm 0.1\%$, overall accuracies are excellent. Error in shock velocity does not cause error in determination of the piezoelectric stress constants.

Typical current pulses observed for X-cut quartz, Z-cut lithium niobate and Y-cut lithium niobate are shown in fig. 4.2. Following a sharp rise in current to an initial value (the initial risetime is due to tilt), the wave shapes show either modest increases in current during the wave transit time for quartz and Z-cut lithium niobate samples, or large increases in current for Y-cut lithium niobate samples. Given our previous discussions of electromechanical coupling, it can be determined that the large increase in current with time in Y-cut lithium niobate is an indication of the pronounced influence of such coupling. It should be noted that current pulse distortions are also significant from samples without proper guard rings [65G1] and subtle but significant distortions

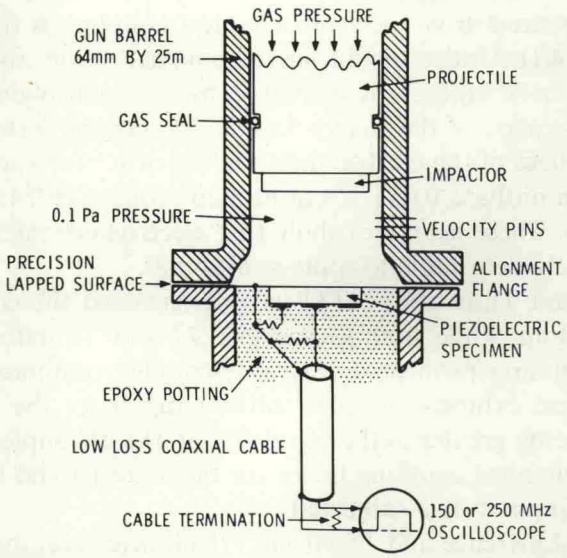

Fig. 4.1. Well-controlled, precisely known strain pulses are applied to piezoelectric samples by impacting them with plates accelerated to a preselected velocity with a smooth-bore compressed gas gun. Misalignment, or "tilt", between the impacting surfaces is typically controlled to within about 250 μrad to assure that the entire face of the sample is impacted in a time short compared to shock-wave transit time. The impact velocity is measured to an accuracy of $\pm 0.1\%$. The short-circuit current pulse resulting from the impact is displayed on high-speed oscilloscopes.

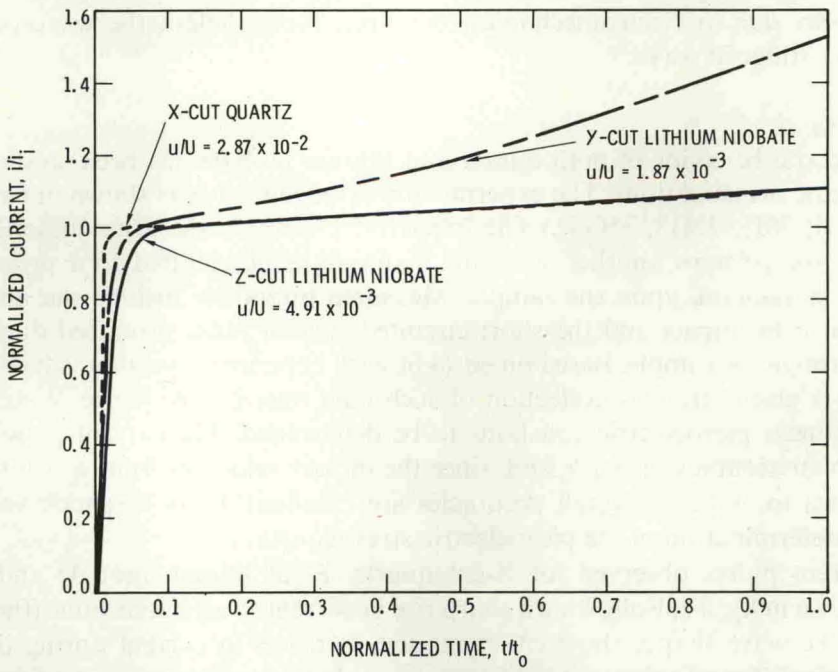

Fig. 4.2. Typical current pulse wave shapes from piezoelectric specimens impacted in the elastic range differ from each other due to the magnitude of the strain, change in permittivity and electromechanical coupling. The typical pulses shown for X-cut quartz [72G3] and Z-cut lithium niobate [77G6] do not deviate greatly from a rectangular shape. However, the typical pulse for Y-cut lithium niobate [77G6] is not rectangular due to the pronounced effect of electromechanical coupling. Most of the deviation from a constant current for quartz is due to finite amplitude strain while that for Z-cut lithium niobate is due to electromechanical coupling (see fig. 4.3). The initial risetime is due to "tilt" between the impactor and sample.

are obtained from samples in the "shorted guard-ring" configuration [75G4].

The measured relationships between piezoelectric polarization and strain for X-cut quartz and Z-cut lithium niobate are found to be well fit by a quadratic relation. In both materials a significant nonlinear piezoelectric effect is indicated. The effect in lithium niobate is particularly notable because the measurements are limited to much smaller strains than those to which quartz can be subjected. The quadratic polymonial fits are used to determine the second- and third-order piezoelectric constants and are summarized in table 4.2. Elastic constants determined in these investigations are summarized in table 3.1 in section 3.1.

Table 4.2
Second- and third-order piezoelectric stress constants of lithium niobate and quartz in the abbreviated notation

Sample	e_{ij} (C/m^2)	e_{ijk} (C/m^2)	e_{ijk}/e_{ij} (C/m^2)
Lithium niobate			
$i=j=k=3$	1.80 ± 0.016	-21 ± 7	-11
$i=j=k=2$	2.37 ± 0.036	21 ± 10	$+9$
$i=1, j=5$	3.83	...	...
Rotated cut	4.65 ± 0.053	0	...
Quartz			
$i=j=k=1$	0.171 ± 0.0009	-2.62 ± 0.05	-15.3

In the case of X-cut quartz there is excellent agreement between second-order constants determined in the shock-compression studies and ultrasonic investigations. The third-order piezoelectric constants for quartz determined from the impact experiments are determined far more accurately than those determined from ultrasonic studies.

For lithium niobate, the second-order constants for shock and ultrasonic studies are in good agreement except for the e_{33} constant which is observed to be higher in shock studies than in ultrasonic investigations [77G6]. This discrepancy is thought to be due to the use of incompletely poled material for the ultrasonic work. The third-order constants for lithium niobate are not determined as accurately as those for X-cut quartz due to the relatively low strains which can be applied before the onset of shock-induced dielectric breakdown (see section 4.6). Nevertheless, the errors of these constants are lower than the order-of-magnitude estimates obtainable by ultrasonic means.

Lithium niobate is strongly ferroelectric yet the material behavior under elastic shock loading is apparently fully described by nonlinear piezoelectricity [77G6]. This is not unreasonable since it is well known that domain realignment with field occurs only in the vicinity of the Curie temperature of 1475 K.

The ratio of third-to-second-order piezoelectric constants has also been determined for X-cut quartz with the acceleration pulse loading method described in ref. [77G5]. Two experiments yielded values for e_{111}/e_{11} of 15.0 and 16.6 [77G5] compared to the ratio of 15.3 determined from the 25 shock loading experiments [72G3].

The determination of piezoelectric constants from current pulses is based on interpretation of wave shapes in the weak-coupling approximation. It is of interest to use the wave shapes to evaluate the degree of approximation involved in the various models of piezoelectric response.

Such an evaluation is shown in fig. 4.3, in which normalized current-time waveforms calculated from various models are shown for X-cut quartz and Z-cut lithium niobate. In both cases the differences between the fully-coupled and weakly-coupled solutions are observed to be about 1 per cent, which is within the accuracy limits of the calculations. Hence, for both quartz and lithium niobate, weakly-coupled solutions appear adequate for interpretation of observed current-time waveforms. On the other hand, the adequacy of the uncoupled solution is significantly different for the two materials. For X-cut quartz the maximum error of about 1 to 1.5 per cent for the nonlinear-uncoupled solution is suitable for all but the most precise interpretation. For Z-cut lithium niobate the maximum error of about 8 per cent for the nonlinear-uncoupled solution is greater than that considered acceptable for most cases. The linear-uncoupled solution is seriously in error in each case.

A unique electrical-to-mechanical coupling effect called "piezoelectric rate coupling" has been predicted to occur in the neighborhood of a shock in *nonlinear* piezoelectric solids [75G5]. The effect appears as a strain gradient in the presence of an electric field rate. The strain gradient apparently persists for only a few nanoseconds or is of such small magnitude that it cannot be observed in careful measurements with a VISAR system since such unpublished measurements by Graham and Asay found no evidence for the expected coupling.

Above or in the vicinity of the Hugoniot elastic limit shock-induced conduction and mechanical yielding cause severe distortions to the idealized piezoelectric response. Well above the Hugoniot elastic limit the three-zone model of Neilson and Benedick [62N1] can be employed to describe and interpret certain dominant features [74G2, 79S2]. An early-time transient observed in quartz [74G2] and lithium niobate [79S2] above the HEL is apparently the result of relaxation of strength [78H2]. The piezoelectric response of Z-cut lithium niobate above the HEL is significantly different from that of X-cut quartz.

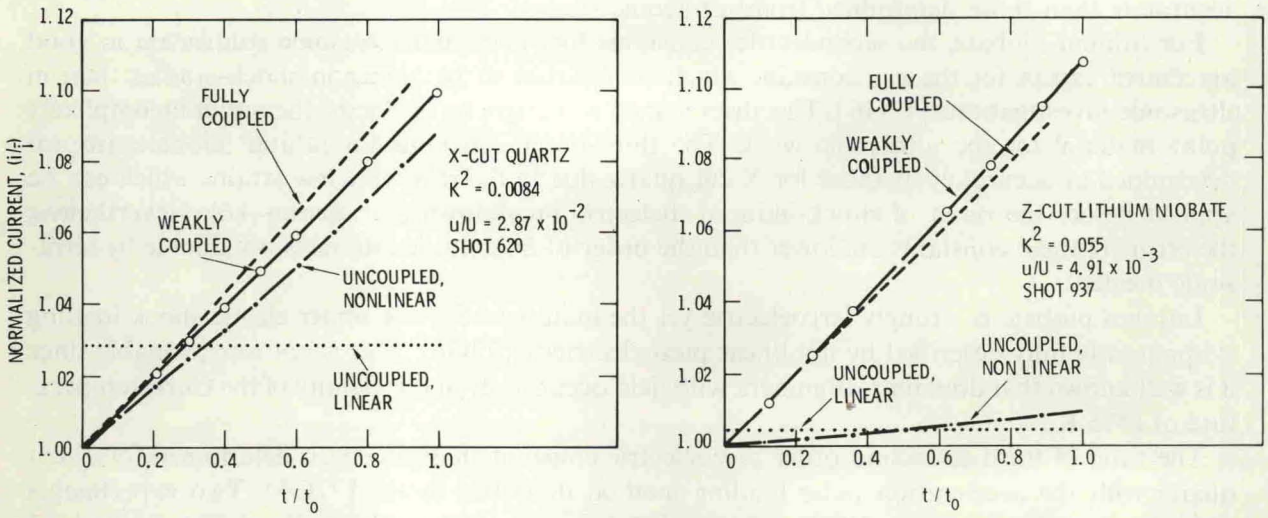

Fig. 4.3. Solutions for normalized current for shock-loaded piezoelectric samples in the linear-uncoupled, nonlinear-uncoupled, weakly-coupled and fully-coupled approximations are shown for X-cut quartz and Z-cut lithium niobate. Lithium niobate has a moderately large electromechanical coupling while quartz has a very small electromechanical coupling. The weakly-coupled solution is that of Thurston [74T1] as modified by Graham [77G6]. In both cases the mechanical boundary conditions correspond to those encountered in the experiments. The experimentally observed current pulses correspond to the fully-coupled solutions within experimental and computational errors. The symbol i is the initial current $i(0+)$.

4.2.3. Summary

The direct nature of the piezoelectric polarization measurements under shock have permitted longitudinal second- and third-order piezoelectric constant determinations for X-cut quartz and Z-cut lithium niobate which are probably the most accurate determined by any method. The precision and detail with which this problem has been studied far exceeds that for other electrical effects under shock loading. Unfortunately, a successful investigation requires numerous samples and conditions of inelastic deformation and shock-induced conduction must be avoided; such conditions cannot be achieved in a wide class of piezoelectric materials. There is hope that the acceleration loading technique, which requires only a single sample whose properties are determined at low strain, can make higher-order piezoelectric constant measurements applicable to a broader class of piezoelectrics. The use of transverse shock loading and detection (see section 3.1) should, in principle, make it possible to determine a full set of higher-order constants. Gupta [79G4] has carried out the first measurement of the piezoelectric response to a shear wave in impacted lithium niobate.

Several microscopic theories of piezoelectricity [72M1, 72M2, 72A5, 74H3] have been proposed but apparently none have been found entirely satisfactory and nonlinear piezoelectricity is not explicitly treated. With such limited second-order theories, physical interpretations of higher-order piezoelectric constants are speculative but such speculations may help to place some constraints on an acceptable piezoelectric theory.

Perhaps the most far-reaching observation from the present measurements under large uniaxial strain and from similar measurements under large hydrostatic pressures [76G4] is that fourth-order piezoelectric effects are negligibly small even though they should be readily detectable at the strain encountered. These observations are in sharp contrast to elastic effects in which fourth-order contributions are readily observed (see, e.g., section 3.1). The details of interatomic interactions which lead to undetectable fourth-order effects cannot be directly determined but it is worthy of note that such behavior can be described in terms of two competing interactions, each with a constant but different strain derivative over a large range of strain. Martin's theory of piezoelectricity applied to zinc blende crystals [72M1, 72M2] is explicitly expressed in terms of two opposing interactions, the rigid ion dipole interaction and a quadrupolar interaction which involves charge redistribution. Helliwell et al. [77H4] have recently used Martin's theory to interpret their nonlinear piezoelectric constant data for CuCl under hydrostatic pressure.

A collection of selected reprints concerning piezoelectricity under shock loading and related piezoelectric gauges has recently been published [78G7].

4.3. Ferroelectrics

The status of knowledge concerning the response of ferroelectric solids to shock compression is in sharp contrast to that concerning piezoelectrics. Whereas the electrical properties of several piezoelectrics are known in quantitative detail under modest shock stresses and in semiquantitative detail at high stresses, the electrical properties of ferroelectrics are described only in a qualitative sense. Relative contributions of dominant physical mechanisms have not been determined and the relation between properties under shock loading and other environments is obscure. The contrast between the piezoelectric and ferroelectric problems under shock loading is a result of their relative complexity; piezoelectrics are the simplest of the electrical materials studied under shock while ferroelectrics are the most complex.

Consider first the stresses imposed on shock-loaded piezoelectrics and ferroelectrics. Piezoelectric crystals investigated have substantial elastic limits and exhibit classical nonlinear elastic behavior. Accordingly, when impacted at stresses in their elastic range, the samples propagate well-defined shock waves. Further, the influence of electrical conditions on mechanical responses is through electromechanical coupling which is generally not dominant and can be quantitatively analyzed. Ferroelectrics exhibit nonsteady, evolving waves at low stresses while still possessing a transition point analogous to a Hugoniot elastic limit at compressive stresses of a few tens of GPa. The cause of this behavior is not understood but it is certainly strongly influenced by electrical states and conditions as well as nonlinear, time-dependent mechanical behavior. In ferroelectrics the influence of electrical conditions is not only through electromechanical coupling, which is typically many times larger than in piezoelectrics, but also through changes in strain accompanying changes in remanent polarization or alignment of domains as influenced by both the stress and the large time-dependent electric fields. All these considerations make it clear that describing the stress or strain histories producing an observed electrical response is difficult.

Consider next the electrical variable. In piezoelectric solids a well-characterized reversible piezoelectric polarization is developed in response to applied strain or stress. The permittivity is independent of history or electric field and, in materials studied to date, only slightly changed by the stress. In ferroelectric solids stress-induced changes in both the remanent polarization and the piezoelectric polarization under shock loading produce electric fields which, themselves, are sufficiently large to further change domain alignment or alter the location of ferroelectric and antiferroelectric phase boundaries. Because changes in domain alignment do not revert upon removal of the electric field, effects of field history are manifest in typical dielectric hysteresis loops relating electric displacement and electric field. Because of the short time scale of the experiment, domain switching times are expected to be significant and electric displacement versus field curves for shocked ferroelectrics cannot be assumed to be those observed under 60 Hz or quasi-static conditions.

At sufficiently high stress, shock-induced electrical conduction, dielectric breakdown and/or dielectric relaxation further complicate the problem as does the occurrence of phase transitions. To further compound the difficulty, single crystal ferroelectrics have not been available.

Given the highly nonlinear, irreversible and strongly-coupled nature of the mechanical and electrical states, it is not difficult to understand why physical processes in shock-loaded ferroelectrics are not well understood and why simple models which describe the response of ferroelectric solids to shock compression in terms of atmospheric pressure dielectric hysteresis loops are not realistic. Unfortunately, much of the work in this area appears to have underestimated the difficulty of the problem which will require persistent systematic efforts for solution.

A short review of work on ferroelectrics has been given by Mineev and Ivanov [76M4] and Novitskii et al. [79N3] have recently summarized their own work and that of others. A more complete summary of work on ferroelectrics is given in table 4.3. Although there have been numerous investigations, they are largely uncoordinated and do not follow a consistent path for compact review.

As was the case for piezoelectrics, pioneering work was carried out by Neilson [57N2]. Reynolds and Seay [61R1, 62R1], Doran [68D3], and Halpin [66H1, 68H1] carried out early investigations of both electrical and mechanical behavior of ferroelectric ceramics. All studies except the limited work of Novitskii et al. [73N2] are on polycrystalline materials.

The sample-to-sample variation in properties of polycrystalline ceramics has presented a

significant limitation. Although large lithium niobate and lithium tantalate crystals are available, no domain alignment or irreversible changes in remanent polarization are observed at room temperature and their electrical responses are piezoelectric, not ferroelectric, in character. (It is interesting to note, however, that lithium tantalate, whose Curie temperature is about 900 K, should exhibit typical ferroelectric behavior at reasonably modest elevated temperatures.)

Important distinctions that can be made for the experimental investigations shown in table 4.3 include whether both electrical and mechanical observations were undertaken and the level of resolution with which mechanical and electrical measurements were accomplished. For mechanical effects, the direct measurement of particle velocity or stress reveals important detail not observed in recorded displacement histories. For electrical effects, investigations in which time-resolved waveforms are measured and interpreted are far more revealing than those in which only peak voltage or charge are measured. Some investigations have been more concerned with analysis of the shocked ferroelectric as a circuit element than with analysis of the physical processes. Investigations have been performed in both the axial mode, in which propagation direction is along the remanent polarization direction, and the normal mode, in which the propagation direction is normal to the polarization direction.

Most of recent work has been accomplished by Lysne and coworkers in the United States, Bauer and coworkers in France, and Novitskii and coworkers in the Soviet Union. Lysne's work has been the most extensive and has ranged from fundamental studies to those which treat the sample as a circuit element. His work in analysis of waveforms has revealed evidence for kinetic effects and dielectric breakdown, and his work with partially poled samples has provided the first data on dielectric hysteresis loops under shock loading [77L4]. Lysne has also provided first evidence and analysis for dielectric relaxation in shock-loaded ferroelectrics [79L1] and has introduced wave reverberation as a tool of experimental investigation.

Bauer and coworkers [76B3, 77B1] have examined the effects of varying composition more thoroughly than other investigators. Their work on lead zirconate/lead titanate (PZT) compositions in the vicinity of the ferroelectric-antiferroelectric phase boundary includes both shock loading and pulsed hydrostatic loading with risetimes of tens of miliseconds. Bauer [77B1] has also identified a well-defined first-order phase transition at 0.2 GPa for shock-loaded PZT 96.5/3.5 with a 1 % Nb_2O_5 additive.

Novitskii and coworkers in the Soviet Union have developed considerable capability for modeling rate-dependent electrical effects. They also point out the importance of careful circuit design [73N2] but their interpretation of Halpin's [66H1] results is based on erroneous inductance values. Their recent review emphasizes the importance of shock-induced conduction [79N3].

Many investigations show the presence of a maximum in observed charge versus stress followed by a minimum after which charge again increases. This apparently is the result of shock-induced conduction which is probably associated with dielectric breakdown. If the sample goes through a phase transition, such behavior can result from the larger fields resulting from a reduced permittivity.

Chen and coworkers [76C3, 76C4, 78B7, 78A1, 78A2] have developed theories of plane-wave propagation in ferroelectrics but detailed comparison between theory and experiment has not yet been attempted. It seems likely that it will be necessary to develop a fully-coupled computer code such as has been developed for piezoelectrics [77L1], but also incorporating kinetic and hysteretic properties, before reasonable progress can be made.

Experimental progress requires consistent, persistent, and systematic efforts which incorporate

Table 4.3
Studies of ferroelectrics under shock loading*

	Density, kg/m^3 Polarization, C/m^2	Stress GPa	Measurements[a]		Conduction	Permittivity	Switching kinetics	Mode[b]	Remarks
			Mech.	Elect.					
Barium titanate									
Reynolds and Seay [61R1]	___; ___	2.4 to 18	Yes, $d(t)$	No	—	—	—	Axial	Two-wave structure
Reynolds and Seay [62R1]	5710; 0.__	2 to 100	Yes, $d(t)$	No	—	—	—	Axial	Room and elevated temperature
Novitskii et al. [73N2]	6050; 0.26	12 to 19	No	Yes, Q	—	—	—	Axial	Crystal
95 % $BaTiO_3$ 5 % $CaTiO_3$									
Reynolds and Seay [61R1]	___; ___	2.8 to 18	Yes, $d(t)$	No	—	—	—	Axial	Two-wave structure
Doran [68D3]	___; ___	0.5 to 30	Yes, $d(t)$	No	—	—	—	Axial	Room and elevated temperature
Linde [67L1]	5540; 0.10	0.35 to 1.9	No	No	—	—	—	Axial	Polarization on shocked and recovered samples
Lead titanate									
Novitskii et al. [73N2]	7950; 0.6 to 0.7	2 to 19	No	Yes, Q	—	—	—	Axial	Crystal
PZT 52/48 + 1 % Nb_2O_5									
Reynolds and Seay [61R1]	___; ___	1.9 to > 25	Yes, $d(t)$	No	—	—	—	Axial	Two-wave structure
Reynolds and Seay [62R1]	7580; 0.32	1.9 to 39	Yes, $d(t)$	Yes, Q	?	—	—	Axial	Two-wave structure
Linde [67L1]	7680; 0.34	0.55 to 0.95	No	Yes, Q	—	—	—	Axial	Polarization on shocked and recovered samples
PZT 54/46 + 1 % Nb_2O_5									
Bauer and Vollrath [76B2]	___; 0.35	0.2 to 0.7	No	Yes, Q	No	—	—	Axial	Maximum charge at 0.45 GPa
PZT 53/47 + 1 % Nb_2O_5									
Zubarev [71Z3]	7300–7400; 0.35	10 to 47	Yes, $d(t)$	Yes, I	Yes, above 2 GPa	—	—	Axial	No residual polarization
Novitskii et al. [72N2]	7160–7370; 0.36	0.5 to 15	Yes, $d(t)$	Yes, Q	Yes	Yes	Yes	Axial	
Novitskii et al. [73N2]	___; ___	0.5 to 2	No	Yes, Q	Yes, 0.5 to 2 GPa	Yes	No	Axial	Principally theory
Novitskii et al. [77N2]	8000; ~ 0.4	1 to 170	Yes, $V(t)$	Yes, I	—	—	—	Axial	Hot pressed, poss. phase trans.
Novitskii et al. [77N2]	7160–7370; 0.36	0.2 to 160	Yes, $V(t)$	Yes, I	—	—	—	Axial	Possible phase transition
Bauer [77B1]	___; 0.33	0.9 to 2	No	Yes, Q	—	—	—	Axial	—
PZT 56/44									
Mock and Holt [78M5]	7550–7580; 0.33	4.4 to 11.8	No	Yes, I	Yes, at 11.8 GPa	—	—	Normal	Capacitor loads
Mock and Holt [78M5]	7500; 0.31	1.5 to 8.8	No	Yes, I	Yes, at 6.8 GPa	—	—	Axial	Polarity effect
PZT 65/35 + 1 % Nb_2O_5									
Cutchen [66C1]	___; ___		No	Yes, Q	Yes	No	No	Axial	Polarity effect
Lysne [73L3]	7870; 0.1, 0.2, 0.3	0.3 to 2.3	Yes	Yes, I	Yes	No	No	Axial	Dielectric breakdown
Lysne and Bartel [75L4]	7870; 0.025 to 0.05	0.5 to 8.0	Yes	Yes, I	Yes	No	Yes	Axial	Multiple reverbation
Lysne [75L2]	___; ___	—	No	No	Yes	No	No	Axial	Data from [73L3]
Lysne [77L4]	___; ___	0.3 to 2.4	No	Yes, I	Yes	No	No	Axial	Residual polarization
Bauer [77B1]	___; 0.34	0.9 to 2.2	No	Yes, Q	—	—	—	Axial	Polarity effect

PZT 75/25 + 1% Nb_2O_5									
Bauer [77B1]	___; 0.34	1.4 to 2.2	No	Yes, Q	—	—	—	Axial	—
PZT 85/15 + 1% Nb_2O_5									
Bauer [77B1]	___; 0.38	1.4 to 2.2	No	Yes, Q	—	—	—	Axial	—
PZT 95/5 + 1% Nb_2O_5									
Halpin [66H1]	7720; 0.34	0.4 to 3.3	No	Yes, I	No	Yes	No	Axial	Normally sintered
Halpin [66H1]	7990; 0.37	0.4 to 2.6	No	Yes, I	No	Yes	No	Axial	Hot pressed
Linde [67L1]	7760; 0.34	0.65 to 1.1	No	No	No	No	No	Axial	Polarization on shocked and recovered samples
Doran [68D3]	7740–7890; ___	0.2 to 14	Yes, $d(t)$	No	—	—	—	Axial	—
Halpin [68H1]	7720; 0.34	—	—	—	Yes	—	—	Axial	Resistivity, data from [66H1]
Halpin [68H1]	7990; 0.34	—	—	—	Yes	—	—	Axial	Resistivity, data from [66H1]
Lysne and Percival [75L5]	7550; 0.29	0.5 to 2.4	No	Yes, I	Yes	Yes	No	Normal	
Lysne and Percival [76L2]	___; ___	—	No	Yes, I	Yes	Yes	Yes	Norm. and Ax.	
Lysne [77L5]	___; 0.29	0.6 to 3.2	No	Yes, I	Yes	Yes		Normal	Depoled stress > 1.6 GPa
Dick and Vorthman [78D1]	7290–7370; 0.3	—	Yes, $V(t)$	Yes, I	No	No	No	Normal	Elect.-Mech. coupling
Mock and Holt [78M5]	7470; 0.3	1.4 to 2.9	No	Yes, I	Yes	No	No	Normal	—
Lysne [79L1]	___; ___	—	—	—	Yes	Yes	Yes	Normal	Interpretation of [77L5] Dielectric relaxation
PZT 95/5 + 0.8% WO_3									
Bauer et al. [76B3]	___; ___	—	No	Yes, Q	Yes	No	No	Axial	—
Bauer [77B1]	___; ___	—	No	Yes, Q	Yes	No	No	Axial	—
Bauer and Vollrath [76B2]	___; ___	1.5 to 2.0	No	Yes, Q	Yes	No	No	Axial	Charge versus resistance
PZT 96.5/3.5 + 1% Nb_2O_5									
Bauer et al. [76B3]	___; ___	0.2 to 1.1	No	Yes, Q	Yes	No	No	Axial	
Bauer [77B1]	___; 0.33	0.2 to 1.7	Yes	Yes, Q	Yes	No	No	Axial	Also study of recovered samples Phase transition at 0.2 GPa
Bauer and Vollrath [76B1]	___; 0.38	0.2 to 8.0	No	Yes, Q	Yes	No	No	Axial	Maximum charge at 1.7 GPa
PSZT 68/7 ($Pb_{0.99}Nb_{0.02}(Zr_{0.68}Ti_{0.07}Sn_{0.25})_{0.98}O_3$)									
Halpin [66H1]	___; ___		No	Yes, I	—	—	—	Axial	
Halpin [68H1]	___; ___		No	Yes, I	—	—	—	Axial	
PSZT 70/30-6 ($Pb_{0.99}Nb_{0.02}[(Zr_{0.70}Sn_{0.30})_{0.94}Ti_{0.06}]_{0.98}O_3$)									
Lysne [75L3]	___; 0.05	0.24 to 0.74	No	Yes, I	Yes	No	Yes	Axial	Reverberating wave; poss. trans., see also [76L2]
$(Pb_{0.715}Ba_{0.285})_{0.991}(Zr_{0.707}Ti_{0.293})_{0.981}Bi_{0.019}O_3$									
Lysne [78L5]	7340; 0	0.24 to 0.88	No	Yes, I	No	Yes	Yes	Axial	Pen or "slim loop" ferroelectric

* See also the recent summary by Novitskii et al. [79N3].

[a] Indication of mechanical (Mech.) measurements are whether displacement versus time is measured, indicated $d(t)$ or whether velocity or stress versus time is measured, indicated $V(t)$. Indication of electrical (Elect.) measurements are whether integrated charge or peak voltage, indicated Q, or current or voltage waveform, indicated I, is measured.

[b] Orientation of remanent polarization is either along the shock direction, called axial mode, or perpendicular to shock direction, called normal mode.

numerous variables on a few selected materials. In order to make a convincing case, variable electrical configurations (e.g., open and short circuit, axial- and normal-mode), variable electrical states (i.e., various initial remanent polarizations), and variable stresses and sample dimensions need to be employed. Time-resolved measurements of both electrical and mechanical waveforms are required. Temperature is an important, but neglected, variable. Compositional studies and the relation of properties under shock loading to those under static high pressure and uniaxial stress need to be carefully examined (see, e.g., Fritz [78F1] and Fritz and Keck [78F2]). Short pulse, multiply-reverberating and acceleration pulse loading will help to elucidate history-dependent electrical and mechanical behavior.

4.4. *Normal dielectrics*

Nonlinear properties of normal dielectrics can be studied in the elastic regime by the method of shock compression in much the same way nonlinear piezoelectric properties have been studied. In the analysis of section 4.2 it was shown that the shape of the current pulse delivered to a short circuit by a shock-compressed piezoelectric disk was influenced by strain-induced changes in permittivity. When a normal dielectric disk is biased by an electric field and is subjected to shock compression, a current pulse is also delivered into an external circuit. In the short-circuit approximation, the amplitude of this current pulse provides a direct measure of the shock-induced change in permittivity of the dielectric.

A normal dielectric may be characterized by eq. $(4.1)_2$ with the piezoelectric terms deleted. For an isotropic dielectric subject to uniaxial strain and a colinear electric field this equation takes the form

$$D_1 = (\varepsilon^{\eta}_{11} + \tfrac{1}{2}\varepsilon^{\eta}_{111}E_1 + \tfrac{1}{2}f_{111}\eta_1)E_1, \qquad D_2 = D_3 = 0. \tag{4.9}$$

Neglecting the small effect of electrostrictive coupling on mechanical behavior, we see from eq. $(4.1)_1$ that shock propagation is not influenced by electrical effects. Under this approximation, a steady shock propagated into the material will divide its thickness into two regions of uniform strain that can be analyzed in the same manner as for the piezoelectric response. In the absence of free charge, eqs. (4.3) and (4.4) applied to an elastic disk of thickness L having an electrode of area A and subject to a potential V yield the relation [68G5] (see also Allison [65A1] and Royce [68M3])

$$\frac{i(t)L^2}{AVU\varepsilon^+} = \left[\frac{u}{U} + \frac{\Delta\varepsilon}{\varepsilon^+}\left(1 + \frac{u}{U}\right) + \left(\frac{\Delta\varepsilon}{\varepsilon^+}\right)^2\right]\left[1 - \frac{ut}{L} + \frac{\Delta\varepsilon}{\varepsilon^+}\left(1 - \frac{t}{t_0}\right)\right]^{-2} \tag{4.10}$$

for the time interval $0 < t < t_0 = L/U$ after impact. In this relation ε^+ is the permittivity of the uncompressed material, i.e., the coefficient of E_1 in eq. $(4.1)_2$ evaluated at $\eta_1 = 0$, $E_1 = V/L$, and $\Delta\varepsilon$ is the change in this coefficient that occurs with passage of the wave. The change in permittivity, which is proportional to the electrostrictive constant f_{111}, is the quantity sought in an experimental measurement.

As with the piezoelectric case, material constants are most easily determined from the initial jump in current, $i(0+)$, which, from eq. (4.10), is

$$\frac{i(0+)t_0}{A} = \left(1 - \frac{1}{\alpha}\left(1 - \frac{u}{U}\right)\right)D_0 \tag{4.11}$$

where D_0 is the initial electric displacement $E\varepsilon^+$ and α is the ratio of strained-to-unstrained permittivity.

Experimental studies within the elastic range have been performed on monocrystalline Al_2O_3 (sapphire) and the nonpiezoelectric Z-cut of quartz. Experiments are performed with a circuit devised by Ingram [68G5] in which a low-loss coaxial cable is used for both application of the potential and monitoring the current. For an applied potential difference of a few kilovolts, a current of about 1 mA is produced at a compression of several percent.

Constants determined from data reported in ref. [68G5] and from the piezoelectric studies of X-cut quartz are shown in table 4.4. The coefficients are found to be constant over the range of strain indicated.

Table 4.4
Electrostrictive constants

Material and orientation	Experiments	Strain range %	f_{iii}[(a)] 10^{-12} F/m
Z-cut Al_2O_3	5	0.3 to 1	$+58 \pm 2$
60° cut Al_2O_3	7	0.3 to 2	$+86 \pm 4$
Z-cut quartz	4	2.4 to 6.5	$+6.0 \pm 0.2$
X-cut quartz[(b)]	—	—	-4 ± 0.1

[(a)] f_{iii} is the electrostrictive constant for the orientation indicated, $\pm$ indicates standard deviation.

[(b)] as determined from piezoelectric current pulse studies (see section 4.2).

Similar studies can be performed above the elastic range if the hydrodynamic model is a suitable approximation to the response of the material. Such studies have provided permittivity data on polyethylene to 25 GPa [70H2], although these studies were complicated by a shock-induced polarization effect. In materials which exhibit shock-induced polarization, a unique phenomenon discussed briefly in section 4.5, permittivities can be determined in a manner analogous to that used for piezoelectric solids [65H1, 70H2]. Hauver [70H2] has used a resonant *LC* circuit to determine permittivities for an organic material, o-nitroanisole. Permittivities observed in shock-compression experiments on ferroelectrics are documented in section 4.3. Lysne [78L5] has recently measured the permittivity change on a "slim loop" ferroelectric ceramic which shows a linear reversible permittivity change with stress from 0.24 to 0.88 GPa.

4.5. Shock-induced polarization

When dielectric or semiconductor samples which are unbiased electrically are subjected to shock loading, it is commonly observed that the loading will cause currents to flow in circuits connecting electrodes on the samples. The maximum polarizations responsible for these currents range from about 0.1 per cent to about 30 per cent of those achieved due to the piezoelectric effect in shock-loaded quartz. If the sample is not piezoelectric, ferroelectric, or an electret, the observed shock-induced polarizations are anomalous when considered in terms of equilibrium thermodynamic processes. The term "shock-induced polarization" is used to describe those anomalous polarizations unique to samples subjected to shock loading. Studies of shock-induced polarization provide basic insight into the non-equilibrium behavior of shock-induced defects.

Work in this area has recently been given comprehensive and critical reviews by Murri et al. [74M3], and Mineev and Ivanov [76M4], and with these reviews available, it is only necessary to briefly consider the principal results. Unfortunately, the review of Mineev and Ivanov is flawed by its dependence on references not available outside the Soviet Union. Graham [79G5] has recently summarized shock-induced polarization work in polymers. Anomalous emf observed at metal and semiconductor thermocouple junctions are considered separately in section 4.11.

Shock-induced polarizations were first observed in the polymeric materials, PMMA, Teflon, C-7 Epoxy and polystyrene by Eichelberger and Hauver [62E1]. Following that work, Allison [65A1] derived an expression for current pulses from shock-loaded materials with polarization relaxation. A number of authors have now derived related or more general relationships for such current pulses and a summary of the characteristics of the various theories is given in table 4.5. This table follows that compiled by Mineev and Ivanov [76M4] with the addition of piezoelectric polarization and dielectric relaxation. Treatments of ferroelectrics are given separately in section 4.3.

Table 4.5
Theories of polarization currents (after Mineev and Ivanov [76M4])

Authors	Polarization relaxation time	Conductivity behind shock	Permittivity	Conductivity ahead of shock	Electrical load	Dielectric relaxation time
Graham et al. [65G1], Graham [72G3]	∞	0	Arbitrary	0	0	∞
Lawrence and Davison [77L1] (fully coupled)	∞	0	Arbitrary	0	Arbitrary	∞
Lysne (see section 4.7)	∞	0	Arbitrary	0	Arbitrary	Arbitrary
Zel'dovich [68Z2]	∞	Arbitrary	Constant	0	0	∞
Graham and Halpin [68G1]	∞	Arbitrary	Constant	0	0	∞
Allison [65A1]	Arbitrary	0	Arbitrary	0	0	∞
Ivanov et al. [68I2]	Arbitrary	Arbitrary	Arbitrary	0	0	∞
Zaidel [68Z1]	Arbitrary	Arbitrary	Arbitrary	Arbitrary	Arbitrary	∞

In general, current pulses due to shock-induced polarization will be affected by polarization relaxation time, electrical conduction, electrical load and dielectric relaxation. For short-circuited conditions in which volume polarization processes are fast compared to the loading time, the initial current jump in all theories is the same and is given by eq. (4.6) in section 4.2. The influence of "tilt" in loading systems on current pulses has been analyzed by Antinenko et al. [75A1].

Very recent work by Lysne [78L6] on dielectric relaxation in shock-damaged dielectrics will necessitate reexamination of work in which shock-induced conduction has been inferred in shock-polarized dielectrics, since dielectric relaxation can be easily confused with conduction (see section 4.7).

Shock-induced polarization has been observed in ionic crystals, polymeric materials, and semiconductors. The most thorough work, and that leading to the development of physical models, is that carried out since 1965 on ionic crystals, principally alkali halides, by Mineev, Ivanov, Novitskii, Tyunyaev and Lisitsyn [76M4]. Early work was reported by Linde et al. [66L3], Ahrens [66A1], and Wong et al. [69W2]. Ionic materials studied include LiF, NaCl, KBr, RbCl, KI, RbI, MgO, CsI, Li^7H and Li^6D. In addition to work on relatively pure crystals of various

crystallographic orientations, the effects of impurities and radiation-induced defects have been investigated.

Although the observed current pulses are generally of complex shape, an "effective polarization", $Q_0 = i(0+)t_0/A = (1 - u/U)P_0/\alpha$, can be computed from the measured initial current and eq. (4.6). This parameter has been found to exhibit consistent behavior among the various ionic crystals. At low stress all the pure ionic crystals show a positive current indicative of a polarization oriented in the shock propagation direction. Although there may be considerable scatter, the effective polarization is observed to increase smoothly with increasing compression until a compression of about 30 per cent is achieved. Above this compression the polarization decreases and, with the exception of MgO and LiF, the sign of the effective polarization of pure ionic crystals is reversed when compressions of about 40 per cent are exceeded. At the highest pressures no polarization signals are detectable.

The collected data on maximum effective polarization for the various ionic crystals are shown in fig. 4.4. In this figure the polarizations are found to be well correlated with cation radius, dielectric constant and an electronic factor, $\gamma = \Delta\varepsilon/E_g a$, where $\Delta\varepsilon$ is the difference between low and high frequency dielectric constants, E_g is the energy gap and a is the lattice parameter. This electronic factor is thought to be a measure of dielectric breakdown strength in ionic crystals. The polarization data of fig. 4.4 indicate that the polarization is independent of anion and roughly the same for a given cation. With the exception of the cesium halides, the effective polarizations correlate well with the cation radius and as the cation size decreases, the polarization increases. The cesium halide crystals are in the CsCl structure while the other crystals are in the NaCl structure. If the more open CsCl structure is accounted for by multiplying the cation radii of the CsI and CsBr by the ratio of the hard-sphere-filled volumes for the sc and fcc structures, their polarization data are brought into agreement with the NaCl-structure crystals.

Based on the various observations, Mineev and his coworkers have concluded that the overall features of shock-induced polarization in ionic crystals below compressions of 30 per cent can be semiquantitatively described by cation-vacancy dipoles resulting from the shock-induced generation of large numbers of point defects and subsequent displacement of the cation over a distance of 1 to 10 lattice parameters in times of about 5×10^{-8} s. Transient defect levels of 10^{23} m^{-3} at compressions of 10 per cent, increasing by an order of magnitude for each subsequent 10 per cent compression, are found to be compatible with the polarization observations and other independent estimates. Relaxation of polarization follows the thermal equilibration of the shock-induced defect structure. The correlation with the electronic factor, γ, suggests that the maximum polarization may be limited by local internal dielectric breakdown.

Although there are still major unresolved questions, including the effects of polymorphic phase transitions in these materials, properties affecting the current pulse wave shapes and the reversal of the sign of the polarization at large compressions, the shock-induced cation-vacancy dipole model appears to be well descriptive of the observed polarization of ionic crystals. Graham [79G5] has recently summarized the data on shock-induced polarization in polymers, and has proposed that the effect arises from mechanically-induced bond scission. In the case of semiconductors, shock-induced generation of point defects is likely to be a dominant mechanism, but no detailed physical model has been proposed.

The difficulty in developing physical models for electrical responses of shock-loaded solids is well indicated by the present problem which required persistent efforts over a period of over ten years before credible physical processes could be identified. The cation displacement model

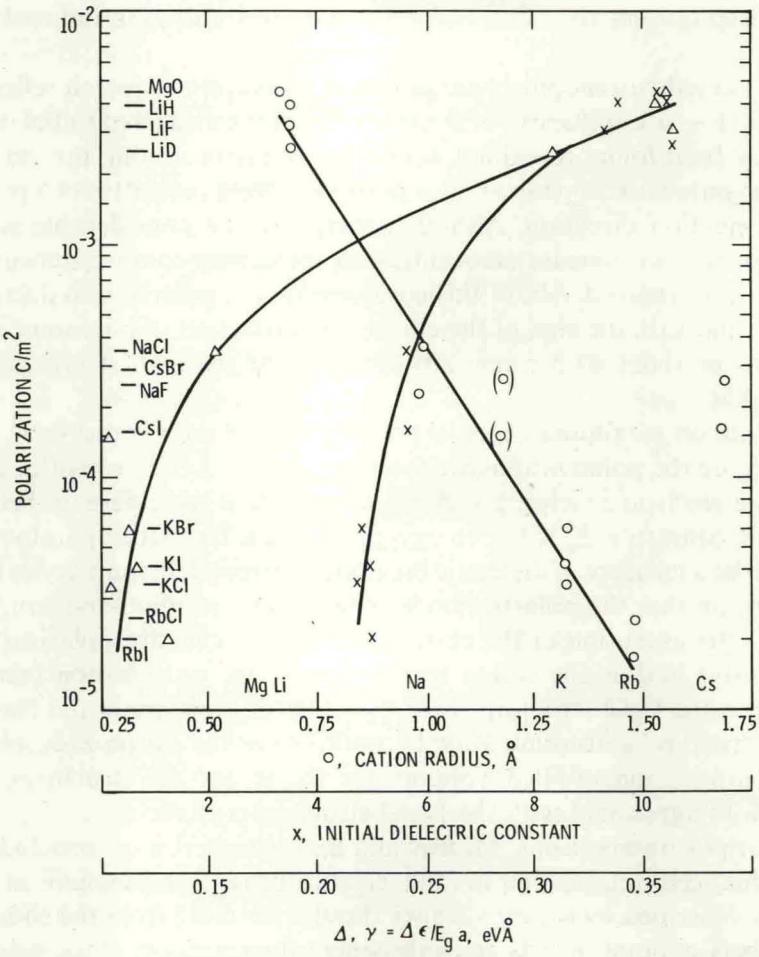

Fig. 4.4. The maximum effective shock-induced polarizations, Q_0, observed for ionic solids for the NaCl structure are observed to correlate well with cation radius, dielectric constant and an electronic factor, γ, which is thought to be a rough measure of dielectric strength. The maximum polarizations are found to be roughly the same for a given cation, independent of the anion. The polarizations observed for cesium halides, which are in the CsCl structure, do not correlate well with the cation radius. Nevertheless, if the cesium halide radii are multiplied by the ratio of hard sphere filled volumes for the sc and fcc structures, the data are as shown in parentheses and the observations are brought into agreement with the NaCl structure crystals. After Mineev and Ivanov [76M4] and Tyunyaev et al. [69T3].

emphasizes the importance of shock-induced defects and their non-equilibrium behavior. The observation of such processes as shock-induced polarization is overt evidence for nonequilibrium effects and should serve to alert us to the nonequilibrium nature of the shock process. It also suggests the use of electrical measurements to probe shock-induced defects.

4.6. Shock-induced conduction

The term "shock-induced conduction" denotes a class of phenomena in which the resistance of good insulators decreases markedly upon shock compression. Few comprehensive investigations

have been conducted, but the available evidence demonstrates that shock-induced conduction is a commonly observed but poorly understood effect. It has been attributed to a variety of physical effects, most unique to shock loading, and may also appear as an experimental artifact.

Shock-induced conduction plays a crucial role in the operation of many electrical devices in which insulating material is subjected to impact or other rapid loading. Piezoelectric and solid-dielectric gauges are limited in their performance by shock-induced conduction. The performance of pulse power supplies based on shock compression of piezoelectric or ferroelectric materials is similarly limited. Knowledge of the behavior of insulators under shock compression is required for interpretation of measurements made using piezoresistant gauges embedded in conducting samples [78B1], for insulation of magnetic compression devices [78H1], and for design of switches operating on the basis of a shock-induced switching between insulating and conducting states. From the scientific standpoint, shock-induced conduction is not only a phenomenon of intrinsic interest, but also one that must be understood in some degree if other shock-induced electrical effects are to be interpreted with assurance.

The literature on conduction under shock loading has been thoroughly reviewed through 1969 by Styris and Duvall [70S3], with less complete treatments being offered by Doran and Linde [66D3] and Keeler [71K2]. Experimental methods have been reviewed by Yakushev [78Y1]. Other related reviews include that of Kormer [68K5] on optical effects and that of Mineev and Ivanov [76M4] on conduction as related to interpretation of shock-induced polarizations. With these prior reviews as a guide to the literature, the present review can more profitably concentrate on general observations. In that regard it is well to observe that most of the work is fragmentary and largely exploratory. Careful and persistent work has been reported for the fluids CCl_4 [68M3] and xenon [71K2] in which detailed comparison between theory and conductivity measurements has been carried out. Such studies in fluids do not experience difficulties with measurement or interpretation which are found in solids.

Except for the thorough analysis developed for NaCl by Kormer [68K5], conduction measurements on alkali halides are summarized by Styris and Duvall [70S3] who also report important unpublished work of Murri and Doran and Doran and Ahrens. Much of the work on alkali halides has been interpreted in terms of intrinsic semiconduction which neglects shock-induced defects. Conductivity is assumed to result from a thermally-activated process and activation energies are determined from resistance measurements at the different temperatures resulting from compression by shocks of various strengths. The activation energies so determined have been used to compute energy gaps.

Such interpretations are open to considerable question and apparently disagree with calculations of the effect of pressure on energy bands. Most of the data are fragmentary (often there is only a single experiment) and the most thorough work (on CsI) consists of only seven experiments. Such limited data not only leave questions of representative material behavior unanswered, but do not permit examination of the question of experimental artifacts, ohmic behavior, transient behavior, sample size effects or heterogeneities caused by shock loading. It appears more likely that the activation energy values cited above are measures of extrinsic semiconduction dominated by shock-induced defects; a strong case for such behavior based on both optical and electrical data is given by Kormer [68K5] (see section 5). Such an electronic configuration can also lead to localized dielectric breakdown at high temperature [69K3]. Even the interpretation in terms of extrinsic semiconduction rests on the assumption that defect concentrations are fixed and independent of compression over the large range of compressions used to achieve the shock

heating. It will be a difficult and demanding job to develop a quantitative physical interpretation of the observed conduction in the alkali halides.

Polymeric materials are widely encountered in shock experiments, yet there are few studies of their electrical resistance in states of shock compression. The most thorough work on polymers is that of Champion [72C1] who measured the resistance of Teflon (polytetrafluoroethylene), low-density polyethylene and high-density polyethylene at pressures from 10 to 55 GPa. Effects of variations in both sample area and thickness were studied and experiments were conducted at several applied voltages. Low-density polyethylene showed a three order-of-magnitude decrease in resistance from 15 to 38 GPa, while high-density polyethylene shows about a two order-of-magnitude decrease in resistance over the same pressure range. The resistance of Teflon remains an order of magnitude higher than that of high-density polyethylene at the same pressures. All materials apparently exhibited a large decrease in resistance at pressures less than 10 GPa. An anomalous absence of any change in resistance was noted for thin (0.6 and 1.3 mm thick) samples, with the observations being confirmed for high-density polyethylene by Hauver [70H2] and for Teflon by Kuleshova [69K4]. Of the polymeric materials studied, Teflon appears to exhibit the highest resistivity under strong shock compression; the apparent resistivity of thick samples is 100 Ωm at 55 GPa. Kuleshova and Pavlovskii [77K3] have recently reported transverse resistance measurements in Kaprolon ($\rho_0 = 1140$ kg/m^3) which they have interpreted in terms of a time-dependent resistivity. Electrical breakdown studies on Kapton, a polyimide film, have recently been reported [78G3, 79G6]. Polymorphic phase transitions observed in a wide variety of polymers [78C2] must be considered in interpretation of resistance measurements in these materials.

Other dielectric materials given limited study are summarized by Styris and Duvall [70S3]. Two materials, MgO and Al_2O_3, are of particular interest. Ahrens [66A1] measured electrical resistances of MgO crystals shock loaded along the [001] direction to a pressure of 92 GPa. He observed an apparent resistivity of only about 10 Ωm, a value that cannot be explained in terms of pressure-induced reduction of energy gap. It appears that shock-induced defects or localized heating due to heterogeneous yielding or localized effects at grain boundaries (see section 3.4) are required to explain the results. The shock-induced polarizations in this material are sufficiently high that self-generated electric fields may cause localized dielectric breakdown and lead to the observed conduction.

The large decreases in resistance observed in shock-loaded crystalline and polycrystalline Al_2O_3 have been summarized by Hawke et al. [78H1]. Although a number of different investigators have reported shock-induced changes in resistance, the measurements are quite limited; nevertheless, they all demonstrate that shock loading of samples with initial room-temperature resistivity greater than 10^{10} Ωm lowers the effective resistivity to between 10^3 and 10^{-4} Ωm [78H1].

Shock-induced conduction in piezoelectrics is differentiated from that in other dielectrics because it is observed under the unusually high electric fields produced by the piezoelectric effect in the thick-sample configuration. Shock-induced conduction observed in quartz and lithium niobate has been identified as dielectric breakdown or a prebreakdown electrical process associated with electric fields in the range of 10^7 to 10^8 V/m. The dielectric strengths under shock loading are less than 10 per cent of the atmospheric-pressure values. Given the high shear stress present in these experiments, it is not difficult to believe that dielectric strength could be reduced, but the physical mechanisms responsible for the observations have not been identified. In spite of interest extending over fifteen years and the conduct of a number of detailed investigations, no physical model for shock-induced dielectric breakdown has been developed. Fortunately, the breakdown

for quartz and lithium niobate occurs well within the elastic range and under conditions in which the strains and electric fields can be accurately calculated.

The sample-polarity anomaly in current pulses from X-quartz quartz shocked above the Hugoniot elastic limit gave the first indication of unusual conduction phenomena in that material [62N2]. Subsequent work [62G1, 68G4, 72G4] showed that anomalies in current pulses in the minus-X orientation were encountered at all fields once a threshold stress of 1.2 GPa was exceeded. The observed rapid reduction in current in an external short circuit, combined with intense localized luminescence indicative of localized high-current densities [62N2, 65B3, 68G4], supply strong evidence to support a breakdown phenomenon.

Certainly the most prominent feature of the breakdown process is its dependence on the polarity of the electric field relative to the shock-velocity vector. This effect is manifest in current pulse anomalies from minus-X orientation samples or positively-oriented samples subjected to short-pulse loading (see fig. 4.5). The individual effects of stress and electric field may be delineated with short-pulse loadings in which fields can be varied by utilizing stress pulses of various durations

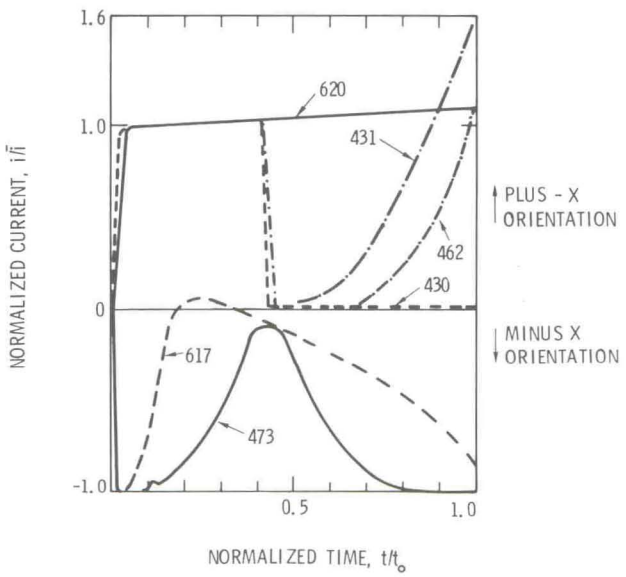

Fig. 4.5. Piezoelectric current accompanying shock waves in X-cut quartz ordinarily exhibit classic piezoelectric behavior as indicated in Shot 620 (2.49 GPa) for long-pulse loading and for Shot 430 (0.942 GPa) for short-pulse loading. In certain ranges of stress and electric field anomalous currents are observed for short-pulse loading such as are shown in Shots 431 (1.90 GPa) and 462 (1.54 GPa). In the minus-X orientation the currents are negative and above a threshold stress of 1.12 $\pm$ 0.7 GPa the waveforms are drastically distorted as shown in Shot 617 (2.1 GPa) and Shot 473 (1.12 GPa). The current pulse distortions are thought to be a consequence of a stress-induced dielectric breakdown initiated above the threshold stress and field. The effect of specimen polarity indicates that negatively charged species which originate at the shock front are the source from which the breakdown proceeds.

[72G4]. As shown in fig. 4.6, these studies provided evidence that the breakdown was characterized by a fixed threshold stress of 1.1 GPa and a fixed threshold field of 2.8×10^7 V/m. Once the threshold stress is exceeded, the conduction is controlled by the field and is independent of the stress. The threshold field is in reasonable agreement with the field of 7×10^7 V/m below which a recovery from breakdown is observed when the field decreases due to the internal conduction [68G4].

A time delay for breakdown has been observed which depends upon the electric field but is,

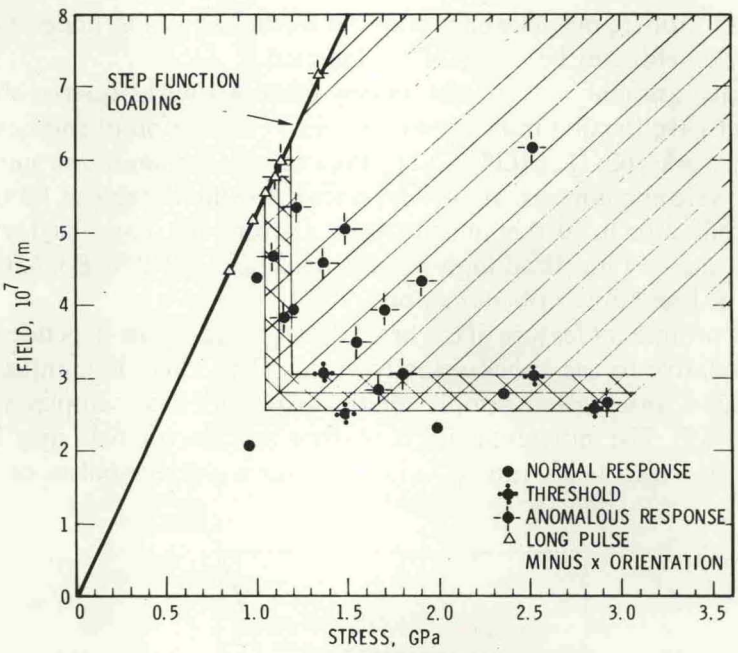

Fig. 4.6. Short-pulse loading can be used to control the electric field in a piezoelectric sample independent of the stress amplitude. Data from such experiments as shown in fig. 4.5 have been used to delineate the region in which anomalous current pulses (thought to be due to dielectric breakdown) are observed. The data shown indicate that a stress threshold of 1.12 GPa and an electric field threshold of 2.5×10^7 V/m must be exceeded to cause the effect. After Graham and Ingram [72G4].

again, independent of stress once the threshold stress is exceeded [75G6]. Such a delay time has also been observed in short-pulse loading experiments [76B5].

It appears that the observed breakdown must be explained in terms of the transient behavior of stress-induced defects even though the stresses are well within the nominal elastic range. Brown [78B5, 79B1] is developing a model whereby stress-induced, high-speed dislocation motion causes high local concentrations of charged vacancies whose diffusion under high electric fields and stress gradients leads to internal flaws and local breakdown. In lithium niobate and aluminum oxide the extent of the breakdown appears to be strongly influenced by strains that develop during growth of the crystal [77G6, 68G5]. In the vicinity of the threshold stress, dielectric relaxation associated with defects may have a significant effect on current observed in the short interval preceding breakdown (see section 4.7).

The effect of shock-induced conduction is less distinct in ferroelectrics than in piezoelectrics but is nevertheless apparent from a number of studies (see table 4.3 and Novitskii [79N3]). Differences in conduction with sample polarity, such as are seen in quartz but of opposite sign, are observed in ferroelectrics (see, e.g., Cutchen [66C1] and Mineev and Ivanov [76M4]).

Resistance measurements on solids undergoing shock-induced insulator-to-metal transitions are of considerable interest and such a transition has been identified from Hugoniot measurements and equation-of-state calculations in iodine [77M1]. Unfortunately, such resistance measurements as have been performed on solids have not yielded any explicit information on the transitions (see the summary of Duvall and Graham [77D6]).

4.7. Dielectric relaxation

In the various electrical response models discussed in the foregoing section of this review, permittivities have been regarded as stress, strain or electric field dependent but not subject to relaxation. Dielectric relaxation or "AC conductivity" is a well-known phenomenon at atmospheric pressure (see, e.g., Daniel [67D1]). Lysne has recently developed models for dielectric relaxation in the thick sample configuration for piezoelectrics [78L3, 78L4, 78L7], ferroelectrics [79L1], and normal dielectrics [78L3, 78L4, 78L7], subjected to dynamic loads [78L7]. These models demonstrate that if dielectric relaxation times are greater than 10^{-9} s and less than 10^{-5} s and if relaxed and instantaneous permittivities differ by more than a few per cent, dielectric relaxation may play a significant role in determining observed electrical response, and may easily be confused with shock-induced conduction. Lysne's work suggests the need for a major reexamination of the interpretation of relaxation effects – polarization, dielectric and conduction – in shock-loaded dielectrics.

Prior considerations of dielectric relaxation are reported by Hauver [70H2] in a private communication from M.H. Rice and on samples in a thin-sample configuration by Yakushev [78Y1].

In Lysne's theories the dielectric polarization is modeled by a Debye relaxation function, which implies an exponential relaxation between the instantaneous permittivity, ε_∞, and the relaxed permittivity, ε, when the field is held constant. The dielectric relaxation time, τ, is a critical parameter characteristic of the material. Lysne's expressions for current pulses require numerical evaluation.

Even though a phenomenological theory of dielectric relaxation may be applied to shock-compression problems, it is not readily apparent what physical effects give rise to significant differences between instantaneous and relaxed permittivities and relaxation times of the order of 10^{-7} s. Most of the solids under consideration do not exhibit relaxation effects in the times appropriate for a shock experiment and on the basis of our atmospheric-pressure or static-high-pressure experience would not be expected to show such effects. Nevertheless, prior sections of this review have demonstrated that shock-compressed solids are subject to localized mechanical and thermal heterogeneities, to phase transitions in which multiple phases may coexist, to local electrical conduction, and to local defect complexes. All of these features of the shock-deformed state evolve on approximately the time scale necessary to explain the observed relaxations. Based on the work of Sillars [37S1], which gives dielectric relaxation parameters for localized dielectric and conductive regions in a dielectric host, Lysne has shown [78L6] that significant relaxation effects are possible. According to Sillars' theory, the effects are highly dependent on shape of the defect.

The possibility of dielectric relaxation phenomena in shock-loaded dielectrics greatly complicates interpretation of electrical responses. Because localized shock-induced defects are known not to be in thermodynamic equilibrium (e.g., see the effects shown in section 4.5), relaxations may be controlled by thermal relaxation of local defects. Questions concerning statistical methods to relate the localized behavior to the continuum level are significant. In composites, viscoelastic and viscoplastic materials, observations such as those on PMMA and alumina-loaded epoxy [78L4], may be the result of mechanical relaxations. Although it will not be easy to interpret real or apparent dielectric relaxations, it is apparent that such relaxations must be considered and since the relaxations are dependent on defects, measurements of dielectric relaxation may provide a new means of investigating these defects.

4.8. Shock demagnetization

Just as the terms *shock-induced polarization* and *shock-induced conduction* describe a number of different physical effects, "shock demagnetization" is a general term that describes changes in ferromagnetic or ferrimagnetic states of shock-loaded samples due to a variety of physical effects. Unlike many conduction and shock-induced polarization effects that are unique to shock loading, dominant effects in shock demagnetization appear to be well described by physical mechanisms encountered in more conventional environments, viz.: (1) second-order pressure-induced phase transitions, (2) first-order polymorphic phase transitions, and (3) stress-induced magnetic anisotropy.

Much of the literature on this subject was reviewed by Royce [71R3] and first- and second-order transitions involving magnetization changes were reviewed by Duvall and Graham [77D6]. This review adds previously unpublished data on several materials.

The first work in this area was carried out by Neilson and coworkers [57A1, 58K1], and was interpreted with the assumption that the pressure and temperature in the shock-compressed material was sufficient to induce a Curie-point transition. Such an interpretation has not provided an explanation for many subsequent observations, however, and persistent studies have been necessary to identify the physical mechanisms and to measure appropriate material properties.

The ideal magnetic sample configuration is not compatible with planar shock loading and this incompatibility severely restricts shock-loading studies. When metallic materials are to be studied, they must be laminated with insulating films to form a sample in which eddy currents are not significant. The composite nature of such a sample introduces uncertainties into the determination of its thermomechanical state under shock compression. As shown in fig. 4.7, four experimental

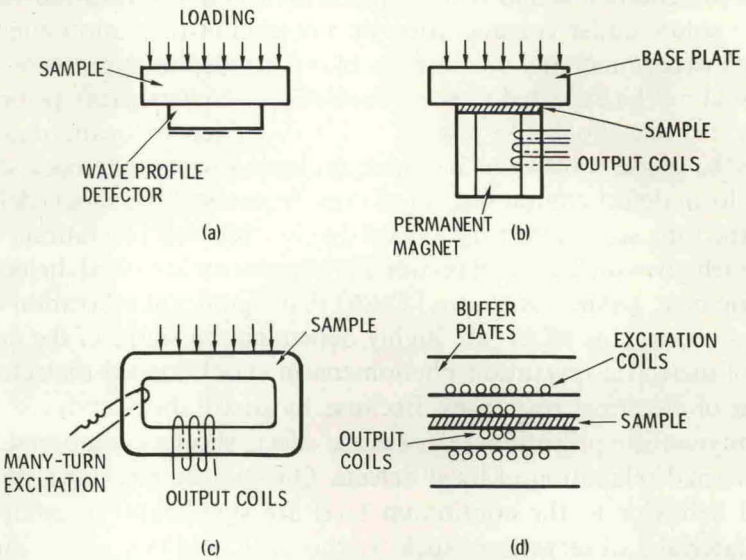

Fig. 4.7. A variety of different techniques are used to observe shock demagnetization. In (a), wave profile measurements are used to determine stress-volume relations in pressure-sensitive ferromagnetic solids [61C1, 66G1]. In (b), a uniaxial, thin-sample configuration is used for absolute demagnetization measurements. If the sample is conductive, the thickness is minimized and it is placed between Al_2O_3 plates to minimize eddy currents [71R3]. In (c), a thick-sample, two-dimensional configuration is obtained by using conventional tapewound magnetic "cores" to minimize eddy currents. This configuration does not give absolute measurements [58K1, 68G3]. In (d), the sample is enclosed by both excitation and pick-up coils. Since the coils are subjected to the loading, the technique is principally useful at low stresses [72G1].

configurations have been used for shock-demagnetization measurements. Novikov and Mineev [74N3] have used a configuration similar to Royce's (4.7b), with a thick-sample variant calibrated by static compression of iron powder mixed with organic encapsulants. Kiselev [75K1] has extended Grady's technique (fig. 4.7d) to a pressure of 33 GPa by placing the entire assembly in an impedance-matching tungsten-paraffin mixture and using an external electromagnet for excitation. Wayne [69W1] has improved upon the analysis of data from the laminated core configuration (fig. 4.7c) by static calibration studies.

A summary of shock-demagnetization investigations is shown in table 4.6. An overall perspective of the effect of pressure on magnetization can be obtained by considering the comprehensive static-high-pressure studies of the pressure derivatives of magnetization in the iron–nickel alloy system. These studies, which are summarized in fig. 29 of the review by Duvall and Graham [77D6], show that alloys having nickel concentrations less than about 28 atomic per cent are stable in the bcc phase and their magnetizations are not sensitive to pressure. When nickel concentration exceeds about 28 atomic per cent, the alloys are stable in the fcc phase but only in the composition range of 28 to 40 atomic per cent nickel are the magnetizations sensitive to pressure. Thus, we expect Curie-point transitions in the fcc alloys at pressure less than, say, 40 GPa in only a limited number of alloys. In the bcc ferromagnetic iron alloys the well-known shock-induced bcc → hcp ($\alpha \rightarrow \varepsilon$) transition is well characterized and this transition would be expected to dominate the behavior of these materials. A summary of these first-order polymorphic phase transitions is given by Duvall and Graham [77D6].

Table 4.6
Observations of shock-induced demagnetization

Materials[a]	Authors	Method[b]
Second-order phase transitions (fcc iron alloys)		
35% Ni 65% Fe (Invar)	Curran [61C1]	I
35% Ni 65% Fe (Invar)	Graham [68G3]	III
35% Ni 65% Fe (Invar)	Clator and Rose [67C3]	III
28.4% Ni 71.6% Fe	Graham et al. [67G2]	I
28.4% Ni 71.6% Fe	Wayne [69W1]	III
$Fe_{0.65}(Ni_{0.94}CO_{0.06})_{0.35}$	Edwards [78E1]	III
$Fe_{0.65}(Ni_{0.92}CO_{0.08})_{0.35}$	Edwards [78E1]	III
49% Ni 51% Fe (Deltamax)	present work	III
First-order phase transitions (bcc iron alloys)		
Iron	Royce [68R4, 71R3]	II
Iron	Wong [69W2]	—
6.3% Si 93.7% Fe (Silectron)	Graham [68G3]	III
6.3% Si 93.7% Fe	Kiselev [75K3]	IV
28.4% Ni 71.6% Fe	present work	III
10% Mn 90% Fe	present work	III
Iron powder/bakelite mixture	Novikov and Mineev [74N3]	II
Stress-induced magnetic anisotropy		
Nickel ferrite	Royce [66R2]	II
Yttrium iron garnet, polycrystalline	Shaner and Royce [68S1]	II
Yttrium iron garnet, polycrystalline	Grady et al. [72G1]	IV
Nickel ferrite	Seay et al. [67S1]	III
48% Co 50% Fe 2 V (Supermendur)	present work	III

[a] Compositions are by atomic fraction or per cent.
[b] Methods refer to fig. 4.7. I is 4.7(a); II is 4.7(b); III is 4.7(c); IV is 4.7(d).

Except for a pronounced nonlinearity at low stresses, magnetization is observed to change smoothly with pressure in fcc alloys. An apparent non-linearity for small magnetizations is probably an artifact related to the sample configuration or the weak magnetic fields employed. In any event, as shown in table 4.7, the pressure derivatives obtained from steeply-rising regions of magnetization versus pressure data are in agreement with static measurements to about 10 per cent.

Table 4.7
Pressure derivatives of magnetization and Curie temperatures (compression is taken as positive)

Material	Static pressure	Shock compression	Reference
$\partial \ln M_s/\partial p$	% GPa^{-1}	% GPa^{-1}	
31.4% Ni 68.6% Fe	−32 to −37	−28 to −33	Wayne [69W1]
35% Ni 65% Fe	−14	−13	See Graham [68G3]
$Fe_{0.65}(Ni_{0.94}Co_{0.06})_{0.35}$	—	−13	Edwards [78E1]
$Fe_{0.65}(Ni_{0.92}Co_{0.08})_{0.35}$	—	−14	Edwards [78E1]
dT_c/dp	K GPa^{-1}	K GPa^{-1}	
28.4% Ni 61.6% Fe	−32 to −57	−58	See Graham et al. [67G2]
35% Ni 65% Fe	−34	—	Edwards and Bartel [74E1]
$Fe_{0.65}(Ni_{0.94}Co_{0.06})_{0.35}$	−39	—	Edwards and Bartel [74E1]
$Fe_{0.65}(Ni_{0.92}Co_{0.08})_{0.35}$	−41	—	Edwards and Bartel [74E1]

Shock-demagnetization measurements on alloys which undergo first-order polymorphic phase transitions show features quite different from those on fcc alloys. In this case, multiple waves propagate in the sample and their interaction after the reflection of the leading wave prevents the entire sample from being demagnetized. As a result, maximum output current is achieved only in pressure ranges in which the first wave is overdriven. Magnetization measurements reported for Silectron [68G3] were analyzed to account for that effect. The pressure of 40 GPa reported by Novikov and Mineev [74N3] to achieve maximum signal from shock-loaded iron composites apparently corresponds to the overdrive pressure. Kiselev's report of incomplete demagnetization of iron at 33 GPa may involve multiple wave effects due to imperfect impedance matching [75K1].

The pressures at which substantial shock demagnetization occurs indicates onset of transitions 14.5 GPa for the 6.3 per cent silicon alloy and 6.5 ± 0.5 GPa for the 28.4 atomic per cent nickel-iron alloy, which are in good agreement with independent determinations from wave profiles [63Z1, 70R1]. Sketchy data on a bcc 10 per cent Mn–Fe alloy indicate substantial demagnetization to have occurred at pressures from 12 to 27 GPa [78G1].

The picture that has emerged from investigations of shock demagnetization due to first- and second-order transitions is one in which response to shock loading corresponds well with static-high-pressure studies of pressure dependencies of magnetization or Curie temperature and with pressure-volume determinations of polymorphic first-order phase transitions under shock loading. Since the fcc iron alloys do not exhibit polymorphic phase transitions, shock demagnetization of most of these alloys is limited to Curie-point transitions occurring behind strong shocks.

Changes in magnetization and Curie temperature considered above are a manifestation of *volume* magnetostriction and are largely independent of shear stress. Materials with large *linear* (i.e., uniaxial) magnetostrictive constants exhibit an inverse effect called "stress-induced magnetic anisotropy" in which the magnetic behavior is determined by the magnitude and sign of the shear

stress and the magnitude of the applied magnetic field. In this phenomenon deviatoric strains cause changes in the atomic crystal fields which determine the magnetic anisotropy and the competition between applied magnetic field and stress-induced magnetic anisotropy. A sufficient change in magnetic anisotropy may lead to a rotation of the equilibrium magnetization direction, which is perceived as "demagnetization" by a detector aligned to sense magnetization in the direction of the applied field.

Royce first tentatively proposed that anomalous shock demagnetization observed for a nickel ferrite ceramic was the result of stress-induced magnetic anisotropy [66R2]. Subsequent work on an yttrium–iron–garnet ceramic (YIG), a ferrite with lower magnetostrictive constants, by Shaner and Royce [68S1] confirmed that stress-induced magnetic anisotropy was the dominant operative mechanism in these materials even though anomalies were noted in the high-pressure behavior. Further evidence for apparent demagnetization by this mechanism was obtained on a nickel ferrite by Seay et al. [67S1]. Wayne et al. [70W1] reported "anomalous" hydrostatic-pressure-induced magnetic anisotropy in polycrystalline nickel ferrite and YIG which was found to arise from localized shear resulting from porosity of the samples.

Since stress-induced magnetic anisotropy is an elastic shear phenomenon, detailed studies are best conducted within the elastic range. Grady [72G1] has performed a careful and detailed experimental and theoretical study of the same YIG material utilized by Shaner and Royce [68S1]. Grady considered calculation of polycrystalline magnetoelastic constants from single crystal constants with both a traditional interacting crystallite assumption and an independent crystallite assumption.

The results of Grady's detailed experimental investigation of YIG within the elastic limit [72G1] with the method of fig. 4.7d is shown in fig. 4.8. The observed demagnetizations are quantitatively modeled by the independent grain assumption and clearly show that stress-induced magnetic anisotropy is responsible for the shock demagnetization.

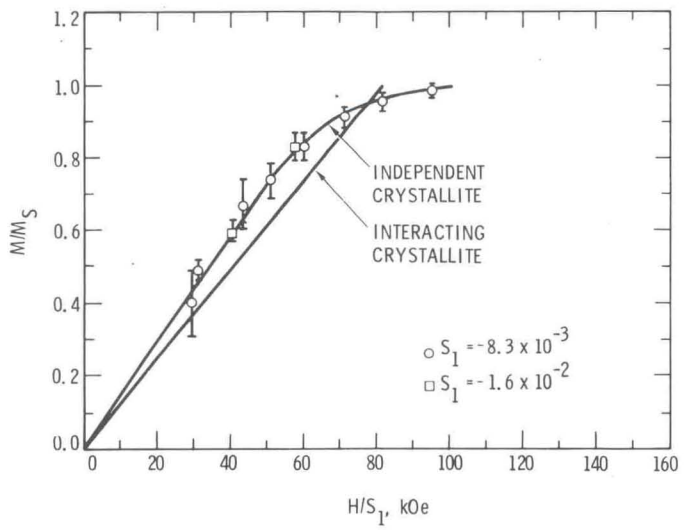

Fig. 4.8. Rotation of the magnetization direction in YIG ceramic samples causes an apparent demagnetization due to stress-induced magnetic anisotropy. Unlike shock demagnetization due to first- and second-order phase transitions, the effect is caused by elastic shear stress. The measured shock data of Grady [72G1] are all within the elastic range and are compared to his calculations with two different methods of computing the polycrystalline behavior from single crystal data.

The high-pressure measurements of Shaner and Royce still remain anomalous. Royce [71R3] proposed that their results could be explained by pressure-sensitive magnetoelastic constants such that $\mathrm{d} \ln B/\mathrm{d}V \approx 5.9$ per cent for each 1 per cent compression. Grady's measurements show no such effect. Heterogeneous yielding could conceivably affect the high-pressure behavior of YIG. Further studies are needed to resolve this anomaly.

Measurements on Supermendur, an iron–cobalt–vanadium alloy (see table 4.6) also indicate an anomalous behavior. Even though the material has a negative magnetostrictive constant and will not exhibit shock-induced demagnetization due to stress-induced magnetic anisotropy under uniaxial strain, a large demagnetization is observed with a sharp knee within the elastic range in the demagnetization versus stress behavior. This large effect has been identified as the result of lateral unloading waves which change the state of stress sufficiently to cause large rotations of magnetizations.

Studies to date indicate that the dominant features of shock demagnetization involving Curie point or polymorphic transitions can be treated by the compressible fluid approximation. Stress-induced magnetic anisotropy, which is inherently a shear phenomenon, is reasonably predicted by magnetoelastic constants.

4.9. Semiconductors

Electrical properties of semiconductors are sensitive to changes in energy band structure and impurities. Hence, it is possible to use fairly simple probes such as sample resistance or self-generated emf measurements or more sophisticated probes such as Hall voltage measurements to obtain reasonably direct information on fundamental properties. Static-high-pressure [63P1] and uniaxial stress [69S2, 60K1, 74B2] have proven to be effective in such studies since both the energy gap and relative level of critical points on the band structure can be changed with isotropic and anisotropic strain. Degeneracies in band structure can also be removed with application of anisotropic strain. Knowledge of such stress effects is essential for interpreting undesirable effects of stress on semi-conductor junction devices [68B4].

Unfortunately, the sensitivity of electrical properties to lattice defects makes it unlikely that measurements above the Hugoniot elastic limit will be subject to straightforward interpretation since inelastic deformation generates copious quantities of defects of essentially unknown character. Such has proven to be the case for resistance measurements above the HEL in germanium [66G1] and silicon [72C4]. Nevertheless, the large Hugoniot elastic limits of both germanium [72G5] and silicon [71G6] permit purely elastic strains of a few per cent to be applied to samples whose electrical properties are being studied.

The various investigations of shock-induced emf generation in semiconductors have been reviewed by Mineev and Ivanov [76M4] and Murri [74M3]. Emf measurements above the HEL in germanium [66G1, 70J2] and silicon [72C4, 71M4] show complex behavior of uncertain physical origin. The various investigations are summarized and reviewed by Mineev and Ivanov [76M4]. Kennedy [69K2] has performed a number of elastic shock-loading experiments on germanium with various carrier signs and concentrations. The results showed no obvious systematic behavior but signals of tenths of volts were routinely observed.

Kennedy and Benedick [67K2, 68K3] were successful in carrying out difficult Hall effect measurements in germanium samples explosively loaded at the upper end of the elastic range. The measurements did not provide sufficient information to develop a physical interpretation.

Even the relatively simple resistance measurements under elastic shock loading cannot be confidently interpreted from shock-compression data alone; it is necessary to call upon related atmospheric and elevated pressure studies. Fortunately, a well-founded picture is available for germanium [64P1] in which theory and experiment have been well reconciled. Depending upon the strain magnitude, the electrical conductivity of germanium under [111] and [100] uniaxial strain is dominated by either anisotropic-strain-induced electron population transfer, anisotropic-strain-induced splitting of the valence band maximum, or strain-induced shifts in energy gap. Uniaxial [111] strain greatly simplifies the conduction band in that sufficiently large strains convert the multivalley conduction band to a single valley conduction band. On the other hand, the valence band becomes more complicated as the degeneracy of the maximum is lifted and energy levels are split. The properties of holes in such a strained configuration present the largest uncertainty.

To plan and fully analyze experimental studies of the effect of adiabatic elastic strain on the electrical conductivity of germanium, C.L. Julian (formerly of this Laboratory) has developed a computer code, "Santa Fe", whose main subroutine, "Chili", calculates conductivity and related diagnostic parameters for [111] and [100] uniaxial strains, uniaxial stresses and hydrostatic pressure. Sources for the theory and data incorporated in the code are summarized in table 4.8.

Table 4.8
Reference sources for strain-dependent conductivity analysis incorporated in Julian's Santa Fe computer code*

Parameter	Author	Reference
General reference, **germanium	Paige	[64P1]
Population transfer model	Herring; Keyes	[55H1]; [60K1]
$np\,(0, T)$	Morin and Maita; Prince	[54M1]; [53P1]
M_n	Paige	[64P1]
$\mu_n\,(S, T)$	Schetzina and McKelvey	[69S2]
$M_p\,(S, T)$	Julian and Lane	[73J3]
$\mu_p\,(S, T)$	Asche et al.	[66A4]
$(\Xi_d + \frac{1}{3}\Xi_u + a) = -4.03$ eV	Paul; Paul and Brooks	[63P1]; [63P3]
b, d	Pollak and Cardona	[68P2]

* Notation: M_n and M_p represent the effective masses of electrons and holes, respectively. The term $(\Xi_d + \frac{1}{3}\Xi_u + a)$ is the change in energy gap with strain for the [111] valley minimum. Ξ_d is the deformation potential for dilation, Ξ_u is the deformation potential for shear and a is the deformation potential for the valence band maximum under hydrostatic pressure, b and d are shear deformation potentials for the valence band maximum for (100) and (111) shear strains, respectively.

** See also the more general work on strain dependencies by Bir and Pikus [74B2].

As is customary, the conductivity is described by independent transport of electrons and holes such that

$$\sigma = ne\mu_n + pe\mu_p, \tag{4.25}$$

where σ is the conductivity, n and p are the numbers of electrons and holes, respectively, μ_n and μ_p are mobilities of electrons and holes, respectively, and e is the electronic charge. If the sample

contains ionized impurities denoted $N_A - N_D$, where N_A is the number of acceptor ions and N_D is the number of donor ions, the *np* product is

$$np = n^2 - (N_A - N_D)n. \tag{4.26}$$

The *np* product at a strain, S_1, and temperature, θ, $np(S_1, \theta)$ of interest can be shown to be

$$np(S_1, \theta)/np(0, \theta) = R_n R_p \exp(-\Delta E_g/k\theta), \tag{4.27}$$

where R_n and R_p are the ratios of density of states effective masses to the 3/2 power of the unstrained to strained electrons and holes, respectively, ΔE_g is the change in energy gap and k is Boltzmann's constant.

Once values for R_n, R_p and ΔE_g are calculated at a given strain, the *np* product is extracted and individual values for n and p are determined from eq. (4.26). The conductivity can then be calculated from eq. (4.25) after the mobilities are calculated. The hole mobility is the principal uncertainty since it has only been measured at small strains. In order to fit data obtained from elastic shock-loading experiments, a hole-mobility cut-off ratio is used as a parameter along with an unknown shear deformation potential. A best fit is then determined from the data for the cut-off ratio and the deformation potential.

The effect of [111] uniaxial strain on conductivity is illustrated in fig. 4.9 by the calculated solid line for which the Santa Fe Code incorporated the parameters shown. (The datum points are to be described later.) At low strain the conductivity change is dominated by changes in electron

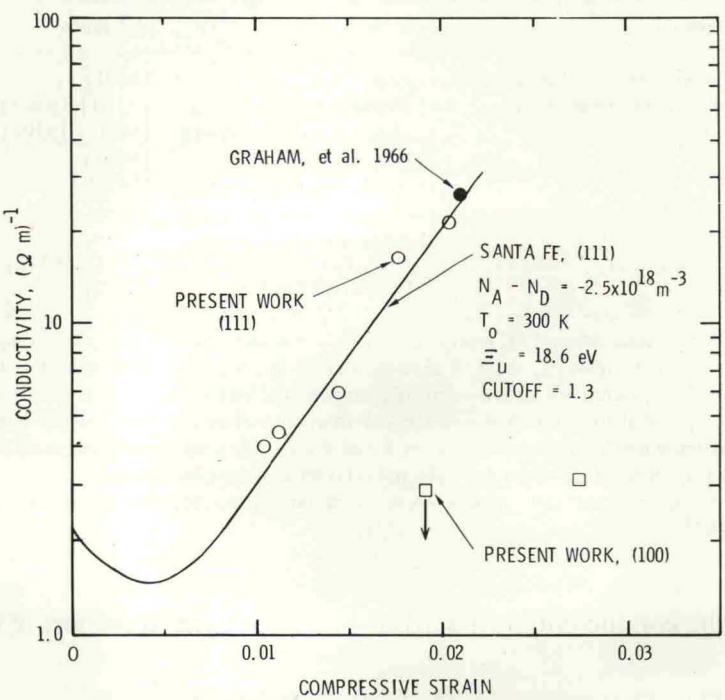

Fig. 4.9. The conductivity of uniaxially-compressed germanium is strongly influenced by changes in energy gap as well as strain-induced changes in mobilities and effective masses. The solid line is calculated with the computer code Santa Fe using impurity carrier concentrations, shear deformation potentials and a hole mobility cut-off ratio chosen to represent the present data. The cut-off affects the location of the minimum while the deformation potential controls the slope at large strain.

mobility accompanying the electron transfer to a single (111) valley; this represents the classic piezoresistive effect for n-type germanium. Above some critical strain the electrons are completely transferred to a single (111) valley and the conductivity is dominated by the decrease in energy gap with compressive strain. Such a complete transfer of electrons to a single valley has been observed by Schetzina and McKelvey [69S2] in uniaxial stress experiments.

There are two experimental investigations of resistivity of germanium under elastic shock compression. The work of Graham et al. [66G1] interpreted limited measurements on [111] Ge on the basis of intrinsic semiconduction without attempting to account for strain-induced changes in mobilities and effective masses. On that basis, the shear deformation potential was found to be about a factor of two too small. In more recent, heretofore unpublished, work Graham and Julian conducted a very similar but more detailed and carefully executed study of [111] and [100] Ge which was fully integrated with code calculations to both plan and interpret experiments.

An extensive program to characterize conventional electrical properties of the samples at atmospheric pressure was carried out by J.D. Kennedy and R.D. Jacobson of this Laboratory. Since each experiment required three crystals (one sample, one impactor and one impedance-matching disk) it was possible to select sample crystals with the best-behaved electrical properties from among a large group of crystals which were nominally all characterized by the supplier as high-purity, n-type. Preshot characterization included four-probe (Van der Pauwe) conductivity and Hall effect measurements from 220 to 300 K which were used to determine the impurity concentrations. Julian's computer code, "Sparrow", incorporated theory and experimental data from prior germanium studies [64P1] to interpret the low temperature results and arrive at the impurity concentrations. Other preshot characterizations included measurements of photo-conductivity and two-probe resistivity measurements at currents from one-fourth to 1 amp. The final sample characterization is performed 500 ns prior to impact loading when the one amp current is pulsed on for the few microseconds of the shock loading.

The [111] orientation samples were found to be n-type with impurity carrier concentrations of from 2.5 to 8 $\times$ 10^{18} m^{-3}. The [100] samples had carrier concentrations of 14 and 18 $\times$ 10^{18} m^{-3}. Calculations with the Sante Fe Code indicated that final conductivities would not be significantly influenced by the observed range of carrier concentrations.

The shock-loading experiment of the work above was as described by Graham et al. [66G1] except that crystals 38 mm in diameter by 4 mm thick were used. A single shock-induced emf measurement at a strain of 2.8 per cent showed a signal of 15 mV, which is negligibly small compared to the several volt resistance measurement.

The data obtained from the resistance measurements are shown in fig. 4.9. The assigned values of conductivity are limited in accuracy because the measured resistance was found to be somewhat time dependent. The [100] datum at the lowest strain was particularly so and a definite resistance value cannot be assigned to that point.

The shear deformation potential for the (111) and (100) valley minima determined by fits to the data of fig. 4.9 are shown in table 4.9 and compared to prior theoretical calculations and experimental observations. The deformation potential of the (111) valley has been extensively investigated and the present value compares favorably to prior work. The error assigned recognizes the uncertainty in final resistivity due to observed time dependence. The distinguishing characteristic of the present value is that it is measured at a considerably larger strain than has heretofore been possible. Unfortunately, the present data are too limited to address the question of nonlinearities in the deformation potentials [77T2].

Table 4.9
Shear deformation potentials

Author	Theoretical/Experimental	$\Xi_u(111)$ eV	$\Xi_u(100)$ eV
Goroff and Kleinman [63G1]	Theoretical (Silicon)	17.3	9.6
Saravia and Brust [69S2]	Theoretical	14.0	7.3
Melz [70M3]	Theoretical (Silicon)	—	7.5
Present work	Experimental	19 ± 2	8.3 ± 1
Schetzina and McKelvey [69S2]	Experimental	16.3 ± 0.3	—
Bulthius [68B4]	Experimental	19.5	—
Balslev [66B1]	Experimental	16.2 ± 0.4	9.2 ± 0.3 (Silicon)
Riskaer [66R1]	Experimental	18.0 ± 0.5	8.5 ± 0.5 (Silicon)
Balslev [65B1]	Experimental	—	8.5 ± 0.2 (Silicon)
Dakhovskii [64D1]	Experimental	16.5	—
Schmidt-Tiedemann [62S1]	Experimental	18.9 ± 1.7	11.3 ± 1.3 (Silicon)
Fritzsche [59F1]	Experimental	19.2 ± 0.4	—

Although the [100] data are quite limited, the shear deformation potential determined is the only measurement for this valley in germanium. At atmospheric pressure and small strains the (100) valley minimum is well above the (111) valley minima and not accessible for measurement. In the present uniaxial strain experiment the (100) valley becomes the minimum point on the conduction band. The observed value agrees well with theoretical calculations on silicon.

The data indicate that elastic shock-compression resistance measurements can provide data on the effects of strain on energy gaps and deformation potentials in semiconductors. Drift mobility measurements on holes in germanium and resistivity measurements on samples with different dopings would appear to be of considerable interest.

4.10. Conductivity of metals

Resistance measurements of hydrostatically compressed metals have provided simple and effective means for detecting the onset of polymorphic phase transitions, for studying electronic properties and for gauging hydrostatic pressures. Similar problems are of interest in shock-compression investigations. The first such studies were reported by Fuller and Price [62F1] on iron shortly after similar static-high-pressure measurements by Balchan and Drickamer [61B1]. The shock measurements showed evidence for a resistance change associated with the $\alpha \rightarrow \varepsilon$ phase transition. Since this early demonstration of the capabilities of resistance measurements, progress toward perfecting methods for quantitative study and analysis has been slow. Upon first examination, most metals show well-defined, approximately linear changes of resistance with shock pressure. Nevertheless, closer examination of theory and experiment has invariably revealed considerable underlying complexity. In spite of the difficulties, the capabilities for studying resistivity of shock-compressed metals have now been well demonstrated in a recent detailed investigation of silver by Dick and Styris [75D1].

The literature on resistance changes in shock-loaded metals has been reviewed by Styris and Duvall [70S3], to a lesser extent by Keeler [71K2], and methods and summary of results on a number of metals reviewed by Murri et al. [74M3]. Experimental methods are reviewed by Yakushev [78Y1]. The extensive literature on Manganin has been reviewed by Murri et al. [74M3]

and Graham and Asay [78G5]. A contemporary summary of studies on other materials is given in table 4.10.

Table 4.10
Investigations of resistance of shock-loaded metals

Metal	Authors	Stress range, GPa	Remarks
Iron	Fuller and Price [62F1]	6 to 37	polymorphic transition
Iron	Wong et al. [68W4]	2 to 18	polymorphic transition
Iron	Royce [68R4], [71R3]		demagnetization currents
Iron	Keeler and Mitchell [69K1]	5 to 37	polymorphic transition
Iron	Keeler [71K2]	5 to 150	very high pressure
Nickel	Wong et al. [68W4]	2 to 14	smooth changes
Copper	Keeler [71K2]	4 to 140	discontinuity at < 140 GPa
Ytterbium	Ginsberg et al. [73G3]	0.1 to 3.3	polymorphic transition, 3.3 GPa
Ytterbium	Murri et al. [74M3]	0.4 to 2.1	
Ytterbium	Grady and Ginsberg [77G3]	0.1 to 0.6	piezoresistive
Ytterbium	Pavlovskii [77P1]	2 to 22	polymorphic transition, 2–3 GPa
Carbon	Horning and Isbel [75H1]	0.4 to 3.4	highly nonlinear behavior
Carbon	Murri et al. [74M3]	0.4 to 1.5	—
Calcium	Murri et al. [74M3]	0.4 to 2.7	—
Lithium	Murri et al. [74M3]	0.4 to 5.4	—
Cadmium	Murri et al. [74M3]	0.4 to 2.8	—
Indium	Murri et al. [74M3]	0.4 to 1.5	—
Lead	Murri et al. [74M3]	1.5 to 1.9	—
Bismuth	Murri et al. [74M3]	1.0 to 1.9	—
Manganin	Fuller and Price [62F1]	6 to 30	first measurements
Manganin	Bernstein and Keough [64B2]	2.4 to 18	
Manganin	Keough and Wong [70K1]	0.6 to 16	various insulators
Manganin	Barsis et al. [70B3]	0.2 to 9	piezoresistive analysis
Manganin	Kanel' et al. [78K2]	2 to 27	residual upon unloading
(For a more complete summary of the various studies on Manganin, see Graham and Asay [78G5] and Murri et al. [74M3].)			
Silver	Dick and Styris [75D1]	2.5 to 12	detailed study

Although the only detailed study is that of Dick and Styris, several general conclusions can be drawn from various other measurements. There is abundant evidence that shock-induced changes in resistance are sensitive to specimen configuration, especially to the host material in which the metallic wire or foil is placed to provide electrical insulation or an approximate mechanical impedance match. This sensitivity apparently results from localized plastic deformation not characteristic of bulk material. The configurational effects can be minimized by careful attention to surface finish, configuration of the metal sample and assembly procedures. Integrity of electrical connections remains a significant consideration but reliable experiments have been reported as high as 140 GPa in copper and iron [71K2].

Following the early observations by Fuller and Price [62F1], a number of investigators measured shock-induced resistance changes in iron (see table 4.10). There is no detailed analysis of these measurements but observed resistances below the transition (corrected for thermal contributions) are substantially different in magnitude and their pressure derivatives are of opposite sign to the

static-high-pressure measurements of Balchan and Drickamer [61B1]. Wong et al. [68W4] have interpreted subtle variations in resistance measurements in the vicinity of 7.5 GPa as evidence for a partial transformation below the established 13 GPa transition but, within a reasonable experimental precision, their data can be equally well fit by a continuous change. This later study shows a sharp change in resistance indicative of a phase transition beginning at 12.5 GPa.

The most complete and systematic study has been performed on silver foil by Dick and Styris [75D1] and the results of their investigation are summarized in fig. 4.10. Shock-compression measurements on silver of two different purities are shown by the upper experimental points. Subtraction of the calculated change in resistivity due to shock heating produces the points which represent the resistivity change due to isothermal shock compression. The difference between the isothermal hydrostatic calculations and the isothermal shock results can be accounted for by the shock-induced generation of large numbers of defects, most likely vacancies. Vacancy concentrations, which under these transient conditions also lead to interstitial concentrations, of about 10^{-3} per lattice site, were found to account for the differences between hydrostatic and isothermal shock-compression resistivities.

In an investigation of ytterbium under shock compression, Grady and Ginsberg [77G3] included active measurements of resistance synchronous with shock decompression. Increases in temperature were negligible at their low stresses (< 1 GPa) and the residual resistance served as

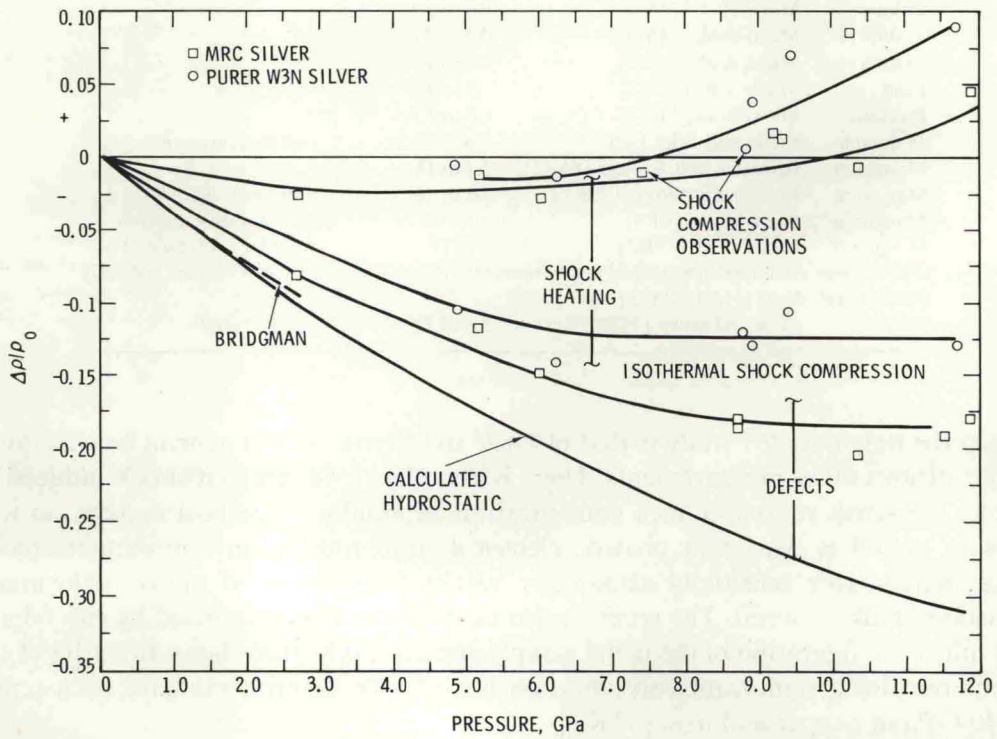

Fig. 4.10. A comprehensive study of silver under shock loading by Dick and Styris [75D1] shows evidence for resistance change due to shock-induced vacancies. The upper group of points are those observed in the shock-loading experiments. The lower group of points results from correcting those data for increases in temperature due to shock heating. The difference between the isothermal shock data and the hydrostatic predictions are evidence for resistivity change due to shock-induced vacancy concentrations of 10^{-3} per lattice site at 10 GPa.

a direct measurement of irreversible effects, most likely attributable to shock-induced defects. Their data, shown in fig. 4.11, indicate that if the defects are not taken into account, poor agreement is observed between their predicted piezoresistive, elastic-plastic model and other observations. Accounting for the observed residual effects brings their results in good agreement with calculations. The synchronous measurement of resistance of the decompressed material adds an additional important diagnostic tool which could be effectively utilized in future studies. Although there are only limited quantitative studies of such residual resistances after Manganin is unloaded [78K2, 79S3], it is recognized that such effects are commonly observed [74M3].

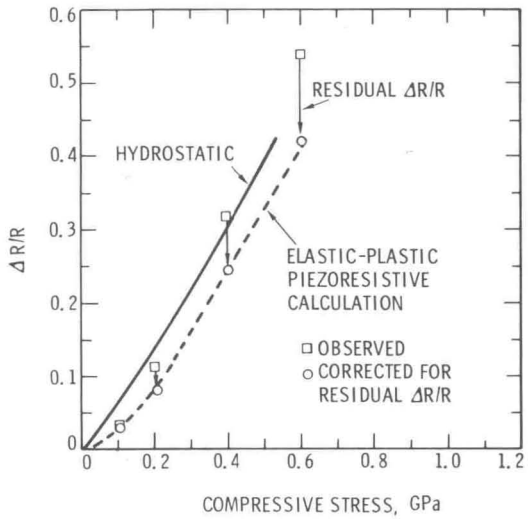

Fig. 4.11. Measurements of resistance change of ytterbium samples subjected to controlled shock compression and decompression show evidence for the change in resistance resulting from shock-induced defects [73G3, 77G3]. When the data describing resistance-change upon loading are corrected for the residual resistance change measured upon decompression, the result is in good agreement with the resistance change computed from elastic-perfectly plastic piezoresistive calculations. The measured resistance change for hydrostatic loading is shown for reference. This investigation provides quantitative data on effects of shock-induced defects on resistivity in the shock-compressed state.

4.11. Thermoelectric junctions

Metallic or semiconductor junctions are of interest for thermoelectric temperature measurements under shock compression. The first measurements of emf values from such junctions were reported by Jacquesson [59J1] in 1959 with a more complete account in 1965 [65C3]. This work and subsequent work by Jacquesson, his coworkers and a number of Soviet scientists showed the existence of emf values twofold or threefold larger than those observed in static-high-pressure studies. After years of experimentation and the development of theories for nonequilibrium electronic effects to account for the anomalously large emf values, it has recently become clear that experimental artifacts are responsible for the anomalously large signals.

Mineev and Ivanov [76M4] have given a summary of experimental observations. Nesterenko [75N2] has summarized and evaluated various theories used to explain the anomaly and pointed out the importance of the interface. Bloomquist and coworkers [78B5, 78B6] have reviewed the

literature and measured signals close to predicted values in experiments with precisely-controlled interfacial conditions.

Buzhinskii and Samylov [70B6] were the first to call attention to dominance of interfacial details in their measurements on ground and polished surfaces and on diffusion-bonded interfaces which showed emf values only about 60 per cent greater than predicted. Furthermore, with good time resolution, they observed emf "flashes" as shock waves crossed interfaces. In careful, detailed optical measurements Urtiew and Grover [74U2] observed high local temperatures at interfaces between transparent and opaque solids. Nesterenko and Staver [74N1] compared emf measurements from polished and slightly roughened interfaces and found that coarse interfaces exhibited emf values about twofold greater than the polished interfaces. Bloomquist [78B5] worked with very carefully prepared diffusion-bonded interfaces with guard rings and measured emf values only about 20 per cent higher than predicted.

Although a significant discrepancy may still exist, it is clear that localized nonequilibrium heating provides the explanation for the anomalous emf values and that the classical thermoelectric effect is the dominant mechanism for the generation of emf at metallic contacts. Given the critical nature of the interface, it remains problematical whether a "perfect" preshock interface can be achieved and if so, whether the localized shock deformation around grains boundaries or other defects will cause significant localized heating. Even though the viability of absolute temperature measurements with metallic contacts is open to question, it should be observed that Mikhailov et al. [76M3] have effectively used thermoelectric measurements to evaluate explosive welding parameters.

The effect of electron heating in most metals is expected to be localized at the shock front, the long electron mean free path and low effective mass in bismuth can lead to electron heating ahead of the shock at low temperatures. Measurements in bismuth at 20 K have shown such an effect [74N2]. Nesterenko and Staver [74N2] show that for most metals at 300 K the electron heating is no more than 10^{-8} m in advance of the shock front.

5. Optical properties

Physical conditions within transparent shock-loaded solids can be effectively probed with optical techniques, yet such work is quite limited. There have been few systematic optical investigations but a variety of measurements have been made and investigators in the Soviet Union have carried out persistent studies on optical properties of alkali halides and fluids at very high pressure. Optical studies up to 1968 are thoroughly reviewed by Kormer [68K5] and limited information is contained in the review by Doran and Linde [66D3]. This information was brought up to date by Murri et al. [74M3]. Because of these reviews, it is sufficient to call attention to important trends and more recent work, particularly refractive index measurements within the elastic range. A summary of measurements and theory of the photoelastic effect are given in the Landölt–Börnstein series [69B1]. Vedam and coworkers have carried out extensive studies of piezooptic effects under static high pressure [66V2, 65V1, 69V1, 76V2] and under uniaxial stress [72S1].

Kormer's review emphasizes investigations at pressures sufficient to produce compression of about 30 to 50 per cent. At these compressions, the samples are subjected to shock heating leading to temperatures ranging from about 500 to 20000 K. Optical measurements summarized include: (1) structure of the shock front. It is found that the optical thickness of the shock is about

10 nm and that it reflects light as a good mirror; (2) refractive index measurements are reported for several alkali halides both below and above anticipated melt conditions and for a number of fluids; (3) absorption coefficients are found to depend strongly on temperature and to be tenfold to hundredfold larger than at room temperature and pressure for several alkali halides; (4) thermal brightness measurements are used to infer melting and equilibrium radiation is observed in some cases; (5) shock-induced luminescence from electrical and other sources is mentioned.

5.1. Index of refraction, photoelasticity

A surprising number of measurements of refractive index on shock-loaded samples have been reported but, except for those reviewed by Kormer [68K5], they are largely uninterpreted. Kormer's measurements involve such large compressions and high temperatures that they are difficult to interpret in the absence of other data. Nevertheless, he found reasonable agreement between his data on the change in index of refraction with shock pressure and static high pressure or conventional piezooptic measurements for LiF, KCl, NaCl, KBr, KI and CsBr. This observation of a linear piezooptic effect to such large compressions is surprising since the effect is thought to be nonlinear [66V3, 67V1] and phase transitions are known to occur in KCl, NaCl and KBr.

The volume and strain dependence of refractive indices [74T2] and low-frequency permittivities have been of interest as indicators of the effect of deformation on electronic polarizabilities. The relative influence of deformation on electronic polarizability, as indicated by index-of-refraction measurements, and on lattice polarizability, as indicated by low-frequency permittivity measurements, is well illustrated by the case of MgO for which the effects of pressure have the same tendencies [66V2]. In the alkali halides index of refraction and low-frequency permittivities have the opposite tendencies with pressure [66V2]. In MgO the decrease in electronic polarizability dominates the change of index of refraction with pressure, whereas the lattice polarizability dominates the change in alkali halides. These considerations make it clear that the change of index of refraction with strain or pressure is too complex to be described by a single simple model. A summary of Mueller's theory in which an empirical factor is used to correct the Lorenz–Lorentz relation for changes in polarizability is given by Vedam and Schmidt [66V2] as is a more general and basic theory by Yamashita and Kurosawa. Samara [75S5] has pointed out the importance of changes in electronic polarizability with pressure.

The collected data on index or refraction obtained at various shock compressions are shown in fig. 5.1. Two types of experiments are available. Those at the largest compression are obtained by Kormer in explosive loading experiments in which states of very high pressure and temperature were achieved but for which the data do not extend to atmospheric pressure conditions. Those data extending continuously from atmospheric pressure are obtained in projectile impact loading experiments. The data of Barker and Hollenbach [70B2] and of Asay and Hayes [75A3] are obtained from velocity interferometer measurements. In compiling the data for fig. 5.1 the relation between index of refraction and the reported changes in fringe frequency is taken from Hardesty [76H1]. The data on sapphire are all well within the elastic range as are those for vitreous silica. Measurements above 6% compression in vitreous silica may be influenced by a possible higher-order phase transition [72G2]. PMMA is viscoelastic to about 7% compression [70B2].

Setchell [79S4] has found that the index of refraction versus strain data for vitreous silica and sapphire can be well fit by a modified Gladstone-Dale relation which incorporates a power law strain dependence. His expression is:

$$\frac{(n-1)}{(n_0-1)} = \frac{v_0}{v}\left[1 - \alpha\left(\frac{v}{v_0} - 1\right)^{\beta}\right], \tag{5.1}$$

where n is the index of the uniaxially-compressed material, n_0 is the initial index of refraction, v_0 the initial specific volume, v the specific volume of the compressed material, and α and β are material constants. For vitreous silica, Setchell found $\alpha = 0.02996$ and $\beta = 0.6571$ and his fit to the data is shown as the solid line on fig. 5.1.

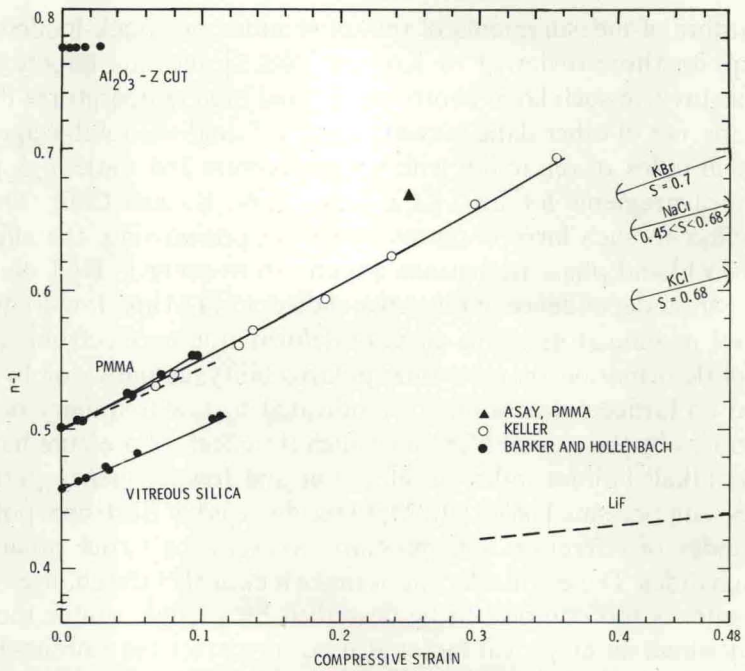

Fig. 5.1. The strain dependence of index of refraction has been investigated under shock loading at relatively small strains (datum points shown) and at large compressions (brackets and dashed lines shown for the right side of the figure). For measurements in the elastic range, the linear relations derived from the shock data are shown by the short dashed lines. The solid lines fit to the sapphire and vitreous silica data are from Setchell's corrected variant of the Gladstone–Dale relation. Most of the large compression data of Kormer [68K5] are off the scale of the figure but the slopes he observed over particular compression ranges are shown within the brackets. The LiF data are from Kormer [68K5]; his data on CsBr are off scale and are not shown. Other data are from Asay and Hayes [75A3], Barker and Hollenbach [70B2], and Keller [68K2].

Setchell [79S4] has also calculated the strain-polarizability coefficient of Mueller [66V2] for both vitreous silica and Z-cut sapphire under uniaxial strain. The resulting functions are found to be distinctly nonlinear. Data on the temperature dependence of the strain-polarizability coefficient can be extracted from elevated temperature measurements of Asay [77A3] at 473 K.

The work of Setchell well demonstrates the capability for studies of strain dependence of polarizability under shock loading which could profitably be carried out in a variety of solids with large Hugoniot elastic limits.

Kormer [68K5] has reported good agreement between his measured coefficients of index of refraction at very high pressures and similar values reported at room temperature and modest

pressure. This is surprising in view of the large temperatures of the shocked materials and the expectation that such phenomena should be nonlinear.

The index-of-refraction measurements of numerous fluids are summarized in fig. 5.2 which follows a similar plot by Kormer with the addition of more recent data by Hardesty [76H1] on nitromethane, by Peterson and Rosenberg [69P2] on gyclerol and ethanol, and by Ahrens and Ruderman [66A3] on hexane and water. For comparison with the data, the Lorenz–Lorentz relations and the Drude relations are shown along with the Gladstone–Dale relation. Also plotted as a dashed line is a temperature-dependent Gladstone–Dale relation which Zel'dovich et al. [61Z1] found to fit the behavior of water to very high compressions. Data on water at compressions of 2 to 20 per cent by Yadav et al. [73Y1] and Zel'dovich et al. [61Z1] are not plotted but they agree with Al'tshuler's values.

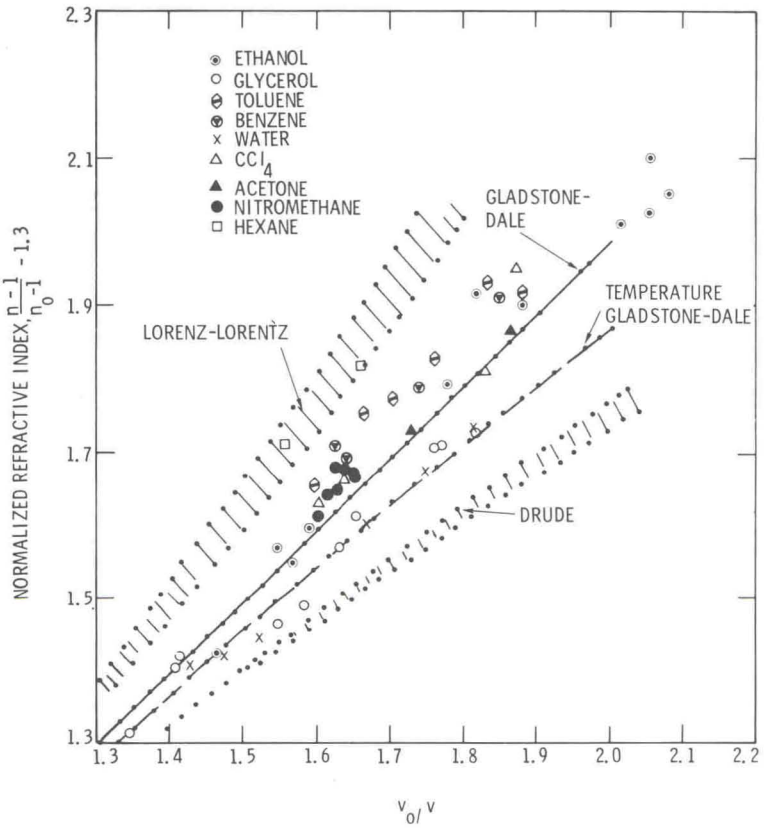

Fig. 5.2. The collected data on index of refraction of shock-loaded fluids give little support to a universal model to describe the effect of compression on refractive index. (After Kormer [68K5].)

The data on hexane seem reasonably well fit by the Lorenz–Lorentz model. Water is well fit by the Gladstone–Dale model at lower compressions [73Y1] and by Zel'dovich's temperature-dependent Gladstone–Dale model at large compressions. Ethanol seems well fit to compressions of 50 per cent by the Gladstone–Dale model. Other fluids do not seem to be particularly well fit by any of the various models, with the Lorenz–Lorentz and Drude models being the least

reasonable. The collected data give little support for the use of a particular model to predict the index of refraction of shock-loaded liquids. Nevertheless, the data may be profitably used to construct empirical relationships.

5.2. Shock-induced luminescence

Luminescence of shock-loaded solids has been observed by a number of different investigators and much of that work is summarized by Doran and Linde [66D3]. The observations can be classified into four different categories: (1) thermal radiation due to homogeneous shock heating; (2) thermal radiation from local electrical discharges; (3) triboluminescence due to fracture; and (4) local effects of imperfections, surfaces, or porosity.

Thermal radiation from transparent shock-loaded solids is thoroughly reviewed by Kormer [68K5]. Measurements of thermal radiation from surfaces of opaque solids are reported by Taylor [63T1], King et al. [68K4], and in considerable detail, by Urtiew and Grover [77U1]. Opaque solids whose temperatures must be measured at surfaces are influenced by the effects of shock interactions at surfaces such as have been reported by Asay [76A4]. Urtiew has minimized this problem with the use of transparent windows for which considerable care must be used to secure a proper interface.

Thermal radiation from intense localized electrical discharges accompanying dielectric breakdown (see section 4.6) is prominent in shock-loaded piezoelectrics and has been studied by Neilson et al. [62N2], Brooks [65B3], and Graham and Halpin [68G4].

Triboluminescence is a loosely defined term relating to observation of luminescence when a solid is fractured. It is difficult to find clear-cut examples but the observations of Brooks [65B3] on shock-loaded vitreous silica show a progressive inward moving luminescence from lateral surfaces which is an effect of this nature.

Luminescence has been observed in shock-loaded porous solids [66D3, 66L2, 62B1, 64B3]. Although it is possible that such luminescence might be due to compression of the trapped gases, Blackburn and Seeley [64B3] have shown that luminescence in porous NaCl did not change between samples shocked in air and those shocked in vacuum. On the other hand, Paterson [64P3] found that the luminescence was influenced by trapped gases.

Luminescence has been observed in shock-loaded porous solids [66D3, 66L2, 62B1, 64B3]. has been reported by Coleburn et al. [65C1] who felt the effect was due to an oxide surface layer. Recent observations of the ejection of small material particles, "fluff", from shock-loaded solids [78A3, 76A4] appear to call for reexamination of such anomalous optical surface effects.

Finally, it should be remarked that localized transient defect production would be expected to cause localized transient thermal effects as would the heterogeneous yielding described in section 3.4.

5.3. Optical absorption

Optical absorption spectra provide a direct probe of electronic properties and measurements under shock loading are of considerable interest. An optical absorption spectrum of ruby between 350 and 700 nm has been measured under shock loading between 15 and 46 GPa by Ahrens and his coworkers [73G1, 79G1]. There is disagreement between the results of the two investigations; the later, more refined, measurement shows a significant nonlinearity in the crystal field parameter

which was not observed in the first work. Both measurements are consistent in the observation of a loss of splitting of the F band above the Hugoniot elastic limit such as would be caused by anisotropic compression. The loss of splitting corresponds to a reduction or loss of shear strength as observed in mechanical measurements (see section 3.4).

Gaffney and Ahrens [73G1] also measured an absorption spectrum for MgO at 46.5 GPa and found it to be featureless. They did find a greater opacity for the shocked material and upon unloading the opacity did not return to its preshock value. No evidence for color centers was found but, as observed by Kormer [68K5], electrons may be in excited states for the duration of the observation time.

The validity of interpretations of optical absorption spectra that neglect shock-induced defect structures is not clear. In particular, it appears that transparent dielectrics would be expected to undergo heterogeneous yielding and leave molten slip bands in the shock-loaded samples. The light beam would then be influenced by having traversed a highly heterogeneous path in addition to influences due to shock-induced defects. In spite of these difficulties in interpretation, the experimental capability seems well developed and persistent efforts should enable such complications to be evaluated.

Urtiew [74U1] has reported a loss of transparency in sapphire between 100 and 130 GPa, Kormer [68K5] reports a loss of transparency in LiF at 70 GPa and Chhabildas and Asay [79C2] have reported a loss of transparency in PMMA between 23 and 25 GPa where a polymorphic transition has been identified [78C2].

Observations of color centers synchronously with shock loading provides direct information on shock-induced defects. A provocative start on such work was reported by Yakusheva et al. [70Y1] who colored NaCl single crystals with ^{60}Co radiation then observed bleaching from yellow to white as shock waves of 3 and 18 GPa were passed through the samples. Such bleaching is thought to be connected with the shock-induced generation of large numbers of electron traps.

5.4. Optical examination of recovered samples

Previous sections of this review have emphasized the importance of shock-induced defects and pointed out that such defects are in transient states. Thus, examination of a shock-loaded sample minutes, hours or days after shock loading would not be expected to reflect defects as they existed at the time of shock loading. Nevertheless, their remanents are revealing and the formation of color centers from shock-induced point defects is of interest. Gager et al. [64G1] found the formation of 10^{14} and 10^{15} F-centers per gram of explosively-loaded MgO. Linde and Doran [66L2] report bleaching of F-centers in NaCl due to shock loading at 1.1 GPa. Additional exposure of shock-loaded crystals to white light and tungsten filament light caused further fast bleaching, broadening and formation of other bands. Such color center observations are promising as probes of shock-induced defects and the limited measurements to date indicate formation of shock-induced vacancies in high concentration.

6. Closing remarks

Shock compression of solids has now been a subject of scientific investigation for some thirty years. During this time the field has expanded from its original concentration on measurement of compressibility to the point where it now encompasses not only the wide ranging subject matter of this review, but also investigations of shock-induced phase transitions, mechanical behavior in both one- and two-dimensional motions, detonation phenomena, and a number of other topics. Great strides have been made in the development of experimental technique and instrumentation. Numerical methods have been devised for solving boundary and initial value problems involving most of the mechanical phenomena under investigation.

Studies of the response of solids to shock compression have led to a number of unique contributions associated with the large compressions and/or high temperatures achieved, the states of uniaxial strain produced, or the extreme rates of deformation encountered. At considerable risk of omission, we note several examples:

1. Discovery of the $\alpha \rightarrow \varepsilon$ phase transformation [55M1] and the $\alpha\gamma\varepsilon$ triple point [62J1] on the phase diagram for ion.
2. Direct synthesis of diamond from graphite [61D1].
3. Acquisition of numerous thermodynamic data at uniquely high compressions [77V1].
4. Calibration of standards for static-high-pressure measurements (see section 3.2.8).
5. Discovery of evidence for electronic transitions at large compression [67R3, 69A2].
6. Observation of an insulator-to-metal transition in iodine by mechanical measurement [77M6].
7. Measurement of physical properties under conditions of large uniaxial elastic strain. Examples include third- and fourth-order elastic constants [72G2, 72G3], second- and third-order piezoelectric constants [72G3, 77G6], shear deformation potentials in germanium (see section 4.9), and strain dependence of optical polarizability [79S4].
8. Investigation of mechanisms of inelastic deformation operative at high strain rate (see sections 3.3–3.7).
9. Observation of growth and decay of shock and acceleration waves [74N4].
10. Observation of shock-induced polarization of normal dielectrics (see section 4.5).

In addition to the specific results just cited, investigations of shock compression have inspired or supported research in a variety of other areas including theoretical determination of the thermodynamic properties of highly compressed matter and continuum-mechanical modeling of the behavior of viscoelastic, viscoplastic, composite, and porous solids at lower stresses. New concepts of fracture mechanics have been developed, new materials have been synthesized, and metallurgical phenomena including those encountered in explosive metalworking have been investigated. Conditions corresponding to those encountered in earth and planetary interiors and as a consequence of meteoritic impact have been reproduced for use in geophysical investigations.

The advent of gun technology has brought the shock-compression experiment from the explosive firing site into the laboratory, and has extended the range of accessible pressures. Recent developments in projectile acceleration and pulsed lasers promise further increase in the pressure attainable in a conventional laboratory environment to values where statistical models of the atom can be shown to be valid. When significant wave structure develops during compression to moderate pressures, or upon decompression, interpretation of experiments can be accomplished only if the relevant part of the stress or particle-velocity history is measured with good time resolution. Such measurements can be done routinely at low stress and have recently been made for pulses having

peak compressive stresses as large as 100 GPa. Unfortunately, the value of such measurements has not been universally recognized and full exploitation of the available methods has yet to be achieved. The development of a true in-situ gauge having time-resolving capability of a few nanoseconds would greatly alleviate the difficulty presently encountered in interpreting wave profiles affected by their interaction with instrumentation or a stress-free surface. Abandonment of the idealized concept of a shock in favor of measurement and interpretation of structured waves opens the possibility of using rapid but continuous loading histories, provided suitable means of producing them are developed.

The problem of measuring the temperature of shock-compressed solids has a long history, but measurements of accuracy sufficient for the development of an equation of state have yet to be made. Such a measurement is of the highest value and any advance in this area most welcome. The apparent inhomogeneity of inelastic deformation suggests that the spatial variation of temperature must also be determined.

In addition to temperature measurement, other non-mechanical diagnostic methods are essential. X-ray diffraction patterns have been obtained for shock-compressed material by flash radiography, but it remains to develop the method to the point where it can be used routinely for investigation of either inelastic deformation mechanisms or structural phase transitions. The development of electrical, optical or other means of investigating the history of defect production during and immediately following passage of a stress pulse would greatly facilitate interpretation of a wide variety of other measurements. In most cases only a few (usually just one) of the available probes have been used to study a particular problem, but examination of past work shows that the most fruitful investigations have often been those in which various techniques have been brought to bear.

Many of the shock phenomena that have been observed remain open to interpretation and many, no doubt, remain to be discovered. At the upper extreme of the experimentally accessible range of compression, effects of the electronic shell structure of atoms on the compressibility of matter have been noted. Efforts to model these effects have been undertaken and, in some cases, are well advanced. Few experiments have been conducted, however, and work in this area seems both possible and useful.

The question of inelastic deformation mechanisms remains open. The well-defined and orderly macroscopic motion detected by instrumentation in current use does not extent to the microscale. On this level rapid inelastic deformation is characterized by the development of high concentrations of a wide variety of lattice defects and their effects are widely cited in this review. In some cases (not well delineated) states of matter unique to the shock-compression process are achieved and the interpretation of observations and the relation between matter in the shocked and quasi-statically compressed states is clouded. The interpretation of electrical and optical observations is particularly at issue. Because of their influence on interpretation of the entire range of shock-compression measurements, deformation mechanisms and defect production deserve priority attention and investigation by all available means. The strong influence of defects on electrical measurements suggests the latter as a probe in conjunction with careful time-resolved mechanical measurements involving both multiple-shock compression and decompression. Recently developed transverse-wave methods deserve full exploitation. Investigation of the structure and properties of material recovered after shock loading would also be helpful, but this work must be done under more carefully controlled conditions and using shorter duration stress pulses than has been customary and must be accompanied by time-resolved measurement of stress history. Examination of

samples recovered after loading at various rates could prove informative.

Many shock-induced phase transformations have been observed, but the rapidity of their occurrence in comparison to the rates observed when they are produced by quasi-static compression, and the effect of shear stress, induced defects, and other peculiarities of the shock environment remain unexplained. Mechanisms of shock-induced conduction in dielectrics remain almost completely unexplored. An area combining complexities of mechanical behavior, phase transformation and electrical response is that of the response of ferroelectric ceramics to shock compression.

Investigations of the response of chemically-reactive media to shock compression (primarily detonation phenomena) have formed a branch of the subject under review since its earliest days, but most work has been concerned with the equation of state of the gaseous detonation products. Much less attention has been devoted to the growth of weak disturbances to steady detonation and few observations have been made of the structure of reactive waves. Considerable advance in this area could be expected to result from investigations in which refined theoretical models and numerical simulation of experiments are combined with time-resolved observations.

Most investigations of geophysical interest have involved the high pressures characteristic of deep-lying earth and planetary strata or meteoritic impact. Investigation of the complex behavior of both rock and soils at the lower stresses of interest in earthquake and mining problems is now possible and, indeed, results of such investigations are beginning to appear in the literature.

Finally, we note the often overlooked utility of the shock-compression method for examining mechanical, piezoelectric, dielectric, optical and other phenomena in the elastic range where its advantage lies with the precisely controlled states of uniaxial strain produced and the fact that the entire range of elastic responses is accessible. Work in this regime to study nonlinear transverse wave phenomena is to be encouraged.

Acknowledgment

This review owes much to our years of association with many past and present members of the shock-wave physics group at Sandia Laboratories. In preparing the manuscript, we have had the benefit of detailed critical appraisals of various sections by J.R. Asay, D.D. Bloomquist, D.E. Grady, and G.A. Samara.

The preparation of the review was supported by the U.S. Department of Energy under Contract AT(29-1)789. Sandia Laboratories is a Department of Energy facility.

References

1920 P1. Parsons, C.A., Philos. Trans. Roy. Soc. A220, 67.
1937 S1. Sillars, R.W., J. Inst. Elect. Engineers (London) 80, 378–394.
1948 C1. Courant, R. and K.O. Friedrichs, Supersonic Flow and Shock Waves (Interscience, New York).
P1. Pack, D.C., W.M. Evans and H.J. James, Proc. Phys. Soc. 60, 1–8.
1952 W1. Wood, D.S., J. Appl. Mech. 19, 521–525.
1953 B1. Bridgman, P.W. and I. Simon, J. Appl. Phys. 24, 405–413.
C1. Coes Jr., L., Science 118, 131–132.
M1. McSkimin, H.J., J. Appl. Phys. 24, 988–997.

P1. Prince, M.B., Phys. Rev. 92, 681–687.

1954 M1. Morin, F.J. and J.P. Maita, Phys. Rev. 94, 1525–1531.

1955 B1. Bundy, F.P., H.T. Hall, H.M. Strong and R.H. Wentorf Jr., Nature 176, 51–55.

G1. Goranson, R.W., D. Bancroft, B.L. Burton, T. Blechar, E.E. Houston, E.F. Gittings and S.A. Landeen, J. Appl. Phys. 26, 1472–1479.

H1. Herring, C., Bell System Technical J. 34, 237–290.

M1. Minshall, S., abstract in Phys. Rev. 98, 271.

M2. Minshall, S., J. Appl. Phys. 26, 463–469.

W1. Walsh, J.M. and R.H. Christian, Phys. Rev. 97, 1544–1556.

1956 B1. Bancroft, D., E.L. Peterson and S. Minshall, J. Appl. Phys. 27, 291–298.

R1. Riabinin, Iu.N., Sov. Phys.-Tech. Phys. 1, 2575–2576.

1957 A1. Anderson, G.W. and F.W. Neilson, Bull. Am. Phys. Soc. 2, 302.

C1. Christian, R.H., Thesis, University of California.

L1. LaRocca, E.W. and L.A. Burkardt, Bull. Am. Phys. Soc. 2, 263.

N1. Nye, J.F., Physical Properties of Crystals (Oxford University Press, Oxford).

N2. Neilson, F.W., Bull. Am. Phys. Soc. 2, 302.

R1. Rice, M.H. and J.M. Walsh, J. Chem. Phys. 26, 824–830.

W1. Walsh, J.M. and M.H. Rice, J. Chem. Phys. 26, 815–823.

W2. Walsh, J.M., M.H. Rice, R.G. McQueen and F.L. Yarger, Phys. Rev. 108, 196–216.

Z1. Zel'dovich, Ia.B., Sov. Phys.-JETP 5, 1287–1288.

1958 A1. Al'tshuler, L.V., K.K. Krupnikov, B.N. Ledenev, V.I. Zhuchikhin and M.I. Brazhnik, Sov. Phys.-JETP 34, 606–614.

A2. Al'tshuler, L.V., K.K. Krupnikov and M.I. Brazhnik, Sov. Phys.-JETP 34, 614–619.

G1. Grover, R., R.H. Christian and B.J. Alder, Bull. Am. Phys. Soc. 3, 230.

K1. Kulterman, R.W., F.W. Neilson and W.B. Benedick, J. Appl. Phys. 29, 500–501.

R1. Rice, M.H., R.G. McQueen and J.M. Walsh, in: Solid State Physics, Vol. 6, eds. F. Seitz and D. Turnbull (Academic Press, New York) pp. 1–63.

S1. Smith, C.S., Trans. Met. Soc. of AIME 212, 574–589.

1959 D1. DeCarli, P.S. and J.C. Jamieson, J. Chem. Phys. 31, 1675–1676.

F1. Fritzsche, H., Phys. Rev. 115, 336–345.

J1. Jacquesson, J., Analyse des constraintes, Bull. du G.A.M.A.C. IV, 4, 33–35.

M1. Morland, L.W., Philos. Trans. Roy. Soc. A251, 341–383.

1960 A1. Al'tshuler, L.V., S.B. Kormer, A.A. Bakanova and R.F. Trunin, Sov. Phys.-JETP 11, 573–579.

A2. Al'tshuler, L.V., S.B. Kormer, M.I. Brazhnik, L.A. Vladimirov, M.P. Speranskaya and A.I. Funtikov, Sov. Phys.-JETP 11, 766–775.

C1. Chao, E.C.T., E.M. Shoemaker and B.M. Madsen, Science 132, 220–222.

D1. Duvall, G.E., D.E. Davenport and J.J. Kelly, International Nickel Co. Report 004-60.

K1. Keys, R.W., in: Solid State Physics, Vol. 11, eds. F. Seitz and D. Turnbull (Academic Press, New York) pp. 149–221.

M1. McQueen, R.G. and S.P. Marsh, J. Appl. Phys. 31, 1253–1269.

T1. Truesdell, C. and R.A. Toupin, in: Handbuch der Physik, Band III/1, ed. S. Flügge (Springer-Verlag, Berlin) pp. 226–858.

1961 A1. Alder, B.J. and R.H. Christian, Phys. Rev. Lett. 7, 367–369.

A2. Al'tshuler, L.V. and A.P. Petrunin, Sov. Phys.-Tech. Phys. 6, 516–522.

B1. Balchan, A.S. and H.G. Drickamer, Rev. Sci. Instruments 32, 308–313.

C1. Curran, D.R., J. Appl. Phys. 32, 1811–1814.

D1. DeCarli, P.S. and J.C. Jamieson, Science 133, 1821–1822.

D2. Duvall, G.E., in: [61S1] pp. 165–202.

E1. Erkman, J.D., J. Appl. Phys. 32, 939–944.

F1. Fowler, C.M., F.S. Minshall and E.G. Zukas, in: [61S1] pp. 275–300.

F2. Fowles, G.R., J. Appl. Phys. 32, 1475–1487.

F3. Fowles, G.R., Stanford Research Institute, Poulter Labs. Tech. Report 003–61.

G1. Graham, R.A., J. Appl. Phys. 32, 555.

G2. Graham, R.A., Rev. Sci. Instruments 32, 1308–1313.

H1. Hopkins, H.G., Appl. Mech. Rev. 14, 417–431.

H2. Hruska, K., Czech. J. Phys. B11, 150–152.

M1. Minshall, F.S., in: [61S1] pp. 249–274.

R1. Reynolds, C.E. and G.E. Seay, J. Appl. Phys. 32, 1401–1402.

S1. Shewmon, P.G. and V.F. Zackay, editors, Response of Metals to High Velocity Deformation (Interscience, New York).

S2. Stishov, S.M. and S.V. Popova, Geochemistry, No. 10, 923.

Z1. Zel'dovich, Ya.B., S.B. Kormer, M.V. Sinitsyn and K.B. Yushko, Sov. Phys.-Doklady 6, 494–496.

1962 A1. Al'tshuler, L.V., A.A. Bakanova and R.F. Trunin, Sov. Phys.-JETP 15, 65–74.
A2. Al'tshuler, L.V., S.B. Kormer, A.A. Bakanova, A.P. Petrunin, A.I. Funtikov and A.A. Gubkin, Sov. Phys.-JETP 14, 986–994.
B1. Blackburn, J.H. and L.B. Seely, Nature 194, 370–371.
C1. Chao, E.T.C., J.J. Fahey, J. Littler and D.J. Milton, J. Geophys. Res. 67, 419–421.
D1. Deal Jr., W.E., in: Modern Very High Pressure Techniques, ed. R.H. Wentorf Jr. (Butterworths, Washington) pp. 200–227.
D2. Dieter, G.E., in: Strengthening Mechanisms in Solids (American Society of Metals, Metals Park, Ohio) pp. 279–340.
D3. Duvall, G.E., Appl. Mech. Rev. 15, 849–854.
E1. Eichelberger, R.J. and G.E. Hauver, in: [62R2] pp. 363–387.
F1. Fuller, P.J.A. and J.H. Price, Nature 193, 262–263.
G1. Graham, R.A., J. Appl. Phys. 33, 1755–1758.
J1. Johnson, P.C., B.A. Stein and R.S. Davis, J. Appl. Phys. 33, 557–561.
J2. Jones, O.E., F.W. Neilson and W.B. Benedick, J. Appl. Phys. 33, 3224–3232.
K1. Kormer, S.B., A.I. Funtikov, V.D. Urlin and A.N. Kolesnikova, Sov. Phys.-JETP 15, 477–488.
K2. Krupnikov, K.K., M.I. Brazhnik and V.P. Krupnikova, Sov. Phys.-JETP 15, 470–476.
N1. Neilson, F.W. and W.B. Benedick, Sandia Corporation Report SCR-502.
N2. Neilson, F.W., W.B. Benedick, W.P. Brooks, R.A. Graham and G.W. Anderson, in: [62R2] pp. 391–419.
R1. Reynolds, C.E. and G.E. Seay, J. Appl. Phys. 33, 2234–2241.
R2. Ribaud, G., editor, Les Ondes de Detonation (Editions du Centre National de la Recherche Scientifique, Paris).
S1. Schmidt-Tiedemann, K.J., in: Proc. Int. Conf. Phys. Semiconductors, Exeter (The Institute of Physics and the Physical Society, London) p. 191.
S2. Skidmore, I.C. and E. Morris, in: Thermodynamics of Nuclear Materials 1962 (International Atomic Energy Agency, Vienna) pp. 173–216.
W1. Wackerle, J., J. Appl. Phys. 33, 922–937.
1963 A1. Al'tshuler, L.V., M.N. Pavlovskii, L.V. Kuleshova and G.V. Simakov, Sov. Phys.-Solid State 5, 203–211.
B1. Blincow, D.W. and D.V. Keller, in: [63W1] pp. 252–263.
B2. Bundy, F.P., J. Chem. Phys. 38, 631–643.
B3. Bundy, F.P. and R.H. Wentorf Jr., J. Chem. Phys. 38, 1144–1149.
C1. Curran, D.R., J. Appl. Phys. 34, 2677–2685.
D1. Doran, D.G., in: High Pressure Measurements, eds. A.A. Giardini and E.C. Lloyd (Butterworths, Washington) pp. 59–86.
D2. Duvall, G.E., International Science and Technology, Apr. 1963, 45–52.
D3. Duvall, G.E. and G.R. Fowles, in: High Pressure Physics and Chemistry, Vol. 2, ed. R.S. Bradley (Academic Press, New York) pp. 209–291.
G1. Goroff, I. and L. Kleinman, Phys. Rev. 132, 1080–1084.
I1. Ivanov, A.G., S.A. Novikov and V.A. Sinitsyn, Sov. Phys.-Solid State 5, 196–202.
K1. Keller, D.V. and J.G. Trulio, J. Appl. Phys. 34, 172–175.
K2. Knopoff, L., in: High Pressure Physics and Chemistry, Vol. 1, ed. R.S. Bradley (Academic Press, New York) pp. 227–245.
K3. Knopoff, L., source in: [63K2], except pp. 247–263.
M1. Milton, D.J. and P.S. DeCarli, Science 140, 670–671.
P1. Paul, W., in: Solids Under Pressure, eds. W. Paul and D.M. Warschauer (McGraw-Hill, New York) pp. 179–249.
P2. Paul, W. and D.M. Warschauer, in: Solids Under Pressure, eds. W. Paul and D.M. Warschauer (McGraw-Hill, New York) pp. 429–448.
P3. Paul, W. and H. Brooks, in: Progress in Semiconductors, Vol. 7, eds. A.F. Gibson and R.E. Burgess (John Wiley, New York) pp. 135–235.
S1. Smith, J.H., in: [63W1] pp. 264–281.
T1. Taylor, J.W., J. Appl. Phys. 34, 2727–2731.
T2. Taylor, J.W. and M.H. Rice, J. Appl. Phys. 34, 364–371.
W1. Williams, I.V., editor, Dynamic Behavior of Materials (American Society for Testing and Materials, Philadelphia).
Z1. Zukas, E.G., C.M. Fowler, F.S. Minshall and J. O'Rourke, Trans. Met. Soc. AIME 227, 746–753.
1964 B1. Barker, L.M., C.D. Lundergan and W. Herrmann, J. Appl. Phys. 35, 1203–1212.
B2. Bernstein, D. and D.D. Keough Jr., J. Appl. Phys. 35, 1471–1474.
B3. Blackburn, J.H. and L.B. Seeley, Nature 202, 276–277.
B4. Butcher, B.M., L.M. Barker, D.E. Munson and C.D. Lundergan, AIAA J. 2, 977–990.
B5. Butcher, B.M. and J.R. Canon, AIAA J. 2, 2174–2179.
D1. Dakhovskii, L.V., Sov. Phys.-Solid State 5, 1695–1699.
D2. Duvall, G.E., in: Stress Waves in Anelastic Solids, eds. H. Kolsky and W. Prager (Springer-Verlag, Berlin) pp. 20–32.
G1. Gager, W.B., M.J. Klein and W.H. Jones, Appl. Phys. Lett. 5, 131–132.
G2. Gibbs, D.F. and G.J. Hill, Philos. Mag. 9, 367–375.
H1. Hearst, J.R., L.B. Geesaman and D.V. Power, J. Appl. Phys. 35, 2145–2150.

J1. Jones, O.E. and J.R. Holland, J. Appl. Phys. 35, 1771–1773.
L1. Lipschutz, M.E., Science 143, 1431–1434.
M1. McQueen, R.G., in: Metallurgy at High Pressures and High Temperatures, eds. K.A. Geschneider Jr. et al. (Gordon and Breach, New York) pp. 44–132.
P1. Paige, E.G.S., in: Progress in Semiconductors, Vol. 8, eds. A.F. Gibson and R.E. Burgess (John Wiley, New York).
P2. Pastine, D.J., J. Appl. Phys. 35, 3407–3414.
P3. Paterson, S., Nature 203, 1057–1059.
W1. Wilkins, M.L., in: Methods of Computational Physics, Vol. 3, eds. B. Alder et al. (Academic Press, New York) pp. 211–263.

1965 A1. Allison, F.E., J. Appl. 36, 2111–2113.
A2. Al'tshuler, L.V., Sov. Phys.-Uspekhi 8, 52–91.
A3. Appleton, A.S., Appl. Materials Res. 4, 195–201.
B1. Balslev, I., Sol. State Comm. 3, 213–218.
B2. Batsanov, S.D., G.E. Blokhina and A.A. Deribas, J. Structural Chem. 6, 209–213.
B3. Brooks, W.P., J. Appl. Phys. 36, 2788–2790.
B4. Brugger, K., J. Appl. Phys. 36, 759–767.
B5. Butcher, B.M. and D.E. Munson, in: [65J1] pp. 295–304.
C1. Coleburn, N.L., M. Solow and R.C. Wiley, J. Appl. Phys. 36, 507–510.
C2. Cowan, G.R., Trans. Met. Soc. AIME 233, 1120–1130.
C3. Crosnier, J., J. Jacquesson and A. Migault, in: [65J1] pp. 627–638.
C4. Curran, D.R., J. Appl. Phys. 36, 2591–2592.
D1. DeCarli, P.S. and D.J. Milton, Science 147, 144–145.
D2. Drickamer, H.G., in: Solid State Physics, Vol. 17, eds. F. Seitz and D. Turnbull (Academic Press, New York) pp. 1–133.
F1. Fuller, P.J.A. and J.H. Price, in: [65J1] pp. 290–294.
G1. Graham, R.A., F.W. Neilson and W.B. Benedick, J. Appl. Phys. 36, 1775–1783.
H1. Hauver, G.E., J. Appl. Phys. 36, 2113–2118.
H2. Hearst, J.R., G.B. Irani and L.B. Geesaman, J. Appl. Phys. 36, 3440–3444.
J1. Jacobs, S.J., editor, Fourth Symp. (Intern.) on Detonation (U.S. Government Printing Office, Washington).
K1. Kennedy, J.D. and W.B. Benedick, private communication.
K2. Kennedy, J.D. and W.B. Benedick, Bull. Am. Phys. Soc. 10, 1112, and private communication.
K3. Klein, M.J., Philos. Mag. 12, 735–739.
L1. Leslie, W.C., D.W. Stevens and M. Cohen, in: High Strength Materials, eds. V.F. Zakay and E.R. Parker (John Wiley, New York) pp. 382–432.
S1. Skidmore, I.C., Appl. Materials Res. 4, 131–147.
T1. Truesdell, C. and W. Noll, in: Handbuch der Physik, Band III/3, ed. S. Flügge (Springer-Verlag, Berlin) pp. 1–602.
T2. Taylor, J.W., J. Appl. Phys. 36, 3146–3150.
V1. Vedam, K. and E.D.D. Schmidt, Sol. State Comm. 3, 373–375.

1966 A1. Ahrens, T.J., J. Appl. Phys. 37, 2532–2541.
A2. Ahrens, T.J. and G.E. Duvall, J. Geophys. Res. 71, 4349–4360.
A3. Ahrens, T.J. and M.H. Ruderman, J. Appl. Phys. 37, 4758–4765.
A4. Asche, M., O.G. Sarbej and V.M. Vasetskii, Phys. Stat. Sol. 18, 749–754.
B1. Balslev, I., Phys. Rev. 143, 636–647.
B2. Besancon, J.E., J. David and J. Vedel, in: Proc. Conf. Megagauss Magnetic Field Generation by Explosives and Related Experiments (Euratom, Brussels) pp. 315–329.
B3. Birch, F., in: Handbook of Physical Constants, ed. S.P. Clark Jr. (Geological Society of America, New York) pp. 97–147.
B4. Butcher, B.M. and C.H. Karnes, J. Appl. Phys. 37, 402–411.
B5. Bechmann, R., in: Landölt-Börnstein Numerical Data and Functional Relationships in Science and Technology, Group III, Vol. 1, eds. K.H. Hellwege and A.M. Hellwege (Springer-Verlag, New York) pp. 124–149.
C1. Cutchen, J.T., J. Appl. Phys. 37, 4745–4750.
D1. Davison, L., J. Mech. Phys. Solids 14, 249–270.
D2. Deribas, A.A., N.L. Dobretsov, V.M. Kudinov and N.I. Zyuzin, Acad. Sci. USSR, Proc. Earth Sci. 168, 127–130.
D3. Doran, D.G. and R.K. Linde, in: Solid State Physics, Vol. 19, eds. F. Seitz and D. Turnbull (Academic Press, New York) pp. 229–290.
D4. Drickamer, H.G., R.W. Lynch, R.L. Clendenen and E.A. Perez-Albuerne, in: Solid State Physics, Vol. 19, eds. F. Seitz and D. Turnbull (Academic Press, New York) pp. 135–228.
G1. Graham, R.A., O.E. Jones and J.R. Holland, J. Phys. Chem. Solids 27, 1519–1529.
H1. Halpin, W.J., J. Appl. Phys. 37, 153–163.
J1. Jones, A.H., W.M. Isbell and C.J. Maiden, J. Appl. Phys. 37, 3493–3499.
K1. Kennedy, J.D. and W.B. Benedick, J. Phys. Chem. Solids 27, 125–127.

K2. Klein, M.J. and J.W. Edington, Philos. Mag. 14, 21–29.
K3. Klein, M.J. and P.S. Rudman, Philos. Mag. 14, 1199–1206.
L1. Leiserowitz, L., G.M.J. Schmidt and A. Shamgar, J. Phys. Chem. Solids 27, 1453–1457.
L2. Linde, R.K. and D.G. Doran, Nature 212, 27–29.
L3. Linde, R.K., W.J. Murri and D.G. Doran, J. Appl. Phys. 37, 2527–2532.
N1. Novikov, S.A., V.A. Sinitsyn, A.G. Ivanov and L.V. Vasil'yev, Phys. Met. Metallography 21, 135–144.
P1. Pastine, D.J. and D. Piacesi, J. Phys. Chem. Solids 27, 1783–1792.
R1. Riskaer, S., Phys. Rev. 152, 845–849.
R2. Royce, E.B., J. Appl. Phys. 37, 4066–4070.
T1. Takeuchi, H. and H. Kanamori, J. Geophys. Res. 71, 3985–3994.
T2. Thurston, R.N., H.J. McSkimin and P. Andreatch Jr., J. Appl. Phys. 37, 267–275.
U1. Urlin, V.D., Sov. Phys.-JETP 22, 341–346.
V1. van Thiel, M. and B.J. Alder, J. Chem. Phys. 44, 1056–1065.
V2. Vedam, K. and E.D.D. Schmidt, Phys. Rev. 146, 548–554.
V3. Vedam, K. and E.D.D. Schmidt, Phys. Rev. 150, 150–151.
Z1. Zel'dovich, Ya.B. and Yu.P. Raizer, Physics of Shock Waves and High Temperature Hydrodynamic Phenomena, in two volumes (Academic Press, New York, 1966 (Vol. 1) and 1967 (Vol. 2)).
Z2. Zukas, E.G., Metals Engineering Quarterly 6, 1–20.

1967 A1. Adadurov, G.A., Z.G. Aliev, L.O. Atovmyan, T.V. Bavina, Yu.G. Borod'ko, O.N. Breusov, A.N. Dremin, A.Kh. Muranevich and S.V. Pershin, Sov. Phys.-Doklady 12, 173–175.
B1. Barnes, J.F., Phys. Rev. 153, 269–275.
B2. Barsch, G.R. and Z.P. Chang, Phys. Stat. Sol. 19, 139–151.
B3. Brillhart, D.C., R.J. DeAngelis, A.G. Preban, J.B. Cohen and P. Gordon, Trans. Met. Soc. AIME 239, 836–843.
B4. Butcher, B.M., J. Appl. Mech. 34, 209–210.
C1. Chaban, A.A., Sov. Phys.-JETP Lett. 6, 381–383.
C2. Chao, E.C.T., Science 156, 192–202.
C3. Clator, I.G. and M.F. Rose, Brit. J. Appl. Phys. 18, 853–855.
C4. Cristescu, N., Dynamic Plasticity (North-Holland, Amsterdam).
D1. Daniel, V.V., Dielectric Relaxation (Academic Press, New York).
D2. DeCarli, P.S., Bull. Am. Phys. Soc. 12, 1127.
E1. Erkman, J.O. and A.B. Christensen, J. Appl. Phys. 38, 5395–5403.
F1. Fowles, R., J. Geophys. Res. 72, 5729–5742.
G1. Graham, R.A., J. Basic Engineering 89, 911–918.
G2. Graham, R.A., D.H. Anderson and J.R. Holland, J. Appl. Phys. 38, 223–229.
H1. Holland, J.R., Acta Met. 15, 691–699.
J1. Johnson, J.N. and W. Band, J. Appl. Phys. 38, 1578–1585.
J2. Jones, O.E., Rev. Sci. Instruments 38, 253–256.
K1. Kelly, J.M. and P.P. Gillis, J. Appl. Phys. 38, 4044–4046.
K2. Kennedy, J.D. and W.B. Benedick, Sol. State Comm. 5, 53–55.
L1. Linde, R.K., J. Appl. Phys. 38, 4839–4842.
M1. McQueen, R.G., J.C. Jamieson and S.P. Marsh, Science 155, 1401–1404.
M2. McQueen, R.G., S.P. Marsh and J.N. Fritz, J. Geophys. Res. 72, 4999–5036.
O1. Otto, H.E. and R. Mikesell, in: Proc. First Int. Conf. of the Center for High Energy Rate Forming, Vol. 2, pp. 7.6.1–7.6.46.
P1. Pastine, D.J., Phys. Rev. Lett. 18, 1187–1189.
R1. Rose, M.F. and F.I. Grace, Brit. J. Appl. Phys. 18, 671–674.
R2. Ross, M. and B. Alder, J. Chem. Phys. 46, 4203–4210.
R3. Royce, E.B., Phys. Rev. 164, 929–943.
R4. Ruoff, A.L., J. Appl. Phys. 38, 4976–4980.
S1. Seay, G.E., R.A. Graham, R.C. Wayne and L.D. Wright, Bull. Am. Phys. Soc. 12, 1129.
S2. Stuetzer, O.M., J. Appl. Phys. 38, 3901–3904.
S3. Stuetzer, O.M., J. Acoustical Soc. America 42, 502–508.
V1. Vedam, K. and R. Srinivasan, Acta Crystallographia 22, 630–634.

1968 A1. Ahrens, T.J., W.H. Gust and E.B. Royce, J. Appl. Phys. 39, 4610–4616.
A2. Ahrens, T.J. and R.K. Linde, in: [68B3] pp. 325–336.
A3. Al'tshuler, L.V., B.N. Moiseev, L.V. Popov, G.V. Simakov and R.F. Trunin, Sov. Phys.-JETP 27, 420–422.
A4. Argous, J.P. and J. Aveillé, in: [68B3] pp. 173–178.
B1. Banks, E.E., J. Iron and Steel Institute 206, 1022–1026.
B2. Barker, L.M., in: [68B3] pp. 483–505.

B3. Berger, J., editor, Behavior of Dense Media Under High Dynamic Pressure (Gordon and Breach, New York).
B4. Bulthius, K., Phillips Research Reports 23, 25–47.
C1. Champion, A.R. and W.B. Benedick, Rev. Sci. Instruments 39, 377–378.
C2. Coleburn, N.L. and J.W. Forbes, J. Chem. Phys. 48, 555–559.
C3. Cowan, G.R., B.W. Dunnington and A.H. Holtzman, U.S. Patent 3401019, Sept. 10, 1968.
D1. Davison, L., Int. J. Solids and Structures 4, 301–322.
D2. Deribas, A., N. Dobretsov, V. Kudinov, V. Maly, A. Serebrjakov and A. Staver, in: [68B3] pp. 385–388.
D3. Doran, D.G., J. Appl. Phys. 39, 40–47.
D4. Dremin, A.N. and O.N. Breusov, Russian Chem. Rev. 37, 392–402.
D5. Duvall, G.E., in: [68F1] pp. 19–29.
F1. French, B.M. and N.M. Short, editor, Shock Metamorphism of Natural Materials (Mono Book Corp., Baltimore).
G1. Gieske, J.H. and G.R. Barsch, Phys. Stat. Sol. 29, 121–131.
G2. Gilman, J.J., Appl. Mech. Rev. 21, 767–783.
G3. Graham, R.A., J. Appl. Phys. 39, 437–439.
G4. Graham, R.A. and W.J. Halpin, J. Appl. Phys. 39, 5077–5082.
G5. Graham, R.A. and G.E. Ingram, in: [68B3] pp. 469–482.
G6. Guess, T.R., Sandia Laboratories Report SC-DR-68-343.
H1. Halpin, W.J., J. Appl. Phys. 39, 3821–3826.
I1. Isbell, W.M., F.H. Shipman and A.H. Jones, General Motors Corp. Report MSL-68-13, AD721920.
I2. Ivanov, A.G., Yu.V. Lisitsyn and E.Z. Novitskii, Sov. Phys.-JETP 27, 153–155.
J1. Jones, G.A. and W.J. Halpin, Rev. Sci. Instruments 39, 258–259.
J2. Jones, O.E. and J.R. Holland, Acta Met. 16, 1037–1045.
K1. Karnes, C.H., in: Mechanical Behavior of Materials Under Dynamic Loads, ed. U.S. Lindholm (Springer-Verlag, New York) pp. 270–293.
K2. Keller, D.V., in: [68B3] pp. 453–460.
K3. Kennedy, J.D., in: [68B3] pp. 407–418.
K4. King, P.J., D.F. Cotgrove and P.M.B. Slate, in: [68B3] pp. 513–520.
K5. Kormer, S.B., Sov. Phys.-Uspekhi 11, 229–254.
L1. Leygonie, J. and J.Cl. Bergon, in: [68B3] pp. 161–172.
M1. McMahon, D.H., J. Acoustical Soc. America 44, 1007–1013.
M2. McQueen, R.G., S.P. Marsh and W.J. Carter, in: [68B3] pp. 66–83.
M3. Mitchell, A.C. and R.N. Keeler, Rev. Sci. Instruments 39, 513–522.
M4. Müller, W.F. and W. Defourneaux, Z. Geophys. 34, 483–504.
P1. Pastine, D.J., Phys. Rev. 175, 905–912.
P2. Pollak, F.H. and M. Cardona, Phys. Rev. 172, 816–837.
R2. Rohde, R.W., J.R. Holland and R.A. Graham, Trans. Met. Soc. AIME 242, 2017–2019.
R3. Rohde, R.W. and O.E. Jones, Rev. Sci. Instruments 39, 313–316.
R4. Royce, E.B., in: [68B3] pp. 419–429.
S1. Shaner, J.W. and E.B. Royce, J. Appl. Phys. 39, 492–493.
T1. Taylor, J.W., in: Dislocation Dynamics, eds. A.R. Rosenfield et al. (McGraw-Hill, New York) pp. 573–589.
T2. Trueb, L.F., J. Appl. Phys. 39, 4707–4716.
W1. Warnica, R.L., General Motors Corp. Report MSL-68-1.
W2. Warnica, R.L., General Motors Corp. Report MSL-68-18.
W3. Wilkins, M.L., in: [68B3] pp. 269–277.
W4. Wong, J.Y., R.K. Linde and P.S. DeCarli, Nature 219, 713–714.
Z1. Zaidel, R.M., Sov. Phys.-JETP 7, 670–672.
Z2. Zel'dovich, Ya.B., Sov. Phys.-JETP 27, 159–162.

1969 A1. Ahrens, T.J., D.L. Anderson and A.E. Ringwood, Reviews of Geophys. 7, 667–707.
A2. Al'tshuler, L.V. and A.A. Bakanova, Sov. Phys.-Uspekhi 11, 678–689.
B1. Bechmann, R., in: Landölt-Börnstein Numerical Data and Functional Relationships in Science and Technology, Group III, Vol. 2, eds. K.H. Hellwege and A.M. Hellwege (Springer-Verlag, New York) pp. 102–125.
B2. Brazhnik, M.I., L.V. Al'tshuler and L.A. Tarasov, Combustion, Explosion and Shock Waves 5, 352–355.
D1. Dulin, I.N., L.V. Al'tshuler, V.Ya. Vashchenko and V.N. Zubarev, Sov. Phys.-Solid State 11, 1016–1020.
F1. Fuller, P.J.A. and J.H. Price, Brit. J. Appl. Phys. (J. Phys. D), Ser. 2, 2, 275–286.
G1. Gilman, J.J., Micromechanics of Flow in Solids (McGraw-Hill, New York).
G2. Group GMX-6, Los Alamos Scientific Laboratory Report LA-4167-MS.
G3. Guess, T.R., Sandia Laboratories Report SC-RR-69-761.

H1. Herrmann, W., in: Wave Propagation in Solids, ed. J. Miklowitz (American Society of Mechanical Engineers, New York) pp. 129–183.
J1. Johnson, J.N. and L.M. Barker, J. Appl. Phys. 40, 4321–4334.
J2. Jones, O.E. and J.D. Mote, J. Appl. Phys. 40, 4920–4928.
K1. Keeler, R.N. and A.C. Mitchell, Sol. State Comm. 7, 271–274.
K2. Kennedy, J.D., private communication.
K3. Klein, N., in: Advances in Electronics and Electron Physics, ed. L. Marton (Academic Press, New York) p. 391.
K4. Kuleshova, L.V., Sov. Phys.-Solid State 11, 886–890.
K5. Kusubov, A.S. and M. van Thiel, J. Appl. Phys. 40, 3776–3780.
K6. Knopoff, L. and J.N. Shapiro, J. Geophys. Res. 74, 1439–1450.
L1. Linde, R.K. and R.C. Crewdson, Scientific American 220/5, 83–91.
L2. Linde, R.K. and P.S. DeCarli, J. Chem. Phys. 50, 319–325.
P1. Paterson, S., Nature 203, 1057–1059.
P2. Peterson, C.F. and J.T. Rosenberg, J. Appl. Phys. 40, 3044–3046.
R1. Rohde, R.W., Acta Met. 17, 353–363.
S1. Saravia, L.R. and D. Brust, Phys. Rev. 178, 1240–1243.
S2. Schetzina, J.F. and J.P. McKelvey, Phys. Rev. 181, 1191–1195.
S3. Shapiro, J.N. and L. Knopoff, J. Geophys. Res. 74, 1435–1438.
T1. Thurston, R.N., J. Acoustical Soc. America 45, 1329–1341.
T2. Trunin, R.F., M.A. Podurets, B.N. Moiseev, G.V. Simakov and L.V. Popov, Sov. Phys.-JETP 29, 630–631.
T3. Tyunyaev, Yu.N., V.N. Mineev, A.G. Ivanov, E.Z. Novitskii and Yu.V. Lisityn, Sov. Phys.-JETP 29, 98–100.
V1. Vedam, K., E.D.D. Schmidt, J.L. Kirk and W.C. Schneider, Materials Res. Bull. 4, 573–580.
V2. Vereshchagin, L.F., G.A. Adadurov, O.N. Breusov, K.P. Burdina, L.N. Burenkova, A.N. Dremin, E.V. Zubova and A.I. Rogacheva, Sov. Phys.-Doklady 13, 896–898.
W1. Wayne, R.C., J. Appl. Phys. 40, 15–22.
W2. Wong, J.Y., J. Appl. Phys. 40, 1789–1791.
W3. Wong, J.Y., R.K. Linde and R.M. White, J. Appl. Phys. 40, 4137–4145.

1970 B1. Barbee Jr., T., L. Seaman and R.C. Crewdson, U.S. Air Force Weapons Laboratory Report AFWL-TR-70-99, AD-878449.
B2. Barker, L.M. and R.E. Hollenbach, J. Appl. Phys. 41, 4208–4226.
B3. Barsis, E., E. Williams and C. Skoog, J. Appl. Phys. 41, 5155–5162.
B4. Boade, R., J. Appl. Phys. 41, 4542–4551.
B5. Brammer, J.A., Sandia Laboratories Report SC-RR-70-124.
B6. Buzhinskii, O.I. and S.V. Samylov, Sov. Phys.-Solid State 11, 2332–2336.
C1. Christman, D.R. and N.H. Froula, AIAA J. 8, 477–482.
C2. Crossland, B. and J.D. Williams, Met. Rev. 144, 79–100.
D1. Dick, R.D., J. Chem. Phys. 52, 6021–6032.
D2. Dick, R.D., R.H. Warnes and J. Skalyo Jr., J. Chem. Phys. 53, 1648–1651.
F1. Fowles, R. and R.F. Williams, J. Appl. Phys. 41, 360–363.
G1. German, V.N., A.A. Bakanova, L.A. Tarasova and Yu.N. Sumulov, Sov. Phys.-Solid State 12, 490–491.
G2. Grover, R., J. Phys. Chem. Solids 31, 2347–2351.
H1. Hankey, R.E. and D.E. Schuele, J. Acoustical Soc. America 48, 190–202.
H2. Hauver, G.E., in: [70J1] pp. 387–397.
H3. Holt, A.C. and M. Ross, Phys. Rev. B1, 2700–2705.
I1. Ingram, G.E. and R.A. Graham, in: [70J1] pp. 369–386.
J1. Jacobs, S.J. and R. Roberts, Fifth Symp. (Intern.) on Detonation (U.S. Government Printing Office, Washington).
J2. Jacquesson, J., J.P. Romain, M. Hallouin and J.C. Desoyer, in: [70J1] pp. 403–412.
J3. Johnson, J.N., O.E. Jones and T.E. Michaels, J. Appl. Phys. 41, 2330–2339.
J4. Jones, A.H., C.J. Maiden and W.M. Isbell, in: Mechanical Behavior of Materials Under Pressure, ed. H.L.D. Pugh (Elsevier, London) pp. 680–747.
K1. Keough, D.D. and J.Y. Wong, J. Appl. Phys. 41, 3508–3515.
K2. Kinslow, R., editor, High Velocity Impact Phenomena (Academic Press, New York).
M1. McQueen, R.G., S.P. Marsh, J.W. Taylor, J.N. Fritz and W.J. Carter, in: [70K2] pp. 293–417 with appendices on pp. 515–568.
M2. Murri, W.J. and G.D. Anderson, J. Appl. Phys. 41, 3521–3525.
M3. Melz, P.J., J. Phys. Chem. Solids 32, 209–221.
N1. Novikov, S.A. and L.M. Sinitsyna, J. Appl. Mech. Tech. Phys. 11, 983–986.
O1. O'Keeffe, D.J., J. Geophys. Res. 75, 1947–1952.
O2. Olinger, B. and J.C. Jamieson, High Temperatures-High Pressures 2, 513–520.

P1. Pujols, H. and F. Boisard, Carbon 8, 781–782.
R1. Rohde, R.W., Acta Met. 18, 903–913.
R2. Ross, M. and K.W. Johnson, Phys. Rev. B2, 4709–4714.
S1. Schuler, K.W., J. Mech. Phys. Solids 18, 277–293.
S2. Skidmore, I.C. and J.W. Lethaby, in: [70J1] pp. 573–579.
S3. Styris, D.L. and G.E. Duvall, High Temperatures-High Pressures 2, 447–499.
T1. Trueb, L.F., J. Appl. Phys. 41, 5029–5030.
V1. Vaidya, S.N. and G.C. Kennedy, J. Chem. Phys. Solids 31, 2329–2345.
W1. Wayne, R.C., G.A. Samara and R.A. Lefever, J. Appl. Phys. 41, 633–640.
Y1. Yakusheva, O.B., V.V. Yakushev and A.N. Dremin, Sov. Phys.-Doklady 14, 1189–1190.

1971 A1. Ahrens, T.J., J.H. Lower and P.L. Lagus, J. Geophys. Res. 76, 518–528.
A2. Ahrens, T.J. and E.S. Gaffney, J. Geophys. Res. 76, 5504–5513.
A3. Al'tshuler, L.V., M.I. Brazhnik and G.S. Telegin, J. Appl. Mech. Tech. Phys. 12, 921–926.
A4. Al'tshuler, L.V. and M.N. Pavlovskii, J. Appl. Mech. Tech. Phys. 12, 161–165.
A5. Al'tshuler, L.V. and M.N. Pavlovskii, J. Appl. Mech. Tech. Phys. 12, 268–272.
A6. Arndt, J., U. Hornemann and W.F. Müller, Phys. and Chem. Glasses 12, 1–7.
B1. Burke, J.J. and V. Weiss, editors, Shock Waves and the Mechanical Properties of Solids (Syracuse University Press, Syracuse, New York).
B2. Babcock, S.G., J.J. Langan, D.B. Norvey, T.E. Michaels, F.L. Schierloh and S.J. Green, U.S. Army Materials and Mechanics Research Center Report AMMRC 71-3 (AD724195).
C1. Caldirola, P. and H. Knoepfel, editors, Proc. Intern. School of Physics "Enrico Fermi", Course XLVII, Physics of High Energy Density (Academic Press, New York).
C2. Carter, W.J., S.P. Marsh, J.N. Fritz and R.G. McQueen, in: [71L1] pp. 147–158.
C3. Christman, D.R., W.M. Isbell and S.G. Babcock, U.S. Defense Atomic Support Agency Report DASA 2501-5, AD728846.
C4. Christman, D.R., W.M. Isbell, S.G. Babcock, A.R. McMillan and S.J. Green, U.S. Defense Nuclear Agency Report DASA 2501-3, AD735966.
C5. Clifton, R.J., in: [71B1] pp. 73–119.
C6. Cowperthwaite, M. and J.H. Blackburn, in: [71L1] pp. 137–145.
C7. Cowperthwaite, M. and R.F. Williams, J. Appl. Phys. 42, 456–462.
C8. Curran, D.R., in: [71B1] pp. 121–138.
D1. Davison, L. and A.L. Stevens, Sandia Laboratories Report SC-TM-70-786.
D2. Duvall, G.E., in: [71C1] pp. 7–50.
E1. Ezra, A.A., Principles and Practice of Explosive Metal Forming (Industrial Newspapers, Ltd., London).
F1. Fournier, C. and A. Oberlin, C.R. Acad. Sci. Paris 272, 977–980.
F2. Fritz, J.N., S.P. Marsh, W.J. Carter and R.G. McQueen, in: [71L1] pp. 201–208.
G1. Gibbons, R.V. and T.J. Ahrens, J. Geophys. Res. 76, 5489–5498.
G2. Gillis, P.P., K.G. Hoge and R.J. Wasley, J. Appl. Phys. 42, 2145–2146.
G3. Graham, R.A. and W.P. Brooks, J. Phys. Chem. Solids 32, 2311–2330.
G4. Grover, R., J. Phys. Chem. Solids 32, 2539–2544.
G5. Gust, W.H. and E.B. Royce, J. Appl. Phys. 42, 276–295.
G6. Gust, W.H. and E.B. Royce, J. Appl. Phys. 42, 1897–1905.
H1. Herrmann, W., in: Applied Mechanics Aspects of Nuclear Effects in Materials, ed. C.C. Wan (American Society of Mechanical Engineers, New York).
H2. Herrmann, W., D.L. Hicks and E.G. Young, in: [71B1] pp. 23–64.
H3. Higgins, G.T., Met. Trans. 2, 1277–1282.
H4. Holt, A.C. and R. Grover, in: [71L1] pp. 131–135.
H5. Hooker, S.V., J.V. Foltz and F.I. Grace, Met. Trans. 2, 2290–2292.
J1. Johnson, J.N., J. Appl. Phys. 42, 5522–5530.
J2. Johnson, J.N. and R.W. Rohde, J. Appl. Phys. 42, 4171–4182.
J3. Jones, O.E., in: Engineering Solids Under Pressure, ed. H.Ll.D. Pugh (Institution of Mechanical Engineers, London) pp. 75–86.
J4. Jones, O.E. and R.A. Graham, in: [71L1] pp. 229–241.
K1. Keeler, R.N., in: [71C1] pp. 51–80.
K2. Keeler, R.N., in: [71C1] pp. 106–126.
K3. Keeler, R.N., in: [71C1] pp. 138–150.
L1. Lloyd, E.C., Accurate Characterization of the High Pressure Environment (U.S. Government Printing Office, Washington).
M1. McMillan, A.R., W.M. Isbell and A.H. Jones, General Motors Corp. Report MSL-70-01, AD 733490.

M2. McQueen, R.G., W.J. Carter, J.N. Fritz and S.P. Marsh, in: [71L1] pp. 219–227.
M4. Mineev, V.N., A.G. Ivanov, Yu.V. Lisitsyn, E.Z. Novitskii and Yu.N. Tyunyaev, Sov. Phys.-JETP 32, 592–598.
N1. Naumann, R.J., J. Appl. Phys. 42, 4945–4954.
P1. Pastine, D.J. and M.J. Carroll, in: [71L1] pp. 91–104.
R1. Royce, E.B., in: [71C1] pp. 80–95.
R2. Royce, E.B., in: [71C1] pp. 95–106.
R3. Royce, E.B., in: [71C1] pp. 126–138.
R4. Royce, E.B., Lawrence Livermore Laboratory Report UCRL-51121.
S1. Seaman, L., T.W. Barbee Jr. and D.R. Curran, U.S. Air Force Weapons Laboratory Report AFWL-TR-71-156.
S2. Stevens, A.L. and F.R. Tuler, J. Appl. Phys. 42, 5665–5670.
S3. Swan, G.W., J. Phys. D: Appl. Phys. 4, 1077–1082.
T1. Thompson, R.B. and C.F. Quate, J. Appl. Phys. 42, 907–919.
T2. Trueb, L.F., J. Appl. Phys. 42, 503–510.
V1. Vaidya, S.N., I.C. Getting and G.C. Kennedy, J. Phys. Chem. Solids 32, 2545–2556.
V2. Vaidya, S.N. and G.C. Kennedy, J. Phys. Chem. Solids 32, 951–964.
Y1. Yakushev, V.V. and A.N. Dremin, Russian J. Phys. Chem. 45, 50–53.
Z1. Zarembo, L.K. and V.A. Krasil'nikov, Sov. Phys.-Uspekhi 13, 778–797.
Z2. Zharkov, V.N. and V.A. Kalinin, Equations of State for Solids at High Pressures and Temperatures, transl. A. Tybulewicz (Consultants Bureau, New York).
Z3. Zubarev, V.N., J. Appl. Mech. Tech. Phys. 13, 263–267.

1972 A1. Ahrens, T.J., Tectonophysics 13, 189–219.
A2. Asay, J.R., G.R. Fowles, G.E. Duvall, M.H. Miles and R.F. Tinder, J. Appl. Phys. 43, 2132–2145.
A3. Asay, J.R., G.R. Fowles and Y. Gupta, J. Appl. Phys. 43, 744–746.
A4. Asay, J.R. and Y.M. Gupta, J. Appl. Phys. 42, 2220–2223.
A5. Arlt, G., in: [72B3] pp. 201–205.
B1. Barbee Jr., T., L. Seeman, R. Crewdson and D. Curran, J. Materials 7, 393–401.
B2. Barker, L.M., Experimental Mechanics 12, 209–215.
B3. Burstein, E., editor, Proc. Intern. School of Physics "Enrico Fermi", Course LII, Atomic Structure and Properties of Solids (Academic Press, New York).
C1. Champion, A.R., J. Appl. Phys. 43, 2216–2220.
C2. Christman, D.R. and F.J. Feistman, U.S. Defense Nuclear Agency Report DNA 2785F, AD 742522.
C3. Christman, D.R., T.E. Michaels, W.M. Isbell and S.G. Babcock, U.S. Defense Nuclear Agency Report DASA 2501-4, AD 738862.
C4. Coleburn, N.L., J.W. Forbes and H.D. Jones, J. Appl. Phys. 43, 5007–5012.
D1. Davison, L. and A.L. Stevens, J. Appl. Phys. 43, 988–994.
D2. Decker, D.L., W.A. Bassett, L. Merrill, H.T. Hall and J.D. Barnett, J. Phys. Chem. Ref. Data 1, 773–835.
E1. Egorov, L.A., E.V. Nitochkina and Yu.K. Orekin, Sov. Phys. JETP Lett. 16, 4–5.
G1. Grady, D.E., G.E. Duvall and E.B. Royce, J. Appl. Phys. 43, 1948–1955.
G2. Graham, R.A., J. Acoustical Soc. America 51, 1576–1581.
G3. Graham, R.A., Phys. Rev. B6, 4779–4792.
G4. Graham, R.A. and G.E. Ingram, J. Appl. Phys. 43, 826–835.
G5. Gust, W.H. and E.B. Royce, J. Appl. Phys. 43, 4437–4442.
H1. Hawke, R.S., D.E. Duerre, J.G. Huebel, H. Klapper, D.J. Steinberg and R.N. Keeler, J. Appl. Phys. 43, 2734–2741.
I1. Isbell, W.M., D.R. Christman and S.G. Babcock, U.S. Defense Nuclear Agency Report DASA 2501-6, AD741217.
J1. Johnson, J.N., J. Appl. Phys. 43, 2074–2082.
J2. Johnson, Q. and A.C. Mitchell, Phys. Rev. Lett. 29, 1369–1371.
J3. Jones, O.E., in: Behavior and Utilization of Explosives in Engineering Design, eds. L. Davison et al. (New Mexico Section, American Society of Mechanical Engineers, Albuquerque) pp. 125–148.
J4. Johnson, Q., A.C. Mitchell and L. Evans, Appl. Phys. Lett. 21, 29–30.
K1. Kalashnikov, N.G., L.V. Kuleshova and M.N. Pavlovskii, J. Appl. Mech. Tech. Phys. 13, 598–601.
K2. Kalitkin, N.N. and L.V. Kuz'mina, Sov. Phys.-Solid State 13, 1938–1942.
K3. Keeler, R.N., in: American Institute of Physics Handbook, ed. D.E. Gray (third ed., McGraw-Hill, New York) pp. 4–96 to 4–104.
K4. Kraut, E.A., T.C. Lim and B.R. Tittman, Ferroelectrics 3, 247–255.
K5. Kurdyumov, A.V., Sov. Phys.-Chrystallography 17, 534–538.
L1. Luukkala, M. and J. Surakka, J. Appl. Phys. 43, 2510–2518.
L2. Lysne, P.C., J. Appl. Phys. 43, 425–431.
L3. Lysne, P.C., J. Chem. Phys. 57, 492–494.

M1. Martin, R.M., Phys. Rev. B5, 1607–1613.
M2. Martin, R.M., in: [72B3] pp. 492–500.
N1. Novitskii, Ye.Z., Ye.S. Tyun'kin, V.N. Mineev and O.A. Kleshchevnikov, in: Goreniye i Vzryv (Izd vo Nauka, Moscow) pp. 602–607 (transl. ADIA-001190).
N2. Nunziato, J.W. and W. Herrmann, Archive Rational Mech. Analysis 47, 272–287.
P1. Podurets, M.A., G.V. Simakov, R.F. Trunin, L.V. Popov and B.N. Moiseev, Sov. Phys.-JETP 35, 375–376.
R1. Rohde, R.W., W.C. Leslie and R.C. Glenn, Met. Trans. 3, 323–328.
R2. Ross, M., J. Phys. Chem. Solids 33, 1105–1114.
S1. Shull, H.E. and K. Vedam, J. Appl. Phys. 43, 3724–3728.
S2. Stevens, A.L., L. Davison and W.E. Warren, J. Appl. Phys. 43, 4922–4927.
S3. Stevens, A.L. and O.E. Jones, J. Appl. Mech. 39, 359–366.
S4. Stöffler, D., Fortschr. Miner. 49, 50–113.
T1. Takahashi, K., Proc. 1971 Int. Conf. on the Mech. Behavior of Materials, Vol. 3 (Society of Materials Science, Japan) pp. 556–562.
T2. Thompson, S.L. and H.S. Lauson, Sandia Laboratories Report SC-RR-710714.
T3. Trunin, R.F., M.A. Podurets, G.V. Simakov, L.V. Popov and B.N. Moiseev, Sov. Phys.-JETP 35, 550–552.

1973 A1. Adadurov, G.A., V.I. Gol'danskii and P.A. Yampol'skii, Mendeleev. Chem. J. 18, 92–103.
A2. Andrews, D.J., J. Phys. Chem. Solids 34, 825–840.
B1. Borich, D.J. and D.E. Mikkola, in: [73R3] pp. 587–604.
B2. Bouchard, M. and F. Claisse, in: [73R3] pp. 619–630.
C1. Carter, W.J., in: [73R3] pp. 171–184.
C2. Carter, W.J., in: Phase Transitions – 1973, Proc. Conf. on Phase Transitions and Their Applications in Materials Science, ed. L.E. Cross (Pergamon Press, New York) pp. 223–234.
C3. Carter, W.J., High Temperatures-High Pressures 5, 313–318.
C4. Chen, P.J., in: Handbuch der Physik, Band VIa/3, ed. S. Flügge (Springer-Verlag, Berlin) pp. 303–402.
C5. Chen, P.J. and M.F. McCarthy, Instituto Lombardo di Scienze, Rendiconti (A) 107, 715–727.
C6. Chojnowski, E.A. and R.W. Cahn, in: [73R3] pp. 631–644.
C7. Chou, P.C. and A.K. Hopkins, editor, Dynamic Response of Materials to Intense Impulsive Loading (U.S. Air Force Materials Laboratory, Wright-Patterson Air Force Base).
C8. Curran, D.R., D.A. Shockey and L. Seaman, J. Appl. Phys. 44, 4025–4038.
D1. Davison, L. and A.L. Stevens, J. Appl. Phys. 44, 668–674.
D2. de Rosset, W., U.S. Army Ballistic Research Laboratories Report BRL-R-1631.
D3. Dietrich, A.M. and V.A. Greenhut, in: [73R3] pp. 645–658.
D4. Duvall, G.E., in: [73C7] pp. 481–516.
D5. Duvall, G.E., in: [73C7] pp. 89–121.
D6. Duvall, G.E., in: [73R3] pp. 1–13.
F1. Fowles, G.R., in: [73R3] pp. 15–31.
F2. Fowles, G.R., in: [73C7] pp. 405–480.
G1. Gaffney, E.S. and T.J. Ahrens, J. Geophys. Res. 78, 5942–5953.
G2. German, V.N., M.A. Podurets and R.F. Trunin, Sov. Phys.-JETP 37, 107.
G3. Ginsberg, M.J., D.E. Grady, P.S. DeCarli and J.T. Rosenberg, Stanford Research Institute Report DNA 3577F.
G4. Graham, R.A., Sol. State Comm. 12, 503–506.
G5. Gupta, Y.M. and G.R. Fowles, in: [73R3] pp. 367–378.
G6. Gust, W.H., A.C. Holt and E.B. Royce, J. Appl. Phys. 44, 550–561.
G7. Grover, R., I.C. Getting and G.C. Kennedy, Phys. Rev. B7, 567–571.
H1. Herrmann, W. and D.L. Hicks, in: [73R3] pp. 57–91.
H2. Herrmann, W. and J.W. Nunziato, in: [73C7] pp. 123–281.
J1. Jones, O.E., in: [73R3] pp. 33–55.
J2. Jones, W.B. and H.I. Dawson, in: [73R3] pp. 443–458.
J3. Julian, C.L. and F.O. Lane Jr., Phys. Rev. B7, 723–728.
K1. Kalashnikov, N.G., M.N. Pavlovskiy, G.V. Simakov and R.F. Trunin, Physics of the Solid Earth, 80–84.
K2. Kingman, P.W., in: [73R3] pp. 659–668.
K3. Kurdyumov, A.V., N.F. Ostrovskaya, A.N. Pilyankevich and I.N. Frantsevich, Sov. Phys.-Doklady 18, 268–269.
L1. Leslie, W.C., in: [73R3] pp. 571–586.
L2. Liu, C.Y., K. Ishizaki, J. Paauwe and I.L. Spain, High Temperatures-High Pressures 5, 359–388.
L3. Lysne, P.C., J. Appl. Phys. 44, 577–582.
L4. Lysne, P.C. and D.R. Hardesty, J. Chem. Phys. 59, 6512–6523.
N1. Novitskii, E.Z., O.A. Kleshchernikov, V.N. Mineev and A.G. Ivanov, Sov. Phys.-Solid State 15, 227–228.

N2. Novitskii, E.Z., V.V. Kolesnikov and R.V. Vedrinskii, Combustion, Explosion and Shock Waves 9, 778–782.
O1. O'Keeffe, D.J. and D.J. Pastine, in: [73R3] pp. 157–169.
O2. Orava, R.N., in: [73R3] pp. 129–155.
P1. Pope, L.E. and A.L. Stevens, in: [73R3] pp. 349–366.
P2. Prieto, F.E. and C. Renero, J. Appl. Phys. 44, 4013–4016.
R1. Read, H.E., in: [73R3] pp. 335–347.
R2. Ritter Jr., J.R., J. Chem. Phys. 59, 1538.
R3. Rohde, R.W., B.M. Butcher, J.R. Holland and C.H. Karnes, editors, Metallurgical Effects at High Strain Rates (Plenum Press, New York).
R4. Ross, M., Phys. Rev. A8, 1466–1474.
S1. Seaman, L., D.A. Shockey and D.R. Curran, in: Proc. Intern. Conf. on Dynamic Crack Propagation, ed. G.C. Sih (Noordhoff, Leyden) pp. 629–647.
S2. Shockey, D.A., C.F. Peterson, D.R. Curran and J.T. Rosenberg, in: New Horizons in Rock Mechanics (American Society of Civil Engineers, New York) pp. 709–738.
S3. Shockey, D.A., L. Seaman and D.R. Curran, in: [73R3] pp. 473–499.
S4. Stevens, A.L., L. Davison and W.E. Warren, in: Proc. Intern. Conf. on Dynamic Crack Propagation, ed. G.C. Sih (Noordhoff, Leyden) pp. 37–48.
S5. Stevens, A.L. and L.E. Pope, in: [73R3] pp. 459–472.
S6. Studt, P.L., E. Nidick, F. Uribe and A.K. Mukherjee, in: [73R3] pp. 379–400.
S7. Swan, G.W., G.E. Duvall and C.K. Thornhill, J. Mech. Phys. Solids 21, 215–227.
T1. Takahashi, K., J. Macromolecular Sci-Phys. B8, 673–689.
T2. Tarasov, B.A., J. Appl. Mech. Tech. Phys. 14, 850–852.
T3. Taylor, J.W., in: [73R3] pp. 101–128.
V1. Vdovykin, G.P., A.N. Dremin, S.V. Pershin and I.D. Shevaleevskii, Combustion, Explosion and Shock Waves 9, 464–468.
Y1. Yadav, H.S., D.S. Murty, S.N. Verma, K.H.C. Sinha, B.M. Gupta and D. Chand, J. Appl. Phys. 44, 2197–2200.
Y2. Yost, W.T. and M.A. Breazeale, J. Appl. Phys. 44, 1909–1910.

1974 A1. Anan'in, A.V., O.N. Breusov, A.N. Dremin, S.V. Pershin, A.I. Rogacheva and V.F. Tatsil, Combustion, Explosion and Shock Waves 10, 504–508.
A2. Anan'in, A.V., O.N. Breusov, A.N. Dremin, S.V. Pershin and V.F. Tatsil, Combustion, Explosion and Shock Waves 10, 372–379.
B1. Bassett, W.A. and T. Takahashi, in: [74W1] pp. 165–247.
B2. Bir, G.L. and G.E. Pikus, Symmetry and Strain-Induced Effects in Semiconductors, transl. P. Shelnitz, ed. D. Louvish (John Wiley, New York).
C1. Clifton, R.J., in: Mechanics Today, Vol. 1, ed. S. Nemat-Nasser (Pergamon Press, New York) pp. 102–167.
D1. Demarest Jr., H.H., J. Phys. Chem. Solids 35, 1393–1404.
D2. Deribas, A.A. and A.M. Staver, Combustion, Explosion and Shock Waves 10, 496–503.
D3. Dobratz, B.M., Lawrence Livermore Laboratory Report UCRL-51319 Rev. 1.
E1. Edwards, L.R. and L.C. Bartel, Phys. Rev. B10, 2044–2048.
F1. Fritz, I.J. and R.A. Graham, J. Appl. Phys. 45, 4124–4125.
G1. Graham, R.A., Proc. Satellite Symp. of the 8th Intern. Congress on Acoustics on Microwave Acoustics (University of Lancaster, England) pp. 124–129.
G2. Graham, R.A., J. Phys. Chem. Solids 35, 355–372.
H1. Herrmann, W., Sandia Laboratories Report SLA-73-0897.
H2. Horie, Y., J. Appl. Phys. 45, 759–764.
H3. Harrison, W.A., Phys. Rev. B10, 767–770.
J1. Johnson, J.N., J. Phys. Chem. Solids 35, 609–616.
J2. Johnson, J.N., D.B. Hayes and J.R. Asay, J. Phys. Chem. Solids 35, 501–515.
M1. Mitchell, A.C., M. van Thiel, N.L. Coleburn and J.W. Forbes, J. Appl. Phys. 45, 3856–3858.
M2. Morgan, J.A., High Temperatures-High Pressures 6, 195–201.
M3. Murri, W.J., D.R. Curran, C.F. Peterson and R.C. Crewdson, in: [74W1] pp. 1–163.
N1. Nesterenko, V.F. and A.M. Staver, Combustion, Explosion and Shock Waves 10, 811–813.
N2. Nesterenko, V.F. and A.M. Staver, Combustion, Explosion and Shock Waves 11, 105–109.
N3. Novikov, V.V. and V.N. Mineev, Sov. Phys.-JETP 40, 717–719.
N4. Nunziato, J.W., E.K. Walsh, K.W. Schuler and L.M. Barker, in: Handbuch der Physik, Band VIa/4, ed. S. Flügge (Springer-Verlag, Berlin) pp. 1–108.
P1. Pastine, D.J. and R.R. Bernecker, J. Appl. Phys. 45, 4458–4468.
R1. Ross, M.J., Chem. Phys. 60, 3634–3644.
S1. Sawaoka, A., T. Soma and S. Saito, Japan J. Appl. Phys. 13, 891–892.

S2. Seaman, L., J. Appl. Phys. 45, 4303–4314.
S3. Shockey, D.A., D.R. Curran, L. Seaman, J.T. Rosenberg and C.F. Peterson, Int. J. Rock Mech. Sci. and Geomech. Abstr. 11, 303–317.
S4. Simakov, G.V., M.N. Pavlovskiy, N.G. Kalashnikov and R.F. Trunin, Phys. of the Solid Earth, 488–492.
S5. Soma, T., A. Sawaoka and S. Saito, Material Res. Bull. 9, 755–762.
S6. Spieglan, M. and J.C. Jamieson, High Temperatures-High Pressures 6, 479–481.
S7. Syono, Y., T. Goto, J. Nakai and Y. Nakagawa, Proc. 4th Int. Conf. on High Pressure (Physico-Chemical Society of Japan) pp. 466–472.
S8. Syono, Y., T. Goto, J. Nakai, Y. Nakagawa and H. Iwasaki, J. Phys. Soc. Japan 37, 442–446.
T1. Thurston, R.N., in: Handbuch der Physik, Band VIa/4, ed. S. Flügge (Springer-Verlag, Berlin) pp. 109–308.
T2. Tsay, Y.F., S.S. Mitra and B. Bendow, Phys. Rev. B10, 1476–1481.
U1. Urtiew, P.A., J. Appl. Phys. 45, 3490–3493.
U2. Urtiew, P.A. and R. Grover, J. Appl. Phys. 45, 140–145.
V1. van Thiel, M., L.B. Hord, W.H. Gust, A.C. Mitchell, M. d'Addario, K. Boutwell, E. Wilbarger and B. Barrett, Phys. of the Earth and Planetary Interiors 9, 57–77.
V2. Vereschagin, L.F., E.N. Yakovlev, B.V. Vinogradov and V.P. Sakun, Sov. Phys.-JETP Lett. 20, 246–297.
W1. Wentorf Jr., R.H., editor, Advances in High Pressure Research, Vol. 4 (Academic Press, New York).
W2. Wentorf Jr., R.H., in: [74W1] pp. 251–281.

1975
A1. Antinenko, A.G., S.S. Nabatov and V.V. Yakushev, Combustion, Explosion and Shock Waves 11, 391–394.
A2. Arvidsson, T.E., Y.M. Gupta and G.E. Duvall, J. Appl. Phys. 46, 4474–4478.
A3. Asay, J.R. and D.B. Hayes, J. Appl. Phys. 46, 4789–4800.
A4. Asay, J.R., D.L. Hicks and D.B. Holdridge, J. Appl. Phys. 46, 4316–4322.
B1. Barker, L.M., J. Appl. Phys. 46, 2544–2547.
B2. Barnes, J.F., in: Thermodynamics of Nuclear Materials 1974, Vol. 1 (International Atomic Energy Agency, Vienna) pp. 327–339.
B3. Bavina, T.V., D.N. Breusov, A.N. Dremin and S.V. Pershin, Combustion, Explosion and Shock Waves 11, 660–662.
C1. Chang, C.P., U.K. Sinha, G. Rai and C.H. Ma, J. Phys. Chem. Solids 36, 1037–1040.
C2. Corrigan, F.R. and F.P. Bundy, J. Chem. Phys. 63, 3812–3820.
D1. Dick, J.J. and D.L. Styris, J. Appl. Phys. 46, 1602–1617.
F1. Flinn, J.E., G.E. Duvall, G.R. Fowles and R.F. Tinder, J. Appl. Phys. 46, 3752–3759.
F2. Fowles, G.R., Phys. Fluids 18, 776–780.
G1. Galbraith, J.M. and L.E. Murr, J. Materials Sci. 10, 2025–2034.
G2. Goto, T., Y. Syono, J. Nakai and Y. Nakagawa, Sci. Reports Res. Inst., Tôhoku University 25, 186–199.
G3. Grady, D.E., W.J. Murri and P.S. DeCarli, J. Geophys. Res. 80, 4857–4861.
G4. Graham, R.A., J. Appl. Phys. 46, 1901–1909.
G5. Graham, R.A. and P.J. Chen, Sol. State Comm. 17, 469–471.
G6. Graham, R.A. and L.C. Yang, J. Appl. Phys. 46, 5300–5301.
G7. Gupta, Y.M., J. Appl. Phys. 46, 3395–3401.
G8. Gupta, Y.M., G.E. Duvall and G.R. Fowles, J. Appl. Phys. 46, 532–546.
G9. Gagnepaign, J.J. and R. Besson, in: Physical Acoustics, Vol. XI, eds. W.P. Mason and R.N. Thurston (Academic Press, New York) pp. 245–289.
H1. Horning, R.R. and W.M. Isbell, Lawrence Livermore Laboratory Report UCRL-51682, Part 7.
H2. Huo, D.T.C. and C.H. Ma, J. Appl. Phys. 46, 699–701.
H3. Huo, D.T.C. and C.H. Ma, Acta Met. 23, 285–288.
K1. Kiselev, A.N., Combustion, Explosion and Shock Waves 11, 804–809.
K2. Korobov, A.I. and V.E. Lyamov, Sov. Phys.-Solid State 17, 932–933.
K3. Kurdyumov, A.V., Sov. Phys.-Doklady 29, 218–219.
K4. Kurdyumov, A.V. and I.N. Frantsevich, Sov. Phys.-Doklady 20, 235–236.
K5. Kurdyumov, A.V., A.N. Pilyankevich, V.P. Alekseevskii and V.V. Yarosh, Sov. Phys.-Tech. Phys. 20, 128–129.
L1. Luzin, A.N., Combustion, Explosion and Shock Waves 11, 744–750.
L2. Lysne, P.C., J. Appl. Phys. 46, 230–232.
L3. Lysne, P.C., J. Appl. Phys. 46, 4078–4079.
L4. Lysne, P.C. and L.C. Bartel, J. Appl. Phys. 46, 222–229.
L5. Lysne, P.C. and C.M. Percival, J. Appl. Phys. 46, 1519–1525.
M1. Morgan, J.A., High Temperatures-High Pressures 7, 65–70.
M2. Murr, L.E. and J.Y. Huang, Materials Sci. and Engineering 19, 115–122.
M3. Murr, L.E. and K.P. Staudhammer, Materials Sci. and Engineering 20, 35–46.
N1. Neal, T., J. Appl. Phys. 46, 2521–2527.

N2. Nesterenko, V.F., Combustion, Explosion and Shock Waves 11, 376–385.
N3. Nordstrom, T.V., R.W. Rohde and D.J. Mottern, Met. Trans. 6A, 1561–1567.
O1. Osugi, J., editor, Proc. Fourth Intern. Conf. on High Pressure (The Physico-Chemical Society of Japan, Kyoto).
P1. Pope, L.E. and J.N. Johnson, J. Appl. Phys. 46, 720–729.
S1. Simonov, I.V. and B.S. Chekin, Combustion, Explosion and Shock Waves 11, 237–242.
S2. Soma, T., A. Sawaoka and S. Saito, in: [75O1] pp. 446–453.
S3. Stein, C., Scripta Met. 9, 67–70.
S4. Swan, G.W. and G.R. Fowles, Phys. Fluids 18, 28–35.
S5. Samara, G.A., Chemical Phys. Lett. 33, 319–321.
T1. Tani, E., T. Soma, A. Sawaoka and S. Saito, Japan J. Appl. Phys. 14, 1605–1606.
Z1. Zhdanov, V.A. and V.V. Polyakov, Sov. Phys.-Solid State 17, 756–757.

1976 A1. Abou-Sayed, A.S. and R.J. Clifton, J. Appl. Phys. 47, 1762–1770.
A2. Abou-Sayed, A.S., R.J. Clifton and L. Hermann, Experimental Mechanics 16, 127–132.
A3. Akashi, T., A. Sawaoka, S. Saito and M. Araki, Japan J. Appl. Phys. 15, 891–892.
A4. Asay, J.R., Appl. Phys. Lett. 29, 284–287.
B1. Bakanova, A.A., V.N. Zubarev, Yu.N. Sutulov and R.F. Trunin, Sov. Phys.-JETP 41, 544–548.
B2. Bauer, F. and K. Vollrath, Ferroelectrics 12, 153–156.
B3. Bauer, F., K. Vollrath, Y. Fetiveau and L. Eyraud, Ferroelectrics 10, 61–64.
B4. Bedford, A., D.S. Drumheller and H.J. Sutherland, in: Mechanics Today, Vol. 3, ed. S. Nemat-Nasser (Pergamon Press) pp. 1–54.
B5. Brown, W.T. and R.A. Graham, Bull. Am. Phys. Soc. 21, 1292.
B6. Bless, S.J. and T.J. Ahrens, J. Geophys. Res. 81, 1935–1942.
C1. Chen, P.J., Selected Topics in Wave Propagation (Noordhoff International Publ., Leyden).
C2. Chen, P.J., L. Davison and M.F. McCarthy, J. Appl. Phys. 47, 4759–4764.
C3. Chen, P.J. and M.F. McCarthy, Archive Rational Mech. Analysis 62, 353–366.
C4. Chen, P.J., M.F. McCarthy and T.R. O'Leary, Archive Rational Mech. Analysis 62, 189–207.
D1. Dandekar, D.P., J. Appl. Phys. 47, 4703–4705.
D2. Dick, J.J., G.E. Duvall and J.E. Vorthman, J. Appl. Phys. 47, 3987–3991.
D3. Dremin, A.N. and G.I. Kanel', J. Appl. Mech. Tech. Phys. 17, 263–267.
D4. Duvall, G.E., in: [76V1] pp. 97–114.
E1. Edwards, D.J., editor, Proc. Sixth Symp. (Intern.) on Detonation, Office of Naval Research Report ACR-221.
G1. Glass, I.I. and S.P. Sharma, AIAA J. 14, 402–404.
G2. Goto, T., Y. Syono, J. Nakai and Y. Nakagawa, Sol. State Comm. 18, 1607–1609.
G3. Grady, D.E., W.J. Murri and K.D. Mahrer, J. Geophys. Res. 81, 889–893.
G4. Graham, R.A., Ferroelectrics 10, 65–69.
G5. Gupta, Y.M., Appl. Phys. Lett. 29, 694–697.
H1. Hardesty, D., J. Appl. Phys. 47, 1994–1998.
H2. Harding, J., Sci. Prog. 63, 575–603.
H3. Herrmann, W., in: [76V1] pp. 1–26.
K1. Kestenbach, H.-J. and M.A. Meyers, Met. Trans. 7A, 1943–1950.
K2. Kirzhnitz, D.A., Yu.E. Lozovik and G.V. Shpatakovskaya, Sov. Phys.-Uspekhi 18, 649–672.
K3. Kurdyumov, A.V., Sov. Phys.-Chrystallography 20, 596–598.
K4. Kurdyumov, A.V., Sov. Phys.-Solid State 17, 1641–1642.
L2. Lysne, P.C. and C.M. Percival, Ferroelectrics 10, 129–133.
M1. Marsh, E.T. and D.E. Mikkola, Scripta Met. 10, 851–856.
M2. Meyers, M.A. and R.N. Orava, Met. Trans. 7A, 179–190.
M3. Mikhailov, A.N., A.N. Dremin and V.P. Fettsov, Combustion, Explosion and Shock Waves 12, 538–545.
M4. Mineev, V.N. and A.G. Ivanov, Sov. Phys.-Uspekhi 19, 400–419.
M5. Murr, L.E., J. Appl. Phys. 47, 1364–1369.
M6. Murr, L.E., O.T. Inal and A.A. Morales, Acta Met. 24, 261–270.
N1. Neal, T., Phys. Rev. B14, 5172–5181.
N2. Nesterenko, V.F., Combustion, Explosion and Shock Waves 11, 376–385.
P1. Pleshanov, A.S., Combustion, Explosion and Shock Waves 12, 416–419.
R1. Rack, H.J., Met. Trans. 7A, 1571–1576. See also, Met. Trans. 8A, 1641–1644.
R2. Romain, J.P., A. Migault and J. Jacquesson, J. Phys. Chem. Solids 37, 1159–1165.
R3. Ross, M. and A.K. McMahan, Phys. Rev. B13, 5154–5157.
S1. Schuler, K.W., P.C. Lysne and A.L. Stevens, Int. J. Rock Mech. Mining Sci. and Geomech. Abstr. 13, 91–95.
S2. Seaman, L., D.R. Curran and D.A. Shockey, J. Appl. Phys. 47, 4814–4826.

T1. Tyunyaev, Yu.N. and V.N. Mineev, Sov. Phys.-Solid State 17, 2069–2070.
V1. Varley, E., editor, Propagation of Shock Waves in Solids (The American Society of Mechanical Engineers, New York).
V2. Vedam, K., J.A. Meyers and G.R. Mariner, J. Appl. Phys. 47, 2443–2446.
Z1. Zhdanov, V.A. and V.V. Polyakov, J. Appl. Mech. Tech. Phys. 17, 699–703.
Z2. Zhdanov, V.A. and V.V. Polyakov, Sov. Phys.-Solid State 17, 2230–2232.
1977 A1. Al'tshuler, L.V., N.N. Kalitkin, L.V. Kuz'mina and B.S. Chekin, Sov. Phys.-JETP 45, 167–171.
A2. Asay, J.R., Sandia Laboratories Report SAND 77-0731.
A3. Asay, J.R., J. Appl. Phys. 48, 2832–2844.
B1. Bauer, F., Thése, University of Lyon.
B2. Bundy, F.P., in: [77S3] Vol. II, pp. 321–338.
C1. Cochran, S. and D. Banner, J. Appl. Phys. 48, 2729–2737.
C2. Curran, D.R., L. Seaman and D.A. Shockey, Phys. Today 30, 46–55.
D1. Davison, L., A.L. Stevens and M.E. Kipp, J. Mech. Phys. Solids 25, 11–28.
D2. Degtyareva, V.F. and V.N. Sikorov, Sov. Phys.-Solid State 19, 1289–1290.
D3. Deribas, A.A. and A.M. Staver, Combustion, Explosion and Shock Waves 13, 410–413.
D4. Dorph, K., Scandinavian J. Met. 6.
D5. Dubovitskii, D.I., abstract in Combustion, Explosion and Shock Waves 13, 421.
D6. Duvall, G.E. and R.A. Graham, Rev. Modern Phys. 49, 523–579.
D7. Duvall, G.E., J. Appl. Phys. 48, 4415.
G1. Graboske, H. and L. Wong, Lawrence Livermore Laboratory Report UCRL 52323.
G2. Grady, D.E., in: [77M7] pp. 389–438.
G3. Grady, D.E. and M.J. Ginsberg, J. Appl. Phys. 48, 2179–2181.
G4. Graham, R.A., Appl. Phys. Lett. 30, 307–309.
G5. Graham, R.A., IEEE Trans. Sonics and Ultrasonics SU-24, 137.
G6. Graham, R.A., J. Appl. Phys. 48, 2153–2163.
G7. Gupta, Y.M., J. Appl. Phys. 48, 5067–5073.
G8. Grover, R., in: Proc. Seventh Symp. on Thermophysical Properties, ed. A. Cezairliyan (The American Society of Mechanical Engineers, New York) pp. 67–74.
H1. Hardy, R.J., J. Phys. Chem. Solids 38, 335–344.
H2. Hardy, R.J. and A.M. Karo, J. Phys. Chem. Solids 38, 905–911.
H3. Hayes, D.B., Sandia Laboratories Report SAND 77-0267C.
H4. Helliwell K., R.C. Hanson and C. Schwab, Proc. 1977 IEEE Ultrasonics Symp. (The Institute of Electrical and Electronics Engineers, New York) pp. 317–320.
K1. Kalthoff, J.F. and D.A. Shockey, J. Appl. Phys. 48, 986–993.
K2. Kim, K.-S., R.J. Clifton and P. Kumar, J. Appl. Phys. 48, 4132–4139.
K3. Kuleshova, L.V. and M.N. Pavlovskii, J. Appl. Mech. Tech. Phys. 18, 689–692.
K4. Kumar, P. and R.J. Clifton, J. Appl. Phys. 48, 4850–4852.
L1. Lawrence, R.J. and L. Davison, in: Proc. Symp. Applications of Computer Methods in Engineering, Vol. II, ed. L.C. Welford Jr., pp. 941–950.
L2. Lipkin, J. and J.R. Asay, J. Appl. Phys. 48, 182–189.
L3. Lysne, P.C., J. Appl. Phys. 48, 1020–1023.
L4. Lysne, P.C., J. Appl. Phys. 48, 1024–1031.
L5. Lysne, P.C., J. Appl. Phys. 48, 4565–4568.
M1. McMahan, A.K. and M. Ross, Phys. Rev. B15, 718–725.
M2. Meier, L.D. and T.J. Ahrens, J. Geophys. Res. 82, 2523–2528.
M3. Meyers, M.A., Materials Sci. and Engineering 30, 99–111.
M4. Meyers, M.A., Met. Trans. 8A, 1581–1583.
M5. Migault, A. and J.P. Romain, J. Phys. Chem. Solids 38, 555–556.
M6. McMahan, A.K., B.L. Hord and M. Ross, Phys. Rev. B15, 726–737.
M7. Manghnani, M.H. and S. Akimoto, editors, High Pressure Research Applications in Geophysics (Academic Press, New York).
N1. Neal, T., J. Phys. Chem. Solids 38, 225–231.
N2. Nesterenko, V.F., abstract in: Combustion, Explosion and Shock Waves 13, 421.
N3. Novitskii, E.Z., V.A. Ogorodnikov and S.Yu. Pinchuk, Combustion, Explosion and Shock Waves 13, 221–224.
P1. Pavlovskii, M.N., Sov. Phys.-JETP 46, 122–126.
R1. Ragan III, C.E., M.G. Silbert and B.C. Diven, J. Appl. Phys. 48, 2860–2870.
R2. Ross, M. and C. Shishkevish, Rand Report R-2056-ARPA.
R3. Ruoff, A.L. and L.C. Chhabildas, Cornell Materials Science Center Report 2853. See also [79T1] pp. 19–32.

S1. Stanton, P.L. and R.A. Graham, Appl. Phys. Lett. 31, 723–725.
S2. Seigel, A.E., in: [77S3] Vol. II, pp. 481–521.
S3. Spain, I.L. and J. Paauwe, editors, High Pressure Technology (Marcel Dekker, New York).
T1. Teslenko, T.S., Combustion, Explosion and Shock Waves 13, 102–106.
T2. Tsay, Y.F. and B. Bendow, Phys. Rev. B16, 2663–2675.
U1. Urtiew, P.A. and R. Grover, J. Appl. Phys. 48, 1122–1126.
V1. van Thiel, M., J. Shaner and E. Salinas, Lawrence Livermore Laboratory Report UCRL 50108, Vols. 1 and 2, Rev. 1, Vol. 3.
W1. Wilson, W.D., in: [77S3] Vol. II, pp. 293–320.

1978 A1. Amos, D.E. and P.J. Chen, J. Appl. Mech. 45, 749–754.
A2. Amos, D.E. and P.J. Chen, to be published.
A3. Asay, J.R., J. Appl. Phys. 49, 6173–6175.
A4. Asay, J.R., L.C. Chhabildas and D.P. Dandekar, private communication.
A5. Asay, J.R. and J. Lipkin, J. Appl. Phys. 49, 4242–4247.
A6. Al'tshuler, L.V., J. Appl. Mech. Tech. Phys. 19, 496–505.
B1. Barlett, R., S. Cochran, L. Erickson, J. Chan, R. Lee and R. Weingart, Bull. Am. Phys. Soc. 23, 37.
B2. Bennett, B.I., J.D. Johnson, G.I. Kerley and G.T. Rood, Los Alamos Scientific Laboratory Report LA-7130.
B3. Bijanki, S. and R.J. Hardy, J. Appl. Phys. 49, 215–222.
B4. Birch, F., J. Geophys. Res. 83, 1257–1268.
B5. Bloomquist, D.D., Thesis, Washington State University.
B6. Bloomquist, D.D., G.E. Duvall and J.J. Dick, Washington State University Report F49620-77-COO34.
B7. Brown, W.T. and P.J. Chen, J. Appl. Phys. 49, 3446–3450.
B8. Brown, W.T. and R.A. Graham, Bull. Am. Phys. Soc. 23, 34.
C1. Cantrell Jr., J.H. and M.A. Breazeale, Phys. Rev. B17, 4864–4870.
C2. Carter, W.J. and S.P. Marsh, private communication.
C3. Chhabildas, L.C., private communication.
D1. Dick, J.J. and J.E. Vorthman, J. Appl. Phys. 49, 2494–2498.
D2. Dubovitskii, F.I., editor, Detonation: Critical Phenomena of Physico-Chemical Transformations in Shock Waves (Academy of Sciences, USSR, Section of Institute of Chemical Physics, Chernogolova).
E1. Edwards, L.R., private communication.
F1. Fritz, I.J., J. Appl. Phys. 49, 4922–4928.
F2. Fritz, I.J. and J.D. Keck, J. Phys. Chem. Solids 39, 1163–1167.
G1. Ganin, E., Y. Komem and A. Rosen, Materials Sci. and Engineering 33, 1–4.
G2. Grady, D.E., to be published.
G3. Graham, R.A., Bull. Am. Phys. Soc. 23, 35.
G4. Graham, R.A., present work.
G5. Graham, R.A. and J.R. Asay, High Temperatures-High Pressures 10, 355–390.
G6. Gupta, Y.M., D.D. Keough, H. Ito, D. Henley and D.F. Walter, Bull. Am. Phys. Soc. 23, 385.
G7. Graham, R.A. and R.P. Reed, Sandia Laboratories Report SAND 78-1911.
H1. Hawke, R.S., D.E. Duerre, J.G. Huebel, R.N. Keeler and W.C. Wallace, J. Appl. Phys. 49, 3298–3303.
H2. Hayes, D.B. and R.A. Graham, Bull. Am. Phys. Soc. 23, 70.
H3. Hruska, C.K., IEEE Trans. Sonics and Ultrasonics SU-25, 198–203.
J1. Jamet, F. and F. Bauer, presented at Symp. HDP, Paris, August 27–31, 1978.
K1. Kanel', G.I., A.M. Molodets and A.N. Dremin, Combustion, Explosion and Shock Waves 13, 772–777.
K2. Kanel', G.I., G.G. Vakhitova and A.N. Dremin, Combustion, Explosion and Shock Waves 14, 244–247.
L1. LaRouche, S. and D.E. Mikkola, Scripta Met. 12, 543–547.
L2. Lee, J.J. and C.H. Ma, J. Materials Sci. 13, 43–46.
L3. Lysne, P.C., J. Appl. Phys. 49, 4180–4185.
L4. Lysne, P.C., J. Appl. Phys. 49, 4186–4190.
L5. Lysne, P.C., J. Appl. Phys. 49, 4296–4297.
L6. Lysne, P.C., Bull. Am. Phys. Soc. 23, 35, and private communication.
L7. Lysne, P.C., unpublished manuscript.
M1. Mao, H.K. and P.M. Bell, Science 200, 1145–1147.
M2. Mao, H.K., P.M. Bell, J.W. Shaner and D.J. Steinberg, J. Appl. Phys. 49, 3276–3283.
M3. McMahan, A.K., Phys. Rev. B17, 1521–1527.
M4. Ming, L.-C. and M.H. Manghnani, J. Appl. Phys. 49, 208–212.
M5. Mock Jr., W. and W.H. Holt, U.S. Naval Surface Weapons Center Report NSWC/DL TR-3781. (See also J. Appl. Phys. 50, 2740–2748.)

M6. Mock Jr., W. and W.H. Holt, U.S. Naval Surface Weapons Center Report NSWC/DL TR-3804. (See also J. Appl. Phys. 49, 5846–5854.)
M7. Moin, E. and L.E. Murr, Scripta Met. 12, 575–576.
M8. Murr, L.E., Scripta Met. 12, 201–206.
M9. Murr, L.E. and D. Kuhlmann-Wilsdorf, Acta Met. 26, 847–857.
M10. Murr, L.E., E. Moin, K. Wongwiwat and K.P. Staudhammer, Scripta Met. 12, 425–429.
M11. Müller, F. and E. Schulte, Z. Naturforsch. 33a, 918–923.
N1. Nellis, W.J., A.C. Mitchell and R.N. Keeler, Bull. Am. Phys. Soc. 23, 105.
N2. Nunziato, J.W. and D.S. Drumheller, Int. J. Solids Structures 14, 545–558.
N3. Nunziato, J.W. and E.K. Walsh, Int. J. Solids Structures 14, 681–689.
R1. Rosenberg, G., Washington State University Report WSU SDL 78-01.
R2. Rack, H.J., Scripta Met. 12, 1007–1010.
S1. Schmidt, R.M., F.W. Davies, B.M. Lempriere and K.A. Holsapple, J. Phys. Chem. Solids 39, 375–385.
S2. Seaman, L., D.R. Curran and R.C. Crewdson, J. Appl. Phys. 49, 5221–5229.
S3. Shockey, D.A., K.C. Dao and R.L. Jones, SRI International Project PYU Report, AD AO57373.
S4. Stanton, P.L. and R.A. Graham, J. Appl. Phys. (submitted).
S5. Steinberg, D., H. Chau, G. Dittbenner and R. Weingart, Lawrence Livermore Laboratory Report UCID 17943.
S6. Syassen, K. and W.B. Holzapfel, J. Appl. Phys. 49, 4427–4429.
T1. Trefilov, V.I., G.I. Savvakin, V.V. Skorokhod, Yu.M. Solonin and A.F. Khienko, Sov. Phys.-Doklady 23, 269–271.
V1. Veeser, L.R. and J.C. Solem, Phys. Rev. Lett. 40, 1391–1394.
W1. Wada, M., T. Nakamura and N. Kinoshita, Philos. Mag. A38, 167–185.
W2. Welch, D.O., G.J. Dienes and A. Paskin, J. Phys. Chem. Solids 39, 589–603.
W3. Wongwitwat, K. and L.E. Murr, Materials Sci. and Engineering 35, 273–285.
W4. Wright, R.N. and D.E. Mikkola, Bull. Am. Phys. Soc. 23, 71.
Y1. Yakushev, V.V., Combustion, Explosion and Shock Waves 14, 131–146.

1979 A1. Ahrens, T.J., J. Geophys. Res. 84, 985–998.
B1. Brown, W.T., Bull. Am. Phys. Soc. 24, 711.
C1. Chhabildas, L.D., H.J. Sutherland and J.R. Asay, J. Appl. Phys., to be published.
C2. Chhabildas, L.C. and J.R. Asay, J. Appl. Phys. 50, 2749–2756.
D1. Davison, L. and M.E. Kipp, in: High Velocity Deformation of Solids, eds. K. Kawata and J. Shioiri (Springer-Verlag, Berlin) 163–175.
D2. DeCarli, P.S., in: [79T1] pp. 940–943.
G1. Goto, T., G.R. Rossman and T.J. Ahrens, in: [79T2] pp. 895–904.
G2. Graham, R.A., in [79T2] pp. 854–869.
G3. Grady, D.E. and R.E. Hollenbach, Geophys. Res. Lett. 6, 73–76.
G4. Gupta, Y.M., private communication.
G5. Graham, R.A., submitted for publication.
G6. Graham, R.A., Bull. Am. Phys. Soc. 24, 711.
K1. Kim, K.S. and R.J. Clifton, private communication.
K2. Koller, L.R. and G.R. Fowles, in: [79T2] pp. 927–934.
K3. Kondo, K., A. Sawaoka and S. Saito, in: [79T2] pp. 905–910.
L1. Lysne, P.C., in: [79T1] pp. 202–209.
M1. Mitchell, A.C. and W.J. Nellis, in: [79T1] pp. 428–434.
M2. McMahan, A.K. and M. Ross, in: [79T2] pp. 920–926.
N1. Nunziato, J.W. and S.C. Cowin, Archive Rational Mech. Analysis, to be published.
N2. Neal, T., in: [79T1] pp. 80–87.
N3. Novitskii, E.Z., V.D. Sadunov and G.Ya. Karpenko, Combustion, Explosion and Shock Waves 14, 505–516.
S1. Saito, S., A. Sawaoka and M. Araki, in: [79T1] pp. 986–993.
S2. Stanton, P.L. and R.A. Graham, J. Appl. Phys., to be published.
S3. Steinberg, D.J. and D.L. Banner, J. Appl. Phys. 235–238.
S4. Setchell, R.E., submitted for publication.
T1. Timmerhaus, K.D. and M.S. Barber, eds., High Pressure Science and Technology, Sixth AIRAPT Conf., Vol. 1, Physical Properties and Material Synthesis (Plenum Press, New York).
T2. Timmerhaus, K.D. and M.S. Barber, eds., High Pressure Science and Technology, Sixth AIRAPT Conf., Vol. 2, Applications and Mechanical Properties (Plenum Press, New York).
T3. Trainor, R.J., J.W. Shaner, J.M. Auerbach and N.C. Holmes, Phys. Rev. Lett. 42, 1154–1157.

Index of frequently used symbols*

Symbol	Name(s) or meaning(s)	Place of definition or first occurrence
A	Area of charge-collecting electrode	4.2.1
a	Coefficient in linear (U, u) relation; lattice constant	2.2; 4.5
b	Coefficient in linear (U, u) relation; Burgers' vector	2.2; 3.3.2
C_v	Specific heat at constant volume	2.2
$C_{ijkl}\ldots$	Elastic stiffness constants in tensor or Voigt notation	3.1
$\boldsymbol{D}(D_i)$	Electric displacement vector	4.2.1
$\boldsymbol{d}(d_i)$	Kinematical displacement vector	2.1
E_g	Energy gap	4.5 and 4.9
$\boldsymbol{E}(E_i)$	Electric field vector	4.2.1
e; $e_{ijkm}\ldots$	Electronic charge; piezoelectric stress constants	4.9
$\boldsymbol{F}(F_{ij})$; $\hat{F}$	Deformation gradient tensor; Maxwell relaxation function	2.1, 3.3.2
f_{ijkl}	Electrostrictive constants	4.2.1
H	Magnetic field	4.8
$\mathscr{H}$	Designates Hugoniot curve on figures	2.2
i	Electric current	4.2.1
$\mathscr{I}$	Designates isentrope on figures	2.2
K	Bulk elastic stiffness; electromagnetic coupling factor	3.1; 4.2.1
L	Initial thickness of material plate	4.4
M, M_s	Magnetization	4.8
N; N_A, N_D	Dislocation density; acceptor and donor ion densities	3.3.2; 4.9
n; n; $\boldsymbol{n}$	Electron density; refractive index; wavefront normal	4.9; 5.1; 2.1
p	Pressure; semiconductor hole density	2.1; 4.9
$\boldsymbol{P}(P_i)$	Polarization vector	4.2.1
Q; Q_0	Electric charge; effective polarization	4.3; 4.5
R; R_n, R_p	Gas constant; ratios	3.2.6; 4.9
$\mathscr{R}$	Designates Rayleigh line on figures	2.2
$\boldsymbol{S}(S_{ij}$ or $S_i)$	Linearized strain tensor	2.1, 3.1
s	Entropy density	2.2
$\mathscr{S}$	Set of shock jump variables	2.2
t	Elapsed time	2.1
$\boldsymbol{t}(t_{ij}$ or $t_i)$	Cauchy stress tensor	2.1, 3.1
U	Material propagation velocity for a plane shock	2.1
$\boldsymbol{u}(u_i)$; u_n	Particle velocity vector; spatial velocity of a shock	2.1
V; V_d	Electrical potential difference; dislocation velocity	4.2.1; 3.3.2
v	Specific volume	2.1
$\boldsymbol{X}(X_i)$, X	Material coordinates (points in reference configuration)	2.1
$\boldsymbol{x}(x_i)$, x	Spatial coordinates (points in space)	2.1
α	Permittivity ratio; coefficient in eq. (5.1)	4.2.1; 5.1
β	Electronic Grüneisen parameter; coefficient in eq. (5.1)	3.2.6; 5.1
γ	Tensor component of shear strain; Grüneisen's parameter; electronic factor	2.1; 2.1; 4.5
δ_{ij}	$= 1$ for $i = j$, 0 otherwise	2.1
ε; ε, ε_{ij}	Internal energy density; dielectric permittivity	2.1; 4.2.1
$\boldsymbol{\eta}(\eta_{ij}$ or $\eta_i)$	Material strain tensor	2.1, 3.1
θ	Absolute temperature	2.2
μ; μ_n, μ_p	Shear stiffness coefficient; electron and hole mobilities	3.1; 4.9
ρ	Mass density	2.1
σ	Electric conductivity	4.9
τ; τ_0	Maximum shear stress or dielectric relaxation time; dislocation back stress	2.1, 4.7; 3.3.2
χ	Thermal diffusivity	3.4

* Special notations used only in a single section are not listed unless deemed to present unusual potential for confusion. Tensile stress and strain are assigned positive sign.

Subscripts		
c	Cold compression curve	3.2.6
e	Electronic contribution; referring to electron	3.2.6; 4.9
ijk ...	Tensoral or Voigt indices	2.1, 3.1
R	Value in reference configuration	2.1
H	Hugoniot curve	2.2
0	(Zero) initial value	
Superscripts		
e	Elastic contribution	3.3.2
HEL	Evaluated at Hugoniot elastic limit	3.1
$\boldsymbol{E}$	Constant electric field	4.2.1
p	Plastic contribution	3.3.2
s	Constant entropy	2.1
θ	Thermal contribution	2.3.6
$+;-$	In advance of a shock; following a shock	2.1
$[\ldots]$	Indicates the jump in a variable across a shock	2.1